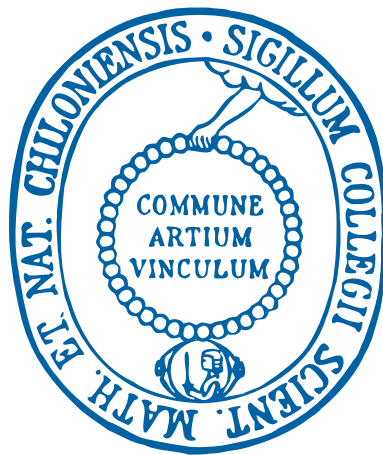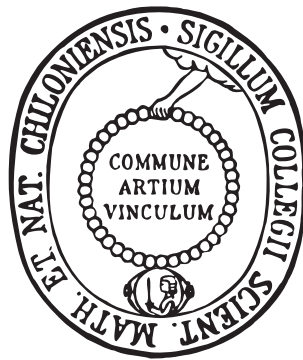# SO208 PLUMEFLUX:
Distribution of Galápagos plume material in the equatorial East Pacific Ocean

Kiel

2014

SO208 PLUMEFLUX:
Distribution of Galápagos plume material in the equatorial East Pacific Ocean

Dissertation

zur Erlangung des Doktorgrades der

Mathematisch-Naturwissenschaftlichen Fakultät

Christian-Albrechts-Universität

zu Kiel

vorgelegt von

Antje Herbrich

Kiel, 2014

Erstgutachter: . . . . Prof. Dr. Kaj Hoernle

Zweitgutachter: . . . . Dr. habil. Jörg Geldmacher

Tag der mündlichen Prüfung: 17.11.2014

Zum Druck genehmigt: Kiel, ... 03.05.2016

Der Dekan

Vorwort

Diese Arbeit stellt ihrer Gesamtheit zwar eine monographische Dissertation dar, dennoch sind die einzelnen Kapitel in ihrem Aufbau so konzipiert, dass sie unabhängig voneinander publiziert werden können. Daraus ergibt sich der Umstand, dass, obwohl eine Einleitung vorangestellt ist, jedes Kapitel für sich eine eigene Einleitung, Diskussion und ein Literaturverzeichnis enthält.

Kapitel 2 wurde zur Veröffentlichung in der internationalen Fachzeitschrift *Lithos* angenommen, während Kapitel 3 und 4 zur Einreichung bei *Geochimica et Cosmochimica Acta* beziehungsweise *Chemical Geology* vorgesehen sind.

Kiel, 30.10.2014
Antje Herbrich

Preface

This dissertation represents in its whole a monograph but is composed of three independent Chapters that are either accepted for publication or in preparation for submission to an international journal. Due to this circumstance and even though this dissertation is prefaced by a comprehensive introduction, each chapter contains an individual introduction, discussion and reference list.

Chapter 2 is accepted for publication in the international journal *Lithos*, while chapter 3 and 4 are in preparation for submission to *Geochimica et Cosmochimica Acta* and *Chemical Geology*, respectively.

Kiel, 30.10.2014
Antje Herbrich

Contents

Zusammenfassung

Gegenstand der vorliegenden Dissertation ist die Untersuchung der Verbreitung von Galápagosplumematerial im äquatorialen Ostpazifik. Am Beispiel des Galápagosplume in Verbindung mit dem benachbarten Galápagosspreizungzentrum (GSC; auch als Cocos-Nazca-Spreizungszentrum (CNS) bezeichnet) soll diese Arbeit zu einem besseren Verständnis von Plume-Rücken-Wechselwirkungen und Materialtransport im oberen Mantel beitragen. Der Schwerpunkt wurde dabei auf die räumliche Ausdehnung von Galápagosplumematerial im äquatorialen Ostpazifik (Teilprojekt 1) und die zeitliche Entwicklung des Galápagosplume-Galápagosspreizungszentrum-Systems (Teilprojekt 2) gelegt. Die dafür analysierten Proben wurden während der Forschungsfahrt SO208 mit dem deutschen Forschungsschiff *Sonne* im Juli/August 2010 gewonnen.

In Teilprojekt 1 geht es um den Ursprung und das Alter von Intraplattenvulkanen (Seamounts) die vor der Küste Nordwest-Costa Ricas/SW Nicaraguas auf dem Teil der Cocosplatte liegen, die am Ostpazifischenrücken (EPR) gebildet wird. In diesem Gebiet gibt es eine ungewöhnlich hohe Anzahl an Seamounts deren Entstehung mit herkömmlichen Modellen nur schwer zu erklären ist. Dabei geht es vor allem darum, ob diese Seamounts am EPR gebildet wurden oder durch einen weiträumigen Transport von Galápagosplumematerial.

Insgesamt wurden 19 dieser Seamounts beprobt und auf ihre geochemische Zusammensetzung (Haupt- und Spurenelemente, Sr-Nd-Pb Isotopenverhältnisse) untersucht. Um die geochemischen Daten in einen zeitlichen Kontext zu setzen, wurden zusätzlich noch ^{40}Ar/^{39}Ar-Altersdatierungen durchgeführt. Die, auf ihr Alter untersuchten Seamounts können in zwei Gruppen unterteilt werden: a) Seamounts mit einem Alter $\pm 2\,$Ma dem der darunter liegenden Kruste, b) Seamounts mit einem Alter mehr als $2\,$Ma jünger als die darunter liegende Kruste.

Geochemisch stellen die Seamounts eine Mischung einer angereicherten Galápagosplumekomponente, mit zwei unterschiedlich verarmten Komponenten dar. Eine dieser ver-

armten Komponenten ist ähnlich der Zusammensetzung wie sie am Ostpazifischen Rücken (EPR) vorkommt. Die zweite verarmte Komponente ist hingegen in den inkompatiblen Elementen stärker verarmt. Seamounts die mit dem Alter der darunter liegenden Kruste korrelieren, müssen am oder in der Nähe des EPR entstanden sein. Ihre Entstehung fällt mit der Zeit des superschnellen Spreizens (180-210 mm/a; Geldmacher *et al.*, 2013) am EPR (zwischen $\sim$23-11 Ma) zusammen. Während dieser Zeit floss, aufgrund der durch das superschnelle Spreizen ausgelösten Sogwirkung, Galápagosplumematerial zum EPR vermischte sich mit verarmten oberen Mantel und eruptierte am oder in der Nähe der Rückenachse.

Seamounts die deutlich jünger als die darunter liegende Kruste sind können nicht durch diesen Mechanismus erklärt werden. Sie deuten vielmehr auf Intraplattenvulkanismus hin. Diese Seamounts stellen geochemisch eine Mischung aus einer angereicherten Ozeaninsel-basaltkomponente, wie die Nördliche Galápagosplumekomponente (Hoernle *et al.*, 2000), mit einer verarmten Komponente aus dem oberen Mantel (z.B. Mitellozeanischer Rück-enbasalt (MORB) oder verarmte Galápagosplumekomponente) dar. Durch den nordwärts gerichteten Fluss von Galápagosplumematerial aufgrund der Lage des Galápagosplume nördlich des GSC wurde Plumematerial bis zu 900 km weit an der Basis der Cocosplatte transportiert und führte aufgrund von adiabtischen Schmelzen zu der Entstehung der Seamounts.

Teilprojekt 2 befasst sich mit der zeitlichen Entwicklung der Wechselwirkung zwischen dem Galápagosplume und dem benachbarten Galápagosspreizungszentrum. Der Galá-pagosplume mit dem angrenzenden Galápagosspreizungszentrum bietet aufgrund der lang-lebigen geochemischen Zonierung des Galápagosplumes ($>$15 Ma; Hoernle *et al.*, 2000; Geldmacher *et al.*, 2003; Werner *et al.*, 2003) eine weltweit einzigartige Möglichkeit Plume-Rücken-Interaktion und Transportprozesse im oberen Mantel zu untersuchen. Dafür wurde eine detaillierte Beprobung der Ozeankruste entlang des GSC an vier Profilen von der GSC-Rückenachse bis zu 60 km nördlich bzw. südlich (Profile 1, 3, 4, 5) der Rückenachse und das Gebiet direkt östlich der 91°W Transformstörung (Studiengebiet 2) durchgeführt.

Profil 1 ($\sim$92°W) erstreckt sich von der Rückenachse am westlichen Galápagosspreizungs-zentrum (WGSC) bis zu 50 km nach Norden. In diesem Bereich des WGSC erfolgt ein starker Eintrag von Galápagoslumematerial in das GSC, sowohl morphologisch als auch geochemisch nachweisbar (z.B. Schilling *et al.*, 2003; Christie *et al.*, 2005; Ingle *et al.*, 2010; Colman *et al.*, 2012). Profil 1 deckt die Entwicklung des WGSC über eine Zeitspanne von 1.6 Ma ab. Diese Proben können durch eine Mischung zweier unterschiedlich ver-

armter Komponenten (MORB und verarmte Galápagosplumekomponente) mit einer angereicherten Komponente erklärt werden. Allerdings bietet keine der Galápagosplumekomponenten die passende Zusammensetzung um als angereichertes Endglied geeignet zu sein. Ein Seamount ca. 23 km nördlich der Rückenachse (Seamount DR63) ist von extremer geochemischer Zusammensetzung und bietet dadurch das angereicherte Endglied für das Mischungssignal aller WGSC-Krustenproben.

Basierend auf ihren Sr-Nd-Pb-Isotopenverhältnissen können die WGSC-Proben in zwei Gruppen unterteilt werden: a) <30 km von der WGSC-Rückenachse und b) >30 km von der WGSC-Rückenachse. Proben beider Gruppen zeigen mit zunehmender Entfernung von der Rückenachse und demnach zunehmenden Alter wenig bis keine geochemische Variationen. Dies deutet auf einen konstanten Plumeeintrag in den letzten ∼1.6 Ma hin. Die Proben der älteren Gruppe (>30 km Entfernung von der Rückenachse) jedoch, scheinen zusätzlich noch durch eine EMII-ähnliche Komponente beeinflusst worden zu sein.

Studiengebiet 2, Profil 3 bis Profil 5 und ein einzelner Seamount auf der Rückenachse wurden am östlichen Galápagosspreizungszentrum (EGSC) beprobt. Das Gebiet östlich der 91°W Transformstörung (∼90°50'W) wird als das Zentrum für den Galápagosplumeeintrag am EGSC verstanden (Studiengebiet 2). Die Proben die aus diesem Bereich analysiert wurden, deuten auf einen Eintrag der zentralen Galápagosplumekomponente hin, die sich weiter nach Osten zunehmend mit einer verarmten Komponente vermischt.

Profil 3 bis Profil 5 wurden von der Rückenachse bis zu 60 km nördlich bzw. südlich der Rückenachse beprobt. Anders als bei Profil 1 ist die zeitliche Entwicklung des EGSC und damit auch die Profile durch Sprünge der Rückenachse zum Plume hin beeinflusst. Aufgrund dessen zeigt die EGSC-Kruste keine lineare Alterszunahme mit zunehmender Entfernung vom Rücken, sondern ist durch Altersprünge von bis zu ∼1.3 Ma gekennzeichnet. Ungeachtet der Altersprünge, deuten die starken geochemischen Variationen in den Proben bis 1.17 Ma in Profil 3 (89°30'W) einen rivalisierenden Eintrag zweier Komponenten an. Sowohl in den inkompatiblen Spurenelementen als auch in den Isotopenverhältnissen zeigt dieses Profil eine große Spannbreite von sehr verarmten bis hin zu stark angereicherten Zusammensetzungen. Zusammen mit geochemischen und morphologischen Anomalien in anderen Profilen (Seamounts/Lava Plateaus) deutet dies auf einen zusätzlich kurzzeitigen Eintrag von angereicherten Plumematerial entlang des EGSC hin.

Literatur

Christie, D. M., Werner, R., Hauff, F., Hoernle, K. & Hanan, B. B., 2005. Morphological and geochemical variations along the eastern Galápagos Spreading Center. *Geochemistry, Geophysics, Geosystems*, **6**, Q01006.

Colman, A., Sinton, J. M., White, S. M., McClinton, J. T., Bowles, J. A., Rubin, K. H., Behn, M. D., Cushman, B., Eason, D. E., Gregg, T. K. P., Grönvold, K., Hidalgo, S., Howell, J., Neill, O. & Russo, C., 2012. Effects of variable magma supply on mid-ocean ridge eruptions: Constraints from mapped lava flow fields along the Galápagos Spreading Center. *Geochemistry, Geophysics, Geosystems*, **13**, Q08014.

Geldmacher, J., Hanan, B. B., Blichert-Toft, J., Harpp, K., Hoernle, K., Hauff, F., Werner, R. & Kerr, A. C., 2003. Hafnium isotopic variations in volcanic rocks from the Caribbean Large Igneous Province and Galápagos hot spot tracks. *Geochemistry, Geophysics, Geosystems*, **4**, 1062.

Geldmacher, J., Höfig, T., Hauff, F., Hoernle, K., Garbe-Schönberg, D. & Wilson, D., 2013. Influence of the Galápagos hotspot on the East Pacific Rise during Miocene superfast spreading. *Geology*, **41**, 183–186.

Hoernle, K., Werner, R., Morgan, J. P., Garbe-Schönberg, D., Bryce, J. & Mrazek, J., 2000. Existence of complex spatial zonation in the Galápagos plume. *Geology*, **28**, 435–438.

Ingle, S., Ito, G., Mahoney, J. J., Chazey, I., William, Sinton, J., Rotella, M. & Christie, D. M., 2010. Mechanisms of geochemical and geophysical variations along the western Galápagos Spreading Center. *Geochemistry, Geophysics, Geosystems*, **11**, Q04003.

Schilling, J.-G., Fontignie, D., Blichert-Toft, J., Kingsley, R. & Tomza, U., 2003. Pb-Hf-Nd-Sr isotope variations along the Galápagos Spreading Center (101 °-83 °W): Constraints on the dispersal of the Galápagos mantle plume. *Geochemistry, Geophysics, Geosystems*, **4**, 8512.

Werner, R., Hoernle, K., Barckhausen, U. & Hauff, F., 2003. Geodynamic evolution of the Galápagos hot spot system (Central East Pacific) over the past 20 m.y.: Constraints from morphology, geochemistry, and magnetic anomalies. *Geochemistry, Geophysics, Geosystems*, **4**, 1108.

Abstract

The main objective of this Dissertation is the investigation of the distribution of Galápagos plume material in the equatorial East Pacific. It provides a more detailed view on the Galápagos plume and the adjacent Galápagos Spreading Center (GSC; also known as Cocos-Nazca-Spreading Center (CNS)) and contributes to further our understanding of plume-ridge interaction and mantle material transport within the earth upper mantle. Of special interest in this context is the far-field lateral transport of plume material (sub-project 1) and the temporal evolution of plume-ridge interaction at the Galápagos plume-Galápagos Spreading Center system (sub-project 2). The necessary sample material in order to address these questions was recovered during the cruise SO208 with the German research vessel R/V *Sonne* in July/August 2010.

The focus of the first sub-project is the determination of age and origin of intraplate seamounts located off the coast of NW Costa Rica/SE Nicaragua, the part of the Cocos Plate that formed at the EPR. This area is characterised by an unusually high abundance of seamounts, that formation can not be explained by the common intraplate volcano model. A crucial question is, whether these seamounts formed at or close to the East Pacific Rise (EPR) or are the result of a far-field transport of Galápagos plume material.

In total, 19 seamounts have been sampled and for their geochemical composition (major and trace elements, Sr-Nd-Pb isotope ratios) analysed. In addition, ^{40}Ar/^{39}Ar plateau ages were determined to be able to allocate the geochemical results into a chronological timeframe. The age dated seamounts can be subdivided into two groups: a) seamounts with ages similar as the underlying crust $\pm 2\,\mathrm{Ma}$, b) seamounts that are more than $2\,\mathrm{Ma}$ younger than the underlying crust.

Geochemically, these seamounts require mixing between one enriched Galápagos component and two different depleted components. One of the depleted end member is similar to lava from the East Pacific Rise (EPR) but the second one is strongly depleted in the incompatible trace elements. Seamounts of similar age as the underlying crust must

have formed at or in close proximity to the EPR. Their ages correlate with the period of superfast-spreading (180-210 mm/a; Geldmacher *et al.*, 2013) at the EPR ($\sim$23-11 Ma ago). During this time, due to increased ridge suction force Galápagos plume material was dragged into the EPR beneath the GSC, mixed with depleted upper mantle and erupted at or close to the EPR ridge axis.

Seamounts of significantly younger age than the underlying crust can't be explained by that mechanism. They rather indicate true intraplate volcanism. These seamounts represent mixing between enriched ocean island basalt, e.g., Northern Galápagos plume component (Hoernle *et al.*, 2000) with an depleted upper mantle component (e.g., mid-ocean ridge basalt (MORB) or depleted Galápagos plume component). Due to a northward transport of plume material along the base of the Cocos Plate, Galápagos plume material was transported up to 900 km and melted due to decompression melting and erupted within the plate leading to the formation of the seamounts. The second sub-project aimed to elucidate the temporal evolution of the interaction between the Galápagos plume and the Galápagos spreading center. The Galápagos plume-ridge-system provides, due to the distinct geochemical zonation of the Galápagos plume ($>$15 Ma; Hoernle *et al.*, 2000; Geldmacher *et al.*, 2003; Werner *et al.*, 2003) a unique possibility to study plume-ridge interaction and transport mechanisms in the upper mantle. For this, ocean crust was sampled in great detail along the GSC just east of the 91°W Transform Fault (Study Area 2) and at four profiles going from the ridge axis up to 60 km north and south (Profile 1, 3, 4, 5).

Profile 1 ($\sim$92°W) was sampled from the ridge axis at the Western Galápagos Spreading Center (WGSC) up to 50 km to the North. This area is thought to be an area of strong plume input at the WGSC, observed both morphologically and geochemically (e.g., Schilling *et al.*, 2003; Christie *et al.*, 2005; Ingle *et al.*, 2010; Colman *et al.*, 2012). Profile 1 covers the evolution of the WGSC over a period of $\sim$1.6 Ma. The crustal samples can be explained by mixing between two different depleted components (MORB and depleted Galápagos plume component) and an enriched component. None of the enriched Galápagos plume component, however, has the appropriate composition to serve as the enriched end member. A seamount located c. 23 km north of the ridge axis (Seamount 63) is of extrem geochemical composition and thus provides the appropriate composition to serve as the enriched end member for all WGSC samples.

Based on their Sr-Nd-Pb isotopic ratio the WGSC samples can be subdivided into two groups: a) $<$30 km from the WGSC axis and b) $>$30 from the WGSC. The samples show only minor variations with increasing distance from the ridge axis and therefore increasing

age, indicating constant plume input in this are for at least the last ∼1.6 Ma. The samples from the >30 km WGSC group, however, seem to be additionally influenced by an enriched mantle (EM)II-like component.

Study Area 2, Profile 3 to Profile 5 and one single on-axis semaount were sampled along the Eastern Galápagos Spreading Center (EGSC). The area east of the 91°W Transform Fault (∼90°50'W) is supposed to be the center of Galápagos plume input at the EGSC Study Area 2). Samples from this area indicate the influx of enriched Zentral Galápagos plume component which becomes progressively diluted along the ridge axis towards east.

Profile 3 to Profile 5 have been sampled up to 60 km to the North and South of the ridge axis. Unlike Profile 1 the temporal evolution of the EGSc and therefor the profiles have been influenced by ridge jumps towards the plume in the past. Because of that the EGSC crust does not show linear age progression with increasing distance from the ridge axis but is characterised by age jumps of up to ∼1.3 Ma. Despite the age jumps the large geochemical variations in Profile 3 samples (89°30'W) up to 1.17 Ma indicate an rivalling input of two different enriched components over time. Both, in incompatible trace elements as well as in isotopic ratios, samples of this Profile range from very depleted to very enriched compositions. Taking other geochemically and/or morphologically anomalies along the Profiles and the ridge axis into account this might indicate short episodes of additional enriched plume material input along the EGSC.

References

Christie, D. M., Werner, R., Hauff, F., Hoernle, K. & Hanan, B. B., 2005. Morphological and geochemical variations along the eastern Galápagos Spreading Center. *Geochemistry, Geophysics, Geosystems*, **6**, Q01006.

Colman, A., Sinton, J. M., White, S. M., McClinton, J. T., Bowles, J. A., Rubin, K. H., Behn, M. D., Cushman, B., Eason, D. E., Gregg, T. K. P., Grönvold, K., Hidalgo, S., Howell, J., Neill, O. & Russo, C., 2012. Effects of variable magma supply on mid-ocean ridge eruptions: Constraints from mapped lava flow fields along the Galápagos Spreading Center. *Geochemistry, Geophysics, Geosystems*, **13**, Q08014.

Geldmacher, J., Hanan, B. B., Blichert-Toft, J., Harpp, K., Hoernle, K., Hauff, F., Werner, R. & Kerr, A. C., 2003. Hafnium isotopic variations in volcanic rocks from the Caribbean Large Igneous Province and Galápagos hot spot tracks. *Geochemistry, Geophysics, Geosystems*, **4**, 1062.

Geldmacher, J., Höfig, T., Hauff, F., Hoernle, K., Garbe-Schönberg, D. & Wilson, D., 2013. Influence of the Galápagos hotspot on the East Pacific Rise during Miocene superfast spreading. *Geology*, **41**, 183–186.

Hoernle, K., Werner, R., Morgan, J. P., Garbe-Schönberg, D., Bryce, J. & Mrazek, J., 2000. Existence of complex spatial zonation in the Galápagos plume. *Geology*, **28**, 435–438.

Ingle, S., Ito, G., Mahoney, J. J., Chazey, I., William, Sinton, J., Rotella, M. & Christie, D. M., 2010. Mechanisms of geochemical and geophysical variations along the western Galápagos Spreading Center. *Geochemistry, Geophysics, Geosystems*, **11**, Q04003.

Schilling, J.-G., Fontignie, D., Blichert-Toft, J., Kingsley, R. & Tomza, U., 2003. Pb-Hf-Nd-Sr isotope variations along the Galápagos Spreading Center (101°-83°W): Constraints on the dispersal of the Galápagos mantle plume. *Geochemistry, Geophysics, Geosystems*, **4**, 8512.

Werner, R., Hoernle, K., Barckhausen, U. & Hauff, F., 2003. Geodynamic evolution of the Galápagos hot spot system (Central East Pacific) over the past 20 m.y.: Constraints from morphology, geochemistry, and magnetic anomalies. *Geochemistry, Geophysics, Geosystems*, **4**, 1108.

Chapter 1

Introduction

1.1 Mid-Ocean Ridges, Mantle Plumes and their Interaction

Mid-ocean ridges (MOR) are the longest mountain ranges on earth. With more than 56.000 km in length they are responsible for the vast majority of global volcanic activity. MORs form as a result of seafloor spreading when tectonic plates move away from each other. Based on the rate the tectonic plates rift apart they are classified as fast- (full-spreading rate of 100-200 mm/yr), intermediate- (50-100 mm/yr), slow- (20-50 mm/yr) and ultra-slow (<20 mm/yr) spreading.

Volcanism at spreading centers takes place in a narrow, only few kilometers wide zone (Macdonald, 1982; Sims *et al.*, 2003; Standish & Sims, 2010; Turner *et al.*, 2011). Melting is caused by adiabatic decompression as a result of the rifting of the divergent plate boundaries (e.g., McKenzie & Bickle, 1988). While melt parameters such as depth of the onset of melting or maximum degree of melting are controlled by mantle temperature, spreading rate and water content of the mantle material (Asimow & Langmuir, 2003; Langmuir & Forsyth, 2007), the melt region width beneath the spreading center, however, seems mainly to be a function of spreading rate. At superfast-spreading ridges the melt region is estimated to be hundreds of kilometer wide, and up to 100 km deep (Team, 1998), but at slow-spreading ridges the melt region is narrower as well as the extent of melting is lower (Montési & Behn, 2007). Furthermore, spreading rate also influences crustal thickness, spreading center morphology and geochemical composition of the erupted material (mainly basalts; Langmuir & Forsyth, 2007). While the majority of the global ocean crust

ranges between 5-7 km thickness (White *et al.*, 2001; Klein, 2003), ocean crust formed at slow to ultraslow-spreading ridges is less than 4 km thick or completely missing (Jokat *et al.*, 2003; Dick *et al.*, 2003; Snow & Edmonds, 2007).

Despite the spreading all MORs have in common, that due to tectonic and magnetic processes, mantle material is accreted to the divergent plate boundaries and thus new ocean crust is constantly build. Therefore, it is generally assumed that with increasing distance from the ridge axis the ocean crust increases in age.

Mantle plumes, on the other hand, are thought to be stationary long-lived cylindrical features originating from deep in the earth's mantle (Morgan, 1971, 1972). The unusual high temperature and/or chemical, fluid rich composition of the upwelling material leads to crustal uplift and eventually to excess volcanism on the surface. In the classic mantle-plume theory they are described as narrow pipe-like structures of hot mantle material, transporting heat from the Earth's core-mantle boundary through the mantle to the surface. When this diapiric structure of hot mantle material reaches the base of the lithosphere it spreads laterally related with extensive decompression melting and causes, in it's initial stage, large volcanic eruptions on the surface, so called Large Igneous Provinces (LIPs; e.g., Farnetani & Richards, 1994; Richards *et al.*, 1989). On a long-term scale, however, due to the movement of lithosphere across the stationary upwelling unusual hot mantle, age progressive volcanic chains form, such as the Hawaiian Islands with the related Emperor Seamount Chain.

It is assumed, that up to 21 of the proposed 30 to 50 hot spots on Earth are located near mid-ocean ridges (Ito & van Keken, 2007). The proximity of a spreading center to a mantle plume and the resulting interaction can lead to geomorphological and geochemical anomalies along the spreading axes that can be observed as far as 1,000 km from the plume (e.g., Christie *et al.*, 2005; Detrick *et al.*, 2002; Ito *et al.*, 2003; Schilling *et al.*, 1976, 1982; Sinton *et al.*, 2003; Vogt, 1976). The Galápagos plume-Galápagos Spreading Center-System is a textbook example for plume-ridge interaction and subject of this dissertation.

1.2   Galápagos plume and Galápagos Spreading Center

At the Galápagos Spreading Center (GSC; also known as Cocos-Nazca Spreading Center (CNS)) the Nazca and Cocos Plate pull away from each other, with an average spreading rate of 62 km/Ma (Meschede & Barckhausen, 2001). The Cocos and Nazca Plate formed as a result of the break up of the Farallon Plate, when a fracture zone passed over the
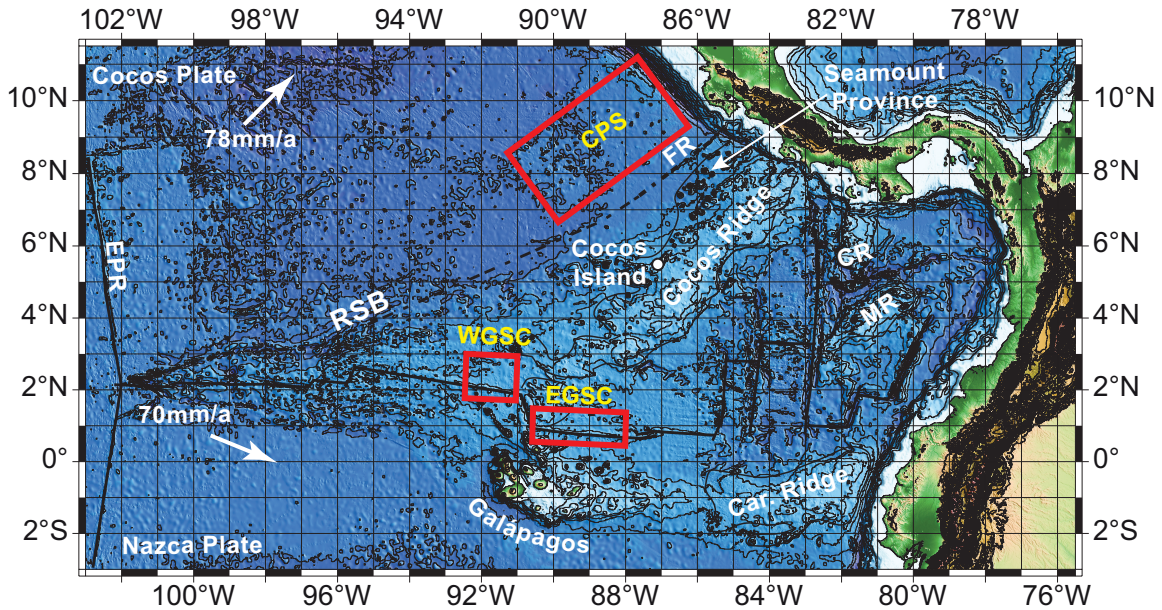
Figure 1.1: Bathymetric map of the Eastern Pacific area including the three location where the samples in this study are from and all major morphological features (EPR – Eastern Pacific Rise, CPS Cocos Plate Seamounts, WGSC Western Galápagos Spreading Center, EGSC Eastern Galápagos Spreading Center, FR – Fischer Ridge, RSB – Rough-Smooth-Boundary, CR – Coiba Ridge, MR – Mapelo Ridge, Catr. Ridge – Carnegie Ridge) data are from The GEBCO_08 Grid, version 20091120, `http://www.gebco.net`.

Galápagos hotspot $\sim$23 Ma ago (Lonsdale, 2005; Lonsdale & Klitgord, 1978). Since then the spreading center has been influenced by the Galápagos hotspot in its immediate proximity. Depending on the relative position of the spreading center to the plume two distinct aseismic hotspot tracks formed – the Cocos Ridge with adjacent Seamount Province on the NE moving Cocos Plate and the Carnegie, Coiba and Malpelo Ridges on the E moving Nazca Plate (Fig. 1.1; e.g., Canales *et al.*, 1997; Harpp *et al.*, 2005; Holden & Dietz, 1972; Werner *et al.*, 2003; Wilson & Hey, 1995). For the last $\sim$5 Ma (Wilson & Hey, 1995) the Galápagos plume is located about 145-215 km south of the GSC (Mittelstaedt *et al.*, 2012).

The Galápagos Archipelago, as the surface expression of the long-lived Galápagos mantle plume, can geochemically be divided into an enriched "horseshoe" shaped region (high Sr and Pb, low Nd) enclosing a depleted area (low Sr and Pb, high Nd) in it's inner part (Eastern Domain; e.g., Geist *et al.*, 1988; Harpp & White, 2001; Hoernle *et al.*, 2000; White & Hofmann, 1978; White *et al.*, 1993). The enriched "horseshoe", however, can additional be sub-divided into three different enriched geochemical domains with distinct isotopic compositions – Northern (containing Wolf, Darwin and Pinta Islands), Central (including Fernandina) and Southern (including Floreana) Galápagos Domain (Fig. 1.2; Hoernle *et al.*, 2000; Geldmacher *et al.*, 2003; Werner *et al.*, 2003). This unique and long-lived

geochemical zonation of the Galápagos plume (Hoernle *et al.*, 2000) provides a powerful tool to to study the interaction between the plume and the ridge but also to reconstruct material transport mechanisms in the upper mantle.

Besides the presence of the aseismic hotspot tracks on the Cocos and Nazca Plate, the interaction of the Galápagos plume with the GSC is also reflected in the geochemistry of the erupted material. In accordance with the geographic distribution of the geochemically distinct domains at the Galápagos Archipelago, the geochemistry of lavas from the hotspot tracks display the same pattern. The recent influence of the Galápagos plume at the GSC can be seen by morphological and geochemical variations along the ridge axis(e.g., Bowles *et al.*, 2014; Colman *et al.*, 2012; Cushman *et al.*, 2004; Detrick *et al.*, 2002; Harpp & Geist, 2002; Kokfelt *et al.*, 2005; Schilling *et al.*, 2003, 1982).
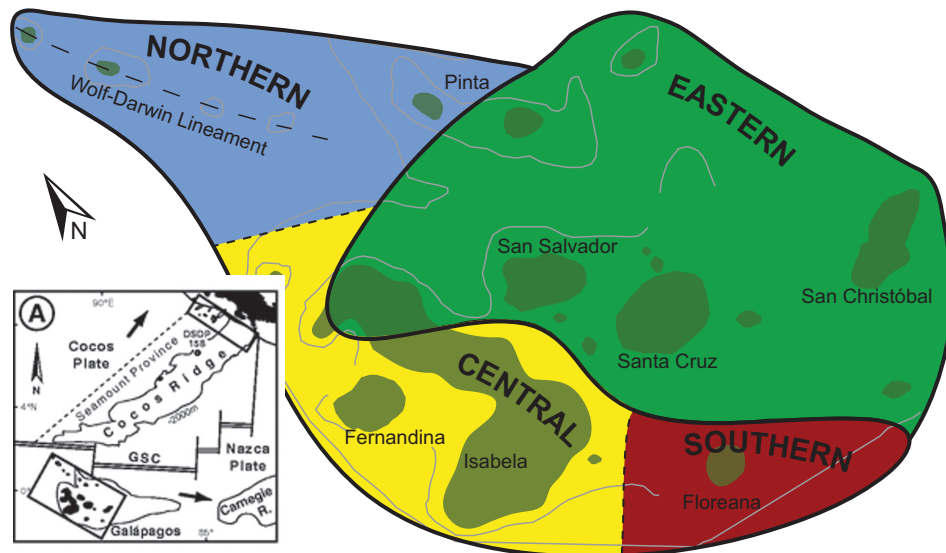
Figure 1.2: Schematic overview of the geochemical zonation of the Galápagos Archipelago after Hoernle *et al.* (2000). The Southern, Central and Northern Galápagos Domains form a "horseshoe"-like pattern enclosing the depleted Eastern Domain. Please note, that the colour code used in this Figure does not correlate with the colours used in the individual chapters.

1.3 Thesis outline

During the R/V SONNE 208 cruise in July/August 2010 we sampled 19 seamounts located off-shore of NW Costa Rica/SW Nicaragua (Cocos Plate Seamounts), oceanic crust at and parallel to the GSC ridge axis (Study Area 2) and 4 profiles perpendicular to the GSC (Profile 1, 3, 4, 5). The major objective was to put constrains on the extent of influence

of Galápagos plume material in the equatorial East Pacific Ocean. The project is divided into two sub-projects dealing with a) the lateral far-field transport of Galápagos plume material and b) to investigate the nature of the input of Galápagos plume material at the GSC over time.

For this, the geochemical composition (major and trace elements and Sr-Nd-Pb isotopes) of the sampled material was determined. In addition, ^{40}Ar/^{39}Ar plateau step ages were determined on samples from the Cocos Plate Seamounts to allocate the geochemistry into a chronological framework. About two-thirds of the geochemical analyses were carried out on fresh volcanic glass, and about one-third on whole rock material.

This dissertation at hand comprises three independent chapters. While Chapter 2 focuses on the far-field influence of Galápagos plume material in the equatorial East Pacific Ocean Chapter 3 and 4 deal with plume-ridge interaction at different segments at the GSC over time.

1.3.1   Chapter 2 Cocos Plate Seamounts

This Chapter deals with intraplate volcanism that is not directly related to a hotspot track and might be instead represent far-field plume influence on the upper mantle. Off-shore of NW Costa Rica and SW Nicaragua, a part of the Cocos Plate that is formed at the EPR, an unusual high frequency of seamounts occur on the ocean floor. Age and origin of these seamounts was unclear prior to this study.

The geochemistry of the Cocos Plate Seamounts (CPS) indicates a derivation from enriched ocean island basalt-like composition, similar to that of the Northern Galápagos Domain and two different depleted compositions. While one of the depleted components seems to be similar to East Pacific Rise (EPR) N-MORB the second one is characterized by more depleted incompatible elements. ^{40}Ar/^{39}Ar age determinations reveal that these seamounts vary in age between ∼7 and 24 Ma. Compared to the age of the underlying crust (paleomagnetic ages; Barckhausen *et al.*, 2001), the seamounts can be divided into near-ridge and intraplate origin. The near-ridge CPS can be explained by the transport of Galápagos plume material to the EPR during super-fast spreading supporting the model of Geldmacher *et al.* (2013). The intraplate seamounts, however, indicate northward flow of Galápagos plume material along the base of the lithosphere. Either due to changes in lithospheric thickness along the crustal seam between the EPR and GSC formed Cocos plate crust or at the edge of a viscous plug of accumulated plume material at the base of the lithosphere, the plume material undergoes decompression melting, resulting in volcanism

that leads to the formation of the seamounts.

1.3.2   Galápagos Spreading Center

Chapter 3 and 4 deal with the temporal evolution in plume-ridge interaction at different locations along the GSC. The GSC is east and west of the 91°W Transform Fault (TF) influenced by different plume components and was therefore divided into a) the Western Galápagos Spreading Center (WGSC) to the west of the 91°W TF (Chapter 3) and b) the Eastern Galápagos Spreading Center (EGSC) to the east of the 91°W TF (Chapter 4).

1.3.2.1   Chapter 3 Western Galápagos Spreading Center

At the WGSC a profile from the ridge axis to 50 km to the north was sampled in order to constrain the nature of plume-ridge interaction over time. The ridge axis of this profile, between 91°40' and 92°W is thought to be as a location where Galápagos plume material enters the ridge axis. The geochemical investigation of the recovered basalts including a small off-axis seamount, permit insights into the temporal evolution of the plume-ridge interaction. Based on their Sr-Nd-Pb isotope geochemistry the samples were divided into young seafloor basalts, less than 30 km distant from the ridge axis and old seafloor basalts more than 30 km distant from the ridge axis. A single seamount turns out to be geochemically unique compared to what is observed on the recent GSC but also on the Galápagos Archipelago. This seamount is significantly more enriched (isotopically and in trace element composition) and serves as the enriched endmember for the crustal samples. The depleted endmember are represented by GSC-N-MORB from >95.5°W an area thought to be free of Galápagos plume influence (Ingle *et al.*, 2010) and depleted Eastern Galápagos Domain (Hoernle *et al.*, 2000). The older samples (>30 km), however, seem to be additionally influenced by a second enriched EMII-like component, as they are shifted towards higher Pb and Sr and lower Nd than the younger samples (<30 km). Within the samples groups there are no significant temporal variations observed with increasing distance from the ridge axis,indicating a relatively constant plume input at this area, for at least ~1.6 Ma.

1.3.2.2   Chapter 4 Eastern Galápagos Spreading Center

The basis for this sub-project was provided by earlier work by Christie *et al.* (2005) and Hoernle et al., (unpub. data) dealing with a detailed geochemical investigation of the Eastern Galápagos Spreading Center ridge axis (EGSC). The authors discovered along the

ridge axis morphological anomalies that coincide with geochemical irregularities. Based on this finding, the locations for the detailed on- and off-axis sampling for this study were determined. With this sub-project the temporal evolution of the EGSC can be reconstructed for the past ∼3.6 Ma. The ridge axis at ∼90°50'W and parallel to it, an area thought to be strongly influenced by the Galápagos plume was sampled in great detail (Study Area 2), in order to further constrain the Galápagos plume component reaching the ridge. From there three profiles perpendicular to the ridge axis and on single on-axis seamount were sampled to classify the nature of plume input in a spatial and temporal framework (Profile 3, 4, 5). In general the geochemical composition of the profile samples can be explained by two component mixing between an enriched OIB-like component, possibly Central Galápagos Domain (as found on the central Galápages Islands) and a depleted N-MORB-like component or the proposed depleted Eastern Galápagos Domain. The largest variations in composition are observed in Profile 3. Here it seems that there is a rivalling input between a depleted and enriched component, represented by short-term changes in composition over time. Morphological anomalies, which are also related to geochemical irregularities, support the model, that even though the main input of Galápagos plume material occurs just east of the 91°W TF, in the area around 90°50'W, small-scale events of local plume input can also be observed along the ridge axis towards the east. If Galápagos plume material reaches the ridge axis only at ∼90°50'W and flows beneath the ridge towards the east the local short-term events might be the result of occasional melting events, but this seems to be rather unlikely. Another possibility would be that plume material spreads radially more like a fan. At the end of this fan small lumps of plume material might separate and mingling with ambient mantle. Eventually it undergoes decompression melting leading to short-therm melting events creating the observed morphological and geochemical anomalies.

References

Asimow, P. D. & Langmuir, C. H., 2003. The importance of water to oceanic mantle melting regimes. *Nature*, **421**, 815–820. 10.1038/nature01429.

Barckhausen, U., Ranero, C. R., von Huene, R., Cande, S. C. & Roeser, H. A., 2001. Revised tectonic boundaries in the Cocos Plate off Costa Rica: Implications for the segmentation of the convergent margin and for plate tectonic models. *Journal of Geophysical Research*, **106**, 19207–19220.

Bowles, J. A., Colman, A., McClinton, J. T., Sinton, J. M., White, S. M. & Rubin, K. H., 2014. Eruptive timing and 200 year episodicity at 92°W on the hot spot-influenced Galápagos Spreading Center derived from geomagnetic paleointensity. *Geochemistry, Geophysics, Geosystems*, **15**, 2211–2224.

Canales, J. P., Dañobeitia, J. J., Detrick, R. S., Hooft, E. E. E., Bartolomé, R. & Naar, D. F., 1997. Variations in axial morphology along the Galápagos spreading center and the influence of the Galápagos hotspot. *Journal of Geophysical Research: Solid Earth*, **102**, 27341–27354.

Christie, D. M., Werner, R., Hauff, F., Hoernle, K. & Hanan, B. B., 2005. Morphological and geochemical variations along the eastern Galápagos Spreading Center. *Geochemistry, Geophysics, Geosystems*, **6**, Q01006.

Colman, A., Sinton, J. M., White, S. M., McClinton, J. T., Bowles, J. A., Rubin, K. H., Behn, M. D., Cushman, B., Eason, D. E., Gregg, T. K. P., Grönvold, K., Hidalgo, S., Howell, J., Neill, O. & Russo, C., 2012. Effects of variable magma supply on mid-ocean ridge eruptions: Constraints from mapped lava flow fields along the Galápagos Spreading Center. *Geochemistry, Geophysics, Geosystems*, **13**, Q08014.

Cushman, B., Sinton, J., Ito, G. & Eaby Dixon, J., 2004. Glass compositions, plume-ridge interaction, and hydrous melting along the Galápagos Spreading Center, 90.5°W to 98°W. *Geochemistry, Geophysics, Geosystems*, **5**, Q08E17.

Detrick, R. S., Sinton, J. M., Ito, G., Canales, J. P., Behn, M., Blacic, T., Cushman, B., Dixon, J. E., Graham, D. W. & Mahoney, J. J., 2002. Correlated geophysical, geochemical, and volcanological manifestations of plume-ridge interaction along the Galápagos Spreading Center. *Geochemistry, Geophysics, Geosystems*, **3**, 8501.

Dick, H. J. B., Lin, J. & Schouten, H., 2003. An ultraslow-spreading class of ocean ridge. *Nature*, **426**, 405–412. 10.1038/nature02128.

Farnetani, C. G. & Richards, M. A., 1994. Numerical investigations of the mantle plume initiation model for flood basalt events. *Journal of Geophysical Research: Solid Earth*, **99**, 13813–13833.

Geist, D. J., White, W. M. & McBirney, A. R., 1988. Plume-asthenosphere mixing beneath the Galápagos archipelago. *Nature*, **333**, 657–660. 10.1038/333657a0.

Geldmacher, J., Hanan, B. B., Blichert-Toft, J., Harpp, K., Hoernle, K., Hauff, F., Werner, R. & Kerr, A. C., 2003. Hafnium isotopic variations in volcanic rocks from the Caribbean Large Igneous Province and Galápagos hot spot tracks. *Geochemistry, Geophysics, Geosystems*, **4**, 1062.

Geldmacher, J., Höfig, T., Hauff, F., Hoernle, K., Garbe-Schönberg, D. & Wilson, D., 2013. Influence of the Galápagos hotspot on the East Pacific Rise during Miocene superfast spreading. *Geology*, **41**, 183–186.

Harpp, K. & Geist, D., 2002. Wolf-Darwin lineament and plume-ridge interaction in northern Galápagos. *Geochemistry, Geophysics, Geosystems*, **3**, 8504.

Harpp, K. S., Wanless, V. D., Otto, R. H., Hoernle, K. & Werner, R., 2005. The Cocos and Carnegie Aseismic Ridges: A Trace Element Record of Long-term Plume-Spreading Center Interaction. *Journal of Petrology*, **46**, 109–133.

Harpp, K. S. & White, W. M., 2001. Tracing a mantle plume: Isotopic and trace element variations of Galápagos seamounts. *Geochemistry, Geophysics, Geosystems*, **2**, 1042.

Hoernle, K., Werner, R., Morgan, J. P., Garbe-Schönberg, D., Bryce, J. & Mrazek, J., 2000. Existence of complex spatial zonation in the Galápagos plume. *Geology*, **28**, 435–438.

Holden, J. C. & Dietz, R. S., 1972. Galápagos Gore, NazCoPac Triple Junction and Carnegie/Cocos Ridges. *Nature*, **235**, 266–269. 10.1038/235266a0.

Ingle, S., Ito, G., Mahoney, J. J., Chazey, I., William, Sinton, J., Rotella, M. & Christie, D. M., 2010. Mechanisms of geochemical and geophysical variations along the western Galápagos Spreading Center. *Geochemistry, Geophysics, Geosystems*, **11**, Q04003.

Ito, G., Lin, J. & Graham, D., 2003. Observational and theoretical studies of the dynamics of mantle plume & mid-ocean ridge interaction. *Reviews of Geophysics*, **41**, 1017.

Ito, G. & van Keken, P. E., 2007. Hot Spots and Melting Anomalies. In: *Treatise on Geophysics* (ed. Editor-in Chief: Gerald, S.), Elsevier, Amsterdam. 371–435.

Jokat, W., Ritzmann, O., Schmidt-Aursch, M. C., Drachev, S., Gauger, S. & Snow, J., 2003. Geophysical evidence for reduced melt production on the Arctic ultraslow Gakkel mid-ocean ridge. *Nature*, **423**, 962–965. 10.1038/nature01706.

Klein, E. M., 2003. 3.13 - Geochemistry of the Igneous Oceanic Crust. In: *Treatise on Geochemistry* (eds. Editors-in Chief: Heinrich, D. H. & Karl, K. T.), Pergamon, Oxford. 433–463.

Kokfelt, T. F., Lundstrom, C., Hoernle, K., Hauff, F. & Werner, R., 2005. Plume-ridge interaction studied at the Galápagos spreading center: Evidence from ^{226}Ra-^{230}Th-^{238}U and ^{231}Pa-^{235}U isotopic disequilibria. *Earth and Planetary Science Letters*, **234**, 165–187.

Langmuir, C. & Forsyth, D., 2007. Mantle melting beneath mid-ocean ridges. *Oceanography*, **20**, 78–89.

Lonsdale, P., 2005. Creation of the Cocos and Nazca plates by fission of the Farallon plate. *Tectonophysics*, **404**, 237–264.

Lonsdale, P. & Klitgord, K. D., 1978. Structure and tectonic history of the eastern Panama Basin. *Geological Society of America Bulletin*, **89**, 981–999.

Macdonald, K. C., 1982. Mid-Ocean Ridges: Fine Scale Tectonic, Volcanic and Hydrothermal Processes Within the Plate Boundary Zone. *Annual Review of Earth and Planetary Sciences*, **10**, 155–190.

McKenzie, D. & Bickle, M. J., 1988. The Volume and Composition of Melt Generated by Extension of the Lithosphere. *Journal of Petrology*, **29**, 625–679.

Meschede, M. & Barckhausen, U., 2001. The relationship of the Cocos and Carnegie ridges: age constraints from paleogeographic reconstructions. *International Journal of Earth Sciences*, **90**, 386–392.

Mittelstaedt, E., Soule, S., Harpp, K., Fornari, D., McKee, C., Tivey, M., Geist, D., Kurz, M. D., Sinton, C. & Mello, C., 2012. Multiple expressions of plume-ridge interaction

in the Galápagos: Volcanic lineaments and ridge jumps. *Geochemistry, Geophysics, Geosystems*, **13**, Q05018.

Montési, L. G. J. & Behn, M. D., 2007. Mantle flow and melting underneath oblique and ultraslow mid-ocean ridges. *Geophysical Research Letters*, **34**, L24307.

Morgan, W. J., 1971. Convection Plumes in the Lower Mantle. *Nature*, **230**, 42–43. 10.1038/230042a0.

Morgan, W. J., 1972. Plate Motions and Deep Mantle Convection. *Geological Society of America Memoirs*, **132**, 7–22.

Richards, M. A., Duncan, R. A. & Courtillot, V. E., 1989. Flood Basalts and Hot-Spot Tracks: Plume Heads and Tails. *Science*, **246**, 103–107.

Schilling, J., Kingsley, R. & Devine, J., 1982. Galápagos Hot Spot-Spreading Center System 1. Spatial Petrological and Geochemical Variations (83°W–111°W). *Journal of Geophysical Research*, **87**, 18.

Schilling, J. G., Anderson, R. N. & Vogt, P., 1976. Rare earth, Fe and Ti variations along the Galápagos spreading centre, and their relationship to the Galápagos mantle plume. *Nature*, **261**, 108–113. 10.1038/261108a0.

Schilling, J.-G., Fontignie, D., Blichert-Toft, J., Kingsley, R. & Tomza, U., 2003. Pb-Hf-Nd-Sr isotope variations along the Galápagos Spreading Center (101°-83°W): Constraints on the dispersal of the Galápagos mantle plume. *Geochemistry, Geophysics, Geosystems*, **4**, 8512.

Sims, K. W. W., Blichert-Toft, J., Fornari, D. J., Perfit, M. R., Goldstein, S. J., Johnson, P., DePaolo, D. J., Hart, S. R., Murrell, M. T., Michael, P. J., Layne, G. D. & Ball, L. A., 2003. Aberrant youth: Chemical and isotopic constraints on the origin of off-axis lavas from the East Pacific Rise, 9-10°N. *Geochemistry, Geophysics, Geosystems*, **4**, 8621.

Sinton, J., Detrick, R., Canales, J. P., Ito, G. & Behn, M., 2003. Morphology and segmentation of the western Galápagos Spreading Center, 90.5°-98°W: Plume-ridge interaction at an intermediate spreading ridge. *Geochemistry, Geophysics, Geosystems*, **4**, 8515.

Snow, J. E. & Edmonds, H. N., 2007. Ultraslow-spreading ridges: Rapid paradigm changes. *Oceanography*, **20**, 90–101.

Standish, J. J. & Sims, K. W. W., 2010. Young off-axis volcanism along the ultraslow-spreading Southwest Indian Ridge. *Nature Geoscience*, **3**, 286–292. 10.1038/ngeo824.

Team, T. M. S., 1998. Imaging the Deep Seismic Structure Beneath a Mid-Ocean Ridge: The MELT Experiment. *Science*, **280**, 1215–1218.

Turner, S., Beier, C., Niu, Y. & Cook, C., 2011. U-Th-Ra disequilibria and the extent of off-axis volcanism across the East Pacific Rise at 9°30'N, 10°30'N, and 11°20'N. *Geochemistry, Geophysics, Geosystems*, **12**, Q0AC12.

Vogt, P. R., 1976. Plumes, subaxial pipe flow, and topography along the Mid-Oceanic Ridge. *Earth and Planetary Science Letters*, **29**, 309–325.

Werner, R., Hoernle, K., Barckhausen, U. & Hauff, F., 2003. Geodynamic evolution of the Galápagos hot spot system (Central East Pacific) over the past 20 m.y.: Constraints from morphology, geochemistry, and magnetic anomalies. *Geochemistry, Geophysics, Geosystems*, **4**, 1108.

White, R. S., Minshull, T. A., Bickle, M. J. & Robinson, C. J., 2001. Melt Generation at Very Slow-Spreading Oceanic Ridges: Constraints from Geochemical and Geophysical Data. *Journal of Petrology*, **42**, 1171–1196.

White, W. M. & Hofmann, A. W., 1978. Geochemistry of the Galápagos Islands: implications for mantle dynamics and evolution. *Year Book Carnegie Inst. Washington*, **77**, 596–606.

White, W. M., McBirney, A. R. & Duncan, R. A., 1993. Petrology and Geochemistry of the Galápagos Islands: Portrait of a Pathological Mantle Plume. *Journal of Geophysical Research*, **98**, 19533–19563.

Wilson, D. S. & Hey, R. N., 1995. History of rift propagation and magnetization intensity for the Cocos-Nazca spreading center. *Journal of Geophysical Research*, **100**, 10041–10056.

Chapter 2

Cocos Plate Seamounts offshore NW Costa Rica: Implications for large-scale distribution of Galápagos plume material in the upper mantle

Antje Herbrich[1*], Kaj Hoernle[1], Reinhard Werner[1], Folkmar Hauff[1], Paul v.d. Bogaard[1], Dieter Garbe-Schönberg[2]

[1] GEOMAR Helmholtz Centre for Ocean Research Kiel, Wischhofstraße 1-3, D-24148 Kiel, Germany

[2] Institute of Geosciences, University of Kiel, Ludewig-Meyn-Strasse 10, D-24118 Kiel, Germany

Abstract

The origin of intraplate volcanism not directly part of a hotspot track, such as diffuse seamount provinces, and the extent of mantle plume influence on the upper mantle remain enigmatic. Here we present new ^{40}Ar/^{39}Ar age data and geochemical (major and trace-element and Sr-Nd-Pb isotopic) data from seamounts on the Cocos Plate presently located offshore of NW Costa Rica and SW Nicaragua. The seamounts ($\sim$7 to 24 Ma) require mixing of an enriched ocean island basalt composition, similar to that of the Northern Galápagos Domain, with two depleted components. One of the depleted components is similar to East Pacific Rise normal mid-ocean ridge basalt and the other has more depleted incompatible elements, either reflecting secondary melting of N-MORB or a depleted Galápagos plume component. Seamounts with ages significantly younger than the ocean crust formed in an intraplate setting and can be explained by northward transport of Galápagos plume material along the base of the Cocos Plate up to 900 km away from the hotspot and 250-500 km north of the Galápagos hotspot track. We propose that melting

occurs due to decompression as the mantle upwells to shallower depth as it flows northwards, either due to changes in lithospheric thickness or as a result of upwelling at the edge of a viscous plug of accumulated plume material at the base of the lithosphere. The tholeiitic to alkaline basalt compositions of the Cocos Plate Seamounts compared to the more silica under-saturated compositions of Hawaiian rejuvenated and arch (alkali basalts to nephelinites) lavas is likely to reflect the significant difference in age ($<$25 vs $\sim$90 Ma) and thus thickness of the lithosphere on which the lavas were erupted.

2.1   Introduction

Although many studies have been carried out to investigate the interaction of hotspots or mantle plumes with a nearby oceanic spreading center (e.g., Geldmacher *et al.*, 2013; Ingle *et al.*, 2010; Ito & Lin, 1995; Kincaid *et al.*, 1995, 1996; Ribe, 1996; Schilling *et al.*, 2003), the extent to which the plume material spreads out along the base of the lithosphere away from the ridge has not been established. At Hawaii, located on old (90 Ma), thick lithosphere, the presence of a 1 km high and $\sim$1,000 m wide bathymetric swell around the active volcanic islands, however, indicates that the proposed underlying mantle plume affects a much larger portion of the upper mantle (e.g., Phipps Morgan *et al.*, 1995). This influence is reflected by young alkaline volcanism along the edge of the swell, leading to the formation of rejuvenated volcanism on Hawaiian Volcanoes and the Hawaiian Arch volcanic fields up to 400 km north and south of the plume center presumably beneath the Big Island of Hawaii (e.g., Clague *et al.*, 1990, 2002; Frey *et al.*, 2000; Lipman *et al.*, 1989).

About 21 of the proposed 30 to 50 hot spots on Earth are, however, located near mid-ocean ridges and interact with young, thin lithosphere, resulting in geomorphological and geochemical anomalies along the spreading axes (e.g., Christie *et al.*, 2005; Detrick *et al.*, 2002; Ito *et al.*, 2003; Sinton *et al.*, 2003). While plume material can influence nearby ridges for distances of up to 1,000 km along-axis (Schilling *et al.*, 1976, 1982; Vogt, 1976), the extent to which plume material that a) does not flow into the ridge system spreads laterally along the base of the lithosphere away from the ridge axis and b) affects the chemical composition of the upper mantle (asthenosphere and possibly lithosphere) is still poorly constrained.

The Galápagos hotspot with the adjacent Cocos-Nazca or Galápagos Spreading Center (GSC) is a classic location to study interaction between a plume and young, thin lithosphere near a spreading center, representing the opposite end-member to the extensively studied Hawaiian system (intraplate hotspot interacting with old, thick lithosphere). Although many studies have investigated the interaction between the Galápagos plume and the GSC and East Pacific Rise (EPR; e.g., Bowles *et al.*, 2014; Christie *et al.*, 2005; Detrick *et al.*, 2002; Geldmacher *et al.*, 2013;

Ingle *et al.*, 2010; Kokfelt *et al.*, 2005; Schilling *et al.*, 1982, 2003; Sinton *et al.*, 2003), the extent to which the plume spreads out along the base of the lithosphere away from the ridge and causes intraplate volcanism has not been established.

Depending on the relative position of the GSC to the Galápagos plume, two distinct aseismic hotspot tracks have formed – the Cocos Ridge on the Cocos Plate and Carnegie Ridge on the Nazca Plate (Fig. 2.1; e.g., Hey, 1977; Holden & Dietz, 1972; Werner *et al.*, 2003; Wilson & Hey, 1995). The hotspot track on the Cocos Plate also consists of a Seamount Province on the northwestern side of the Cocos Ridge (von Huene *et al.*, 1995). Systematic variations in basalt chemistry along the GSC are explained by transport of Galápagos plume material to and then along the spreading center (Christie *et al.*, 2005; Detrick *et al.*, 2002; Ingle *et al.*, 2010; Kokfelt *et al.*, 2005; Pedersen & Furnes, 2001; Schilling *et al.*, 1976, 2003), but today's influence of the hotspot can only be detected as far as 99.5°W, ~1,000 km from the Galápagos Islands (Schilling *et al.*, 2003). Geldmacher *et al.* (2013) proposed that Galápagos plume material reached the main EPR ridge system (currently located 1,100 km west of the Galápagos) during times of superfast EPR spreading (22.5-11 Ma ago), possibly by increased "ridge suction" forces, and thus affected the formation of the Cocos Plate crust that was formed along the EPR during this time interval.

A number of observations support transport of Galápagos plume material beneath the Cocos Plate. Off the coast of Costa Rica, drill cores from ODP-Leg 170 (Fig. 2.1a) contained sills with Galápagos-type geochemical compositions (<16 Ma; Sadofsky *et al.*, 2009, and references therein) intruded into Cocos Plate crust that is between 22.1 and 24.1 Ma old (Barckhausen *et al.*, 2001). In addition, unusual young lavas occur within the Cocos and Carnegie Ridge hotspot tracks (O'Connor *et al.*, 2007), which also contain the geochemical characteristics of magmas from the Galápagos plume (Harpp *et al.*, 2005; Werner *et al.*, 2003), but not necessarily in accordance with the geochemical composition of the surrounding, older hotspot track volcanic rocks. Hence the significantly younger age of these intraplate volcanic rocks that have Galápagos-type compositions may reflect active plume outflow over several hundreds of kilometers, consistent with low seismic velocities within the upper asthenosphere beneath the Cocos Hotspot track (O'Connor *et al.*, 2007).

We sampled 19 dispersed seamounts located 800-1,300 km away from the presumed plume center at Fernandina, and 250-500 km north of the morphological hotspot track (Cocos Ridge) during R/V Sonne cruise SO208 "PLUMEFLUX" in July 2010. Our major goal was to determine if these seamounts show any evidence for the involvement of Galápagos plume material, in order to constrain further the distribution of Galápagos plume material, in order to constrain further the distribution of Galápagos plume material in the upper mantle and to elucidate the origin of these seamounts, referred to as Cocos Plate Seamounts (CPS; Fig. 2.1). Here we present ^{40}Ar/^{39}Ar age data from 9 and geochemistry of all sampled CPS in order to unravel the origin of this intraplate volcanism. We show that a) these seamounts formed both on- and off-axis of the EPR and b)
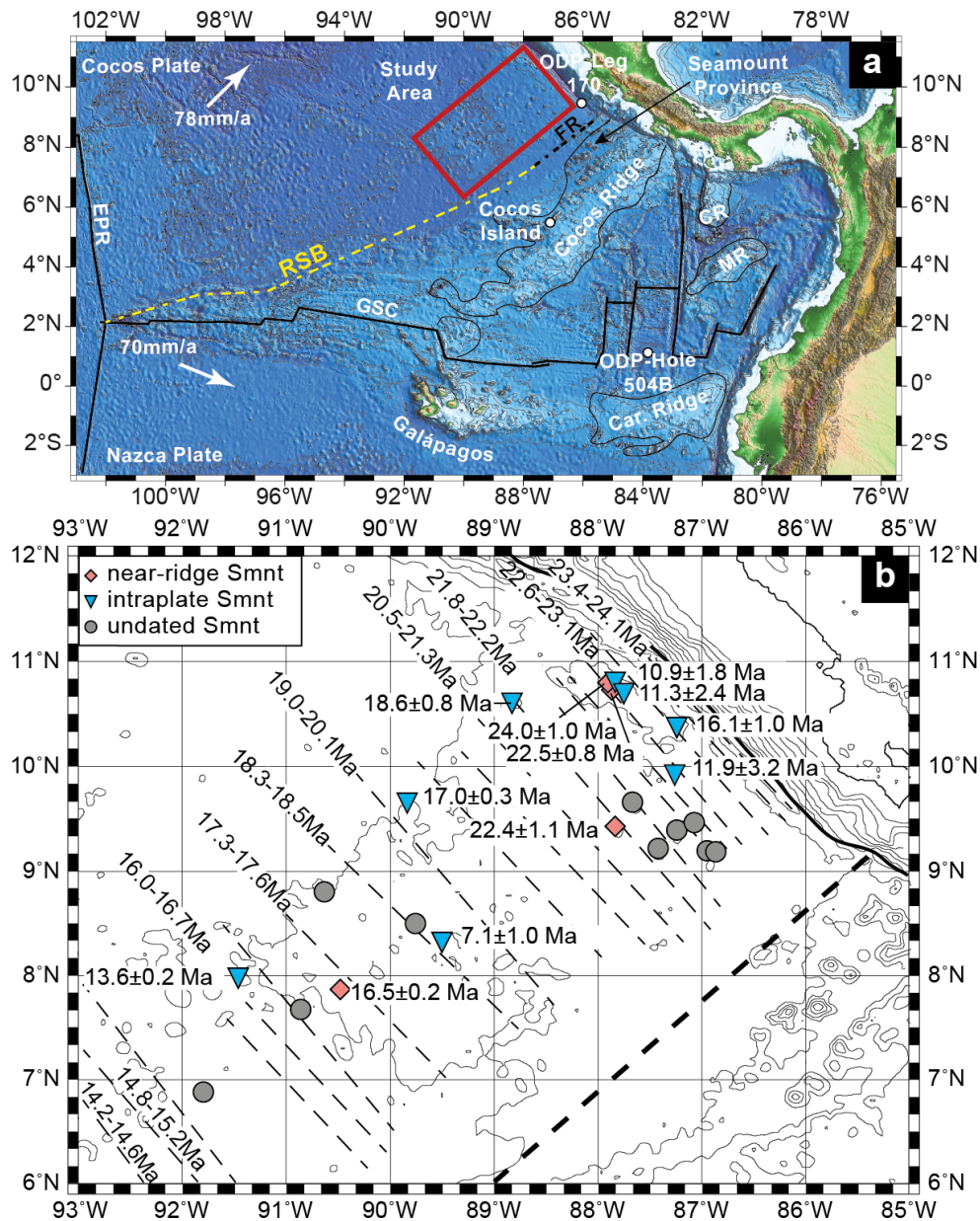
Figure 2.1: a) Bathymetric overview map of the equatorial East Pacific area showing the major bathymetric features (data are from The GEBCO_08 Grid, version 20091120, http://www.gebco.net; GSC – Galápagos Spreading Center; EPR – East Pacific Rise; CR – Coiba Ridge; MR – Mapelo Ridge; Car. Ridge – Carnegie Ridge, FR – Fisher Ridge, RSB – rough smooth boundary). The rectangle encloses the study area with b) showing a blow up of the study area. Crustal ages inferred from paleomagnetic data are displayed along stippled lines (Barckhausen et al., 2001). Diamonds mark seamounts with ^{40}Ar/^{39}Ar ages <2 Ma younger than the underlying crust, inverted triangles mark seamounts >2 Ma younger than the ocean crust, circles mark geochemically studied seamounts, which were dated. Plate motion vectors are from Wilson (1996); Barckhausen et al. (2001).

that flow of Galápagos Northern Domain plume material both along the GSC and EPR and also along the base of the lithosphere can explain the intraplate seamount volcanism up to 900 km away from the hotspot.

2.2   Regional Background

The Galápagos Archipelago thought to be the surface expression of a long-lived mantle plume (e.g., Duncan & Hargraves, 1984; Morgan, 1971), originating from the Earth's lower mantle (Graham *et al.*, 1993; Montelli *et al.*, 2006). It is spatially zoned in geochemistry with lavas with radiogenic Sr and Pb and unradiogenic Nd isotope ratios erupting in a horseshoe-shaped region surrounding an area where the volcanic products reflect a isotopically depleted composition, similar to N-MORB (e.g., Geist *et al.*, 1988; Harpp & White, 2001; White *et al.*, 1993) or depleted plume material (Hoernle *et al.*, 2000). Based on the isotopic composition of the erupted lavas, the "horseshoe" has been subdivided into three distinct enriched geographic domains – Northern (containing Wolf, Darwin and Pinta Islands), Central (including Fernandina) and Southern (including Floreana) Galápagos Domains (Geldmacher *et al.*, 2003; Hoernle *et al.*, 2000; Werner *et al.*, 2003). The Central Domain, however, may represent a mixture of Southern and Northern Domains plus depleted material (Hoernle *et al.*, 2000). Therefore the Galápagos hotspot could either reflect an asymmetrically zoned plume with three (Hoernle *et al.*, 2000) or two compositional end-members (Rohde *et al.*, 2013), forming vertical stripes or filaments in the plume conduit (Farnetani & Hofmann, 2009; Lohmann *et al.*, 2009).

The Nazca and Cocos Plates formed due to the break up of the Farallon Plate, which was most likely caused by a fracture zone passing over the Galápagos hotspot ∼23 Ma ago (Lonsdale, 2005; Lonsdale & Klitgord, 1978). The north-south-trending East Pacific Rise borderes the Cocos Plate in the west and the east-west-trending Galápagos Spreading Center borders it in the south. In the east, the Cocos Plate subducts along the Central American Trench with convergence rates varying between 85-88 mm/a (DeMets *et al.*, 1990).

A rough-smooth boundary (RSB; ∼2-5 km width; see dashed line in 2.1) separates the smoother crust that forms at the EPR in the north from the rough seafloor that forms at the GSC in the south (Fisher *et al.*, 2003). The Cocos Ridge and Seamount Province are located on the crust formed at the GSC and are geochemically zoned at their older end similar to the Galápagos Archipelago (Harpp *et al.*, 2005; Hoernle *et al.*, 2000; Werner *et al.*, 2003). The Cocos Plate that formed at the EPR contains abundant large, randomly distributed seamounts, including the study area (shown in box in 2.1) located ∼250-500 km northwest of the Cocos Ridge. The CPS, covering <5% of the seafloor, are located at depths of 1,500 to 3,800 m below sea level (b.s.l.). They reach elevations of up to 2,000 m above the surrounding seafloor and have diameters of up

to 10-14 km. Absence of signs of sea surface erosion point to formation beneath sea level.

The morphology of the CPS ranges from irregular to cone-shaped edifices. Close to the Central American Trench, they have been dissected by faults related to the bending of the subducting Cocos Plate. Some, mainly circular shaped seamounts with $\sim$4 km diameter at their base, are characterized by central craters, which are located between 3,500 and 3,800 m b.s.l. A representative selection of CPS bathymetry is provided in the electronic appendices (Fig. A.1). Highly vesicular volcaniclastic samples containing particles, such as "Limu o Pele"(thin flakes of volcanic glass formed when magma bubbles burst), are strong indicators for explosive fragmentation of the erupted lavas at great water depths.

2.3 Sample preparation

Fresh volcanic glass was chipped off on board of the ship and further processed at GEOMAR (Kiel, Germany). The glass chips were wrapped in tubular film and paper and carefully crushed with a hammer. Manganese crusts and altered rims were cut off from whole-rock samples, which were then crushed into smaller pieces using a jaw crusher. Both volcanic glasses and whole-rock fragments were sieved preserving the fractions between 250 μm and 2 mm and repeatedly washed with de-ionized water in an ultrasonic bath to remove dust-sized particles by decantation until a clear solution was obtained. The material was then dried overnight at 50°C and chips of the fractions 0.5-1 mm and 250-500 μm were carefully examined and handpicked under a binocular microscope. The freshest glass and whole-rock fragments (without coatings or vesicle fill) were picked for subsequent chemical analyses. Whole-rock chips were pulverized in a two-step process using an agate mortar grinder and a oscillating disc mill or planetary ball mill, depending on the amount of available material. A subset of 0.5-1.0 mm sized glass and whole-rock chips was used for Sr, Nd and Pb isotope analyses.

2.3.1 ^{40}Ar/^{39}Ar dating methods

Eleven rock samples from nine seamounts were dated (Table 2.3.1; Fig. 2.2) using the ^{40}Ar/^{39}Ar laser step-heating technique. Matrix (n=5) and glass (n=9) particles were hand-picked from crushed and sieved splits (250-500 μm) and washed and cleaned using an ultrasonic disintegrator.

Separates were irradiated for 6 hrs in aluminum trays and capsules in the cadmium shielded RODEO tube of the HFR facilities (NRG, Petten, The Netherlands). The neutron flux was monitored using Taylor Creek Rhyolite Sanidine (TCR-2: 27.87 $\pm$ 0.04 Ma; Lanphere & Dalrymple (2000)). ^{40}Ar/^{39} laser step-heating analyses were carried out at the GEOMAR Geochronology Lab using a 20 W SpectraPhysics Argon-Ion laser and an MAP 216 series noble gas mass spectrometer. Ar isotope ratios from mass spectrometry were corrected for mass discrimination, background and
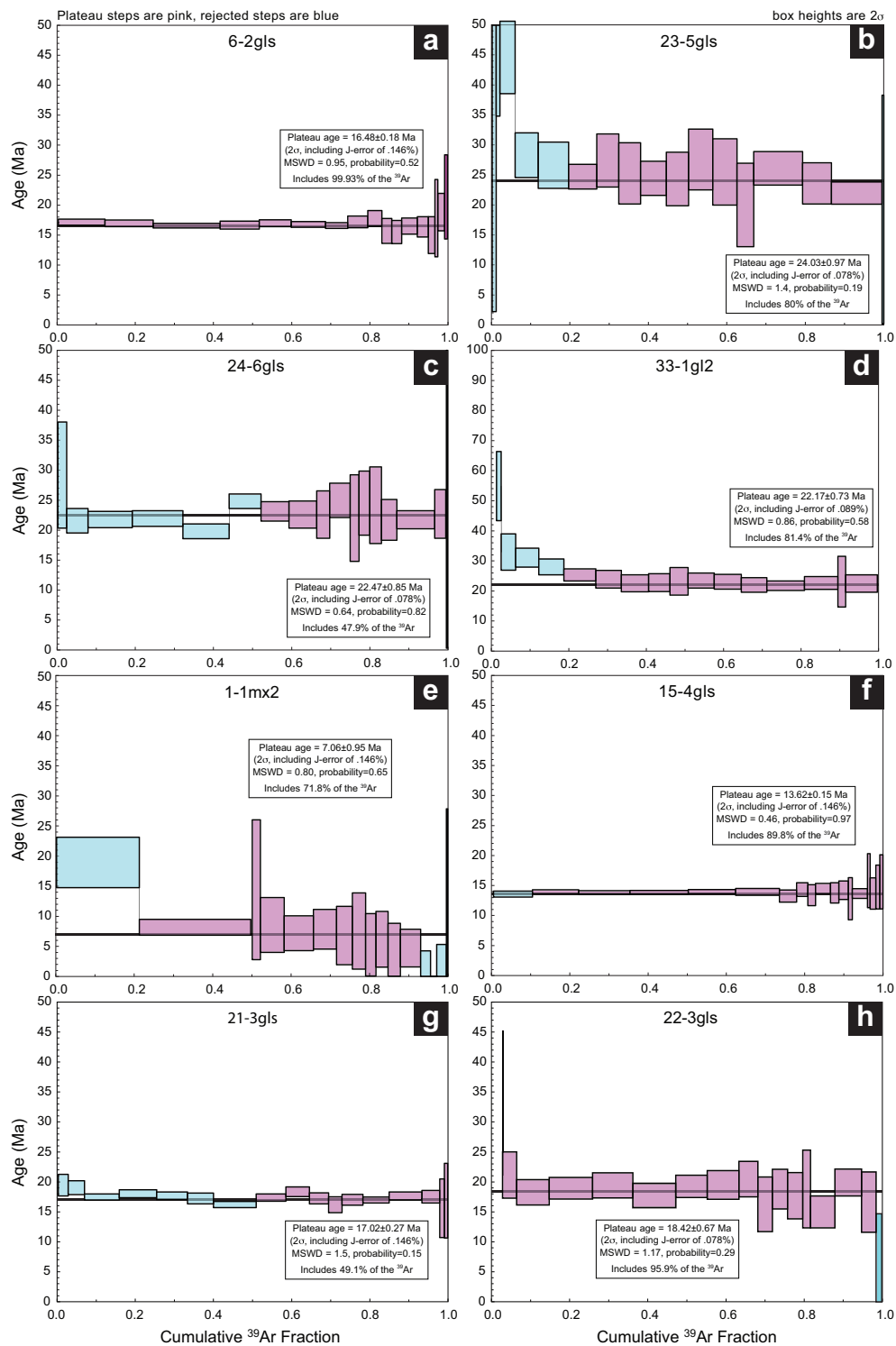
Figure 2.2: Representative selection of plateau diagrams, the full set is available in the online appendix. Plateau diagrams a-d for seamounts formed near the EPR ridge axis and e-h for seamounts formed in an intraplate setting.

blank values, and J-value gradients. Correction factors applied to interfering neutron reactions on Ca and K are $(^{40}\text{Ar}/^{39}\text{Ar})$ K: 0.00183, $(^{39}\text{Ar}/^{37}\text{Ar}$ Ca: 0.000699, and $(^{36}\text{Ar}/^{37}\text{Ar})$ Ca: 0.000270; Wijbrans *et al.* (2007)).

Table 2.1: $^{40}\text{Ar}/^{39}\text{Ar}$ step-heating results. Selected age spectra shown in Fig. 2.2 are in italic

Sample (SO208)	Analysis ID	Plateau age ±2SE	MSWD	Probability	^{39}Ar %	steps	Plateau step A.I.
Pan-Cake							
DR1-1_wr	1-1mx2	7.1 ±1.0	0.80	0.65	71.8	2 to 14	<5E-4
GUATBO1							
DR6-2	6-2gls	16.5 ±0.2	0.95	0.52	99.9	2 to 20	<1E-4
SPIEGELEI							
DR15-4	15-4gls	13.6 ±0.2	0.46	0.97	89.8	3 to 20	<1E-4
PICKEL							
DR21-3	21-3gls	17.0 ±0.3	1.50	0.15	49.1	9 to 18	<5E-5
UNNAMED							
TVG22-3	22-3gls	18.4 ±0.7	1.17	0.29	95.9	2 to 16	<5E-5
TVG22-3	22-3gl2	18.7 ±0.5	1.20	0.26	65.3	9 to 20	<5E-5
wtd. Mean	22-3gl	18.6 ±0.8	0.15	0.70			
BEND FAULT							
DR23-5	23-5gls	24.0 ±1.0	1.40	0.19	80.0	6 to 16	<5E-5
DR24-6	24-6gls	22.5 ±0.9	0.64	0.82	47.9	7 to 20	<5E-5
DR25-2_wr	25-2mxs	10.0 ±2.5	1.15	0.29	52.4	2 to 20	<5E-5
DR25-2_wr	25-2mx2	11.0 ±0.9	1.30	0.24	65.0	2 to 15	<5E-4
wtd. Mean	25-2mx	10.9 ±1.8	0.14	0.71			
LITTLE BEND							
DR26-2_wr	26-2mxs	11.3 ±2.4	1.40	0.12	55.6	2 to 20	<1E-4
SCHRIPPE							
DR30-4_wr	30-4mxs	16.1 ±1.0	0.92	0.55	59.5	2 to 17	<1E-3
KRINGEL							
DR33-1	33-1gls	22.7 ±0.9	1.30	0.23	88.4	4 to 16	<5E-5
DR33-1	33-1gl2	22.2 ±0.7	0.86	0.58	81.4	7 to 18	<1E-5
wtd. Mean	33-1gl	22.4 ±1.1	0.23	0.63			

MSWD = Mean Squared Weighted Deviates

A.I. = Alteration index = $((^{36}\text{Ar}/^{39}\text{Ar}) - 0.000268*(^{37}\text{Ar}/^{39}\text{Ar}))*(J/0.01)/(^{37}\text{Ar}/^{39}\text{Ar})$

The step-heating data are evaluated on age spectra diagrams (apparent age and error versus cumulative ^{39}Ar) to detect plateaus (>3 consecutive steps comprising >50% of the ^{39}Ar released, with ages overlapping within 2 sigma errors). Plateau ages represent the inverse-variance weighted mean of the plateau step ages and errors. The MSDW (mean square weighted deviates; should be «3) and POF (probability of fit; should be >0.05 at 2σ=95% confidence levels; Baksi (1999)) are used to evaluate the statistical robustness of

plateaus and plateau ages.

2.3.2 Major elements

Major-element compositions of fresh glass were obtained using the JEOL JXA-8200 Electron Microprobe (EPMA) at GEOMAR on mounted chips. A single mount (ø=1") contained up to 36 samples with three to four chips from each sample immersed in a two-component epoxy resin-based adhesive. The major-element concentrations were determined with an accelerating voltage of 15 kV and a spot size of 5 μm. Five spots per sample were measured and averaged. Standards used were VG-A99 (basaltic glass, Makaopuhi Lava Lake, HI) for P_2O_5, FeO, SiO_2, K_2O, CaO, TiO_2, VG-2 (basaltic glass, Juan de Fuca Ridge) for Na_2O, MgO, Al_2O_3, MnO and Scapolite (Meionite, Brazil) for SO_3 and Cl (Jarosewich *et al.*, 1980). The reproducibility for all elements is below 3% relative standard deviation (RSD, except for P_2O_5 with 6.2%RSD and MnO 20.2%RSD and with an accuracy better than 2%, except 12.2% for MnO.

Major-elements of whole-rock and glass samples were determined by X-Ray Fluorescence Analyses (XRF) on fused pellets using a Magix Pro PW 2540 XRF at the Institute of Mineralogy and Petrography at the University of Hamburg and for three samples by inductively coupled plasma optical emission spectrometry (ICP-OES) at Acme Analytical Laboratories (Vancouver) Ltd. Loss on ignition (LOI) was determined by mass differences after glowing 1 g of sample in a furnace at 1,050°C for several hours. For XRF measurements, the following standards were measured along with the samples JGB-1, JB-3, JB-2, JA-3, JG-3 and JG-2. The accuracy for most of the elements lies within 3% of the reference values suggested by GeoReM (`http://georem.mpch-mainz.gwdg.de/`).

ICP-OES instrument stability was determined by repeated measurements of STD SO-18 and all elements reproduce better than 1%RSD except for P_2O_5 with 4.8%RSD and MnO with 1.4%RSD. The reproducibility was controlled by duplicate sample digests (SO208 DR53-1, DR55-2) which was below 1%RSD, except P_2O_5 with 3.8%RSD. Three procedural blanks were measured to monitor external contributions during sample preparation, which were found to be insignificant (<0.01 for SiO_2, Al_2O_3, MgO, CaO, Na_2O, K_2O, TiO_2, P_2O_5, MnO, <0.04 for Fe_2O_3 and <0.002 for Cr_2O_3). The international reference materials BIR-1 (USGS Reykjanes Peninsula basalt) and BCR-2 (USGS Columbia River basalt) measured along with the samples compare within 5% of the values recommended by GeoReM. Major-element data of the analyzed CPS samples are provided in the appendix (Table A).

2.3.3 Trace elements

Trace-element concentrations of glass chips were determined by laser ablation inductively coupled plasma mass spectrometry (LA-ICP-MS) at the Institute of Geoscience, University of Kiel, using a Coherent GeoLasPro Plus 193 nm Excimer laser coupled to an Agilent 7500cs quadrupole ICP-MS. A newly designed large-volume ablation cell (LDHCLAC cell, Trace-element and Microanalysis Group, ETH Zürich) was used in all experiments. Spot size of the laser beam was 80 μm with a repetition rate of 10 Hz and 80 s total acquisition time. The blank signal was measured 20 s prior to each ablation and used for calculation of the actual detection limits. Helium being the carrier gas @ 1.0 l/min was subsequently mixed with Argon @ 0.8 l/min before introduction into the ICP-MS. Calcium (44 m/z) was used for internal standardization. The software Glitter (Macquarie Univ., Australia) was used for data integration of time-resolved signals.

Glass SRM NIST612 (preferred values from Jochum *et al.*, 2011; Pearce *et al.*, 1997) was used for instrument calibration, and analytical quality was monitored by repeat analyses of the glass reference material (RM) BCR-2G. Additionally, at the beginning and end of each analytical session (one per day), the MPI-DING glass RMs KL-2G (Kilauea basalt), St.HS. 6/80-G (St. Helens andesite), GOR128-G and GOR132-G (Gorgona komatiites; Jochum *et al.*, 2006) were analyzed and used for a second step of matrix-matched calibration. Typically, precision as estimated from 40 (DING glasses) to 400 (BCR-2G) repeat analyses was better than 4%RSD (1σ) for all elements at concentrations significantly above detection limits. Accuracy of results for all analyzed RM can be evaluated from Table A2 in the electronic appendix. Average precision of duplicate sample analyses performed during different sessions on different days was 5%rel. (range 1-8%rel.) except Mo, and Cs (12 and 16%rel.).

Trace-elements of whole-rock samples have been analyzed by solution ICP-MS using an AGILENT 7500cs ICP-MS quadrupole instrument at the Institute of Geosciences, University of Kiel. Between 100 and 250 mg sample powder was digested during a multi-step table-top procedure in sealed PFA vials, following the method described in Garbe-Schönberg (1993) with few modifications. Prior to analysis the final solution was diluted 50-fold and spiked to 2.5 μg/l beryllium, indium, rhenium for internal standardization. Analytical accuracy is monitored through international rock standards of BIR-1, BHVO-2 and BCR-2 that were digested and analyzed along with the samples. The measured values for the standards typically lie within 3% of the values recommended by GeoReM. Precision is better than 1%rel. for replicates of sample digests and instrumental analysis. Trace-element data for the samples and standards for Laser and solution ICP-MS is provided in the appendix Table A, Table A.4, and Table A.5 respectively.

2.3.4 Isotopic data

Thermal ionization mass spectrometry (TIME) at GEOMAR was used to determine radiogenic isotope ratios of Sr, Nd and Pb double spike (DS). The isotope analyses were carried out on 100-250 mg of volcanic glass and/or whole-rock chips weighted into 15 ml PFA vials. First, the chips were leached in 2 N HCl at 70°C for one hour and repeatedly rinsed with 18.2 MΩ/cm H_2O to remove possible signs of alteration and the effects of sample handling. Then the samples were dissolved in a 5:1 mixture of concentrated ultra-pure HF and HNO_3 at 150°C for 48 hours. Element separation followed the method described in Hoernle *et al.* (2008).

Pb isotope ratios were determined on a Finnigan MAT262 RPQ2+, operating in static multi-collection mode. All Pb isotope ratios were mass bias corrected using the ^{207}Pb-^{204}Pb double spike technique of Hoernle *et al.* (2011). The reproducibility of NBS981 (n=36) is ^{206}Pb/^{204}Pb=16.9413$\pm$0.0024 (2σ), ^{207}Pb/^{204}Pb=15.4988$\pm$0.0025 (2σ), and ^{208}Pb/^{204}Pb=36.7236$\pm$0.0063 (2σ). Replicate analysis (n=6) of samples in terms of separate sample digests are within the external errors of NBS981.

The measurements of Sr and Nd isotopic ratios were performed on a Thermo Scientific TRITON, operating in static multi-collection mode. Sr and Nd isotope ratios were normalized within run to ^{86}Sr/^{88}Sr=0.1194 and ^{146}Nd/^{144}Nd=0.7219, respectively. All Sr isotope data are reported relative to NBS987 with ^{86}Sr/^{88}Sr=0.710250$\pm$0.000010 (2σ; n=63). The Nd isotope data are reported relative to the La Jolla standard with ^{143}Nd/^{144}Nd=0.511850$\pm$0.000007 (2σ; n=45). Our in-house Nd monitor Spex gave ^{143}Nd/^{144}Nd=0.511715$\pm$0.000006 (2σ; n=38) for the same period. Samples were replicated within the external errors of NBS987 and La Jolla. Some whole-rock chips, however, yielded high, seawater-altered

^{87}Sr/^{86}Sr and thus were reanalyzed on powders that were leached with 6 N HCl at 150°C for 72 hours and then repeatedly rinsed in 18.2 MΩ/cm H$_2$O prior to dissolution. As is evident from Sr-Nd isotope correlations (not shown), this measure resulted in ^{87}Sr/^{86}Sr ratios closer to magmatic values. Replicate analyses of tholeiitic sample SO208 DR1-1 (inverted triangles below the NHRL in 2.7a) yielded Nd isotope ratios within error but ^{206}Pb/^{204}Pb could not be reproduced (4 digests of separate handpicked chip populations) within error. Replication of the Nd isotope ratio is consistent with the Sm-Nd isotope system being relatively resistant to seawater alteration due to the fluid immobility of the Rare Earth Elements (REE). The high μ (=^{238}U/^{204}Pb) $\sim$42 and low Th/U of $\sim$0.30 values of this sample indicate a complex alteration history for this sample with variable U uptake and loss through seawater alteration leading to an undercorrection for radiogenic ingrowth. Isotope data including initial values are provided in the appendix Table A for Sr and Nd and Table A.6 for Pb.

2.4 Results

2.4.1 ^{40}Ar/^{39}Ar age dating

The analyses were carried out on glass (gl, 9 analyses) and/or matrix (mx, 5 analyses) material. The ^{40}Ar/^{39}Ar ages for the Cocos Plate Seamounts range from 7.1 ± 1.0 Ma to 24.0 ± 1.0 Ma, but no clear age progression or correlation with estimated crustal age (Barckhausen *et al.*, 2001) is observed (Table 2.3.1). A representative selection of plateau diagrams is shown in Figure 2.2 (plateau diagrams of all dated samples, including multiple age determinations are shown in appendix Figure A2). Multiple ^{40}Ar/^{39}Ar ages determined on different splits of the same sample set usually reproduced within error (TVG22-3, DR25-2, DR33-1). Samples from three different dredge hauls on Bend Fault Seamount yielded widely differing ages of 24.0 ± 1.0 Ma (DR23-5) and 22.5 ± 0.9 Ma (DR24-6) respectively, and 10.9 ± 1.8 Ma (DR25-2_wr; a weighted mean age) with an age difference of $\sim$12 Ma. A sample from nearby Little Bend Seamount yielded a similar age of 11.3 ± 2.4 Ma (DR26-2_wr) to the younger sample from Bend Fault Seamount.

^{40}Ar/^{39}Ar ages along with the geomagnetic polarity ages of the underlying ocean crust are shown in Table 2.4.1. In order to determine if the samples formed on or near the spreading center or in an intraplate setting, we have divided our samples into the following groups:

1. near-ridge CPS samples (DR6-2, DR23-5, DR24-6, DR33-1) within 2 Ma of the estimated paleomagnetic crustal ages and therefore formed <130 km away from the ridge axis, based on a half spreading rate of 65 mm a$^-$1 Lonsdale (1988);

2. intraplate CPS samples (DR1-1, DR15-4, DR21-3, TVG22-3, DR25-2, D26-2, DR30-4) with ages more than 2 Ma younger than the estimated paleomagnetic crustal age beneath the volcano and thus formed more than 130 km away from the EPR ridge;

3. undated CPS samples for which no ages were determined.

Table 2.2: Seamount name, sample number, rock type, sample location, crustal age beneath seamount (Barckhausen *et al.*, 2001) and ^{40}Ar/^{39}Ar plateau age ±2Sigma error for seamounts (ages marked with * represent weighted mean ages). The samples are divided into near-ridge, intraplate and undated groups. Note that samples from "Bend Fault" seamount display large age variations ranging from near-ridge to intraplate settings.

Sample No. (SO208)	rock-type	Lat	Long	Geomagnetic Polarity Timescale		^{40}Ar/^{39}Ar Dating		Difference	
		°N	°W	Interval Ma	Chron	Age Ma ±2SE (M)		Ma	
				min max				min max	
Near-ridge Seamount Samples									
Egg									
DR6-2	AB	7.84	90.47	17.3 17.6	5D	16.5	0.2	0.8	1.1
Bend Fault									
DR23-5	TH	10.77	87.89	22.6 24.1	6B-6C	24.0	1.0	-1.4	0.1
DR23-5_wr	TH	10.77	87.89	22.6 24.1	6B-6C				
DR24-6	TH	10.76	87.87	22.6 24.1	6B-6C	22.5	0.9	0.1	1.6
Kringel									
DR33-1	TH	9.41	87.84	21.8 21.9	6AA	22.4*	1.1	-0.6	-0.5
DR33-1_wr	TH	9.41	87.84	21.8 21.9	6AA				
Intraplate Seamount Samples									
Pan-Cake									
DR1-1_wr	TH	8.22	89.51	18.3 18.8	5E	7.1	1.0	11.2	11.7
Spiegelei									
DR15-4	HW	7.95	91.47	16.0 16.7	5C	13.6	0.2	2.4	3.1
DR15-4_wr	HW	7.95	91.47	16.0 16.7	5C				
Pickel									
DR21-3	AB	9.63	89.84	19.0 20.1	6	17.0	0.3	2.0	3.1
DR21-3_wr	AB	9.63	89.84	19.0 20.1	6				
Unnamed									
TVG22-3	TH	10.59	88.83	21.8 21.9	6AA	18.6*	0.8	3.2	3.3
Bend Fault									
DR25-2	TH	10.79	87.84	22.6 24.1	6B-6C				

... continued

Sample No. (SO208)	rock-type	Lat	Long	Geomagnetic Polarity Timescale		Chron	^{40}Ar/^{39}Ar Dating		Difference	
		°N	°W	Interval Ma		Chron	Age Ma ±2SE (M)		Ma	
				min	max				min	max
DR25-2_wr	TH	10.79	87.84	22.6	24.1	6B-6C	10.9*	1.8	11.7	13.2
Little Bend										
DR26-2_wr	TH	10.69	87.76	22.6	24.1	6B-6C	11.3	2.4	11.3	12.8
Schrippe										
DR30-4_wr	TH	10.41	87.25	23.4	24.1	6C	16.1	1.0	7.3	8.0
Undated Seamounts Samples										
Pan-Cake										
DR1-5	TH	8.22	89.51	18.3	18.8	6e				
Half-Moon										
DR2-1_wr	TH	8.47	89.76	18.3	18.8	5E				
Boxer										
DR7-2_wr	TH	7.64	90.87	16.0	16.7	5C				
Horseshoe										
DR9-5_wr	TH	6.90	91.59	14.8	16.7	5B-5C				
Spiegelei										
DR15-5	HW	7.95	91.47	16.0	16.7	5C				
DR15-6_wr	HW	7.95	91.47	16.0	16.7	5C				
Eye										
DR17-1	TH	8.75	90.72	17.3	18.8	5D-5E				
DR17-1_wr	TH	8.75	90.72	17.3	18.8	5D-5E				
DR17-7	TH	8.75	90.72	17.3	18.8	5D-5E				
DR17-19	TH	8.75	90.72	17.3	18.8	5D-5E				
DR17-20	TH	8.75	90.72	17.3	18.8	5D-5E				
Pickel										
DR21-1	AB	9.63	89.84	19.0	20.1	6				
DR21-2	TH	9.63	89.84	19.0	20.1	6				

. . . continued

Sample No. (SO208)	rock-type	Lat	Long	Geomagnetic Polarity Timescale			^{40}Ar/^{39}Ar Dating	Difference	
		°N	°W	Interval Ma		Chron	Age Ma ±2SE (M)	Ma	
				min	max			min	max
Unnamed									
TVG22-1	TH	10.59	88.83	21.8	21.9	6AA			
TVG22-4_wr	TH	10.59	88.83	21.8	21.9	6AA			
Bend Fault									
DR23-1_wr	TH	10.77	87.89	22.6	24.1	6B-6C			
DR23-6	TH	10.77	87.89	22.6	24.1	6B-6C			
DR24-2_wr	TH	10.76	87.87	22.6	24.1	6B-6C			
DR24-20_wr	TH	10.76	87.87	22.6	24.1	6B-6C			
DR25-4	TH	10.79	87.84	22.6	24.1	6B-6C			
DR25-10_wr	TH	10.79	87.84	22.6	24.1	6B-6C			
Little Bend									
DR26-3	TH	10.69	87.76	22.6	24.1	6B-6C			
Schrippe									
DR30-1	AB	10.41	87.25	23.4	24.1	6C			
DR30-1_wr	TH	10.41	87.25	23.4	24.1	6C			
DR30-2	HW	10.41	87.25	23.4	24.1	6C			
Ammonit									
DR31-1	TH	9.90	87.27	22.6	23.1	6B			
DR31-2	TH	9.90	87.27	22.6	23.1	6B			
DR31-2_wr	TH	9.90	87.27	22.6	23.1	6B			
DR31-3_wr	TH	9.90	87.27	22.6	23.1	6B			
Guardian									
DR32-1	TH	9.64	87.68	22.2	22.3	6AA1			
DR32-2_wr	TH	9.64	87.68	22.2	22.3	6AA2			
DR32-6_wr	TH	9.64	87.68	22.2	22.3	6AA3			
Bagel									

. . . continued

Sample No. (SO208)	rock-type	Lat	Long	Geomagnetic Polarity Timescale		^{40}Ar/^{39}Ar Dating	Difference
		°N	°W	Interval Ma	Chron	Age Ma ±2SE (M)	Ma
				min max			min max
DR36-1_wr	TH	9.14	87.42	21.8 22.3	6AA-6AA1		
Ojo							
DR37-1_wr	TH	9.37	87.25	22.6 23.1	6B		
DR37-3_wr	TH	9.37	87.25	22.6 23.1	6B		
Zecke							
DR38-1	TH	9.45	87.08	22.6 23.1	6B		
DR38-2	TH	9.45	87.08	22.6 23.1	6B		
DR38-4_wr	TH	9.45	87.08	22.6 23.1	6B		
Hook							
DR39-1_wr	TH	9.14	86.94	22.6 23.1	6B		
DR39-2_wr	TH	9.14	86.94	22.6 23.1	6B		
DR39-8-VC	TH	9.14	86.94	22.6 23.1	6B		
DR39-9-VC	TH	9.14	86.94	22.6 23.1	6B		
DR40-1_wr	TH	9.15	86.92	22.6 23.1	6B		

2.4.2   Petrography

In general the condition of the sampled glasses and whole-rocks varies from fresh to moderately altered. Signs of alteration include altered olivine, vesicles filled with secondary minerals, such as calcite and zeolites, veins of calcite or zeolite, and thin coatings of Mn. Such material was avoided by handpicking of the samples to obtain the freshest material. Fresh glass rinds were found on some of the samples. Most samples are characterized by a glomeropophyric texture with varying amounts of olivine and plagioclase. clinopyroxene, spinel and Fe-Ti-oxide (magnetite, ilmenite) phenocrysts are present in some samples.

Samples from seamounts formed near-ridge contain olivine and plagioclase as the main phenocrysts and clinopyroxene is sometimes present in the groundmass. Samples from intraplate seamounts contain phenocrysts and glomerocrysts of primarily plagioclase, clinopyroxene and Fe-Ti-oxides (ilmenite or magnetite) but in some cases also olivine. Some olivine crystals have spinel inclusions and are associated with glomerocrysts of plagioclase of varying size. Samples from seamounts that were not dated represent a mixture of near-ridge and intraplate seamount groups.

2.4.3   Major elements

On the total alkali versus silica (TAS; Fig. 2.3; Le Maitre *et al.*, 1989) diagram the CPS formed in close proximity to the EPR ridge axis have tholeiitic composition with the exception of one slightly alkaline basalt. Seamounts formed in an intraplate setting range from tholeiitic to alkaline basalt to hawaiite composition (Fig. 2.3). The MgO contents of the samples vary between 9.3 and 3.1 wt.% and Mg-numbers (Mg#=mol(Mg/(Mg+Fe^{2+}))) from 0.67 to 0.37, indicating the presence of some fairly primitive compositions. Samples generally do not form good correlations on binary diagrams with MgO (Fig. 2.4). With decreasing MgO, crude increases are observed for Al$_2$O$_3$, TiO$_2$, Na$_2$O, P$_2$O$_5$ and K$_2$O (e.g., Fig. 2.4d). The alkaline basalts and hawaiites generally have lower CaO but higher TiO$_2$, Na$_2$O and P$_2$O$_5$ (e.g., Fig. 2.4b) than the tholeiitic samples at a given MgO. The lack of good correlations on diagrams with MgO implies that the lavas from the seamounts are not the product of crystal fractionation from a common parental magma, which is also evident from the presence of both tholeiitic and alkalic compositions.

   Although most mafic (MgO >7 wt.%) CPS lavas overlap with reference EPR-MORB between 10°N and 10°S (gray field), the CPS evolve differently from EPR-MORB. In contrast to EPR lavas where SiO$_2$, FeO^T (FeO + Fe$_2$O$_3$), TiO$_2$ and P$_2$O$_5$ increase with decreasing MgO, the tholeiitic samples from the seamounts show no increase in these oxides with increasing differentiation (Fig. 2.4a, c). The lack of an increase in FeO^T and TiO$_2$ with decreasing MgO, suggests differentiation of magnetite. CaO contents of the seamount lavas remain either constant or decrease, as in EPR-MORB, with decreasing MgO. Al$_2$O$_3$ decreases with decreasing MgO in EPR-MORB, in the CPS lavas it increases to 4 wt.% MgO, indicating clinopyroxene fractionation before significant plagioclase fractionation (Fig. 2.4b, d).
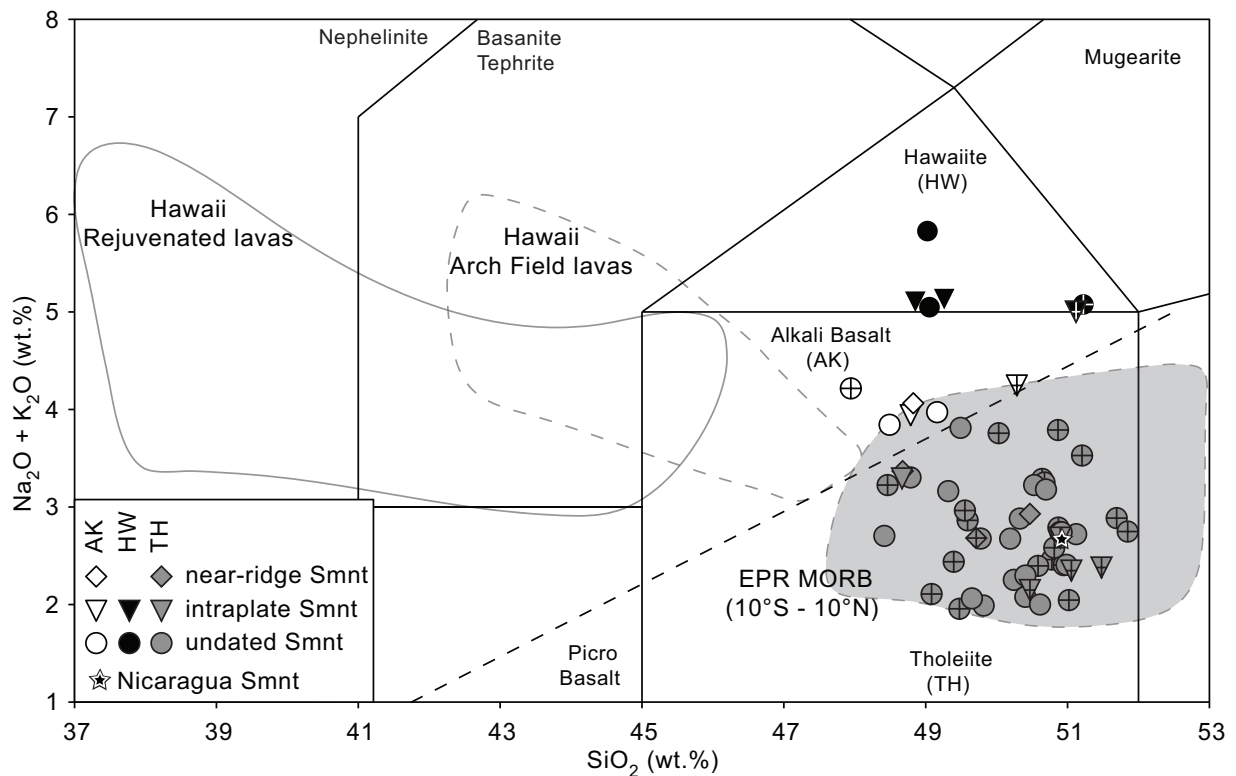
Figure 2.3: Silica versus total alkali-diagram (after Le Maitre *et al.*, 1989) of the seamount samples, field for EPR-MORB between 10°N and 10°S (gray field; PetDB `http://www.earthchem.org/petdb`), field for Hawaii Arch Field (open field with dashed outline; GEOROCK `http://georoc.mpch-mainz.gwdg.de/georoc/Entry.html`) and rejuvenated lavas (open field with solid outline; Clague & Frey, 1982) and Nicaragua Smnt sampled during R/V Sonne cruise SO144 (star; Werner *et al.*, 2003). Subdivision of volcanic rocks into alkaline and tholeiitic is after MacDonald & Katsura (1964). According to their major-element composition the Cocos Plate Seamount samples can be subdivided into Hawaiite (HW, black symbols), Alkali Basalts (AK, open symbols) and Tholeiites (TH, dark gray symbols). Symbols with a cross (+) denote that whole-rock material was analyzed, all other analyses were made on fresh handpicked glass.
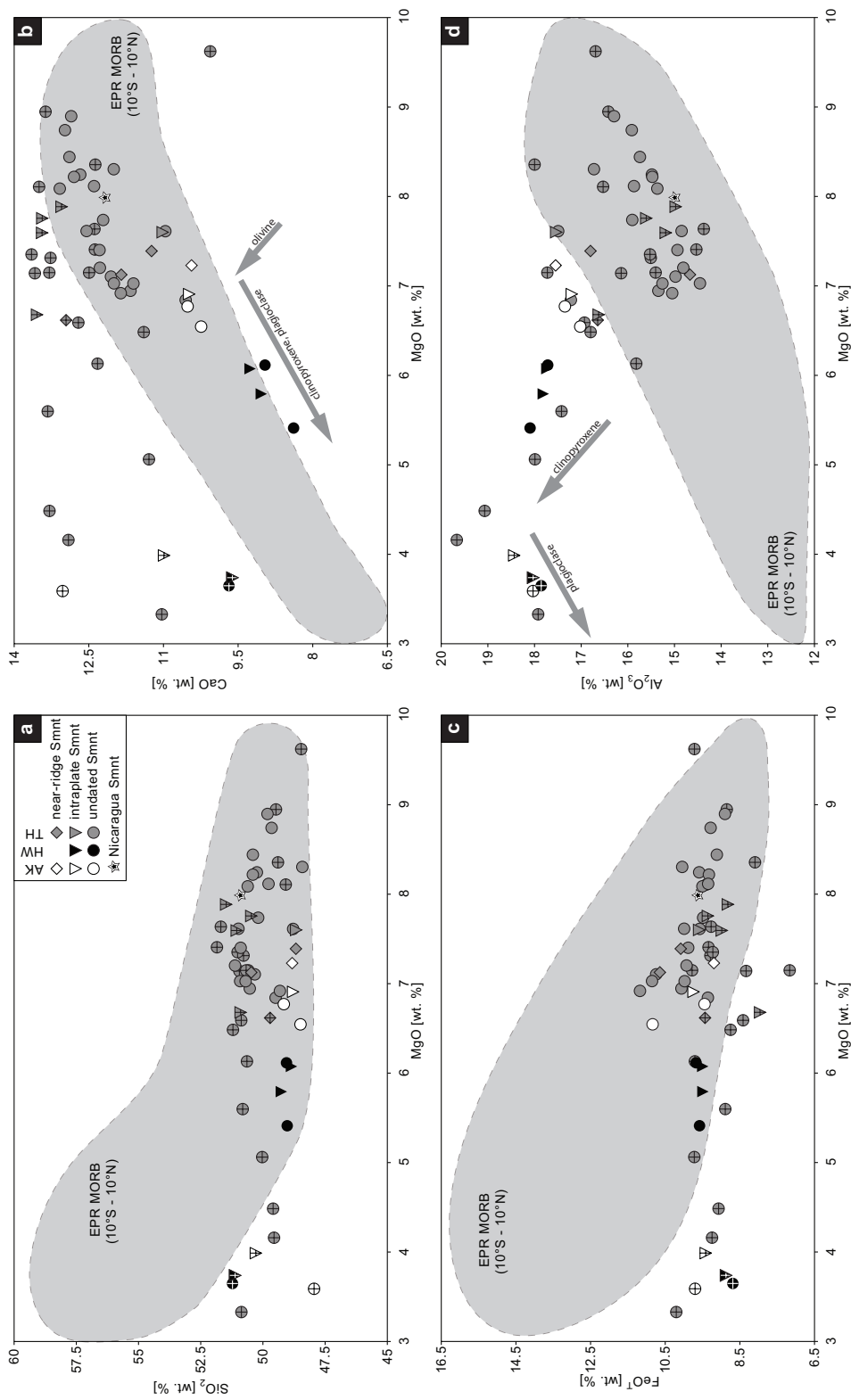
Figure 2.4: Major-element compositions of the Cocos Plate Seamounts compared with EPR-MORB between 10°N and 10°S. Major-element data have been normalized to 100% on a volatile-free basis. Symbols with a cross (+) mark whole-rock samples. In general the mafic samples (MgO ≥7 wt.%) overlap with the EPR-MORB field whereas samples with MgO <7 wt.% tend to higher Al_2O_3 and lower SiO_2, FeO^T. In a) Cocos Plate Seamount samples overlap the low SiO_2 end of the EPR array in samples with MgO >5 wt.%, after that the seamounts samples increase less steep compared to EPR-MORB. In b) no clear fractionation trend is observed indicating that the seamounts are not derived from the same parental magma. In c) FeO^T (total iron as FeO) shows almost no correlation with decreasing MgO. In d) Al_2O_3 increases with degreasing MgO in contrast to the EPR-trend indicating that cpx is a more important fractionating phase in the CPS than in the EPR lavas.

2.4.4   Trace elements

The CPS lavas display a wide range in trace-element composition ranging from highly-depleted incompatible element compositions, slightly more depleted than common D- and N-MORB through E-MORB to more OIB-like compositions (Gale *et al.*, 2013, Fig. 2.5). The most depleted compositions overlap with depleted compositions a) from the Galápagos Islands, such as found on Genovesa (Fig. 2.6a; White *et al.*, 1993) and b) EPR-MORB formed during superfast spreading, when the ridge was contaminated with Galápagos plume material that got progressively depleted in incompatible elements due to ongoing melt extraction while flowing beneath the ridge system (Geldmacher *et al.*, 2013, Fig. 2.6a).

Trace-element compositions of lavas formed near-ridge fall between average N-MORB and OIB (Fig. 2.5a). Lavas formed in an intraplate setting display greater variations in highly-to-moderately incompatible element composition, with some being more depleted than D-MORB (Fig. 2.5b). Highly incompatible elements show a large range in concentrations, for example Nb varies from 1.3 ppm for DR1-1_wr to 57.8 ppm for DR15-4. In the mafic samples with MgO >7 wt.%, the alkaline basalt has the greatest incompatible element enrichment (e.g., highest La/Yb ratios) and also the most heavily fractionated HREE element ratios (with the highest Sm/Yb and Tb/Yb) and TiO_2/Yb,, above those commonly observed in MORB (Fig. 2.6b), indicating the presence of small amounts of residual garnet. Lavas from the undated seamount group show a similar range in highly-to-moderately incompatible element compositions as the dated seamount groups but cover a much wider range (e.g., Nb ranging from 0.53 ppm for DR31-2 to 92.5 ppm for DR30-2). No clear differentiation between the three different age groups can be made, except that intraplate and undated seamount samples show a larger range than observed for near-ridge seamount samples.

More to less incompatible element ratios (e.g., Nb/Yb, La/Yb, La/Sm, Sm/Yb, Tb/Yb, TiO_2/Yb) form positive correlations (e.g., Fig. 2.6a, b). On a Nb/Yb versus TiO_2/Yb plot (Fig. 2.6b; after Pearce, 2008), all mafic samples (MgO >7 wt.%) plot within or on the boundary of the N-MORB array.

2.4.5   Isotope Ratios

The measured Sr-Nd-Pb isotope ratios of the CPS lavas are highly variable and range from depleted MORB-like ratios to enriched OIB-like compositions. Initial isotope ratios are shown, uassuming $^{40}Ar/^{39}$ ages for dated samples apply to all samples in a dredge and assuming that samples from undated dredges have the same age as the underlying crust (thus representing a maximum age for the samples). Maximum corrections for radiogenic ingrowth of ^{143}Nd, ^{206}Pb and ^{208}Pb are significant and indicated by a double headed arrow in Figure 2.7.

Overall the lavas form a positive correlation on Pb isotope correlation diagrams (e.g., Fig. 2.7a) and an inverse correlation on Pb versus Nd isotope diagram (Fig. 2.7b) with the alkaline samples having the most enriched isotopic compositions and tholeiitic the most depleted. Isotope correlation diagrams of Pb and Nd with Sr (not shown) describe a similar pattern with an inverse correlation on the Sr versus Nd diagram and a positive correlation on the Pb versus Sr plot. Even though the freshest material was picked for isotope analyses the correlation plots with Sr show signs of alteration for some samples with elevated $^{87}Sr/^{86}Sr$ ratios for a given $^{143}Nd/^{144}Nd$ ratio. Seamount SO144-1 (also called "Nicaragua Seamount" Werner *et al.*, 2003) is located further to the north, off the coast of Nicaragua, and plots at the depleted
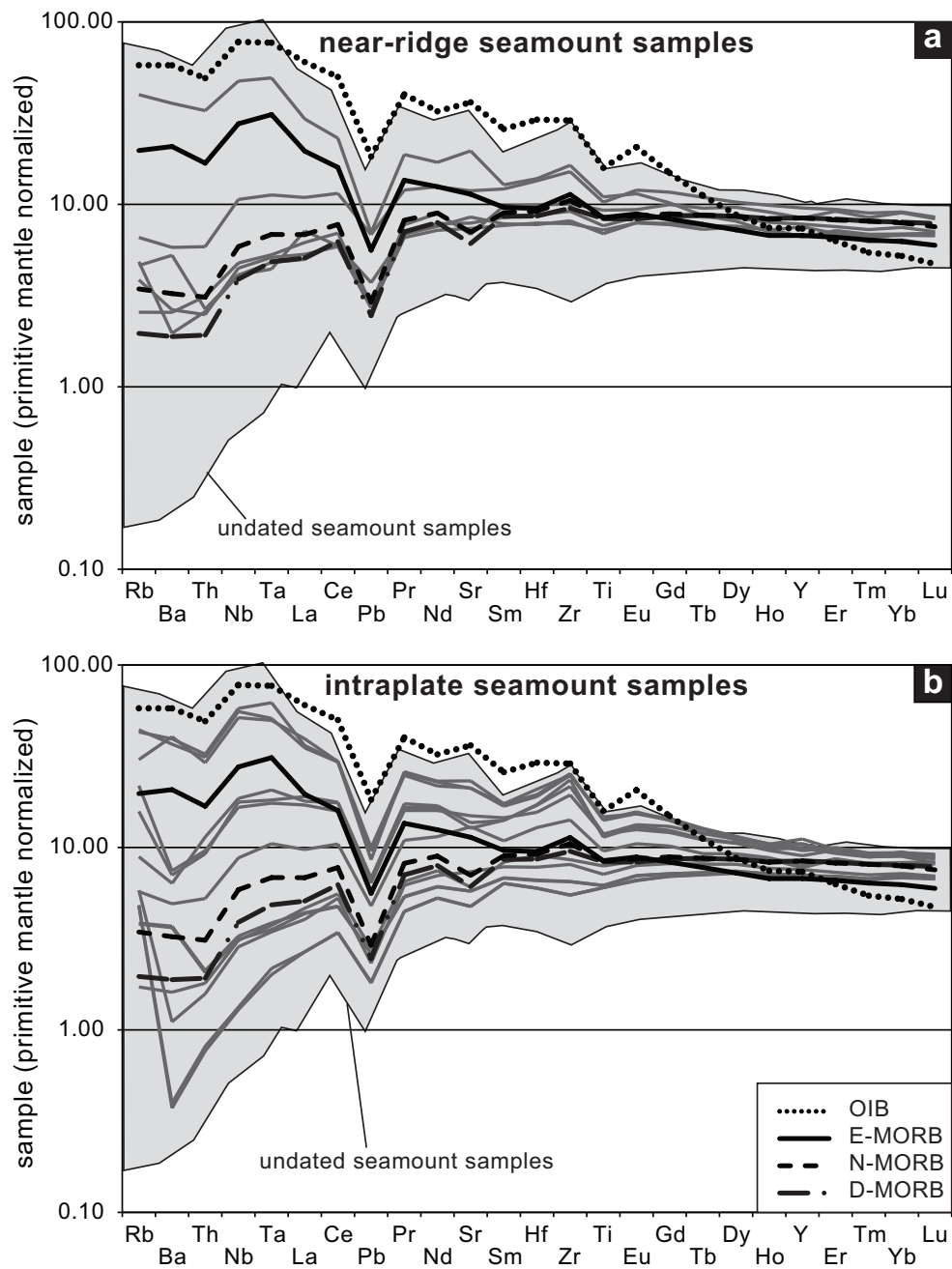
Figure 2.5: Multi element diagram for Cocos Plate Seamount lavas compared to average D-, N- & E-MORB (Gale *et al.*, 2013) and OIB patterns (Sun & McDonough, 1989). Incompatible element concentrations have been normalized to primitive mantle Hofmann (1988). a) Incompatible element patterns of near-ridge seamount group samples have compositions similar to N- to E-MORB except one sample with OIB-like pattern. b) Incompatible element patterns of intraplate seamount group range from below D-MORB to OIB. Undated seamounts are shown by grey field and cover a similar range in composition as the intraplate seamount group.
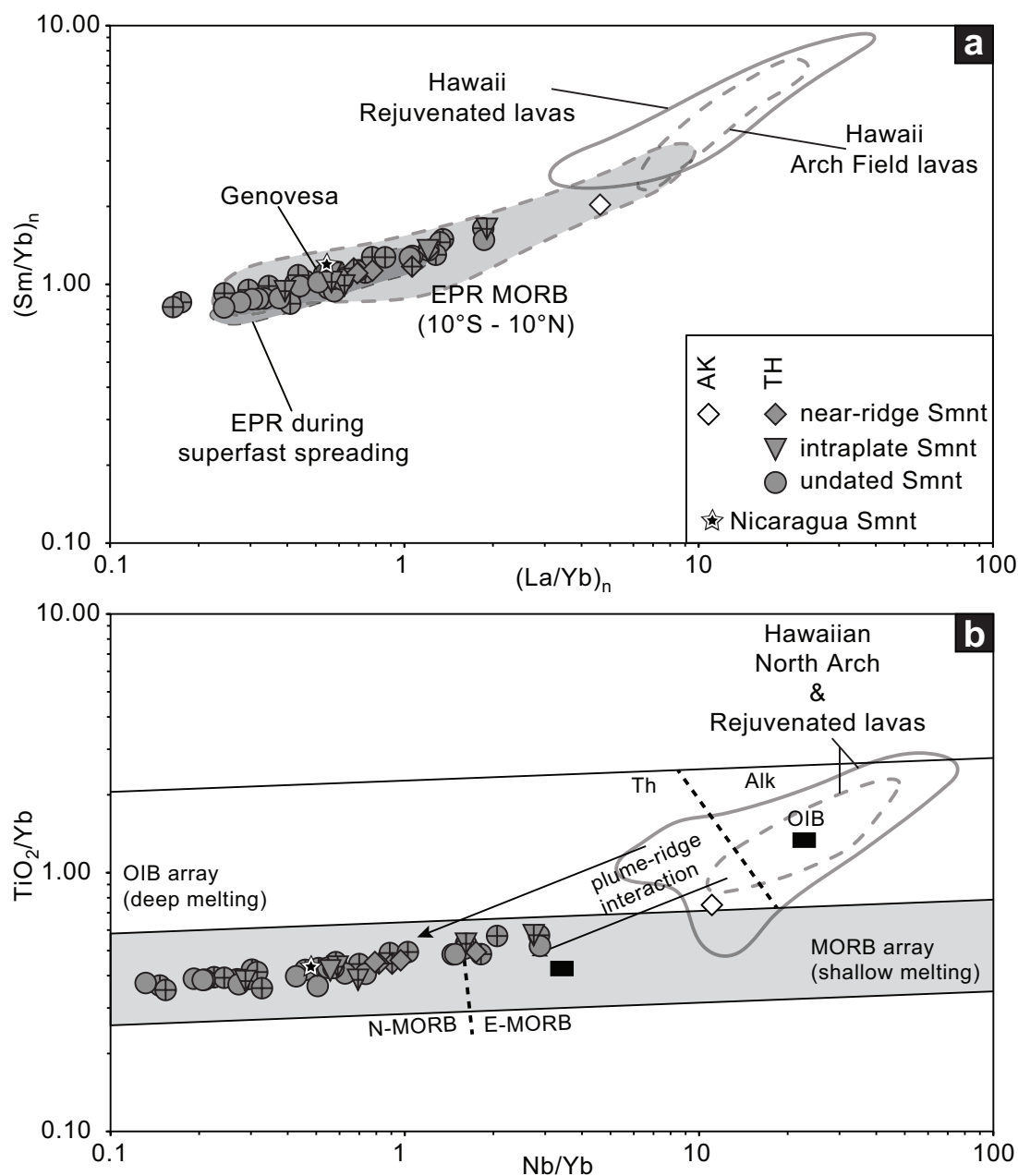
Figure 2.6: a) $(La/Yb)_n$ versus $(Sm/Yb)_n$ (n indicates normalization to Primitive Mantle after Hofmann (1988)) for samples with MgO >7 wt.%, shows that the Cocos Plate Seamount lavas have similar or slightly more depleted compositions than reference EPR-MORB from 10°S-10°N (PetDB) but overlap largely withCocos Plate ocean crust formed during superfast spreading at the EPR (Geldmacher *et al.*, 2013). b) Nb/Yb versus TiO_2/Yb after Pearce (2008) for samples with MgO >7 wt.%, indicates that melting occurred at shallower depths within the spinel stability field, similar to those at which MORB is generated, consistent with the MORB-like $(Sm/Yb)_n$ ratios. Hawaiian Arch and rejuvenated lavas have more alkaline compositions and most likely formed by lower degrees of melting (higher La/Yb) at greater depths within the garnet stability field ($\geq$70-80 km; Green & Ringwood, 1967; Ringwood, 1967; Robinson & Wood, 1998). Symbols with a cross (+) indicate analyses of whole-rock samples. Symbols with no cross are analyses of glass. Hawaii rejuvenated lavas (open field with solid outline; Clague & Frey, 1982; Garcia *et al.*, 2010).
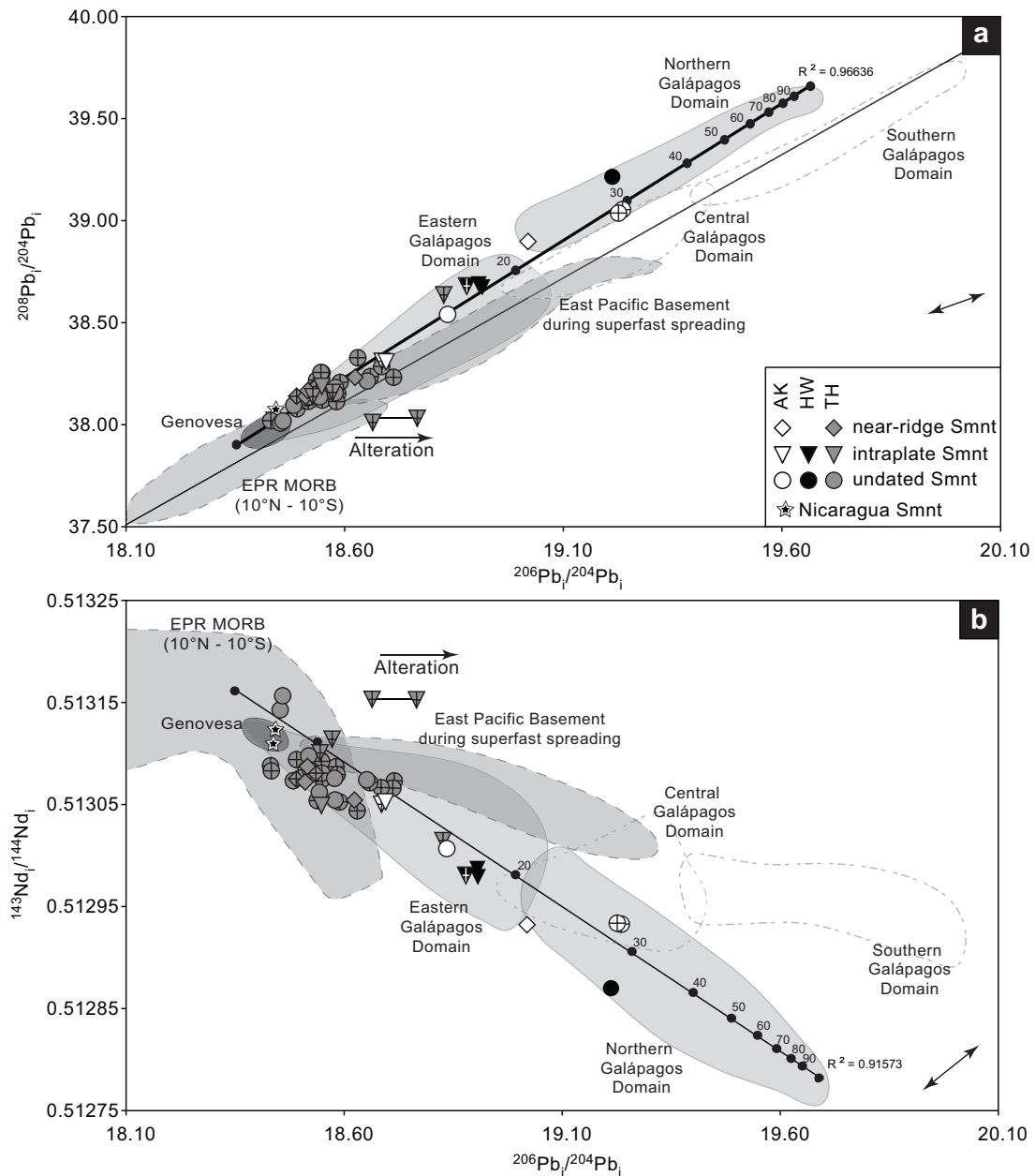
Figure 2.7: Initial $^{206}Pb/^{204}Pb$ versus $^{208}Pb/^{204}Pb$ and $^{143}Nd/^{144}Nd$ isotope ratios of CPS form positive and negative correlations respectively, which extend from depleted EPR-MORB-like and/or depleted Galápagos (e.g., Genovesa) components to the enriched Northern Galápagos domain plume composition (Harpp & White, 2001; Hoernle *et al.*, 2000; Werner *et al.*, 2003; White *et al.*, 1993). Thin black line marks NHRL after Hart (1984). The black line is a calculated mixing line between SO81 10/17 (Hoernle *et al.*, 2000), the most enriched end-member from the Northern Galápagos domain, and sample 2 DR-1 (SO144; Harpp *et al.*, 2005; Werner *et al.*, 2003), depleted MORB-like end-member from the Cocos Plate crust. Black circles on the thick black line represent increments of 10% mixing proportions of the Northern Galápagos Component. For comparison, Cocos Plate crust formed during super fast spreading at the EPR (Geldmacher *et al.*, 2013) represents a mixture between a depleted MORB-like component and the enriched Central Galápagos domain suggesting, that the Central component is flowing beneath the GSC to the EPR whereas the Northern component is flowing northwards along the base of the Cocos Plate lithosphere. Symbols with a cross (+) denote that whole-rock material was analyzed. Symbols without a cross denote glass. Arrow label "Alteration" " indicates that two replicates (separately prepared and analyzed chips) of sample SO208 DR1-1 have been affected by seawater alteration (see text for more details). Analytical errors are significantly smaller than symbol size.

end of the CPS array. Noteworthy is that EPRbasement formed during superfast spreading trends into the Central Galápagos domain, while the CPS lavas trend into the Northern Galápagos Domain field.

2.5 Discussion

2.5.1 Source components contributing to the geochemical composition of the Cocos Plate Seamount lavas

The CPS lavas have many major and trace-element similarities with MORB from the EPR. Basaltic samples fall almost completely within the equatorial EPR field on the TAS diagram (Fig. 2.3). The most mafic samples (MgO >7 wt.%) almost completely overlap the MORB field in major and minor elements (e.g., Fig. 2.4). The incompatible trace-element compositions of the CPS lavas completely overlap the N- and E-MORB range from the equatorial EPR, but extend to slightly more depleted incompatible element abundances (Fig. 2.6a) and more to less incompatible element ratios (Fig. 2.6b). These differences require either a) variations in conditions of melting from MORB, e.g., higher and lower degrees of melting and/or remelting (previous melt extraction) to derive the more depleted compositions, or b) involvement of more enriched and depleted source material than generally present in the MORB source, e.g., enriched and depleted plume components as occur at the Galápagos hotspot (Harpp & White, 2001; Hoernle *et al.*, 2000; White *et al.*, 1993). Low TiO_2/Yb, Sm/Yb and Tb/Yb (not shown) of the samples point to generation through shallow melting, consistent with upwelling and melting beneath young (<25 Ma) crust and thus thin lithosphere, even for the intraplate seamounts.
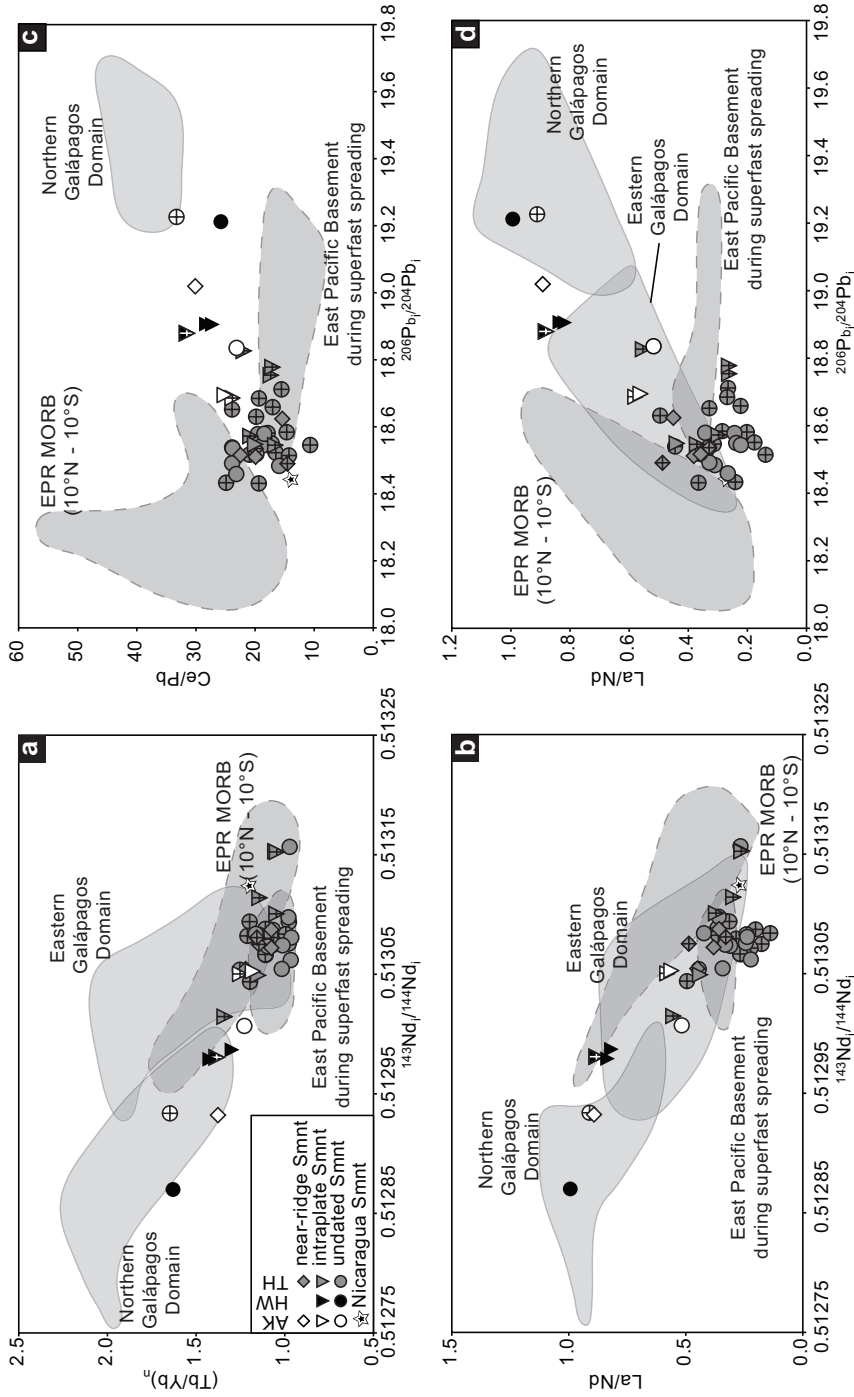
Figure 2.8: Nd and Pb isotope ratios versus incompatible trace element ratios (($Tb/Yb)_n$, La/Nd, Ce/Pb). To explain the non linear correlations of the samples, especially on plots where the ratios on both axis have the same denominator (b and c), three sources are required: 1) enriched Northern Galápagos domain, 2) depleted EPR-MORB between 10°N and 10°S, and 3) remelted residual EPR-MORB and/or Eastern Galápagos domain material. Galápagos Domains from PetDB, EPR during superfast spreading from Geldmacher et al. (2013). EPR-MORB between 10°N and 10°S from PetDB, EPR during superfast spreading from Geldmacher et al. (2013). EPR-MORB between 10°N and 10°S from Harpp & White (2001); Hoernle et al. (2000); Werner et al. (2003); White et al. (1993), EPR-MORB between 10°N and 10°S from PetDB, EPR during superfast spreading from Geldmacher et al. (2013).

The isotope data for the seamount lavas require the involvement of an enriched OIB type component. The positive correlations formed on the Pb vs Pb and Sr isotope diagrams and negative correlation on Sr and Pb versus Nd isotope diagrams can be explained by mixing of a Northern Galápagos Domain component (located on the northern side of the plume; Geldmacher *et al.*, 2003; Hoernle *et al.*, 2000; Werner *et al.*, 2003) with either the equatorial EPR-MORB source or a depleted Galápagos plume component, such as observed in Genovesa lavas (Fig. 2.7). Specifically, two component mixing between the most enriched northern Galápagos end-member as represented by sample SO81-10/17 from the Seamount Province offshore Costa Rica (Hoernle *et al.*, 2000) and a depleted MORB-like end-member represented by sample SO144 2DR-1 from the fossil GSC between the Carnegie and Malpelo Ridges (Harpp *et al.*, 2005; Werner *et al.*, 2003) in a 30:70 proportion (solid black mixing line with increments of 10% in Fig. 2.7) can explain the isotope data.

Correlations of isotope with incompatible element ratios, however, indicate that at least two depleted components must be present with similar (but not identical, for example in Nd) isotopic compositions. Correlations of Pb and Nd isotope ratios with incompatible element ratios (e.g., Tb/Yb, La/Nd and Ce/Pb) of the seamount lavas (Fig. 2.8) are not consistent with two component mixing. In particular, plots with ratios with the same denominator (e.g., $^{143}Nd/^{144}Nd$ vs. La/Nd and $^{206}Pb/^{204}Pb$ vs. Ce/Pb) should produce well-defined linear correlations if only two components are involved. Therefore, at least two depleted components are required to explain the variability in samples with low Tb/Yb, La/Nd and Ce/Pb. One of these components could be EPR-MORB, but the second component with lower Tb/Yb, La/Nd and Ce/Pb could either be depleted plume material or EPR-MORB that has undergone more than one stage of melting (melt extraction event). The later process was proposed by Geldmacher *et al.* (2013), to explain the lower concentrations of incompatible element ratios in Galápagos plume material reaching the EPR during superfast spreading in the Miocene.

2.5.2 Formation of near-ridge seamounts

The three Cocos Plate Seamounts with similar ages to the underlying crust (22.4-24 Ma) have similar trace-element and nearly similar or just slightly more enriched isotopic compositions to EPR-MORB of similar age, e.g., ocean crust drilled at Deep Sea Drilling Project (DSDP) Site 495. This ocean crust formed at the EPR at ∼5°N just at the beginning of EPR superfast spreading and the onset of Galápagos plume material reaching the EPR (Fig. 2.9). The newly formed GSC is likely to have opened a pathway for mantle material to flow westward from the Galápagos plume into the EPR (Geldmacher *et al.*, 2013), which was enhanced by the onset of superfast spreading. As shown by Niu & Hékinian (2004), the flow of plume material to a spreading ridge ("ridge suction") increases with spreading rate. During the peak of superfast spreading (between 18 and 11 Ma ago), the composition of equatorial EPR-MORB formed between 3°S and 7°N shows clear evidence for the influx of isotopically enriched Galápagos plume material displaying a peak $^{206}Pb/^{204}Pb$ isotope ratio at ∼17 Ma. The third near-ridge seamount sample (open diamond in Fig. 2.9) erupted at around 16.5 Ma ago shortly after the geochemical peak in EPR generated crust and yields the most radiogenic Pb isotope ratios of all near-ridge seamount samples in accordance with the proposed model of Geldmacher *et al.* (2013, thick black temporal isotopic evolution curve in Fig. 2.9). Therefore, we propose that the near-ridge seamount samples represent seamounts that formed in close proximity to the EPR with varying isotopic composition depending on the flux of plume material
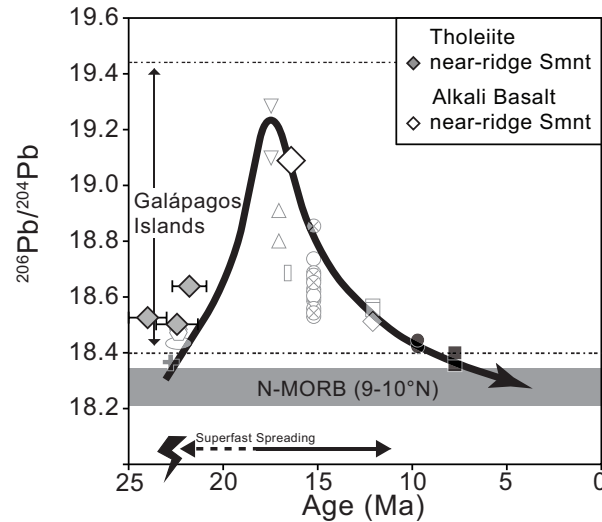
Figure 2.9: $^{206}Pb/^{204}Pb$ versus age (after Geldmacher *et al.*, 2013). The near-ridge seamounts (diamonds) plot along the geochemical trend (thick black line) for Cocos Plate crust formed at the EPR, during superfast spreading. The three samples from the two oldest seamounts overlap with EPR crust that was generated at the onset of Galápagos plume material spreading beneath the EPR. The third seamount formed shortly after the peak of input of Galápagos plume material into the EPR. Shown are also the errors for the older samples (gray squares). For the alkali sample (open square) the error is within symbol size.

spreading along the EPR axis.

2.5.3   Formation of intraplate Cocos Plate Seamounts

2.5.3.1   Transport of plume material beneath the Cocos Plate

The major-element geochemistry of the intraplate seamount group is consistent with an intraplate origin. On the MgO versus Al_2O_3 diagram, the more evolved (lower MgO) samples deviate completely from the MORB differentiation array. The increase in Al_2O_3 and decrease in CaO with decreasing MgO for the younger (and some undated) samples indicates that olivine and clinopyroxene are the main fractionating phases in these samples between MgO of 8 to 4 wt.%. Olivine and clinopyroxene on the liquidus instead of olivine and plagioclase points to high-pressure crystal fractionation (>0.5 GPa or ∼15-17 km depth), resulting from the shrinkage of the plagioclase in favor of the clinopyroxene stability field with increasing pressure (e.g., Bernstein, 1994; Thompson, 1974; Yoder & Tilley, 1962). Deeper depth of differentiation than for EPR lavas is consistent with these seamounts having formed on thicker crust, i.e., well off-axis or in an intraplate setting, compatible with the younger ages obtained on some of these samples.

Approximately half of the intraplate samples have more enriched (radiogenic) Pb isotope compositions than EPR-MORB (Fig. 2.7), but it is unlikely that enriched plume material flowing beneath the GSC to the EPR and was then transported along the deepening base of the lithosphere away from the EPR ridge axis. Plate tectonic reconstructions of the paleo-positions where the younger seamounts formed (after Meschede & Barckhausen, 2001) are displayed in Fig. 2.10a-f. In accordance with Werner *et al.* (2003),
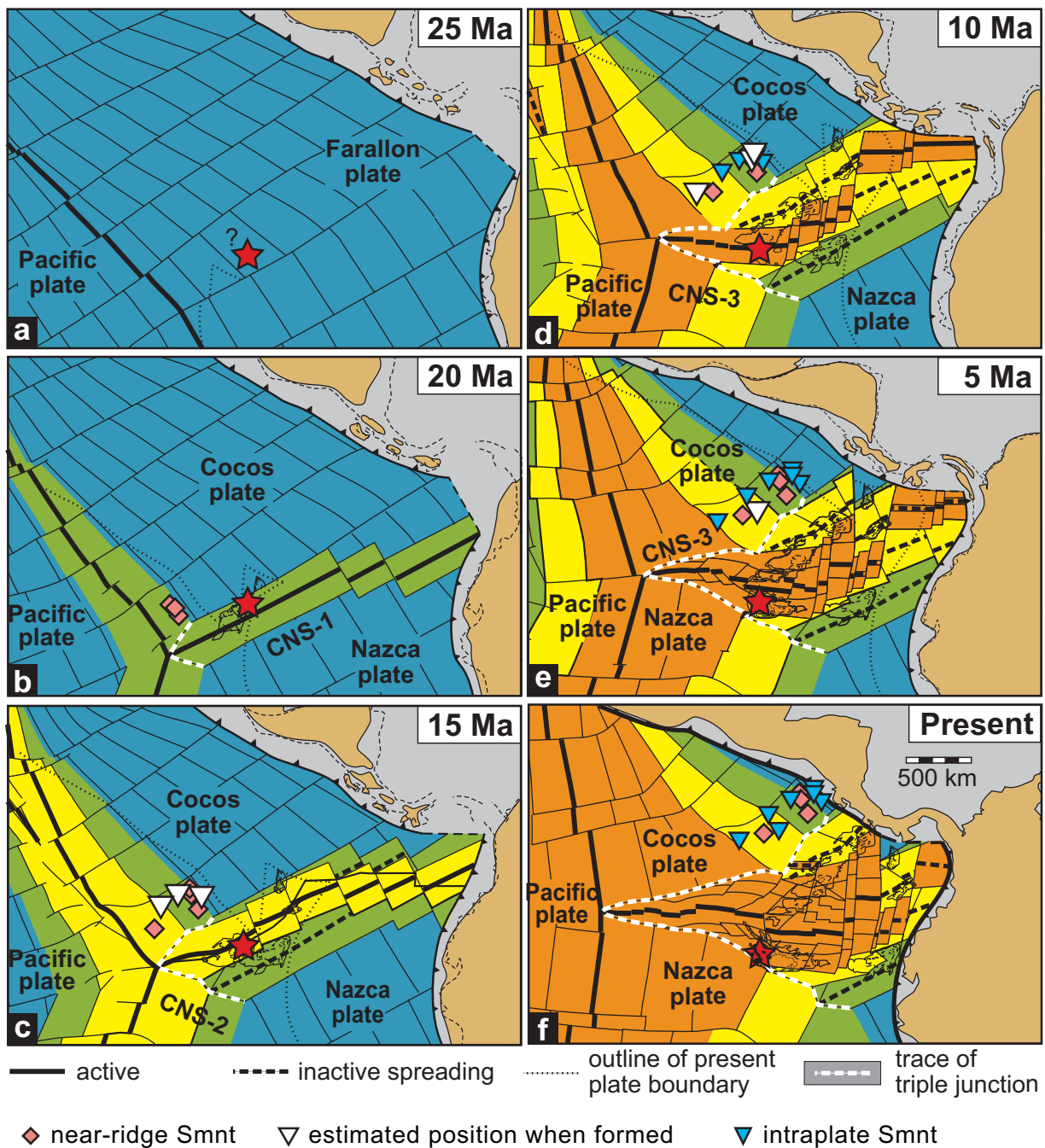
Figure 2.10: Reconstruction of paleo-positions of near-ridge and intraplate seamounts (paleo-tectonic reconstruction after Meschede & Barckhausen, 2001). Open symbols mark the approximate position were seamounts formed based on an average plate velocity of 78 mm/year. The black star marks the estimated position of the Galápagos hotspot. The seamounts formed between 400 and 900 km away from the current Galápagos hotspot position during times when the GSC was above or to the south of the Galápagos hotspot (Werner *et al.*, 2003).

the position of the GSC relative to the Galápagos hotspot changed several times due to multiple ridge jumps, abandoning old (dashed thick black lines in Fig. 2.10) and establishing new (solid thick black lines in Fig.2.10) ridge systems. These ridge jumps resulted in varying configurations between the plume and the GSC. Assuming a fixed position of the Galápagos hotspot and an average Cocos Plate motion velocity of 78 mm/a to the NE for the past 24 Ma (personal communication with U.Barckhausen), the seamounts formed between 400 and 900 km away from the hotspot, when it was located either north or directly beneath the GSC.

On the isotope correlation diagrams, the seamount samples form linear arrays that can be explained through mixing of up to 30% Northern Galápagos plume component with shallow depleted, presumably upper asthenosphere and/or lithospheric mantle. Therefore mantle from the northern domain of the Galápagos plume appears to have spread out at least 400-900 km northwards beneath the Cocos Plate. In contrast, Central and/or Southern Domain Galápagos plume material appears to have flowed along the GSC into the EPR during superfast spreading (see Fig. 2.7 and Geldmacher *et al.*, 2013). These observations are consistent with plume-ridge interaction of a zoned mantle plume with the northern portion (Northern Domain) of the Galápagos plume being primarily located north of the GSC and the central and southern portions (Central and Southern Domains) primarily beneath or south of the GSC during the formation of the CPS from 23 to 7 Ma. Cessation of seamount formation after 7.1 Ma (the age of the youngest seamount; Fig. 2.10e) coincides with the GSC moving to the north of the plume (Sallarès *et al.*, 2003; Werner *et al.*, 2003; Wilson & Hey, 1995). The location of the spreading center north of the hotspot no doubt inhibited plume material from flowing beneath the Cocos Plate as it did during the Early to Middle Miocene when the GSC was more or less above the plume.

2.5.3.2   Model for the Origin of the intraplate Cocos Plate Seamounts

In this section, we propose two end-member type models to explain the origin of the Cocos Plate Seamounts (Fig. 2.11). An important factor in the origin of these intraplate volcanic structures is that they formed on EPR generated crust/lithosphere. Bearing in mind the geochemical composition of the CPS lavas, the formation of the Cocos Plate Seamounts requires northward lateral transport of Galápagos plume material.

The first model is based on differences in crustal and/or lithospheric thickness between EPR and GSC generated crust/lithosphere. The crust formed at the GSC near the Galápagos hotspot is >8 km thick (Detrick *et al.*, 2002), whereas crust generated further away from the hotspot at the EPR at present is thinner (4-6.5 km between 9-10°N; Aghaei *et al.*, 2014; Klein, 2003). Investigations of the seismic structure of the hotspot tracks yielded crustal thicknesses varying from ∼17-21 km for the Cocos Ridge and ∼13-19 km for the Carnegie Ridge (Sallarès *et al.*, 2003; Walther, 2003). The differences in crustal thickness alone lead to differences in possible lithospheric thickness of up to 14 km going away from the hotspot.

Since the geochemistry indicates that shallow melting of enriched Galápagos plume material is involved in the origin of these seamounts (Fig. 2.6), we propose that plume material from the Northern zone of the Galápagos plume flowed northwards along the base of the lithosphere. As the plume material flows, it incorporates depleted asthenosphere (Phipps Morgan & Morgan, 1999). As this stirred together mantle flows from the base of the thicker GSC lithosphere to thinner EPR lithosphere, it ascends and melts by decompression (Fig. 2.11a). Even though the seamounts formed on EPR crust formed during super-fast spreading when Galápagos material contributed to crustal formation, there is likely to have been an
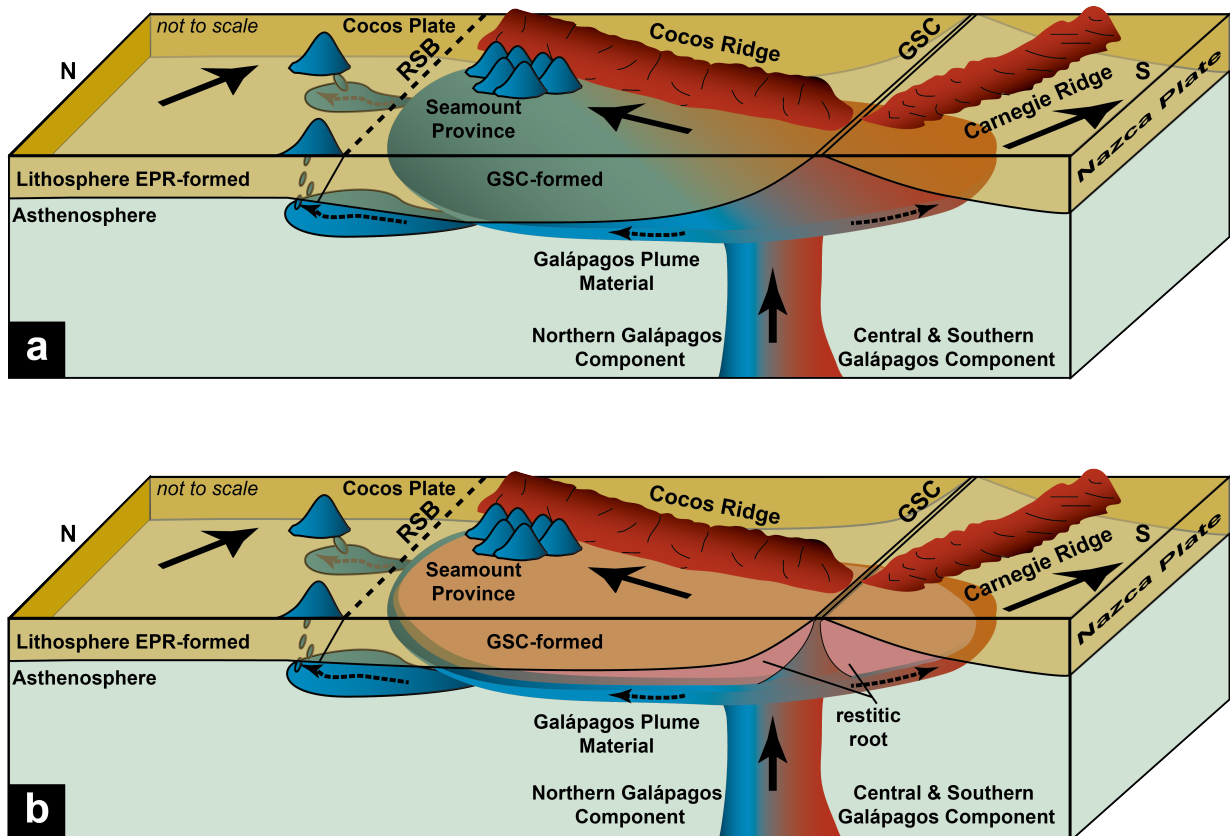
Figure 2.11: Two end-member models for formation of the Cocos Plate Seamounts. a) Enriched Northern Galápagos domain (blue part of the conduit) material spreads away from the plume stem and flows flows northwards along the base of the Cocos Plate lithosphere. As the plume mantle flows and ascends along the thinning lithosphere to the north, it undergoes decompression melting causing the formation of the Cocos Plate Seamounts. A likely inverted step in the base of the lithosphere at the Rough Smooth-Boundary (RSB), denoting the boundary between crust formed at the GSC and EPR, could enhance upwelling beneath the southernmost EPR generated lithosphere. b) Dehydration of upwelling plume material through melt extraction could lead to the formation of a viscous restitic root (Hall & Kincaid, 2003) above the plume and beneath the GSC, which would serve to deflect fertile plume material at depth away from the center of the upwelling plume. Northward flow of plume material along the thinning restite would allow plume mantle to continue to ascend and melt by decompression. In accordance with both possible models, seamounts would preferentially form at places where melt pools and/or where there are weaknesses in the lithosphere.

inverted step in lithospheric thickness between crust formed along the two different spreading centers or at the RSB. Once plume material reached the EPR, it would have been diverted both north and south along the ridge, thus at the triple junction there would have been an abrupt decrease in the amount of plume material flowing in either direction along the EPR. Such an inverted step in the base of the lithosphere would have facilitated upwelling to the north of the RSB, causing enhanced decompression melting.

The formation of seamounts and their exact locations are likely to reflect preferential ascension of plume material, including entrained asthenosphere, at the shallowest parts (e.g., inverted troughs) in the base of the lithosphere, where melts can pool and then ascend to the surface (e.g., Demidjuk *et al.*, 2007). Lithospheric weaknesses, e.g., tectonic structures such as fracture zones, are also likely to have served as pathways to channelize magmas ascending to the surface. Such pathways can also be used by later melts, as is evidenced at Bend Fault seamount where at least two episodes of volcanism more than 10 Ma apart are recorded.

The second model to explain the far-field lateral transport and melting of Galápagos plume material is the deflection of ascending plume material at the base of a restitic viscous plug at the base of the lithosphere (Fig. 2.11b; Hall & Kincaid, 2003). Higher seismic velocity observed beneath hotspots is likely to reflect the presence of higher viscosity plume residue, resulting from dehydration through melt extraction from the central region of an upwelling plume (Phipps Morgan *et al.*, 1995). Upwelling plume material that encounters such a high viscosity lid cannot ascend any further and is therefore deflected horizontally until it reaches the margins of the restitic plug. At the edge of the viscous lid, the fertile plume mantle can ascend further resulting in melting beneath the overlying Cocos Plate, generating intraplate volcanism, far away from the ridge and plume center (Hall & Kincaid, 2003). Ponding of restitic plume material beneath the thin lithosphere beneath the spreading center could allow some of the upwelling plume material to be deflected northwards away from the plume and the ridge. Of course, some fertile plume material still manages to upwell beneath the ridge to generate new crust at the ridge, facilitated by extension and separation of the restitic plug directly beneath the ridge. The aforementioned models are not mutually exclusive and could both contribute to the formation of intraplate volcanism beyond the morphological hotspot track(s) formed by the plume.

Based on satellite altimetry (Smith & Sandwell, 1997), the Cocos Plate Seamount province may be twice the size of the study area, extending to the SW parallel to the RSB onto crust that is ~6-8 Ma in age. The absence of the seamount province on the younger crust most likely reflects the GSC passing northwards over the hotspot, cutting the flow of plume magma to the north.

2.5.4   Comparison with the Arch Volcanic Fields near Hawaii

Here we compare the Cocos Plate Seamounts with the North and South Arch Volcanism related to the Hawaiian hotspot, but not a part of the morphological Hawaiian hotspot track, to evaluate if they may have formed by similar mechanisms. The Hawaiian-Emperor seamount chain is the most pronounced bathymetric anomaly related to a hotspot track that is characterized by a narrow (100-200 km), 5,800 km long volcanic tail extending from the active Hawaiian Volcanoes to Kamchatka (Duncan & Keller, 2004). The width of the hotspot track and seismic tomographic images (e.g., Montelli *et al.*, 2004, 2006) suggest that it is being fed by a mantle plume (conduit) of similar diameter to the width of the hotspot track. Nevertheless, large outpourings of silica-undersaturated volcanic rocks (alkali basalts, basanites and

nephelinites) have been found to the north of the islands near the Molokaii Fracture Zone (North Arch Volcanic Field) and southeast of the Big Island (South Arch Volcanic Field) and are thought to be related to the Hawaiian hotspot as discussed below (red areas in Fig. 2.12b).

The North Arch Field is located 200-400 km north of Oahu and covers an area of 25,000 km^2 erupted within the last c. 2 Ma. Although ∼100 volcanic edifices, ranging from steep-sided cones to ridge-like structures to low shields, have been identified, most of this volcanic province is covered by sheet flows, less than 10 m thick in most places, resulting in an estimated volume of 1,000-1,250 km^3 for the North Arch Field (Clague *et al.*, 2002; Frey *et al.*, 2000) and have been referred to as "alkalic flood basalts" (Clague *et al.*, 1990). The extensive lava fields of the Hawaiian North Arch are related to fissure eruptions along pre-existing zones of crustal weakness, such as the 75 km long NNW trending faults related to the Molokaii Fracture Zone (Clague *et al.*, 2002). The South Arch volcanic field, located 175-200 km south of the Big Island of Hawaii, comprises several young lava fields, formed within the last c. 10 ka, with the largest one covering an area of 35 by 50 km (Lipman *et al.*, 1989). The major and trace-element and Sr, Nd and Pb isotopic compositions of the Arch lavas are similar to the rejuvenated stage volcanism on the Hawaiian Island volcanoes, which generally occurs several million years after the main volcanic shield has formed when the volcano is no longer located over the hotspot. Therefore it is likely that the rejuvenated stage and Arch lavas were formed by similar processes and have a common origin (e.g., Frey *et al.*, 2000; Yang *et al.*, 2003).

The CPS and Arch lavas show a number of distinct but also some similar features and geochemical characteristics. Despite the weaker buoyancy flux of the Galápagos plume, the CPS were formed at greater distances from the hotspot (400-900 km) than the Arch lavas (within 400 km of the Hawaiian Islands). The Cocos Plate Seamounts, however, form larger volcanic structures (up to 2,000 m high and 14 km along the longest axis) than the Arch lavas (<700 m high and <7 km long), but cover a much smaller area (≥2,100 km^2) and the volume of the seamount structures (∼620 km^3, estimated from bathymetric mapping data after Yeo *et al.*, 2013) are much lower. There is no evidence for extensive extrusions of sheet flows over large areas of the seafloor associated with the CPS, but even if such massive outpourings of sheet flows occurred, they have, no doubt, been covered by sediments. Therefore it is not possibly to compare volumes of CPS-province volcanism with that of the Arch lavas.

The Arch lavas have distinct major and trace-element compositions from the Cocos Plate Seamounts. The silica-undersaturated nature (Fig. 2.2) and the high 1) concentrations of incompatible elements, 2) more to less incompatible element ratios (e.g., La/Yb, La/Sm, Nb/Yb) and 3) middle to heavy rare earth element ratios (e.g., Sm/Yb, Tb/Yb) and TiO$_2$/Yb ratios (Fig. 2.5), despite depleted isotopic compositions of the Arch and rejuvenated lavas point to generation by low degrees of partial melting of peridotite within the garnet stability field (e.g., Clague & Frey, 1982; Frey *et al.*, 2000). In contrast to the Arch lavas, the Cocos Plate Seamount province consists of primarily tholeiitie with lesser volumes of alkaline basalt and hawaiite compositions, which formed through melting of spinel peridotite at shallow depths with minor amounts of garnet only in the residuum of the alkalic magmas (Fig. 2.6). In summary, the difference in major and trace-element compositions can be explained through high degrees of melting beneath young (<25 Ma), thin (∼40-50 km) lithosphere to produce the Cocos Plate Seamounts and low degrees of melting beneath old (∼90 Ma), thick (90-100 km) lithosphere the silica-undersaturated Arch and rejuvenated lavas.

Although the isotopic compositions of the Arch lavas and CPS are distinct, they both point to mixing
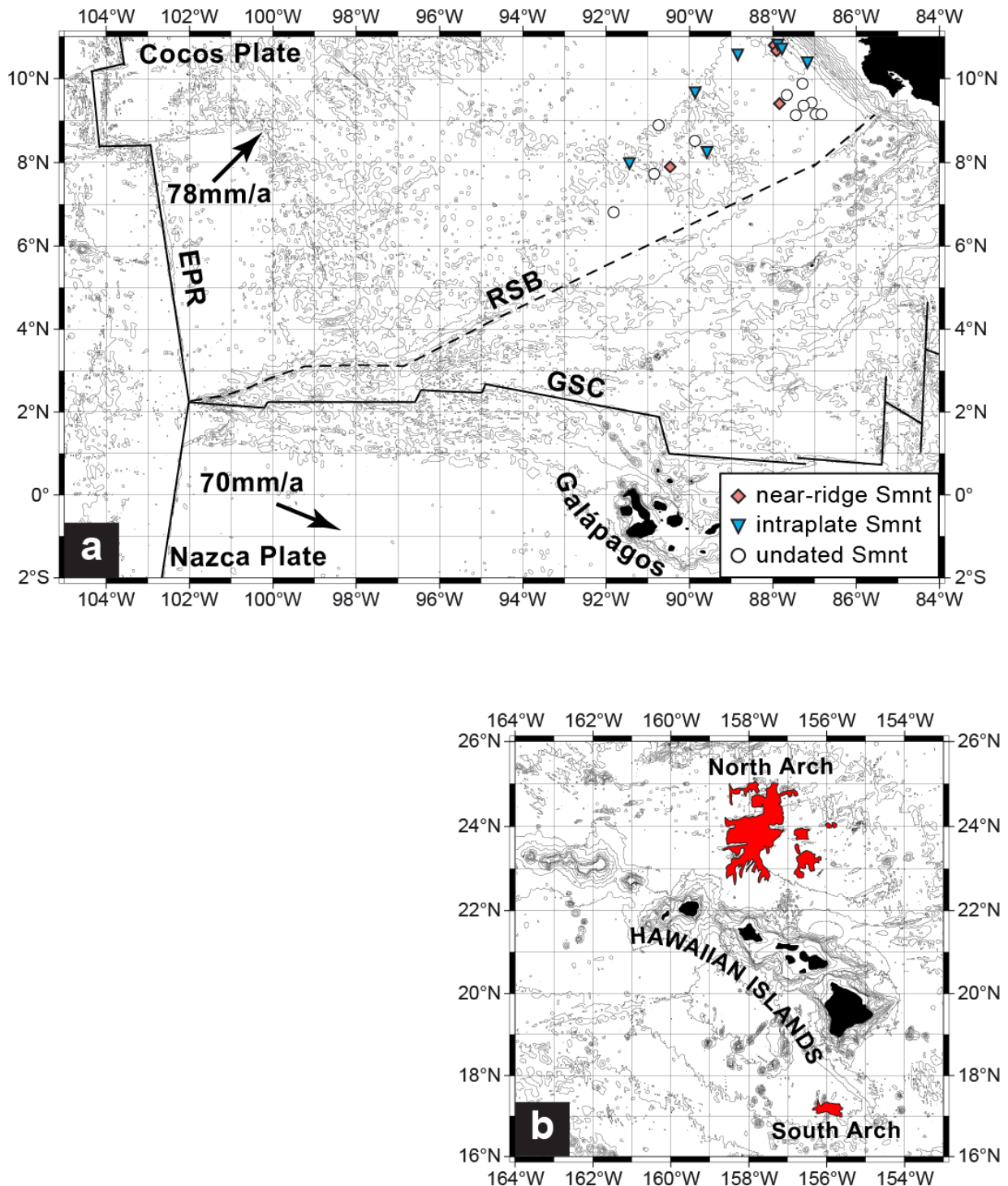
Figure 2.12: Comparative map of a) Galápagos and b) Hawaii to visualize the differences in the distance and nature of the far-field transport of plume material. In a) far-field lateral transport of Galápagos plume material leads to the formation of individual volcanic edifices between 400-900 km away from the presumed plume center (CPS; red symbols). Note that due to spreading along the GSC and plate motion, the present location of the Miocene CPS is further from the Galápagos hotspot (relative position reflected by closest part of the hotspot track) then when they formed. In b) The North and South Arch volcanic fields (red areas) of the Hawaiian Islands formed closer to the Hawaiian plume center (175-400 km) and represent rather large outpourings of lava on the seafloor. Outlines for the Arch Fields after Bianco *et al.* (2005).

of plume material with depleted upper asthenosphere and/or lithosphere. The Sr-Nd-Pb isotopic compositions of the Arch and rejuvenated lavas are intermediate between the Hawaiian plume and Pacific MORB fields (Frey *et al.*, 2000). The high ^{3}He/^{4}He of up to $20\,$Ra in the South Arch lavas clearly indicates the presence of a plume component (Frey *et al.*, 2000). The source is thought to be a mixture of a Hawaiian plume component with a depleted mid-ocean ridge basalt component (Yang *et al.*, 2003), similar to the CPS. As discussed above, the isotope geochemistry of the CPS can be explained by mixing of an enriched plume-derived component with a depleted component similar to MORB and to a remelted depleted component either from the upper mantle or the plume. Therefore in both areas the volcanism is ultimately related to the interaction of plume material with the upper mantle as the plume material spreads out in the uppermost asthenosphere.

The occurrence of widespread secondary volcanism at Hawaii has been attributed to different mechanisms including a second melting zone in the plume material spreading laterally along the base of the lithosphere (Ribe & Christensen, 1999), decompression melting during lithospheric flexural uplift that surrounds the growing shield volcanoes (Bianco *et al.*, 2005) or interaction of the laterally spreading plume material with the irregular (washboard type) base of the lithosphere generated by small scale convection (Ballmer *et al.*, 2011). For the Hawaiian North Arch volcanism, Yamamoto & Morgan (2009) proposed that off-chain volcanism is related to an offset in lithospheric thickness at the Molokaii Fracture Zone. North of the Molokaii Fracture Zone, the lithosphere is younger and therefore thinner, resulting in increased melting and greater swell height (Phipps Morgan *et al.*, 1995). A similar situation applies to the CPS that formed just north of the transition from thicker, plume-ridge-interaction-influenced GSC lithosphere to thinner, normal mid-ocean-ridge-type lithosphere formed at the EPR.

2.6   Conclusions

^{40}Ar/^{39}Ar age dating show that the Cocos Plate Seamounts range in age from 22.5 to $7.1\,$Ma and that some have similar ages to the underlying crust ($\pm\,2$ Ma) and thus formed near-ridge and others, more than $2\,$Ma younger than the underlying crust, formed in an intraplate setting. Seamounts that formed in close proximity to the ridge provide further support for the Geldmacher *et al.* (2013) model, that due to increased ridge suction during super-fast spreading at the EPR, Galápagos plume material flowed beneath the newly formed GSC into the EPR. In contrast, intraplate seamounts can be explained by large-scale distribution of plume material along the base of the lithosphere during times when the hotspot was located north or directly below the GSC. We propose that flow of Northern Galápagos plume material northwards from the base of the thicker GSC generated crust to thinner EPR crust or along the base of a viscous restitic root upwelling at its edges (or both) resulted in decompression melting that formed the seamounts. In general, the seamount lavas represent a mixture of variable proportions of the enriched Northern Galápagos plume component with a depleted component most likely MORB-like asthenosphere and/or lithosphere but possibly also residual plume material. In comparison to Hawaiian Arch volcanism, represented by voluminous eruptions of highly silica-undersaturated melts, the formation of the Cocos Plate Seamounts, consisting of silica-saturated and slightly undersaturated melts, no doubt reflects spreading out and melting to higher degrees and shallower depths beneath younger and thus thinner lithosphere. The presumably greater volume of the Arch volcanism at Hawaii is likely to reflect the higher buoyancy flux of the Hawaiian

plume compared to the Galápagos plume.

Acknowledgements

References

Aghaei, O., Nedimovic, M. R., Carton, H., Carbotte, S. M., Canales, J. P. & Mutter, J. C., 2014. Crustal thickness and Moho character of the fast-spreading East Pacific Rise from 9°42'N to 9°57'N from poststack-migrated 3-D MCS data. *Geochemistry, Geophysics, Geosystems*, **15**, 634–657.

Baksi, A. K., 1999. Reevaluation of Plate Motion Models Based on Hotspot Tracks in the Atlantic and Indian Oceans. *The Journal of Geology*, **107**, 13–26.

Ballmer, M. D., Ito, G., van Hunen, J. & Tackley, P. J., 2011. Spatial and temporal variability in Hawaiian hotspot volcanism induced by small-scale convection. *Nature Geoscience*, **4**, 457–460.

Barckhausen, U., Ranero, C. R., von Huene, R., Cande, S. C. & Roeser, H. A., 2001. Revised tectonic boundaries in the Cocos Plate off Costa Rica: Implications for the segmentation of the convergent margin and for plate tectonic models. *Journal of Geophysical Research*, **106**, 19207–19220.

Bernstein, S., 1994. High-pressure fractionation in rift-related basaltic magmatism: Faeroe plateau basalts. *Geology*, **22**, 815–818.

Bianco, T. A., Ito, G., Becker, J. M. & Garcia, M. O., 2005. Secondary Hawaiian volcanism formed by flexural arch decompression. *Geochemistry, Geophysics, Geosystems*, **6**, Q08009.

Bowles, J. A., Colman, A., McClinton, J. T., Sinton, J. M., White, S. M. & Rubin, K. H., 2014. Eruptive timing and 200 year episodicity at 92°W on the hot spot-influenced Galápagos Spreading Center derived from geomagnetic paleointensity. *Geochemistry, Geophysics, Geosystems*, **15**, 2211–2224.

Christie, D. M., Werner, R., Hauff, F., Hoernle, K. & Hanan, B. B., 2005. Morphological and geochemical variations along the eastern Galápagos Spreading Center. *Geochemistry, Geophysics, Geosystems*, **6**, Q01006.

Clague, D. A. & Frey, F. A., 1982. Petrology and Trace Element Geochemistry of the Honolulu Volcanics, Oahu: Implications for the Oceanic Mantle below Hawaii. *Journal of Petrology*, **23**, 447–504.

Clague, D. A., Holcomb, R. T., Sinton, J. M., Detrick, R. S. & Torresan, M. E., 1990. Pliocene and Pleistocene alkalic flood basalts on the seafloor north of the Hawaiian islands. *Earth and Planetary Science Letters*, **98**, 175–191.

Clague, D. A., Uto, K., Satake, K. & Davis, A. S., 2002. Eruption Style and Flow Emplacement in the Submarine North Arch Volcanic Field, Hawaii. In: *Hawaiian Volcanoes: Deep Underwater Perspectives* (eds. Takahashi, E., Lipman, P. W., Garcia, M. O., Naka, J. & Aramaki, S.), American Geophysical Union. 65–84.

DeMets, C., Gordon, R. G., Argus, D. F. & Stein, S., 1990. Current plate motions. *Geophysical Journal International*, **101**, 425–478.

Demidjuk, Z., Turner, S., Sandiford, M., George, R., Foden, J. & Etheridge, M., 2007. U-series isotope and geodynamic constraints on mantle melting processes beneath the Newer Volcanic Province in South Australia. *Earth and Planetary Science Letters*, **261**, 517–533.

Detrick, R. S., Sinton, J. M., Ito, G., Canales, J. P., Behn, M., Blacic, T., Cushman, B., Dixon, J. E., Graham, D. W. & Mahoney, J. J., 2002. Correlated geophysical, geochemical, and volcanological manifestations of plume-ridge interaction along the Galápagos Spreading Center. *Geochemistry, Geophysics, Geosystems*, **3**, 8501.

Duncan, R. A. & Hargraves, R. B., 1984. Plate tectonic evolution of the Caribbean region in the mantle reference frame. *Geological Society of America Memoirs*, **162**, 81–94.

Duncan, R. A. & Keller, R. A., 2004. Radiometric ages for basement rocks from the Emperor Seamounts, ODP Leg 197. *Geochemistry, Geophysics, Geosystems*, **5**, Q08L03.

Farnetani, C. G. & Hofmann, A. W., 2009. Dynamics and internal structure of a lower mantle plume conduit. *Earth and Planetary Science Letters*, **282**, 314–322.

Fisher, A. T., Stein, C. A., Harris, R. N., Wang, K., Silver, E. A., Pfender, M., Hutnak, M., Cherkaoui, A., Bodzin, R. & Villinger, H., 2003. Abrupt thermal transition reveals hydrothermal boundary and role of seamounts within the Cocos Plate. *Geophysical Research Letters*, **30**, 1550.

Frey, F. A., Clague, D., Mahoney, J. J. & Sinton, J. M., 2000. Volcanism at the Edge of the Hawaiian Plume: Petrogenesis of Submarine Alkalic Lavas from the North Arch Volcanic Field. *Journal of Petrology*, **41**, 667–691.

Gale, A., Dalton, C. A., Langmuir, C. H., Su, Y. & Schilling, J.-G., 2013. The mean composition of ocean ridge basalts. *Geochemistry, Geophysics, Geosystems*, **14**, 489–518.

Garbe-Schönberg, C.-D., 1993. Simultaneous determination of thirty-seven trace elements in twenty-eight international rock standards by ICP-MS. *Geostandards Newsletter*, **17**, 81–97.

Garcia, M. O., Swinnard, L., Weis, D., Greene, A. R., Tagami, T., Sano, H. & Gandy, C. E., 2010. Petrology, Geochemistry and Geochronology of Kaua'i Lavas over 4.5 Myr: Implications for the Origin of Rejuvenated Volcanism and the Evolution of the Hawaiian Plume. *Journal of Petrology*, **51**, 1507–1540.

Geist, D. J., White, W. M. & McBirney, A. R., 1988. Plume-asthenosphere mixing beneath the Galápagos archipelago. *Nature*, **333**, 657–660.

Geldmacher, J., Hanan, B. B., Blichert-Toft, J., Harpp, K., Hoernle, K., Hauff, F., Werner, R. & Kerr, A. C., 2003. Hafnium isotopic variations in volcanic rocks from the Caribbean Large Igneous Province and Galápagos hot spot tracks. *Geochemistry, Geophysics, Geosystems*, **4**, 1062.

Geldmacher, J., Höfig, T., Hauff, F., Hoernle, K., Garbe-Schönberg, D. & Wilson, D., 2013. Influence of the Galápagos hotspot on the East Pacific Rise during Miocene superfast spreading. *Geology*, **41**, 183–186.

Graham, D. W., Christie, D. M., Harpp, K. S. & Lupton, J. E., 1993. Mantle Plume Helium in Submarine Basalts from the Galápagos Platform. *Science*, **262**, 2023–2026.

Green, D. H. & Ringwood, A. E., 1967. The stability fields of aluminous pyroxene peridotite and garnet peridotite and their relevance in upper mantle structure. *Earth and Planetary Science Letters*, **3**, 151–160.

Hall, P. S. & Kincaid, C., 2003. Melting, dehydration, and the dynamics of off-axis plume-ridge interaction. *Geochemistry, Geophysics, Geosystems*, **4**, 8510.

Harpp, K. S., Wanless, V. D., Otto, R. H., Hoernle, K. & Werner, R., 2005. The Cocos and Carnegie Aseismic Ridges: A Trace Element Record of Long-term Plume-Spreading Center Interaction. *Journal of Petrology*, **46**, 109–133.

Harpp, K. S. & White, W. M., 2001. Tracing a mantle plume: Isotopic and trace element variations of Galápagos seamounts. *Geochemistry, Geophysics, Geosystems*, **2**, 1042.

Hart, S. R., 1984. A large-scale isotope anomaly in the Southern Hemisphere mantle. *Nature*, **309**, 753–757.

Hey, R., 1977. Tectonic evolution of the Cocos-Nazca spreading center. *Geological Society of America Bulletin*, **88**, 1404–1420.

Hoernle, K., Abt, D. L., Fischer, K. M., Nichols, H., Hauff, F., Abers, G. A., van den Bogaard, P., Heydolph, K., Alvarado, G., Protti, M. & Strauch, W., 2008. Arc-parallel flow in the mantle wedge beneath Costa Rica and Nicaragua. *Nature*, **451**, 1094–1098.

Hoernle, K., Hauff, F., Kokfelt, T. F., Haase, K., Garbe-Schönberg, D. & Werner, R., 2011. On- and off-axis chemical heterogeneities along the South Atlantic Mid-Ocean-Ridge (5-11°S): Shallow or deep recycling of ocean crust and/or intraplate volcanism? *Earth and Planetary Science Letters*, **306**, 86–97.

Hoernle, K., Werner, R., Morgan, J. P., Garbe-Schönberg, D., Bryce, J. & Mrazek, J., 2000. Existence of complex spatial zonation in the Galápagos plume. *Geology*, **28**, 435–438.

Hofmann, A. W., 1988. Chemical differentiation of the Earth: the relationship between mantle, continental crust, and oceanic crust. *Earth and Planetary Science Letters*, **90**, 297–314.

Holden, J. C. & Dietz, R. S., 1972. Galápagos Gore, NazCoPac Triple Junction and Carnegie/Cocos Ridges. *Nature*, **235**, 266–269.

Ingle, S., Ito, G., Mahoney, J. J., Chazey, I., William, Sinton, J., Rotella, M. & Christie, D. M., 2010. Mechanisms of geochemical and geophysical variations along the western Galápagos Spreading Center. *Geochemistry, Geophysics, Geosystems*, **11**, Q04003.

Ito, G. & Lin, J., 1995. Oceanic spreading center-hotspot interactions: Constraints from along-isochron bathymetric and gravity anomalies. *Geology*, **23**, 657–660.

Ito, G., Lin, J. & Graham, D., 2003. Observational and theoretical studies of the dynamics of mantle plume & mid-ocean ridge interaction. *Reviews of Geophysics*, **41**, 1017.

Jarosewich, E., Nelen, J. A. & Norberg, J. A., 1980. Reference Samples for Electron Microprobe Analysis*. *Geostandards Newsletter*, **4**, 43–47.

Jochum, K. P., Stoll, B., Herwig, K., Willbold, M., Hofmann, A. W., Amini, M., Aarburg, S., Abouchami, W., Hellebrand, E., Mocek, B., Raczek, I., Stracke, A., Alard, O., Bouman, C., Becker, S., Dücking, M., Brätz, H., Klemd, R., de Bruin, D., Canil, D., Cornell, D., de Hoog, C.-J., Dalpé, C., Danyushevsky, L., Eisenhauer, A., Gao, Y., Snow, J. E., Groschopf, N., Günther, D., Latkoczy, C., Guillong, M., Hauri, E. H., Höfer, H. E., Lahaye, Y., Horz, K., Jacob, D. E., Kasemann, S. A., Kent, A. J. R., Ludwig, T., Zack, T., Mason, P. R. D., Meixner, A., Rosner, M., Misawa, K., Nash, B. P., Pfänder, J., Premo, W. R., Sun, W. D., Tiepolo, M., Vannucci, R., Vennemann, T., Wayne, D. & Woodhead, J. D., 2006. MPI-DING reference glasses for in situ microanalysis: new reference values for element concentrations and isotope ratios. *Geochemistry, Geophysics, Geosystems*, **7**, Q02008.

Jochum, K. P., Weis, U., Stoll, B., Kuzmin, D., Yang, Q., Raczek, I., Jacob, D. E., Stracke, A., Birbaum, K., Frick, D. A., Günther, D. & Enzweiler, J., 2011. Determination of Reference Values for NIST SRM 610–617 Glasses Following ISO Guidelines. *Geostandards and Geoanalytical Research*.

Kincaid, C., Ito, G. & Gable, C., 1995. Laboratory investigation of the interaction of off-axis mantle plumes and spreading centres. *Nature*, **376**, 758–761.

Kincaid, C., Schilling, J. G. & Gable, C., 1996. The dynamics of off-axis plume-ridge interaction in the uppermost mantle. *Earth and Planetary Science Letters*, **137**, 29–43.

Klein, E. M., 2003. 3.13 - Geochemistry of the Igneous Oceanic Crust. In: *Treatise on Geochemistry* (eds. Editors-in Chief: Heinrich, D. H. & Karl, K. T.), Pergamon, Oxford. 433–463.

Kokfelt, T. F., Lundstrom, C., Hoernle, K., Hauff, F. & Werner, R., 2005. Plume-ridge interaction studied at the Galápagos spreading center: Evidence from ^{226}Ra-^{230}Th-^{238}U and ^{231}Pa-^{235}U isotopic disequilibria. *Earth and Planetary Science Letters*, **234**, 165–187.

Lanphere, M. A. & Dalrymple, G. B., 2000. First-principles calibration of ^{38}Ar tracers: Implications for the ages of ^{40}Ar/^{39}Ar fluence monitors. *U.S. Geological Survey Professional Paper*, 10.

Le Maitre, R. W., Bateman, P., Dudek, A., Keller, J., Lameyre, J., Le Bas, M. J., Sabine, P. A., Schmid, R., Sorensen, H., Streckeisen, A., Woolley, A. R. & Zanettin, B., 1989. *A classification of igneous rocks and glossary of terms, recommendations of the International Union of Geological Sciences, Subcommission on the Systematics of Igneous Rocks.* Blackwell Scientific. Oxford. GB.

Lipman, P. W., Clague, D. A., Moore, J. G. & Holcomb, R. T., 1989. South Arch volcanic field-Newly identified young lava flows on the sea floor south of the Hawaiian Ridge. *Geology*, **17**, 611–614.

Lohmann, F. C., Hort, M. & Phipps Morgan, J., 2009. Flood basalts and ocean island basalts: A deep source or shallow entrainment? *Earth and Planetary Science Letters*, **284**, 553–563.

Lonsdale, P., 1988. Structural Pattern of the Galápagos Microplate and Evolution of the Galápagos Triple Junctions. *Journal of Geophysical Research: Solid Earth*, **93**, 13551–13574.

Lonsdale, P., 2005. Creation of the Cocos and Nazca plates by fission of the Farallon plate. *Tectonophysics*, **404**, 237–264.

Lonsdale, P. & Klitgord, K. D., 1978. Structure and tectonic history of the eastern Panama Basin. *Geological Society of America Bulletin*, **89**, 981–999.

MacDonald, G. A. & Katsura, T., 1964. Chemical Composition of Hawaiian Lavas1. *Journal of Petrology*, **5**, 82–133.

Meschede, M. & Barckhausen, U., 2001. The relationship of the Cocos and Carnegie ridges: age constraints from paleogeographic reconstructions. *International Journal of Earth Sciences*, **90**, 386–392.

Montelli, R., Nolet, G., Dahlen, F. A. & Masters, G., 2006. A catalogue of deep mantle plumes: New results from finite-frequency tomography. *Geochemistry, Geophysics, Geosystems*, **7**, Q11007.

Montelli, R., Nolet, G., Dahlen, F. A., Masters, G., Engdahl, E. R. & Hung, S.-H., 2004. Finite-Frequency Tomography Reveals a Variety of Plumes in the Mantle. *Science*, **303**, 338–343.

Morgan, W. J., 1971. Convection Plumes in the Lower Mantle. *Nature*, **230**, 42–43.

Niu, Y. & Hékinian, R., 2004. Ridge suction drives plume-ridge interactions. In: *Oceanic Hotspots* (eds. Hékinian, R. & Stoffers, P.), Springer-Verlag, New York. 285–307.

O'Connor, J. M., Stoffers, P., Wijbrans, J. R. & Worthington, T. J., 2007. Migration of widespread long-lived volcanism across the Galápagos Volcanic Province: Evidence for a broad hotspot melting anomaly? *Earth and Planetary Science Letters*, **263**, 339–354.

Pearce, J. A., 2008. Geochemical fingerprinting of oceanic basalts with applications to ophiolite classification and the search for Archean oceanic crust. *Lithos*, **100**, 14–48.

Pearce, N. J. G., Perkins, W. T., Westgate, J. A., Gorton, M. P., Jackson, S. E., Neal, C. R. & Chenery, S. P., 1997. A compilation of new and published major and trace element data for NIST SRM 610 and NIST SRM 612 glass reference materials. *Geostandards Newsletter*, **21**, 115–144.

Pedersen, R. B. & Furnes, H., 2001. Nd- and Pb-isotopic variations through the upper oceanic crust in DSDP/ODP Hole 504B, Costa Rica Rift. *Earth and Planetary Science Letters*, **189**, 221–235.

Phipps Morgan, J. & Morgan, W. J., 1999. Two-stage melting and the geochemical evolution of the mantle: a recipe for mantle plum-pudding. *Earth and Planetary Science Letters*, **170**, 215–239.

Phipps Morgan, J., Morgan, W. J. & Price, E., 1995. Hotspot melting generates both hotspot volcanism and a hotspot swell? *Journal of Geophysical Research: Solid Earth*, **100**, 8045–8062.

Ribe, N. M., 1996. The dynamics of plume-ridge interaction 2. Off-ridge plumes. *Journal of Geophysical Research*, **101**, 16195–16204.

Ribe, N. M. & Christensen, U. R., 1999. The dynamical origin of Hawaiian volcanism. *Earth and Planetary Science Letters*, **171**, 517–531.

Ringwood, A. E., 1967. The pyroxene-garnet transformation in the earth's mantle. *Earth and Planetary Science Letters*, **2**, 255–263.

Robinson, J. A. C. & Wood, B. J., 1998. The depth of the spinel to garnet transition at the peridotite solidus. *Earth and Planetary Science Letters*, **164**, 277–284.

Rohde, J., Hoernle, K., Hauff, F., Werner, R., O'Connor, J., Class, C., Garbe-Schönberg, D. & Jokat, W., 2013. 70 Ma chemical zonation of the Tristan-Gough hotspot track. *Geology*, **41**, 335–338.

Sadofsky, S., Hoernle, K., Duggen, S., Hauff, F., Werner, R. & Garbe-Schönberg, D., 2009. Geochemical variations in the Cocos Plate subducting beneath Central America: implications for the composition of arc volcanism and the extent of the Galápagos Hotspot influence on the Cocos oceanic crust. *International Journal of Earth Sciences*, **98**, 901–913.

Sallarès, V., Charvis, P., Flueh, E. R. & Bialas, J., 2003. Seismic structure of Cocos and Malpelo Volcanic Ridges and implications for hot spot-ridge interaction. *Journal of Geophysical Research: Solid Earth*, **108**, 2564.

Schilling, J., Kingsley, R. & Devine, J., 1982. Galápagos Hot Spot-Spreading Center System 1. Spatial Petrological and Geochemical Variations (83°W–111°W). *Journal of Geophysical Research*, **87**, 18.

Schilling, J. G., Anderson, R. N. & Vogt, P., 1976. Rare earth, Fe and Ti variations along the Galápagos spreading centre, and their relationship to the Galápagos mantle plume. *Nature*, **261**, 108–113.

Schilling, J.-G., Fontignie, D., Blichert-Toft, J., Kingsley, R. & Tomza, U., 2003. Pb-Hf-Nd-Sr isotope variations along the Galápagos Spreading Center (101°-83°W): Constraints on the dispersal of the Galápagos mantle plume. *Geochemistry, Geophysics, Geosystems*, **4**, 8512.

Sinton, J., Detrick, R., Canales, J. P., Ito, G. & Behn, M., 2003. Morphology and segmentation of the western Galápagos Spreading Center, 90.5°-98°W: Plume-ridge interaction at an intermediate spreading ridge. *Geochemistry, Geophysics, Geosystems*, **4**, 8515.

Smith, W. H. F. & Sandwell, D. T., 1997. Global Sea Floor Topography from Satellite Altimetry and Ship Depth Soundings. *Science*, **277**, 1956–1962.

Sun, S.-s. & McDonough, W. F., 1989. Chemical and isotopic systematics of oceanic basalts: implications for mantle composition and processes. *Geological Society, London, Special Publications*, **42**, 313–345.

Thompson, R. N., 1974. Primary basalts and magma genesis. *Contributions to Mineralogy and Petrology*, **45**, 317–341.

Vogt, P. R., 1976. Plumes, subaxial pipe flow, and topography along the Mid-Oceanic Ridge. *Earth and Planetary Science Letters*, **29**, 309–325.

von Huene, R., Bialas, J., Flueh, E., Cropp, B., Csernok, T., Fabel, E., Hoffmann, J., Emeis, K., Holler, P., Jeschke, G., Leandro M., C., Fernandéz, I. P., Chavarria S., J., Florez H., A., Escobedo Z., D., León, R. & Barrios L., O., 1995. Morphotectonics of the Pacific convergent margin of Costa Rica. *Geological Society of America Special Papers*, **295**, 291–308.

Walther, C. H. E., 2003. The crustal structure of the Cocos ridge off Costa Rica. *Journal of Geophysical Research: Solid Earth*, **108**, 2136.

Werner, R., Hoernle, K., Barckhausen, U. & Hauff, F., 2003. Geodynamic evolution of the Galápagos hot spot system (Central East Pacific) over the past 20 m.y.: Constraints from morphology, geochemistry, and magnetic anomalies. *Geochemistry, Geophysics, Geosystems*, **4**, 1108.

White, W. M., McBirney, A. R. & Duncan, R. A., 1993. Petrology and Geochemistry of the Galápagos Islands: Portrait of a Pathological Mantle Plume. *Journal of Geophysical Research*, **98**, 19533–19563.

Wijbrans, J., Németh, K., Martin, U. & Balogh, K., 2007. $^{40}Ar/^{39}Ar$ geochronology of Neogene phreatomagmatic volcanism in the western Pannonian Basin, Hungary. *Journal of Volcanology and Geothermal Research*, **164**, 193–204.

Wilson, D. S., 1996. Fastest known spreading on the Miocene Cocos-Pacific Plate Boundary. *Geophysical Research Letters*, **23**, 3003–3006.

Wilson, D. S. & Hey, R. N., 1995. History of rift propagation and magnetization intensity for the Cocos-Nazca spreading center. *Journal of Geophysical Research*, **100**, 10041–10056.

Yamamoto, M. & Morgan, J. P., 2009. North Arch volcanic fields near Hawaii are evidence favouring the restite-root hypothesis for the origin of hotspot swells. *Terra Nova*, **21**, 452–466.

Yang, H.-J., Frey, F. A. & Clague, D. A., 2003. Constraints on the Source Components of Lavas Forming the Hawaiian North Arch and Honolulu Volcanics. *Journal of Petrology*, **44**, 603–627.

Yeo, I. A., Clague, D. A., Martin, J. F., Paduan, J. B. & Caress, D. W., 2013. Preeruptive flow focussing in dikes feeding historical pillow ridges on the Juan de Fuca and Gorda Ridges. *Geochemistry, Geophysics, Geosystems*, **14**, 3586–3599.

Yoder, H. S. & Tilley, C. E., 1962. Origin of Basalt Magmas: An Experimental Study of Natural and Synthetic Rock Systems. *Journal of Petrology*, **3**, 342–532.

Chapter 3

A 1.6 Ma record of plume-ridge interaction at the Western Galápagos Spreading Center (91°40-92°00'W)

Antje Herbrich[1*], Kaj Hoernle[1,2], Folkmar Hauff[1], Reinhard Werner[1], Dieter Garbe-Schönberg[2], Scott White[3]

[1] GEOMAR Helmholtz Centre for Ocean Research Kiel, Wischhofstraße 1-3, D-24148 Kiel, Germany

[2] Institute of Geosciences, University of Kiel, Ludewig-Meyn-Strasse 10, D-24118 Kiel, Germany

[3] Department of Earth and Ocean Sciences, University of South Carolina, Columbia, South Carolina, USA

Abstract

Interaction between mantle plumes and mid-ocean ridges has primarily been documented by spatial variations of plume influence along mid-ocean ridges. On the R/V SONNE 208 cruise, we recovered basalts between 91°40' and 92°00'W from the ocean crust basement along a profile from the axis of the Western Galápagos Spreading Center (WGSC) to 50 km north of the ridge axis and from a small seamount located 23 km north of the spreading axis. The geochemical composition of fresh glass and a few whole rock samples ranges from tholeiites to basaltic andesites. Almost all samples have incompatible element abundances and Sr-Nd-Pb isotopic compositions

intermediate between depleted basalts from the Galápagos Spreading Center (at >95.5°W) and the Galápagos Archipelago and are similar to enriched mid-ocean ridge basalts. No systematic variations with distance from the ridge axis are observed in incompatible element or isotope ratios in the samples located within 30 km of the ridge axis, but these samples form crude linear arrays on isotope correlation diagrams. Although none of the components identified thus far in the Galápagos Archipelago have the appropriate composition to serve as the enriched end-member for the basement samples <30 km from WGSC, samples from an off-axis seamount have appropriate end member compositions. The <30 km basement sample arrays can be generated by mixing of 20-40 % enriched melts forming the seamount with 60-80 % depleted melts similar in composition to lavas from the WGSC located at >95.5°W and from the Eastern Galápagos Domain. With increasing distance from 30 to 50 km, $^{87}Sr/^{86}Sr$, $^{207}Pb/^{204}Pb$ and $^{208}Pb/^{204}Pb$ increase and $^{143}Nd/^{144}Nd$ isotope ratios decrease, trending towards an enriched mantle two (EMII) type composition. These samples require a source distinct from the younger seafloor lavas, all known Galápagos lavas, and the intraplate seamount. The plume material that reached the WGSC over the last ∼1.6 Ma has a distinct composition from that sourcing the Wolf-Darwin seamounts to the south of the WGSC. We propose that the Northern Domain of the zoned Galápagos plume is spatially and temporally heterogeneous with the plume material flowing from the outermost rim of the Galápagos plume beneath and to the north of the spreading axis at subsolidus depths.

3.1   Introduction

Geochemical anomalies along mid-ocean ridges near ocean islands and seamount hotspot systems (e.g., Azores, St. Helena, Tristan, Galápagos and Louisville Seamounts) have been interpreted to reflect interaction between mantle plumes and the mid-ocean ridge system (e.g., Beier *et al.*, 2012, 2011; Bourdon *et al.*, 2005; Gente *et al.*, 2003; Gibson *et al.*, 2015; Schilling, 1975, 1991; Schilling *et al.*, 2003, 1985; White *et al.*, 1979). These studies have focused on looking at geochemical variations in basalt chemistry along the ridge axis and thus provide a present-day snap-shot of plume-ridge interaction. We provide the first detailed sampling along a profile perpendicular to the ridge axis in order to evaluate plume-ridge interaction through time.

The Galápagos hotspot and the adjacent Galápagos Spreading Center (GSC; also known as Cocos-Nazca Spreading Center) represent a classic example of interaction between an off-axis mantle plume and an adjacent spreading center (Ingle *et al.*, 2010; Schilling, 1991; Schilling *et al.*, 2003, 1985; Yu *et al.*, 1997). The long-lived mantle plume and its interaction with the GSC over the last 23 Ma is expressed at the surface by the Galápagos archipelago and hotspot tracks on the northeast-moving Cocos Plate, consisting of the Cocos aseismic ridge and related seamount province to the north, and on the eastward-moving Nazca Plate, including Carnegie, Malpelo and

Coiba aseismic ridges (Fig. 3.1; e.g., Canales *et al.*, 1997; Handschumacher, 1976; Hey & Vogt, 1977; Wilson & Hey, 1995).

Studies of the trace element and isotope geochemistry of the Galápagos archipelago lavas show that the archipelago is geochemically zoned with an enriched east-facing, horseshoe-shaped region enclosing a depleted region in its inner part (e.g., Geist *et al.*, 1988; Harpp & White, 2001; White & Hofmann, 1978; White *et al.*, 1993). The enriched horseshoe can be subdivided into three distinct geochemical domains going from north to south – Northern, Central and Southern Galápagos Domains (Geldmacher *et al.*, 2003; Hoernle *et al.*, 2000; Werner *et al.*, 2003). The composition of the Central Galápagos Domain, however, could also reflect mixing of Northern Galápagos Domain (NGD) material with Southern Galápagos Domain material plus a depleted component resulting from an asymmetrically zoned plume with either three or two compositional end-members (Hoernle *et al.*, 2000; Rohde *et al.*, 2013). The relative geographic position of the enriched domains has remained constant over the last $\sim$20 Ma (Hoernle *et al.*, 2000, 2002; Werner *et al.*, 2003), leading to the proposition that the hotspot shows long-term geochemical zonation. The interaction of the zoned Galápagos mantle plume with the adjacent GSC provides a unique opportunity to study material transport mechanisms within the earth's mantle.

Recent seismic tomographic studies of the upper 300 km of the mantle beneath the Galápagos archipelago provide a picture of the interaction of the Galápagos plume with the GSC (Villagómez *et al.*, 2014, and references therein). The observed low-velocity seismic anomaly below the archipelago is interpreted to represent an upwelling mantle plume located between 90.5 to 91.5°W that bends northwards at depths below the peridotite solidus ($\geq$80 km) feeding the western and eastern GSC. The input of Galápagos material into the GSC can be observed by changes in ridge morphology and crustal thickness, but also in changes of the geochemical composition of the erupted material (e.g., Canales *et al.*, 2002; Christie *et al.*, 2005; Colman *et al.*, 2012; Harpp *et al.*, 2003, 2005; Ingle *et al.*, 2010; Ito & Lin, 1995; Kokfelt *et al.*, 2005; Schilling *et al.*, 2003, 1982). U-series isotope data point to transport of the plume material to the ridge in solid state (Kokfelt *et al.*, 2005) rather than as melt (Hall & Kincaid, 2003). Recently, Gibson *et al.* (2015) proposed a more dynamically complex (two-stage) model for plume ridge interaction inferring a confined long-term flow of plume material to a fixed position at the GSC ridge axis below the peridotite solidus.

We sampled a profile perpendicular to the Western Galápagos Spreading Center (Fig. 3.1; WGSC) from 91°56'W on the ridge axis to 91°48'W at 50 km from the ridge axis on the R/V SONNE 208 cruise. All samples are located within 8 km from the profile line, except DR69 and DR72, which are 17-23 km from the profile line. The profile was collected north of the spreading center to avoid overprinting by younger lavas derived from plume material flowing to the ridge that formed the Wolf-Darwin lineaments (e.g., Harpp & Geist, 2002; Mittelstaedt *et al.*, 2012; Sinton *et al.*, 2003). These lineaments consist of arcuate chains of volcanic seamounts and islands
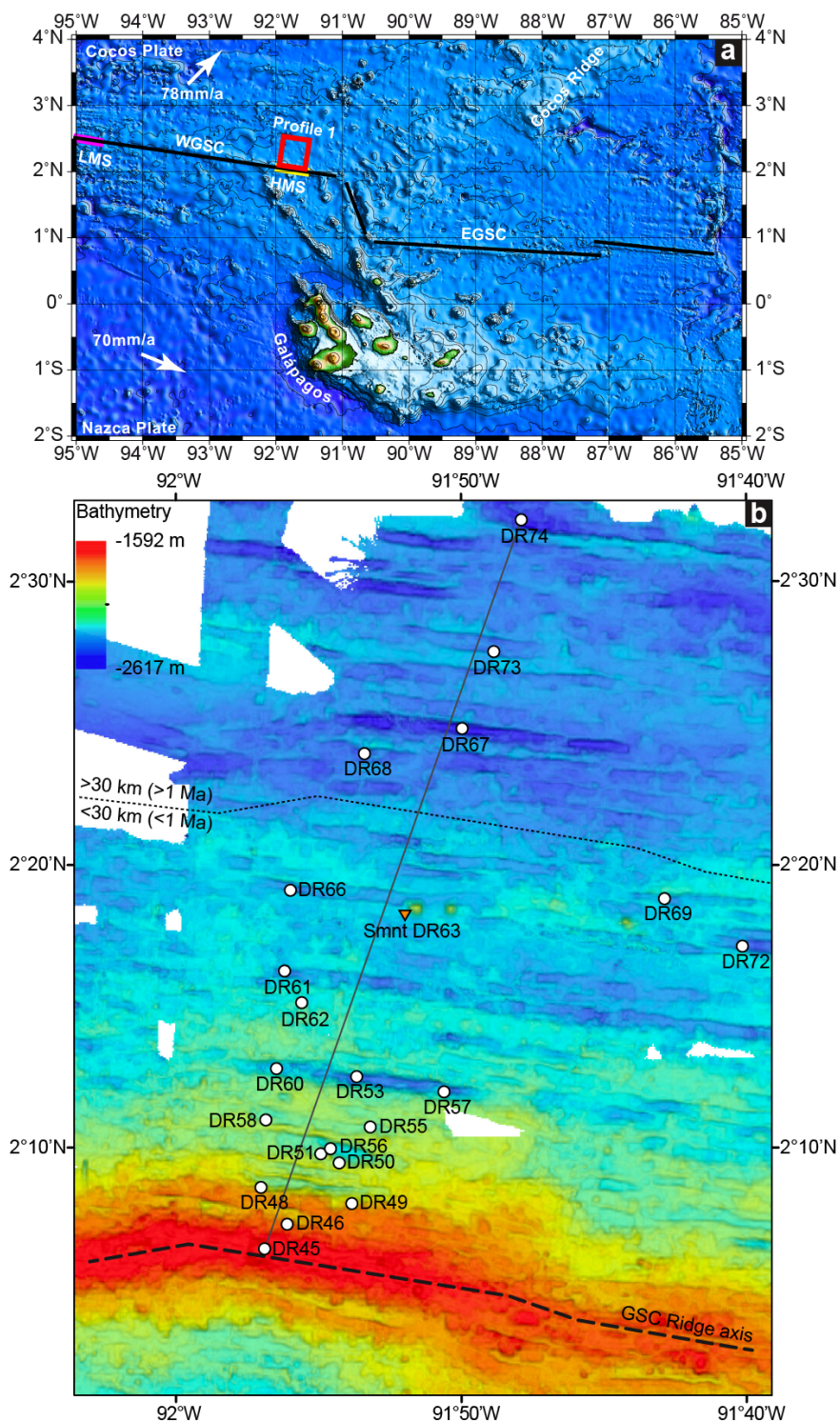
Figure 3.1: a) Bathymetric map of the Eastern Pacific area including all major morphological features (GSC refers to Galápagos Spreading Center). During cruise SO208 Leg 2 an off-axis profile (red box) was sampled by dredging north of the WGSC. The purple and yellow part of the GSC axis marks the High (HMS) and Low Magma Supply (LMS) Area after Colman *et al.* (2012), respectively (for more information see text). b) Detailed bathymetric map of the WGSC off-axis profile based on SIMRAD120 multibeam data with sample locations (circles). Map contains data collected on R/V SONNE cruise SO208 and a compilation of other cruises (White, 2015, data DOI: http://doi.org/10.1594/IEDA/321842).

(up to ∼1.8 Ma old Sinton *et al.*, 1996; White *et al.*, 1993; Mittelstaedt *et al.*, 2012) that radiate northwards from Pinta Island in the northern part of the Galápagos Archipelago to different locations along the WGSC. Here we report geochemical analyses (major and trace elements and Sr-Nd-Pd isotope ratios) of volcanic glass and whole rock samples in order to constrain the temporal variations in plume-ridge interaction along a restricted length of the WGSC over time.

3.2   Geologic Setting of the Sample Area

The profile begins at the ridge crest of the WGSC segment located between 02°07' and 02°32'N and 91°36' and 92°00'W (Fig. 3.1b, Table 3.2) between the two westernmost Wolf-Darwin lineaments. The ridge crest in the study area is characterized by axial high morphology, cut by a 10-40 m deep axial summit graben, associated with high magma supply enhanced by the Galápagos plume (Canales *et al.*, 2002; Colman *et al.*, 2012; Detrick *et al.*, 2002; Sinton *et al.*, 2003). Beneath the spreading axis, a melt lens has been seismically detected at ∼1.6 km depth (Blacic et al., 2004). A detailed geological map of this High Magma Supply (HMS) area along with a geochemical characterization of individual lava units can be found in Colman *et al.* (2012); McClinton & White (2015); McClinton *et al.* (2013).

Table 3.1: Sample locations and distance from GSC ridge axis in km.

Sample location	Latitude (°N)	Longitude (°W)	distance from GSC in km	Age (Ma)
on-axis Smnt				
SO208 DR45	2.11	91.95	0.26	0
off-axis Smnt				
SO208 DR63	2.30	91.87	23.13	0.77
young seafloor basalts <30 km from ridge				
SO208 DR46	2.12	91.95	1.91	0.06
SO208 DR48	2.14	91.95	4.13	0.14
SO208 DR49	2.13	91.90	3.65	0.12
SO208 DR50	2.16	91.92	6.17	0.21
SO208 DR51	2.16	91.91	6.61	0.22
SO208 DR53	2.21	91.89	12.00	0.40
SO208 DR55	2.18	91.88	8.70	0.29
SO208 DR56	2.17	91.91	7.04	0.23
SO208 DR57	2.20	91.84	11.48	0.38
SO208 DR58	2.18	91.95	8.61	0.29
SO208 DR60	2.21	91.94	11.83	0.39

. . . continued

Sample location	Latitude (°N)	Longitude (°W)	distance from GSC in km	Age (Ma)
SO208 DR61	2.27	91.93	18.26	0.61
SO208 DR62	2.25	91.92	16.26	0.54
SO208 DR66	2.32	91.93	23.39	0.78
SO208 DR69	2.31	91.71	28.26	0.94
SO208 DR72	2.29	91.67	24.26	0.81
old seafloor basalts > 30km from ridge axis				
SO208 DR67	2.41	91.83	34.26	1.07
SO208 DR68	2.40	91.89	32.61	1.02
SO208 DR73	2.46	91.81	39.57	1.24
SO208 DR74	2.54	91.80	48.26	1.51

The area north of the ridge axis (to about 02°12'N) is characterized by well-defined abyssal hill morphology, i.e., alternating ridge and valley type structures, oriented sub-parallel to the ridge axis with the basins reaching depths of 2,000 m below sea level (b.s.l.). Further to the north (between 02°12' and 02°32'N), variations in the morphology become progressively less pronounced. Most abyssal hills have relatively steep and linear south-facing scarps but gentle slopes made up of multiple short scarps dipping to the north, suggesting that the abyssal hill morphology is tectonically controlled. The depth of the basins increases to the north as the seafloor regionally subsides, reaching a maximum depth of 2,600 m b.s.l.

This area also shows evidence of small-scale, off-axis volcanism represented by conical edifices, such as the seamount dredged at location DR63 about 23 km north of the spreading axis (herein after called Seamount 63; inverted triangle in Fig. 3.1b). Using half-spreading rates of 30 km/Ma for the last 1.4 Ma and 32 km/Ma for crust generated more >1.4 Ma ago Mittelstaedt *et al.* (2012), the profile covers ∼1.6 Ma of ocean crust formation.

3.3   Sample Background and analytical methods

The samples analyzed in this study were obtained by dredging during cruise SO208 with the German research vessel SONNE in July/August 2010. Pillow and sheet lava fragments, often with fresh glass rims up to several centimeters thick, were recovered up to 50 km off-axis of the WGSC. Fresh volcanic glass was chipped off on board and further processed at GEOMAR (Kiel, Germany). A detailed description of the sample treatment is given in Herbrich *et al.* (2015).

Major element compositions were mainly obtained on fresh glass by using the JEOL JXA-8200 Electron Microprobe (EPMA) at GEOMAR on mounted glass chips following the methods

outlined in Herbrich *et al.* (2015). Major element compositions of additional whole rock samples were determined by X-Ray Fluorescence Analysis (XRF) on fused pellets using a Magix Pro PW 2540 XRF at the Institute of Mineralogy and Petrography at the University of Hamburg. Accuracy for major elements for all methods used is generally better than 3% of the reference values. See Herbrich *et al.* (2015) for more details on accuracy of reference materials. Comparability of major element determination of fresh volcanic glass and whole rock samples was verified by analyzing two glass samples (SO208 DR99-1, SO208 DR107-1) as chip and powder by EPMA and XRF respectively. For SiO_2, Al_2O_3, FeO^T, CaO, TiO_2 and P_2O_5 the contents are within 2%, for MgO and Na_2O within 5%, for K_2O within 6% and for MnO within 9%. The full set of major element composition of all WGSC Profile 1 samples can be found in the appendix Table B.1.

Trace element concentrations of glass chips and whole rock samples were determined by laser ablation and solution inductively coupled plasma mass spectrometry ((LA)-ICP-MS), at the Institute of Geoscience, University of Kiel using a Agilent 7500cs quadrupole ICP-MS for dissolved samples or in combination with a Coherent GeoLasPro Plus 193 nm Excimer laser for chips. Trace element concentrations on glass chips where determined with five spot analyses per sample. Sample digestion procedure for solution ICP-MS followed the method described in Garbe-Schönberg (1993). Reproducibility was usually better than 4% RSD (1σ) for reference material and 5% RSD for duplicate sample analyses. The accuracy of the reference material lies within 3% of the preferred GEOREM values (http://georem.mpch-mainz.gwdg.de/). Trace element data of all WGSC Profile 1 samples is presented in the appendix Table B.2.

Radiogenic isotope ratios of Sr, Nd and Pb double spike (DS) of whole rock and glass samples were analyzed by Thermal ionization mass spectrometry (TIMS) at GEOMAR (Kiel, Germany). Element separation followed the method described in Hoernle *et al.* (2008). A Finnigan MAT262 RPQ^{2+}, operating in static multi-collection mode was used to determine Pb isotope ratios, whereas all Pb isotope ratios were mass bias corrected using the ^{207}Pb-^{204}Pb double spike technique described in Hoernle *et al.* (2011). Sr and Nd isotopic ratios were measured on a Thermo Scientific TRITON, operating in static multi-collection mode. Replicate analyses (n=4) of samples for Pb, Sr and Nd were reproduced within the external error for the reference standard material. Details on sample digestion, leaching of sample material, accuracy and precision are given in Herbrich *et al.* (2015). All Pb isotope ratios are reported relative to NBS981 (n=36) with ^{206}Pb/^{204}Pb=16.9413 ± 0.0024 (2σ), ^{207}Pb/^{204}Pb=15.4988 ± 0.0025 (2σ), and ^{208}Pb/^{204}Pb=36.7236 ± 0.0063 (2σ). The reproducibility of NBS987 (n=63) is ^{86}Sr/^{88}Sr=0.710250 ± 0.000010 (2σ). The Nd isotope data are reported relative to the La Jolla standard with ^{143}Nd/^{144}Nd=0.511850 ± 0.000007 (2σ; n=45) or to our in-house Nd monitor Spex with ^{143}Nd/^{144}Nd=0.511715 ± 0.000006 (2σ; n=38). Radiogenic Isotope ratios of Sr, Nd and Pb of all WGSC Profile 1 samples are provided in the appendix Table B.4.

3.4   Results

Inspection of the glasses under a binocular microscope and in thin sections (n=34), as well as sums between 98.3-99.9 for the glass samples (Table A1) indicate that they have undergone no or only minimal alteration. The whole rock samples vary from fresh to moderately altered with increasing distance from the ridge axis and thus presumably with increasing age. Signs of alteration include 1) the formation of palagonite and iron oxides, 2) alteration rinds around pillow rims and zones along cooling cracks, 3) partial filling and lining of vesicles with calcite and secondary minerals or with very thin Mn-coatings, and 4) formation of Mn crusts up to 1-2 cm in thickness. Such material was, however, avoided by handpicking to obtain the freshest material possible for analyses.

The vast majority of the sampled material is pyroxene- and/or plagioclase-bearing lava. Olivine, spinel and Fe-Ti-oxide (magnetite, ilmenite) phenocrysts are present in some samples. The small Seamount 63, located about 23 km north of the ridge axis, was the only location where highly vesicular (40-45% vesicles) basaltic lava with relatively abundant (1-2%) fresh olivine phenocrysts was recovered.

Based on their isotope geochemistry (see below), the samples have been divided into three groups:

(a) WGSC basement <30 km from the ridge axis (circles),

(b) WGSC basement >30 km away from the ridge axis (squares) and

(c) Seamount 63 sample (filled, inverted triangle).

3.4.1   Major element compositions

On the total alkali versus silica (TAS; Fig. 3.2 Le Maitre *et al.*, 1989) diagram the samples range from tholeiitic basalt to basaltic andesite (Fig. 3.2) with SiO_2=48.5-53.5 wt.% and MgO 2.9-8.8 wt.%. Their Mg-numbers ($Mg\#=mol[Mg/(Mg+Fe^{2+})]$) vary from 0.62 to 0.24, reflecting relatively primitive (Smnt DR63 with MgO=8.8 wt.% and basement sample DR56-2_wr with MgO=8.3 wt.%) to evolved (DR72 and DR74 with MgO of 2.9 and 4.4 wt.% respectively) basaltic compositions.

Major element concentrations plotted against MgO delineate reasonably well-defined trends consistent with shallow level magma differentiation for WGSC basement samples (Fig. 3.3). In general, FeO^T ($\sum$Fe as FeO), TiO_2, P_2O_5, Na_2O and K_2O increase with decreasing MgO while CaO and Al_2O_3 decrease. These observations are typical for the differentiation of tholeiitic melts and consistent with fractionation of the observed phenocryst assemblage of olivine + plagioclase + clinopyroxene. The on-axis DR45 tholeiitic seamount samples (triangles) fall on the trend formed by the <30 km WGSC basement (circles). The >30 km WGSC ocean crust basement
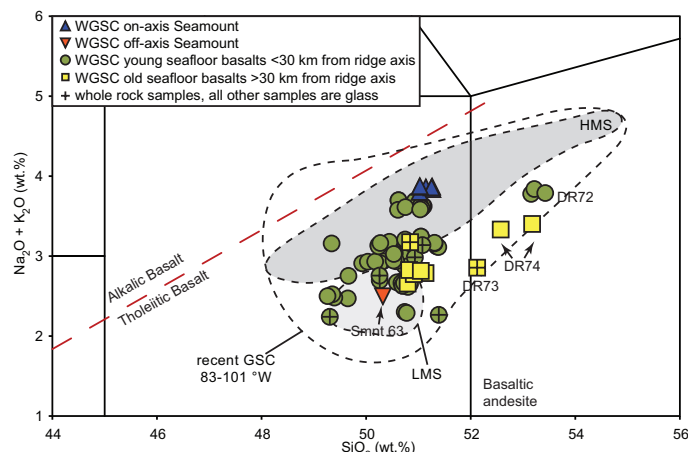
Figure 3.2: Silica versus total alkali diagram (after Le Maitre *et al.*, 1989) of glass and whole rock (denoted with a "+" within the symbol) samples from the WGSC off-axis profile. Alkali basalt / tholeiite division after MacDonald & Katsura (1964); HMS – High Magma Supply area and LMS – Low Magma Supply area of the WGSC at 92°05'-91°51'W and 95°04'-94°48'W respectively, after Colman *et al.* (2012). Recent GSC on-axis data from Christie *et al.* (2005); Cushman *et al.* (2004); Schilling *et al.* (1982).

samples (squares) overlaps with the <30 km WGSC basement in SiO_2, CaO, FeO^T, Al_2O_3 but deviates to lower TiO_2, P_2O_5 and Na_2O with decreasing MgO. Basaltic andesite lavas from both groups (DR72, <30 km WGSC basement and DR74, >30 km WGSC basement) show the greatest deviation of Na_2O and TiO_2 from the fractionation array indicating possible fractionation of Ti-bearing phases (e.g., ilmenite) and more albite-rich plagioclase during advanced stages of melt differentiation. The shallower trend for P_2O_5 in the >30 km group points to apatite fractionation.

Seamount sample DR63, the most mafic tholeiite (MgO=8.8 wt.%) of the entire sample suite, lies at the primitive end of the fractionation lines for CaO, FeO^T, Na_2O, but is shifted towards higher values for TiO_2, P_2O_5 and K_2O and to lower values for Al_2O_3 than a projection of the fractionation trend for the ocean crust basement samples to higher MgO values. Notably, on MgO versus CaO and Al_2O_3 diagrams, the majority of the off-axis WGSC basement samples plot within the High Magma Supply (HMS) field of the present-day ridge axis between 92°05'-91°51'W (Colman *et al.*, 2012, yellow part of the GSC in Fig. 3.1a, dark gray field in Fig. 3.2 and 3.3), which forms the southern (young) end of our off-axis profile. On the other MgO diagrams, the most mafic basement samples fall largely in the Low Magma Supply area (LMS Colman *et al.*, 2012, purple part of the GSC in Fig. 3.1a, light gray field in Fig. 3.2 and 3.3).

3.4.2 Trace elements

Primitive-mantle-normalized trace element patterns of the <30 km WGSC group (grey lines, Fig. 3.4a) are similar to enriched mid-ocean ridge basalt (E-MORB) patterns with highly to moderately incompatible trace element concentrations falling between the Northern Galápagos Domain
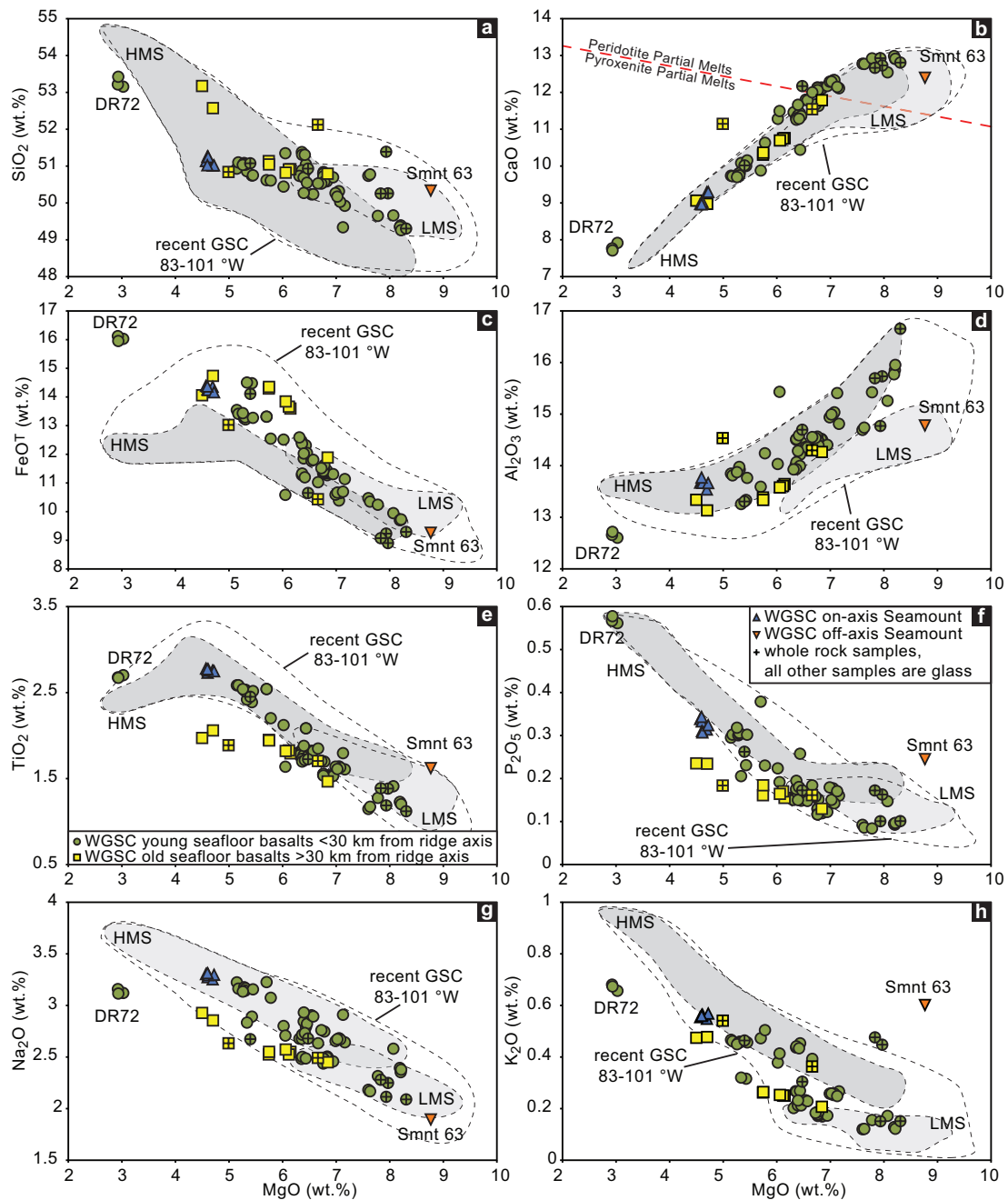
Figure 3.3: Major element concentrations versus MgO for the WGSC off-axis profile compared to WGSC on-axis samples showing typical tholeiitic fractionation trends for shallow magma differentiation of olivine + plagioclase + clinopyroxene. HMS – High Magma Supply area and LMS – Low Magma Supply area after Colman *et al.* (2012). Recent GSC on-axis data between 83-101°W contains data from Christie *et al.* (2005); Colman *et al.* (2012); Cushman *et al.* (2004); Schilling *et al.* (1982). The red dashed line discriminates between pyroxenitic and peridotitic source lithologies but is only applicable to melts that only have olivine on the liquidus. Olivine fractionation drives compositions parallel to the boundary, increasing CaO with decreasing MgO. Fractionation of clinopyroxene and plagioclase will cause CaO to decrease with decreasing MgO, which begins to happen in samples with MgO <8 wt.%. For more information see Herzberg & Asimow (2008).

samples and the WGSC normal-mid-ocean-ridge basalt (N-MORB) sampled at >95.5°W. The WGSC located at >95.5°W does not appear to be influenced by the Galápagos plume and thus should represent local upper mantle (Ingle *et al.*, 2010). The least incompatible elements, including the heavy rare earth elements (HREE), Y and Ti, show a very slight negative slope (e.g., $(Sm/Yb)_n$=1.0-1.4). The patterns for the on-axis DR45 seamount (blue lines) are similar to the other <30 km group samples, but are shifted to higher overall concentrations of all the incompatible elements, except similarly or more evolved samples. Off-axis seamount sample DR63 (red lines in Fig. 3.4a), the most mafic of all the samples, cross cuts the other patterns in heavy to intermediate rare earth elements, Zr, Hf, Ti and Y (displaying a negative slope) and has some of the highest highly incompatible element abundances. Its pattern falls largely within the field for the Northern Galápagos Domain, illustrating ocean island basalt type characteristics (see Fig. 3.4a).

The >30 km WGSC basement samples (Fig. 3.4b) have similar trace element abundances as the <30 km WGSC basement, displaying E-MORB type geochemical characteristics. The most evolved samples (basaltic andesite, DR 74) are, similar to DR72, enriched in all trace elements. Incompatible element ratios plotted versus distance from the WGSC ridge axis do not show any systematic variations with distance (age) over the entire profile. Variations in ratios at single locations, however, are significant, but show a range similar to that observed for today's ridge axis (not shown).

On the Nb/Yb versus Th/Yb and TiO_2/Yb discrimination diagrams (Fig. 3.5; after Pearce, 2008), the off-axis profile samples form a tight and well-correlated array. The WGSC basement samples including those from the on-axis seamount DR45 plot in the MORB-OIB array in the E-MORB range. The off-axis seamount DR63 samples are shifted towards OIB compositions on the Nb/Yb versus Th/Yb plot (Fig. 3.5a) and plot in the OIB array on the Nb/Yb versus TiO_2/Yb diagram (Fig. 3.5b). The most evolved samples from DR72 and DR74 fall have lower TiO_2/Yb than the other samples as a result of Fe-Ti oxide fractionation. DR74 plots above the array formed by the other profile samples on the Nb/Yb versus Th/Yb plot (Fig. 3.5a), reflecting preferential removal of Yb due to its lower incompatibility compared with Th and Nb.

3.4.3   Isotopic data

Variations in Sr, Nd and Pb isotope ratios are fairly limited for each group. The <30 km group has $^{87}Sr/^{86}Sr$=0.70291-0.70307, $^{143}Nd/^{144}Nd$=0.512975-0.513022, $^{206}Pb/^{204}Pb$=18.852-19.086, $^{207}Pb/^{204}Pb$=15.575-15.607, $^{208}Pb/^{204}Pb$=38.656-38.937. The >30 km group overlaps or has slightly higher values compared to the <30 km WGSC basement samples ($^{87}Sr/^{86}Sr$=0.70309-0.70324, $^{143}Nd/^{144}Nd$=0.512964-0.512989, $^{206}Pb/^{204}Pb$=18.958-19.018, $^{207}Pb/^{204}Pb$=15.590-15.619, $^{208}Pb/^{204}Pb$=38,844-39.005). On plots of distance from the spreading axis vs. isotope ratio (Fig.
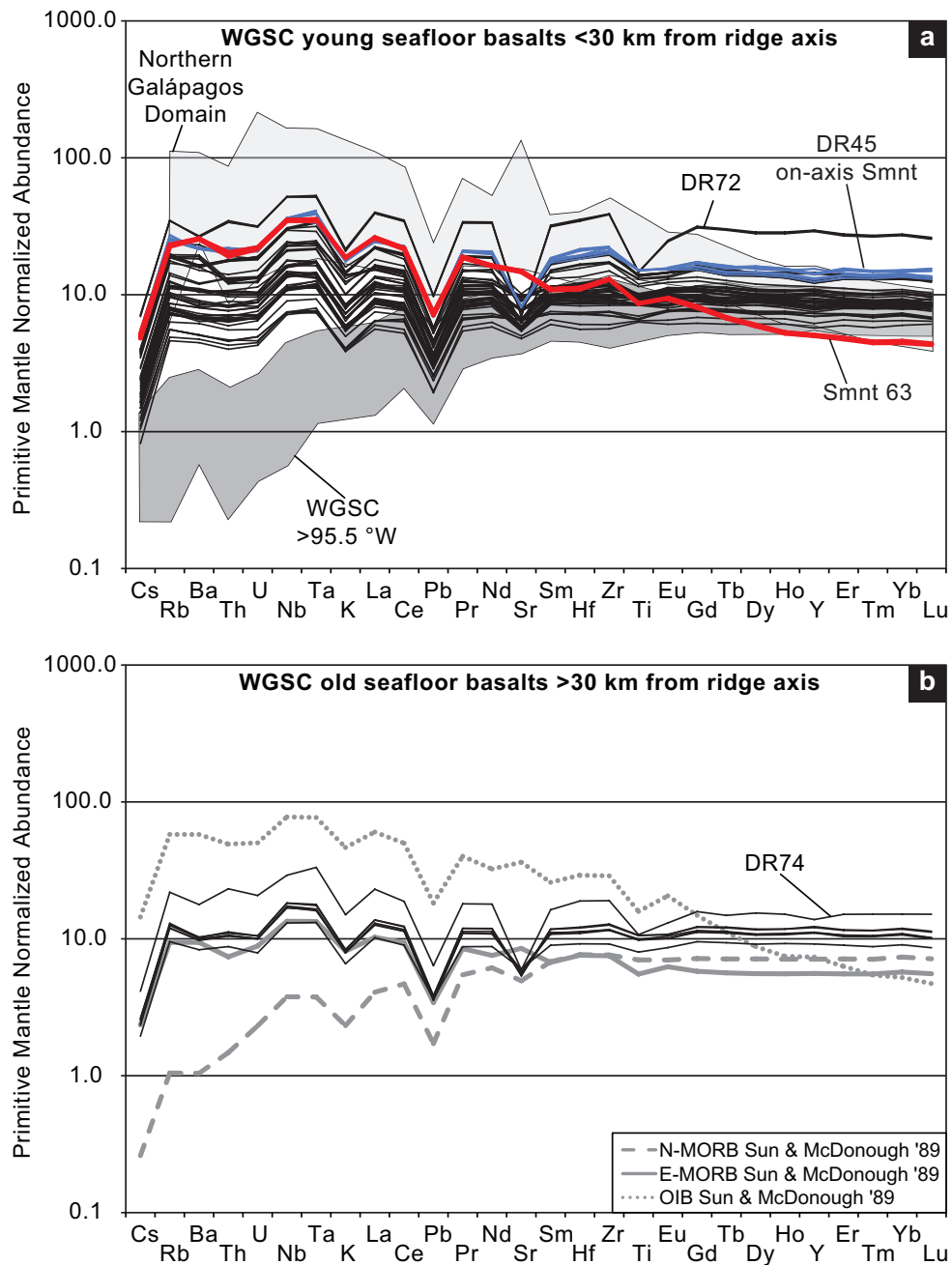
Figure 3.4: Primitive mantle normalized multi-element diagram a) <30 km WGSC basement samples lie between WGSC N-MORB and NGD. Off-axis seamount samples (red line) have similar incompatible trace element abundances than <30 km WGSC basement but are lower than NGD and are depleted in HREE. On-axis seamount samples (blue line) follow in incompatible trace element concentrations the pattern of the most enriched samples, similar to off-axis seamount samples, but clearly deviate in moderate incompatible to compatible elements significantly from the off-axis seamount. b) >30 km WGSC samples are similar to <30 km WGSC basement. In both diagrams the most evolved samples (DR72, DR74) have the highest trace element abundances, overlapping the NGD. Data for Northern Galápagos Domain are from Harpp *et al.* (2005); Harpp & White (2001); Hoernle *et al.* (2000); White *et al.* (1993). Data for WGSC >95.5°W are from Ingle *et al.* (2010).
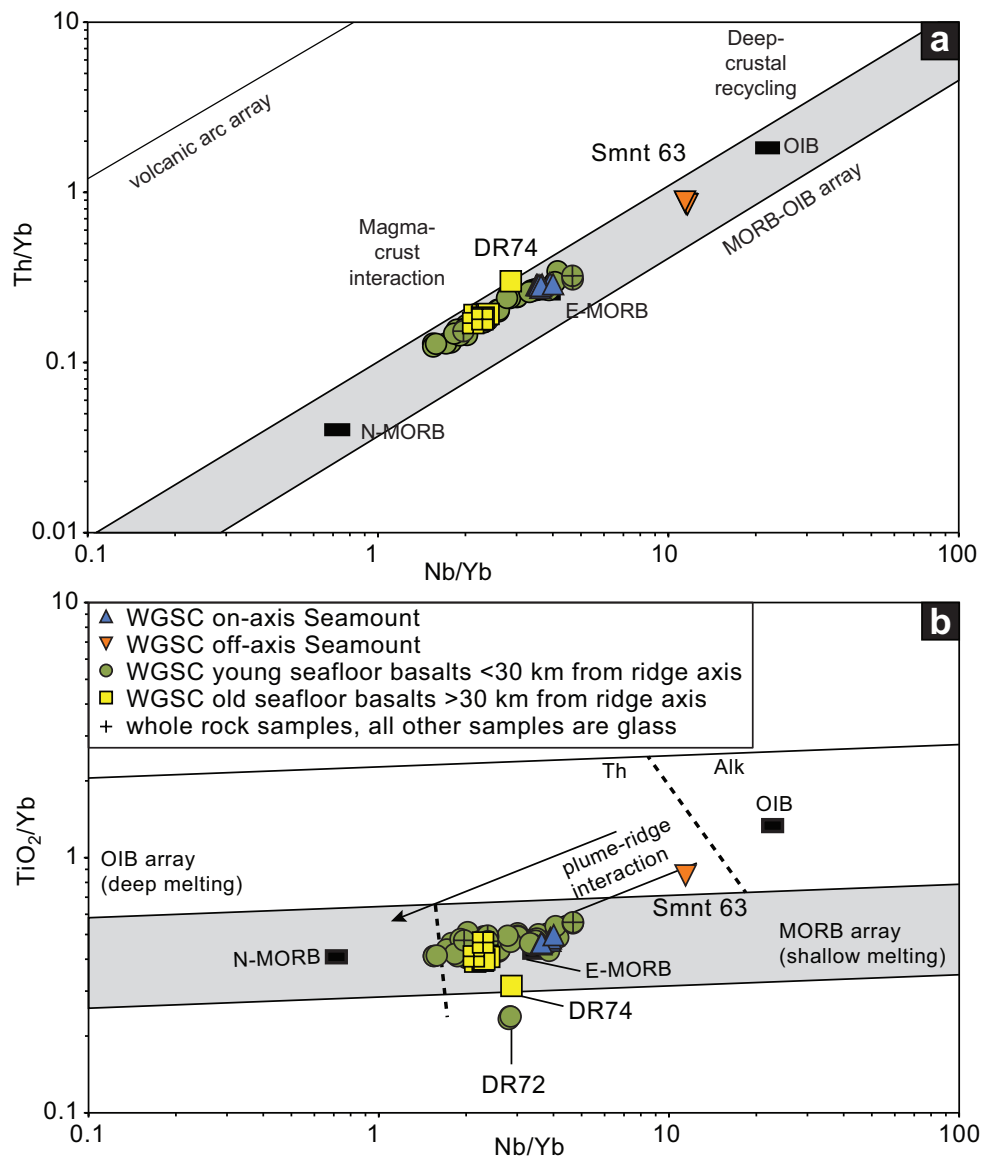
Figure 3.5: Nb/Yb versus Th/Yb and TiO_2/Yb after Pearce (2008). a) All WGSC samples and the on- and off-axis seamounts plot within the MORB-OIB array. There is no difference between the younger (<30 km) and older (>30 km) WGSC basement samples as they form a tight array similar to E-MORB composition. Seamount 63, however, plots far off the main array, towards OIB. b) Nb/Yb versus TiO_2/Yb provides a good proxy to distinguish between shallow and deep melting. In the presence of garnet in the source Yb will be retained and therefore basalts with a significant amount of residual garnet (like OIB) melt at greater depths and therefore plot above the MORB array, like Seamount 63 samples. The WGSC basement samples and the on-axis seamount (DR45) plot in the MORB array and therefore indicate shallow melting.

3.6), the $<30\,\mathrm{km}$ WGSC basement samples show no systematic variation with increasing distance from the ridge axis and therefore increasing age of the crust to $\sim1.0\,\mathrm{Ma}$. For the $>30\,\mathrm{km}$ WGSC basement, $^{87}\mathrm{Sr}/^{86}\mathrm{Sr}$, $^{207}\mathrm{Pb}/^{204}\mathrm{Pb}$ and $^{208}\mathrm{Pb}/^{204}\mathrm{Pb}$ isotope ratios increase while the $^{143}\mathrm{Nd}/^{144}\mathrm{Nd}$ ratio decreases with increasing distance from the GSC. The off-axis seamount has the most radiogenic $^{207}\mathrm{Pb}/^{204}\mathrm{Pb}$, $^{208}\mathrm{Pb}/^{204}\mathrm{Pb}$ and Sr and unradiogenic Nd ratios in the entire profile.

The WGSC off-axis basement forms two distinct geochemical groups in radiogenic isotope space. The $<30\,\mathrm{km}$ WGSC basement samples form an inverse correlation on the $^{87}\mathrm{Sr}/^{86}\mathrm{Sr}$ versus $^{143}\mathrm{Nd}/^{144}\mathrm{Nd}$ and $^{206}\mathrm{Pb}/^{204}\mathrm{Pb}$ versus $^{143}\mathrm{Nd}/^{144}\mathrm{Nd}$ isotope ratio plots (Fig. 3.7 & 3.8c) and positive correlations on $^{206}\mathrm{Pb}/^{204}\mathrm{Pb}$ versus $^{207}\mathrm{Pb}/^{204}\mathrm{Pb}$ and $^{208}\mathrm{Pb}/^{204}\mathrm{Pb}$ correlation diagrams (Fig. 3.8a-b). The $<30\,\mathrm{km}$ WGSC basement samples, including the on-axis seamount samples, fall between N-MORB from the WGSC at $>95.5°\mathrm{W}$ and the Galápagos Archipelago lavas. On all isotope correlation diagrams, except Pb vs Nd isotope ratios, the Northern Galápagos Domain Hoernle *et al.* (NGD; as defined by 2000); Werner *et al.* (NGD; as defined by 2003) could serve as the enriched end-member. On the Pb versus Nd isotope diagram, however, the Central Galápagos Domain Hoernle *et al.* (CGD; as defined by 2000); Werner *et al.* (CGD; as defined by 2003) forms the enriched end-member. Therefore the enriched component needed to generate the WGSC data array is distinct from the components found in the Galápagos Archipelago thus far. Seamount 63 samples have more enriched isotopic compositions than the underlying WGSC basement, displaying more radiogenic Sr and Pb and less radiogenic Nd isotope ratios. The seamount samples are distinct from any samples from the Galápagos Islands and associated submarine volcanism, having higher $^{207}\mathrm{Pb}/^{204}\mathrm{Pb}$ and $^{208}\mathrm{Pb}/^{204}\mathrm{Pb}$ for a given $^{206}\mathrm{Pb}/^{204}\mathrm{Pb}$ than the Galápagos samples. In contrast to the $<30\,\mathrm{km}$ basement samples, the $>30\,\mathrm{km}$ WGSC samples have more radiogenic $^{87}\mathrm{Sr}/^{86}\mathrm{Sr}$ at similar $^{143}\mathrm{Nd}/^{144}\mathrm{Nd}$ (Fig. 3.7) and extend to more radiogenic $^{207}\mathrm{Pb}/^{204}\mathrm{Pb}$ and $^{208}\mathrm{Pb}/^{204}\mathrm{Pb}$ and to less radiogenic Nd isotopic compositions at similar $^{206}\mathrm{Pb}/^{204}\mathrm{Pb}$ ratios (Fig. 3.8). In summary, they extend from the main ($<30\,\mathrm{km}$) crustal array towards a sediment or enriched mantle type composition.

3.5　Discussion

At mid-ocean ridges new magma from the mantle emerges constantly, creating new oceanic crust, which spreads away from the ridge. Therefore the age of the crust generally increases with increasing distance from the ridge axis. Complications with this simple model can arise, for example, when ridge jumps take place. Ridge jumps are particularly likely when the spreading center is located near a hotspot, due to capture of the ridge by the plume (e.g., Mittelstaedt *et al.*, 2012; Gibson *et al.*, 2015). Although synthetic models of magnetic anomaly profiles provide evidence for a ridge jump at $\sim1.0\,\mathrm{Ma}$ ago north of the eastern (E) GSC, no evidence has been
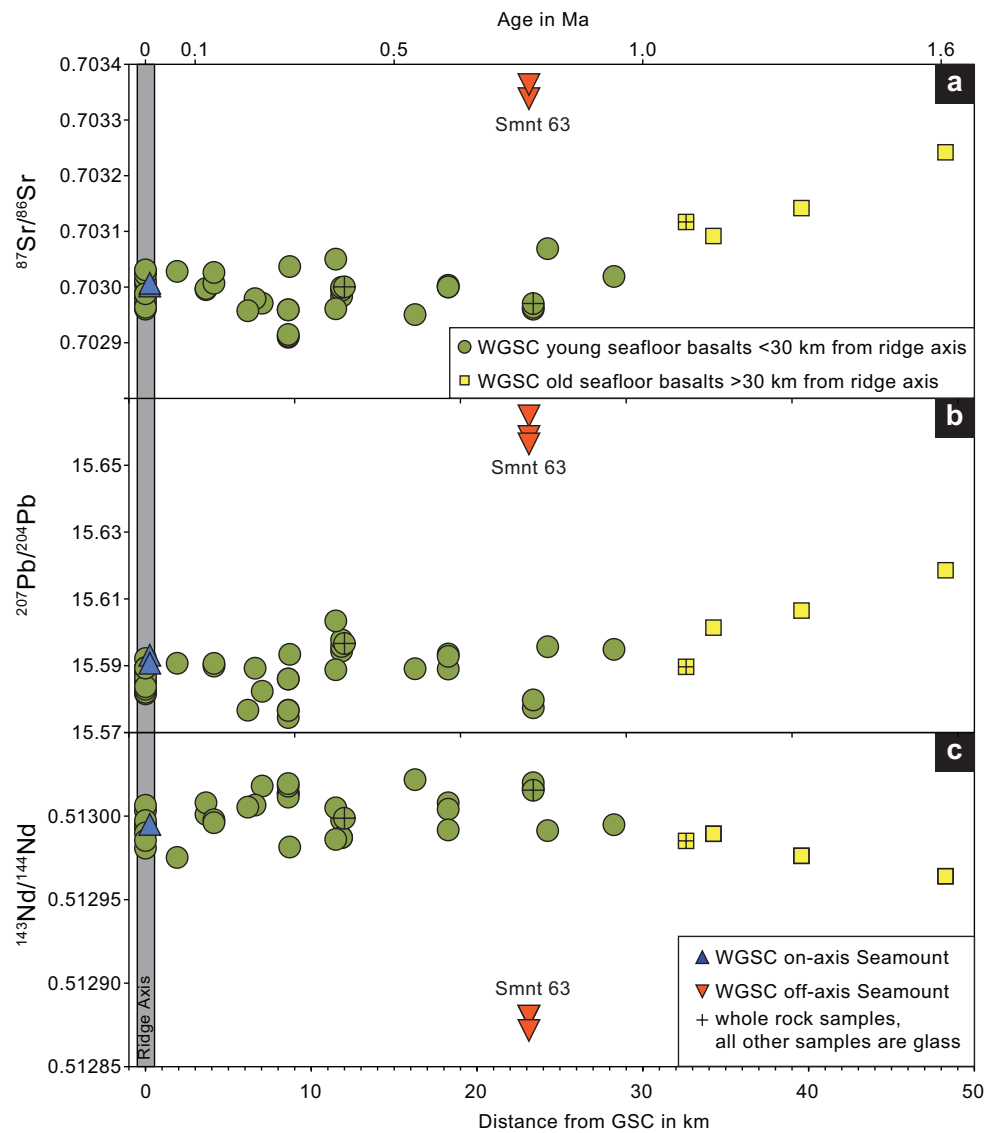
Figure 3.6: Sr-Nd-Pb isotopic variations along the WGSC off-axis profile. <30 km WGSC basement (circles) shows minor variation while >30 km WGSC basement (squares) deviates significantly from the trend, towards more radiogenic Sr and Pb and lower Nd, indicating the presence of a different enriched source involved in their formation. The gray bar symbolizes the WGSC ridge axis. Ages on top x-axis were calculated based on half-spreading rates of 30 km/Ma for the last 1.4 Ma and 32 km/Ma for lavas up to 1.6 Ma old (Mittelstaedt *et al.*, 2012).
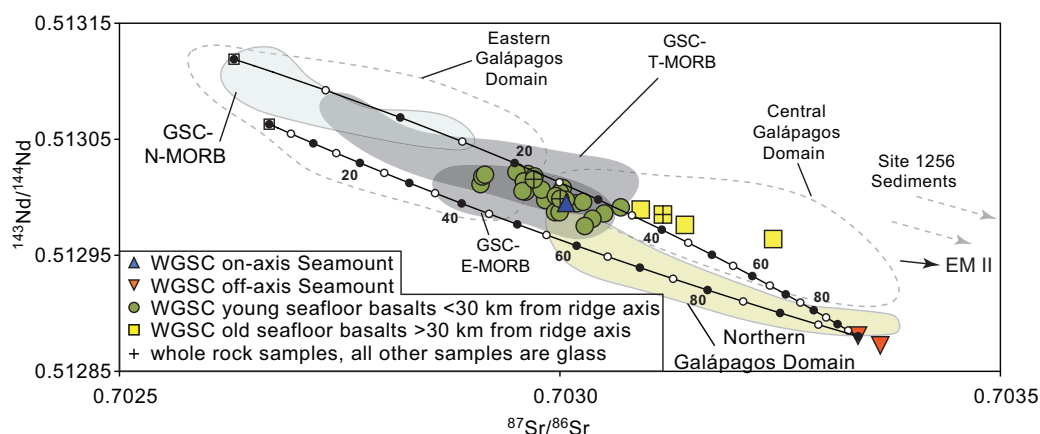
Figure 3.7: Sr versus Nd isotope correlation plot. The samples of the WGSC off-axis profile lie on discrete mixing lines between GSC N-MORB >95.5°W (Ingle *et al.*, 2010), Eastern Galápagos Domain (White *et al.*, 1993) and Seamount 63 with the most enriched composition in Sr and the most depleted in Nd. Black circles on the mixing trajectories represent 10% mixing intervals. Accordingly, the WGSC off-axis array could be produced by three component mixing of c. 20-40% enriched component (DR63) with 60-80% depleted component, represented by sample 92D-1 of GSC N-MORB from Ingle *et al.* (2010) and SC-163 of Eastern Galápagos Domain from White *et al.* (1993). The samples taken at >30 km distance from the GSC (squares) is displaced towards higher $^{87}Sr/^{86}Sr$ than the <30 km WGSC basement array, indicating contribution from an EM II-like component. E-MORB (91.0-92.7°W) to Transitional (T)-MORB (92.7-95.5°W) to N-MORB (95.5-98°W Detrick *et al.*, 2002; Ingle *et al.*, 2010; Sinton *et al.*, 2003) fields are also shown. Galápagos Domain fields from White *et al.* (1993); Site 1256 data from Höfig *et al.* (2014), GMAT Mn-crust data from Frank *et al.* (1999).
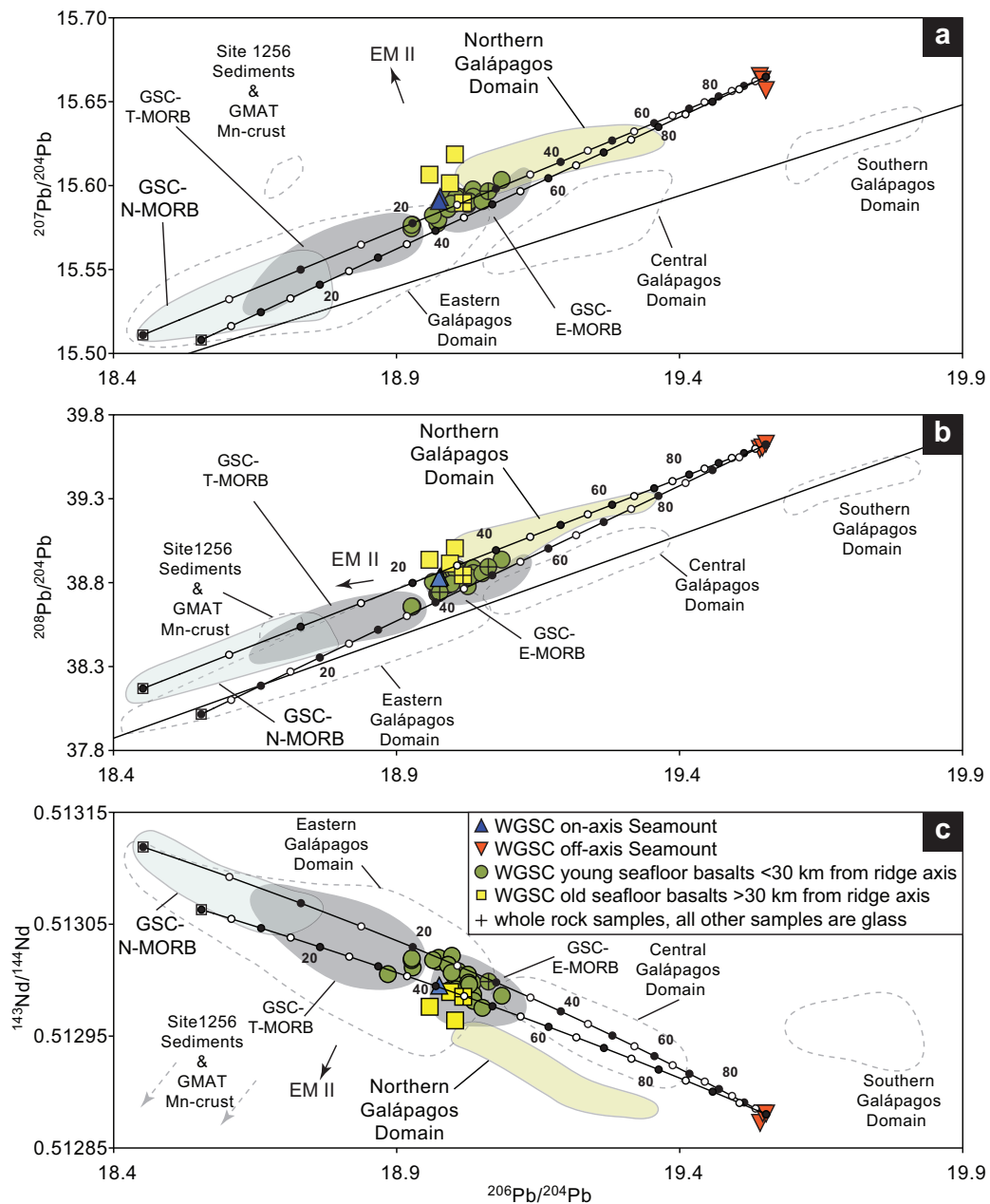
Figure 3.8: ^{206}Pb/^{204}Pb versus (a) ^{207}Pb/^{204}Pb, (b) ^{208}Pb/^{204}Pb and (c) ^{143}Nd/^{144}Nd isotope correlation plot with the Galápagos Domains from White *et al.* (1993) and GSC N-MORB from Ingle *et al.* (2010). The WGSC off-axis profile samples lie between two discrete mixing lines and can be explained through three-component mixing between DR63 as the enriched end-member and samples 92D-1 (Ingle *et al.*, 2010) and SC-163 (White *et al.*, 1993) at the depleted end. The >30 km WGSC basement samples deviate from the <30 km WGSC basement array towards higher ^{207}Pb/^{204}Pb, ^{208}Pb/^{204}Pb and lower ^{143}Nd/^{144}Nd for a given ^{206}Pb/^{204}Pb. The elevated ^{207}Pb/^{204}Pb and ^{208}Pb/^{204}Pb ratios cannot be explained by assimilation of <1.0 Ma old sediments and Mn crusts because their ^{207}Pb/^{204}Pb and ^{208}Pb/^{204}Pb ratios are not high enough. Dark gray areas (GSC T-MORB and GSC E-MORB) from Ingle *et al.* (2010), Galápagos Domain fields from White *et al.* (1993); Site 1256 data from Höfig *et al.* (2014), GMAT Mn-crust data from Frank *et al.* (1999).

found for a ridge jump within the sampled section (see e.g., synthetic magnetic model for a profile at 91°45'W from 1.5 to 3.0°N; Fig. 7b in Mittelstaedt *et al.* (2012)). Therefore, using the half-spreading rates for the WGSC at 91°45'W from Mittelstaedt *et al.* (2012), the sampled crust appears to increase systematically in age from the WGSC ridge axis to ~1.6 Ma.

3.5.1 Melting conditions and geochemical variations with age

Mafic compositions can provide some insight to the source lithology. The MgO vs. CaO binary diagram can be used to distinguish between pyroxenitic and peridotitic source lithologies (Herzberg & Asimow, 2008). In Fig. 3.3b, the seamount and most mafic samples with MgO >8 wt.% recovered within 30 km from the WGSC plot within the field for peridotite partial melts being located above the dividing line separating peridotite from pyroxenite melts (dashed line in Fig. 3.3b; calculated with CaO=13.81-0.274MgO after Herzberg & Asimow (2008). For samples plotting above the boundary line, identification of a peridotitic source is a robust result, because fractionation of olivine alone will drive the melts towards lower MgO and higher CaO but parallel to the boundary. Plagioclase or clinopyroxene fractionation, however, will lower CaO and thus drive the compositions across the boundary into the pyroxenite melt field with decreasing MgO as is the case for crustal melts with MgO <8 wt.%. Using olivine chemistry, Vidito *et al.* (2013) also proposed a peridotitic (pyroxenite-free) source for the Wolf and Darwin Islands located in the Galápagos Northern Domain just south of the WGSC.

The presence of residual garnet provides information about the depth of melting. Fractionation of the heavy rare earth elements (HREE) occurs when garnet is present in the residuum but not if only spinel is residual. The nearly flat HREE patterns (e.g., $(Sm/Yb)_n$=1.0-1.4 and $(Tb/Yb)_n$=1.0-1.2; where n indicates normalization to primitive mantle) are consistent with garnet being largely absent in the integrated melt column residuum except for Seamount 63 samples with steep HREE patterns (e.g., $(Sm/Yb)_n$=2.4 and $(Tb/Yb)_n$=1.5). The TiO_2/Yb ratio (Fig. 3.5b) can also provide information about deep vs. shallow melting (Pearce, 2008). On the Nb/Yb vs. TiO_2/Yb plot, all WGSC basement and the on-axis seamount samples (DR45) plot in the MORB array, pointing towards shallow melting, while the off-axis seamount samples (DR63) plot above the array. Since Ti is fractioned from Yb by garnet, the elevated ratios of Seamount 63 samples indicate residual garnet in the peridotitic source, indicating that final equilibration of the seamount lavas with their source took place at depths in excess of ~80 km. Taken together with the elevated ratios of more to less incompatible elements (e.g., (Nb/Yb)=11.4-11.6, (Th/Yb)=~0.8 and $(La/Yb)_n$=~5.8) for the Seamount 63 samples, the seamount lavas appear to have formed at greater depth by lower degrees of melting than the ocean crust basement samples formed at the spreading center. Since the seamount shows no evidence of having been split, it must have formed off-axis (north of the WGSC) in a near-ridge but intraplate setting. The more radiogenic Sr and

Pb and the less radiogenic Nd isotope ratios indicate that Smnt. 63 was derived from a source with higher time-integrated U/Pb ratio or HIMU type source material, probably preferentially sampled as a result of lower degrees of melting at greater depth. In conclusion, fertile plume material must be able to pass under the ridge at subsolidus depths of ≥ 80 km.

Plots of distance from the ridge axis versus incompatible elements and/or isotope ratios provide information about the geochemical evolution at the ridge axis over time and reveal temporal fluctuations in material input or changes in melt parameters, e.g., degree of melting. No systematic variations in either incompatible element ratios (not shown) or isotope ratios, however, were observed in the <30 km (<1.0 Ma) group samples (Fig. 3.6). Variations within the <30 km WGSC sample group lie largely within the range of the recent WGSC lavas, reflecting only minor variations in the proportions of isotopically enriched and depleted source materials through time. The limited data set for the >30 km WGSC basement samples define a crude trend towards higher ^{207}Pb/^{204}Pb, ^{208}Pb/^{204}Pb and ^{87}Sr/^{86}Sr and lower ^{143}Nd/^{144}Nd compositions with increasing distance from the ridge, suggesting a greater influence of an enriched component in the past. With decreasing age from c. 1.6 to 1.0 Ma, however, this source was slowly replaced by less enriched source material. The role of an isotopically more enriched source for the >30 km WGSC basement samples and whether it could be the same source as sampled by seamount DR63 is explored further below using isotope correlation diagrams.

3.5.2 Defining source end-members and mixing relationships for the younger WGSC (<30 km group)

Along the Western Galápagos Spreading Center three groups of MORB (N-, T- and E-MORB) have been identified, based on their compositional and morphological characteristics (e.g. Cushman *et al.*, 2004; Ingle *et al.*, 2010; Schilling *et al.*, 1983; Sinton *et al.*, 2003). With increasing distance from the 91°W Transform Fault (TF), overall the morphology changes from axial high to axial valley type character, mirrored by a change in geochemical composition from E-MORB (91.0-92.7°W) to Transitional (T)-MORB (92.7-95.5°W) to N-MORB (95.5-98°W Detrick *et al.*, 2002; Ingle *et al.*, 2010; Sinton *et al.*, 2003). Along our profile at 92°W, we only found E-MORB type compositions with the samples from the <30 km part of the profile plotting within the on-axis E-MORB field. Therefore the chemical compositions being produced at the ridge through plume-ridge interaction has remained relatively stable for the last ~ 1.0 Ma.

The systematic westward decrease in degree of geochemical enrichment along the WGSC is generally attributed to a diminishing supply of Galápagos plume material to the spreading center with increasing distance from the hotspot. It is a matter of ongoing discussion, whether the decreasing plume signal reflects radial outflow of plume material along the base of the lithosphere and into the spreading center at various locations (Ribe & Delattre, 1998; Shorttle *et al.*, 2010).

Alternatively, it could reflect input of plume material into the GSC west and east of the 91°W TF followed by lateral flow and dilution of plume material as it flows beneath the ridge axis to the west and east and therefore away from the 91°W TF (e.g., Gibson *et al.*, 2015; Ingle *et al.*, 2010; Kokfelt *et al.*, 2005; Schilling *et al.*, 2003). Finally, a combination of both alternatives has also been proposed (e.g., Geldmacher *et al.*, 2013). Regardless of the route that plume material takes to get to the ridge and whether or not it flows laterally beneath the ridge, the plume material becomes systematically diluted through mixing with depleted upper mantle farther from the plume.

The Sr-Nd-Pb isotopic ratios from the <30 km WGSC basement samples form short but reasonably well-correlated arrays on isotope correlation diagrams (Fig. 3.7-3.8), which lie roughly between the fields of local GSC N-MORB from >95.5°W, an area thought to be uninfluenced by contributions from the Galápagos plume (Ingle *et al.*, 2010), and enriched geochemical domains of the Galápagos Archipelago (White *et al.*, 1993).

The isotopically enriched end of the <30 km WGSC basement lavas extends to and overlaps the field of the NGD on the uranogenic and thorogenic diagrams (Fig. 3.8a, b), and possibly on the $^{87}Sr/^{86}Sr$ versus $^{143}Nd/^{144}Nd$ diagram (Fig. 3.7). On the $^{206}Pb/^{204}Pb$ versus $^{143}Nd/^{144}Nd$ isotope correlation diagram (Fig. 3.8), the <30 km WGSC off-axis samples trend, however, towards the Central Galápagos Domain. Therefore none of the previously identified Galápagos geochemical domains successfully meets a single enriched end-member status in all of the mixing arrays. The material reaching the WGSC appears to have a distinct composition from the sampled seamounts and islands within the Northern Galápagos Domain, ranging from historic to ~1.6 Ma in age. Interestingly samples from the northern (seamount) domain of the older parts of the hotspot track (c. 11-15 Ma) and seamounts on the EPR generated part of the Cocos Plate have similar geochemical characteristics to the Northern Galápagos Domain, indicating that this is a long-lived component of the Galápagos hotspot (Herbrich *et al.*, 2015; Hoernle *et al.*, 2000; Werner *et al.*, 2003). Evidence of the Northern Domain signature has even been found in young arc volcanism from Central Costa Rica to Central Nicaragua, reflecting recycling of still older Northern Domain material subducted beneath Costa Rica (Hoernle *et al.*, 2008; Gazel *et al.*, 2009). In conclusion, the mantle reaching the WGSC over the last 1.6 Ma has distinct compositions compared to the products of the Galápagos hotspot recognized thus far.

In contrast to Galápagos Archipelago volcanism, Seamount DR63 has the appropriate composition to serve as the enriched end-member on all isotope correlation diagrams, as well as on incompatible trace element diagrams. Mixing lines between seamount DR63 and the most depleted sample (92D-1) from the WGSC between 95.5 and 98°W (Ingle *et al.*, 2010) pass through the <30 km WGSC group samples on all isotope correlation diagrams but only through the upper portion of the arrays on the $^{87}Sr/^{86}Sr$ vs. $^{143}Nd/^{144}Nd$ (Fig. 3.7), the $^{206}Pb/^{204}Pb$ vs. $^{208}Pb/^{204}Pb$, $^{143}Nd/^{144}Nd$ (Fig. 3.8) and $^{87}Sr/^{86}Sr$ (not shown) isotope diagrams. Therefore an additional enriched or depleted component is also required. The width of the WGSC <30 km off-axis group array can be

generated, e.g., if a second depleted component with lower $^{143}Nd/^{144}Nd$ and $^{208}Pb/^{204}Pb$, but slightly higher $^{206}Pb/^{204}Pb$ isotope ratio is also involved in the mixing (Fig. 3.7). This composition plots outside of the GSC-N-MORB field (>95.5°W), but plots in the Eastern Galápagos Domain field. Notably, the GSC-N-MORB field overlaps in all isotope correlation diagrams with the Eastern Galápagos Domain except on the thorogenic lead isotope diagram where the GSC-N-MORB is shifted to higher $^{208}Pb/^{204}Pb$ ratios for a given $^{206}Pb/^{204}Pb$ ratio with no overlap at the lowest $^{206}Pb/^{204}Pb$ ratios of ~18.5, consistent with the Eastern Domain lavas being derived from the plume rather than ambient upper mantle (Hoernle *et al.*, 2000; Werner *et al.*, 2003). Sample SC-163 from Santa Cruz Island (from White *et al.*, 1993) could serve as the potential second depleted (plume) end member. Simple mixing calculations indicate that the array of <30 km WGSC off-axis crust can be generated by mixing of 20-40% enriched component (DR63) with 60-80% mixture of GSC-N-MORB and a Galápagos Eastern Domain component.

3.5.3   Defining source end-members and mixing relationships for the older WGSC (>30 km group)

Only samples from four locations at >30 km from the WGSC were recovered with glass being obtained at three sites but only whole rocks at the fourth. Compared with the younger WGSC samples, the older WGSC samples become more enriched with increasing distance from the ridge axis and thus presumably with increasing age between 1.0-1.6 Ma ago. On the isotope correlation diagrams (Fig. 3.7-3.8), the older (>30 km) WGSC off-axis group samples deviate from the field of the younger (<30 km) WGSC basement, extending to more radiogenic $^{207}Pb/^{204}Pb$, $^{208}Pb/^{204}Pb$ and less radiogenic $^{143}Nd/^{144}Nd$ isotope ratios at a given $^{206}Pb/^{204}Pb$ along with overall higher $^{87}Sr/^{86}Sr$. In Sr-Nd isotope space (Fig. 3.7), the older >30 km samples plot within the field of the Central Galápagos Domain, whereas on the uranogenic and thorogenic Pb and the $^{206}Pb/^{204}Pb$ versus $^{143}Nd/^{144}Nd$ isotope diagram isotope diagrams, they plot outside of the Central Galápagos Domain and trend away from the Northern Domain. Therefore, the >30 km group does not have a composition that consistently plots in a single Galápagos domain. On the uranogenic Pb isotope diagrams, the two samples taken furthest from the WGSC have higher $^{207}Pb/^{204}Pb$ than Galápagos samples with similar $^{206}Pb/^{204}Pb$. In comparison to the <30 km group, these samples are shifted towards a sediment or an Enriched Mantle (EM) II type component.

The displacement of the >30 km WGSC samples towards more enriched compositions is intriguing. Since the full geochemical range was found in fresh volcanic glass, post-magmatic alteration effects seem unlikely to have created this pattern. This notion is corroborated by the smoothness of multi-element patterns that are free of alteration induced enrichments and/or depletions of fluid mobile elements, such as Cs, Rb, Ba, U and K. In addition, Nd and Pb are difficult to mobilize with cold seawater and seawater only has very low abundances of these elements and

very different isotopic compositions compared to E-MORB type seafloor, making post-eruption contamination unlikely. Therefore the change in isotopic signature appears to be of magmatic origin.

The most extreme enriched signature occurs in the most evolved basaltic andesite (sample DR74), suggesting that the enrichment may reflect assimilation during magma differentiation. A small addition of marine sediment (even $<1.0\%$) is sufficient to elevate the composition of a melt lying on the NHRL (Northern Hemisphere Reference Line) to higher $^{207}Pb/^{204}Pb$ (e.g., Geldmacher *et al.*, 2003). The area around 92°W has been described as intensely faulted with strong bottom currents (Colman *et al.*, 2012), allowing sediments to be collected within the fault traces and potentially come into contact with ascending magma. Another possibility is outflow of lava over sediment accompanied by incorporation of sediment into lava flows or hydrothermal leaching of water saturated sediments during the eruption. Also the magmas and/or erupted lavas could be contaminated by Mn crusts, which are present on whole rock samples from $>30\,km$ from the WGSC. These processes may lead to minute but rapid, spatially limited changes in the isotopic composition of melt. Local $<1.0\,Ma$ old sediments (IODP Site 1256 Höfig *et al.*, 2014) and Mn crusts (GMAT 14D Frank *et al.*, 1999), however, have lower $^{208}Pb/^{204}Pb$ than the younger lavas and mixing lines between the $<30\,km$ WGSC lavas and the $<1.0\,Ma$ sediments and Mn crusts cannot explain the increased $^{208}Pb/^{204}Pb$ in the $>30\,km$ WGSC lavas or the high $^{207}Pb/^{204}Pb$ ratio of sample DR74-1 (Fig. 3.8). Therefore mixing of local sediment and Mn crusts with $<30\,km$ WGSC lavas, e.g. sediment assimilation, is not a viable explanation for the distinct isotopic composition of the older crust, suggesting that the more enriched compositions reflect involvement of EMII type source material.

An EMII type component that could serve as the enriched end-member for the $>30\,km$ WGSC off-axis crust has not been reported previously for the Galápagos Archipelago (e.g., Harpp & White, 2001; White *et al.*, 1993), the GSC (Schilling *et al.*, 2003; Ingle *et al.*, 2010) or the hotspot tracks (Hoernle *et al.*, 2000; Werner *et al.*, 2003). The EMII type source does not plot within or on an extension of the Galápagos domain arrays (including data from the archipelago and the hotspot tracks) on the Pb isotope diagrams, as is the case with Smnt. 63. Therefore, there is some question as to whether this component is intrinsic to the Galápagos plume, i.e., derived from the plume source. Alternatively, it could reflect a heterogeneity in the upper mantle beneath the ridge or could be upper or lower mantle, or transition zone, material entrained by the plume during ascent. Both lithospheric and asthenospheric mantle located above a subducting slab can be enriched by fluids or melts from subducting sediments, leading to an EMII type composition. Metasomatized (enriched) subcontinental lithospheric mantle with an EMII like composition could be delaminated and thus carried to various locations in the mantle and could conceivably even contaminate the source of the Galápagos hotspot, believed to be derived from the core-mantle boundary based on high $^{3}He/^{4}He$ ratios in Galápagos lavas (Graham *et al.*, 1993; Kurz & Geist,
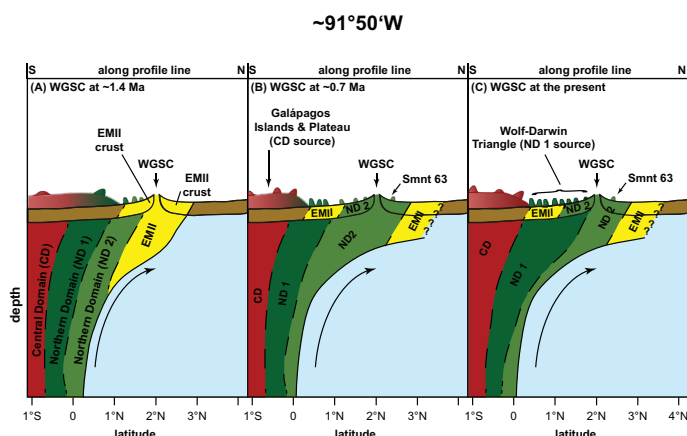
Figure 3.9: South to north profiles at ∼91°50' W extending from the center of the plume (Central Galá-pagos Domain or CD) to north of the WGSC at (A) 1.4 Ma, (B) 0.7 Ma and (C) the present, illustrating the geochemical evolution of plume-ridge-interaction at the WGSC. A) Between >1.6 and 1.0 Ma ago, an EMII-type component, possibly entrained during upwelling of the plume (yellow field), is melted at the WGSC. B-C) Between 1.0 Ma and the present, mantle representing a mixture of upper mantle and Seamount 63 source material (light green) from the northern margin of the plume is melted to form mag-mas along the GSC (termed Northern Domain 2 or ND2). The material sampled within the Wolf-Darwin Triangle (Northern Domain 1 or ND1) has a slightly different composition (dark green) than the material that erupted at the WGSC thus far, therefore the Northern Galápagos Domain appears to have a het-erogeneous composition, most likely reflecting a subtle change in composition in the northernmost plume margin.

1999), seismic evidence for perturbations of the transition zone beneath the hotspot (Hooft *et al.*, 2003) and seismic tomographic (Montelli *et al.*, 2006, 2004) studies.

3.5.4   Model for plume-ridge interaction over the last ∼1.6 Ma

Seismic tomography of the upper mantle beneath the Galápagos Archipelago shows that the low velocity anomaly associated with the Galápagos plume rises into the upper mantle beneath the westernmost islands but bends to the north at a depth of ∼100 km between ∼90-92°W (Villagómez *et al.*, 2014). Although the presently available tomography doesn't resolve the anomaly north of 1°N latitude, it is clear that the northern part of the plume must reach the WGSC located just north of 2°N.

The two groups of seafloor lavas formed over the last ∼1.6 Ma along and north (Smnt. 63) of the WGSC have distinct compositional characteristics compared to lavas from the Galápagos Archipelago and Hotspot Tracks. Although most of the incompatible element and isotope corre-lations for the <1.0 Ma (<30 km WGSC basement samples) seafloor lavas and Smnt. 63, located north of the WGSC, could be explained through stirring together Galápagos Northern Domain and depleted upper mantle source material or melts, such a mixture cannot explain their composi-tion of the <1.0 Ma lavas on the Pb vs. Nd isotope diagrams. The similarity of the <1.0 Ma lavas

and Smnt. 63 compositions to the Northern Domain and their generation north of the Northern Domain suggest that the source material is derived from the Galápagos plume, representing either a spatial or temporal change in Northern Domain composition. Since the <1.0 Ma WGSC generated crustal composition has not been found in the northern part of the Galápagos hotspot tracks thus far, we propose that the WGSC is sampling the northernmost edge of the upwelling plume. Due to lower upwelling rates and probably cooler temperatures on the plume margin, we suggest that this part of the plume does not produce enough magma to contribute to the morphologic hotspot track when this part of the plume doesn't upwell beneath a spreading center.

The formation of Smnt. 63 north of the WGSC indicates that fertile plume material must be able to flow beneath the ridge at depths within the garnet peridotite stability field (≥80 km). After passing under the ridge, the plume source of Smnt. 63 upwelled and melted by decompression to low degrees (compared to the melts generated beneath the WGSC) in the garnet stability field, sampling only the most enriched portions of the upwelling mantle package. Thus these melts show more extreme isotopic compositions (HIMU-like, reflecting more radiogenic Pb isotopic composition) of this source than the melts generated beneath the ridge. In conclusion, seamount DR63 provides important documentation that Galápagos Plume material can be transferred across the GSC, requiring a deep segregation of plume material from the northward inclined main plume conduit.

Concerning the change in composition of the seafloor lavas at c. 1.0 Ma, it is interesting to note that a ridge jump has been proposed at 1 Ma for the EGSC (e.g., Mittelstaedt *et al.*, 2012). Although there is no evidence for a ridge jump at this time in the magnetic data from profiles perpendicular to the WGSC, the ridge jump may have somehow influenced mantle flow changing the source material feeding the WGSC. We see, however, evidence that this change took place over at least half a million years. The EMII type composition begins to change towards the <1.0 Ma by ∼1.5 Ma and possibly even before then. Therefore we don't believe that the ridge jump in the EGSC caused this change. Since there is no evidence for an EMII like composition, as seen in ∼1.0-1.6 Ma seafloor north of the WGSC, within the Galápagos hotspot thus far, we propose that the EMII type component is not intrinsic within the plume and suggest it may represent mantle enriched above a subduction zone that was entrained along the northern margin of the plume.

In Figure 3.9, we show a schematic illustration of the geochemical evolution of plume-ridge along the WGSC over the last 1.6 Ma. At 1.6 Ma, the WGSC was located closer to the Galápagos hotspot and sampled EMII-like mantle (yellow; >30 km basement), possibly entrained by the upwelling plume (Fig. 3.9a). The ridge migrated away from the hotspot to the north at a half-spreading rate of ∼32 km/Ma until 1.4 Ma when the half spreading rate to the north decreased to ∼30 km/Ma (Mittelstaedt *et al.*, 2012). At ∼1.4 Ma, the composition of the ocean crust that was formed began changing in composition towards that of the <1.0 Ma (<30 km WGSC basement samples) composition (Fig. 3.9b). At 1.0 Ma, the EMII-like component was exhausted, showing

that the boundary between the two compositionally different packages of mantle has flowed north-wards of the WGSC. For the next 1.0 Ma, mantle with Smnt. 63-type composition (lighter green, ND2) was stirred together with depleted upper mantle, upwelled beneath the ridge and melted to form new ocean crust. Some of the plume mantle was able to pass beneath the ridge within the garnet peridotite stability field without being stirred together with ambient upper mantle. Low-degree melting of this mantle through decompression north of the WGSC produced Smnt. 63 with more enriched plume-like isotopic composition. Magmatism along the Wolf-Darwin-lineaments, to the south of the WGSC, has a slightly different composition (darker green, ND1) from the material erupted at the WGSC over the last 1.4 Ma, indicating that there must be a boundary between the two types of mantle components (Fig. 3.9c). This part of the Northern Galápagos Domain, however, is presently located to the south but presumably fairly close to the WGSC. In the future, it is likely that this second boundary will also pass beneath the ridge, such that the future WGSC ocean crust will have a similar composition to lavas from the Wolf-Darwin-Triangle.

3.6   Summary and Conclusions

In this paper, we present for the first time a detailed profile going from the axis of a mid-ocean ridge (Western Galápagos Spreading Center or WGSC) to 50 km north of the axis with a sampling interval of generally <5 km but in all cases <10 km. Using half-spreading rates from paleomagnetic data (Mittelstaedt *et al.*, 2012), we estimate that this profile covers ~1.6 Ma of spreading history along the WGSC. Two distinct compositional groups can be identified with the samples from <30 km from the ridge axis (<1.0 Ma) showing no systematic variations in geochemistry with time, whereas those from >30 km from the ridge axis (~1.0-1.6 Ma) display increasing Sr and Pb isotope ratios and decreasing Nd isotope ratios with increasing distance from the spreading center (and thus age). All samples generally have compositions intermediate between the enriched Galápagos plume domains and N-MORB from the GSC at >95.5°W. Nevertheless, these samples cannot simply be explained through mixing of a Northern Galápagos Domain component with depleted components. An enriched off-axis (intraplate) seamount, presently ~23 km north of the ridge axis has the appropriate composition to serve as the enriched end-member, having an isotopic composition similar to the Northern Galápagos Domain except on the Pb vs. Nd isotope diagram. Mixing this component with 1) a depleted N-MORB type component as is present along the WGSC at >95.5°W and 2) a depleted component falling within the Eastern Galápagos Domain that could possibly reflect a depleted plume component can explain the range in <30 km (<1.0 Ma) MOR generated ocean crust. The >30 km samples indicate the presence of a third type of enriched component that feed the ridge axis between 1.0-1.6 Ma ago, characterized by an EMII-like isotopic composition, unlike anything found in the Galápagos Archipelago thus far.

Therefore we believe it may be a batch of enriched mantle entrained by the rising Galápagos plume. In conclusion, the differences in the composition of the on-ridge to 50 km (1.6 Ma) off-axis samples cannot simply be explained by mixing present-day Galápagos components with different amounts of upper MORB source mantle but also requires subtle differences in both the spatial and temporal composition of the northern portion of the zoned Galápagos plume and possibly entrainment of enriched EMII-like mantle by the plume.

Acknowledgements

References

Beier, C., Haase, K. M. & Turner, S. P., 2012. Conditions of melting beneath the Azores. *Lithos*, **144–145**, 1–11.

Beier, C., Vanderkluysen, L., Regelous, M., Mahoney, J. J. & Garbe-Schönberg, D., 2011. Lithospheric control on geochemical composition along the Louisville Seamount Chain. *Geochemistry, Geophysics, Geosystems*, **12**, Q0AM01.

Bourdon, B., Turner, S. P. & Ribe, N. M., 2005. Partial melting and upwelling rates beneath the Azores from a U-series isotope perspective. *Earth and Planetary Science Letters*, **239**, 42–56.

Canales, J. P., Dañobeitia, J. J., Detrick, R. S., Hooft, E. E. E., Bartolomé, R. & Naar, D. F., 1997. Variations in axial morphology along the Galápagos spreading center and the influence of the Galápagos hotspot. *Journal of Geophysical Research: Solid Earth*, **102**, 27341–27354.

Canales, J. P., Ito, G., Detrick, R. S. & Sinton, J., 2002. Crustal thickness along the western Galápagos Spreading Center and the compensation of the Galápagos hotspot swell. *Earth and Planetary Science Letters*, **203**, 311–327.

Christie, D. M., Werner, R., Hauff, F., Hoernle, K. & Hanan, B. B., 2005. Morphological and geochemical variations along the eastern Galápagos Spreading Center. *Geochemistry, Geophysics, Geosystems*, **6**, Q01006.

Colman, A., Sinton, J. M., White, S. M., McClinton, J. T., Bowles, J. A., Rubin, K. H., Behn, M. D., Cushman, B., Eason, D. E., Gregg, T. K. P., Grönvold, K., Hidalgo, S., Howell, J., Neill, O. & Russo, C., 2012. Effects of variable magma supply on mid-ocean ridge eruptions: Constraints from mapped lava flow fields along the Galápagos Spreading Center. *Geochemistry, Geophysics, Geosystems*, **13**, Q08014.

Cushman, B., Sinton, J., Ito, G. & Eaby Dixon, J., 2004. Glass compositions, plume-ridge interaction, and hydrous melting along the Galápagos Spreading Center, 90.5° W to 98° W. *Geochemistry, Geophysics, Geosystems*, **5**, Q08E17.

Detrick, R. S., Sinton, J. M., Ito, G., Canales, J. P., Behn, M., Blacic, T., Cushman, B., Dixon, J. E., Graham, D. W. & Mahoney, J. J., 2002. Correlated geophysical, geochemical, and volcanological manifestations of plume-ridge interaction along the Galápagos Spreading Center. *Geochemistry, Geophysics, Geosystems*, **3**, 8501.

Frank, M., Reynolds, B. C. & Keith O'Nions, R., 1999. Nd and Pb isotopes in Atlantic and Pacific water masses before and after closure of the Panama gateway. *Geology*, **27**, 1147–1150.

Garbe-Schönberg, C.-D., 1993. Simultaneous determination of thirty-seven trace elements in twenty-eight international rock standards by ICP-MS. *Geostandards Newsletter*, **17**, 81–97.

Gazel, E., Carr, M. J., Hoernle, K., Feigenson, M. D., Szymanski, D., Hauff, F. & van den Bogaard, P., 2009. Galápagos-OIB signature in southern Central America: Mantle refertilization by arc-hot spot interaction. *Geochemistry, Geophysics, Geosystems*, **10**, Q02S11.

Geist, D. J., White, W. M. & McBirney, A. R., 1988. Plume-asthenosphere mixing beneath the Galápagos archipelago. *Nature*, **333**, 657–660.

Geldmacher, J., Hanan, B. B., Blichert-Toft, J., Harpp, K., Hoernle, K., Hauff, F., Werner, R. & Kerr, A. C., 2003. Hafnium isotopic variations in volcanic rocks from the Caribbean Large Igneous Province and Galápagos hot spot tracks. *Geochem. Geophys. Geosyst.*, **4**, 1062.

Geldmacher, J., Höfig, T., Hauff, F., Hoernle, K., Garbe-Schönberg, D. & Wilson, D., 2013. Influence of the Galápagos hotspot on the East Pacific Rise during Miocene superfast spreading. *Geology*, **41**, 183–186.

Gente, P., Dyment, J., Maia, M. & Goslin, J., 2003. Interaction between the Mid-Atlantic Ridge and the Azores hot spot during the last 85 Myr: Emplacement and rifting of the hot spot-derived plateaus. *Geochemistry, Geophysics, Geosystems*, **4**, 8514.

Gibson, S. A., Geist, D. J. & Richards, M. A., 2015. Mantle plume capture, anchoring, and outflow during Galápagos plume-ridge interaction. *Geochemistry, Geophysics, Geosystems*, **16**, 1634–1655.

Graham, D. W., Christie, D. M., Harpp, K. S. & Lupton, J. E., 1993. Mantle Plume Helium in Submarine Basalts from the Galápagos Platform. *Science*, **262**, 2023–2026.

Hall, P. S. & Kincaid, C., 2003. Melting, dehydration, and the dynamics of off-axis plume-ridge interaction. *Geochemistry, Geophysics, Geosystems*, **4**, 8510.

Handschumacher, D. W., 1976. Post-Eocene Plate Tectonics of the Eastern Pacific. In: *The Geophysics of the Pacific Ocean Basin and Its Margin*, American Geophysical Union. 177–202.

Harpp, K. & Geist, D., 2002. Wolf-Darwin lineament and plume-ridge interaction in northern Galápagos. *Geochemistry, Geophysics, Geosystems*, **3**, 8504.

Harpp, K. S., Fornari, D. J., Geist, D. J. & Kurz, M. D., 2003. Genovesa Submarine Ridge: A manifestation of plume-ridge interaction in the northern Galápagos Islands. *Geochemistry, Geophysics, Geosystems*, **4**, 8511.

Harpp, K. S., Wanless, V. D., Otto, R. H., Hoernle, K. & Werner, R., 2005. The Cocos and Carnegie Aseismic Ridges: A Trace Element Record of Long-term Plume-Spreading Center Interaction. *Journal of Petrology*, **46**, 109–133.

Harpp, K. S. & White, W. M., 2001. Tracing a mantle plume: Isotopic and trace element variations of Galápagos seamounts. *Geochemistry, Geophysics, Geosystems*, **2**, 1042.

Herbrich, A., Hoernle, K., Werner, R., Hauff, F., Bogaard, P. v. d. & Garbe-Schönberg, D., 2015. Cocos Plate Seamounts offshore NW Costa Rica and SW Nicaragua: Implications for large-scale distribution of Galápagos plume material in the upper mantle. *Lithos*, **212–215**, 214–230.

Herzberg, C. & Asimow, P. D., 2008. Petrology of some oceanic island basalts: PRIMELT2.XLS software for primary magma calculation. *Geochemistry, Geophysics, Geosystems*, **9**, Q09001.

Hey, R. & Vogt, P., 1977. Spreading center jumps and sub-axial asthenosphere flow near the Galápagos hotspot. *Tectonophysics*, **37**, 41–52.

Hoernle, K., Abt, D. L., Fischer, K. M., Nichols, H., Hauff, F., Abers, G. A., van den Bogaard, P., Heydolph, K., Alvarado, G., Protti, M. & Strauch, W., 2008. Arc-parallel flow in the mantle wedge beneath Costa Rica and Nicaragua. *Nature*, **451**, 1094–1097.

Hoernle, K., Hauff, F., Kokfelt, T. F., Haase, K., Garbe-Schönberg, D. & Werner, R., 2011. On- and off-axis chemical heterogeneities along the South Atlantic Mid-Ocean-Ridge (5-11° S): Shallow or deep recycling of ocean crust and/or intraplate volcanism? *Earth and Planetary Science Letters*, **306**, 86–97.

Hoernle, K., van den Bogaard, P., Werner, R., Lissinna, B., Hauff, F., Alvarado, G. & Garbe-Schönberg, D., 2002. Missing history (16–71 Ma) of the Galápagos hotspot: Implications for the tectonic and biological evolution of the Americas. *Geology*, **30**, 795–798.

Hoernle, K., Werner, R., Morgan, J. P., Garbe-Schönberg, D., Bryce, J. & Mrazek, J., 2000. Existence of complex spatial zonation in the Galápagos plume. *Geology*, **28**, 435–438.

Höfig, T. W., Geldmacher, J., Hoernle, K., Hauff, F., Duggen, S. & Garbe-Schönberg, D., 2014. From the lavas to the gabbros: 1.25 km of geochemical characterization of upper oceanic crust at ODP/IODP Site 1256, eastern equatorial Pacific. *Lithos*, **210–211**, 289–312.

Hooft, E. E. E., Toomey, D. R. & Solomon, S. C., 2003. Anomalously thin transition zone beneath the Galápagos hotspot. *Earth and Planetary Science Letters*, **216**, 55–64.

Ingle, S., Ito, G., Mahoney, J. J., Chazey, I., William, Sinton, J., Rotella, M. & Christie, D. M., 2010. Mechanisms of geochemical and geophysical variations along the western Galápagos Spreading Center. *Geochemistry, Geophysics, Geosystems*, **11**, Q04003.

Ito, G. & Lin, J., 1995. Oceanic spreading center-hotspot interactions: Constraints from along-isochron bathymetric and gravity anomalies. *Geology*, **23**, 657–660.

Kokfelt, T. F., Lundstrom, C., Hoernle, K., Hauff, F. & Werner, R., 2005. Plume-ridge interaction studied at the Galápagos spreading center: Evidence from ^{226}Ra-^{230}Th-^{238}U and ^{231}Pa-^{235}U isotopic disequilibria. *Earth and Planetary Science Letters*, **234**, 165–187.

Kurz, M. D. & Geist, D., 1999. Dynamics of the Galapagos hotspot from helium isotope geochemistry. *Geochimica et Cosmochimica Acta*, **63**, 4139–4156.

Le Maitre, R. W., Bateman, P., Dudek, A., Keller, J., Lameyre, J., Le Bas, M. J., Sabine, P. A., Schmid, R., Sorensen, H., Streckeisen, A., Woolley, A. R. & Zanettin, B., 1989. *A classification of igneous rocks and glossary of terms, recommendations of the International Union of Geological Sciences, Subcommission on the Systematics of Igneous Rocks*. Blackwell Scientific. Oxford. GB.

MacDonald, G. A. & Katsura, T., 1964. Chemical Composition of Hawaiian Lavas1. *Journal of Petrology*, **5**, 82–133.

McClinton, J. T. & White, S. M., 2015. Emplacement of submarine lava flow fields: A geomorphological model from the Niños eruption at the Galápagos Spreading Center. *Geochemistry, Geophysics, Geosystems*, **16**, 899–911.

McClinton, T., White, S. M., Colman, A. & Sinton, J. M., 2013. Reconstructing lava flow emplacement processes at the hot spot-affected Galápagos Spreading Center, 95° W and 92° W. *Geochemistry, Geophysics, Geosystems*, **14**, 2731–2756.

Mittelstaedt, E., Soule, S., Harpp, K., Fornari, D., McKee, C., Tivey, M., Geist, D., Kurz, M. D., Sinton, C. & Mello, C., 2012. Multiple expressions of plume-ridge interaction in the Galápagos: Volcanic lineaments and ridge jumps. *Geochemistry, Geophysics, Geosystems*, **13**, Q05018.

Montelli, R., Nolet, G., Dahlen, F. A. & Masters, G., 2006. A catalogue of deep mantle plumes: New results from finite-frequency tomography. *Geochemistry, Geophysics, Geosystems*, **7**, Q11007.

Montelli, R., Nolet, G., Dahlen, F. A., Masters, G., Engdahl, E. R. & Hung, S.-H., 2004. Finite-Frequency Tomography Reveals a Variety of Plumes in the Mantle. *Science*, **303**, 338–343.

Pearce, J. A., 2008. Geochemical fingerprinting of oceanic basalts with applications to ophiolite classification and the search for Archean oceanic crust. *Lithos*, **100**, 14–48.

Ribe, N. M. & Delattre, W. L., 1998. The dynamics of plume–ridge interaction—III. The effects of ridge migration. *Geophysical Journal International*, **133**, 511–518.

Rohde, J., Hoernle, K., Hauff, F., Werner, R., O'Connor, J., Class, C., Garbe-Schönberg, D. & Jokat, W., 2013. 70 Ma chemical zonation of the Tristan-Gough hotspot track. *Geology*, **41**, 335–338.

Schilling, J., Kingsley, R. & Devine, J., 1982. Galápagos Hot Spot-Spreading Center System 1. Spatial Petrological and Geochemical Variations (83° W-111° W). *Journal of Geophysical Research*, **87**, 18.

Schilling, J. G., 1975. Azores mantle blob: Rare-earth evidence. *Earth and Planetary Science Letters*, **25**, 103–115.

Schilling, J.-G., 1991. Fluxes and excess temperatures of mantle plumes inferred from their interaction with migrating mid-ocean ridges. *Nature*, **352**, 397–403.

Schilling, J.-G., Fontignie, D., Blichert-Toft, J., Kingsley, R. & Tomza, U., 2003. Pb-Hf-Nd-Sr isotope variations along the Galápagos Spreading Center (101°-83° W): Constraints on the dispersal of the Galápagos mantle plume. *Geochemistry, Geophysics, Geosystems*, **4**, 8512.

Schilling, J. G., Thompson, G., Kingsley, R. & Humphris, S., 1985. Hotspot[mdash]migrating ridge interaction in the South Atlantic. *Nature*, **313**, 187–191.

Schilling, J. G., Zajac, M., Evans, R., Johnston, T., White, W., Devine, J. D. & Kingsley, R., 1983. Petrologic and geochemical variations along the Mid-Atlantic Ridge from 29° N to 73° N. *American Journal of Science*, **283**, 510–586.

Shorttle, O., Maclennan, J. & Jones, S. M., 2010. Control of the symmetry of plume-ridge interaction by spreading ridge geometry. *Geochemistry, Geophysics, Geosystems*, **11**, Q0AC05.

Sinton, C. W., Christie, D. M. & Duncan, R. A., 1996. Geochronology of Galápagos seamounts. *Journal of Geophysical Research*, **101**, 13689–13700.

Sinton, J., Detrick, R., Canales, J. P., Ito, G. & Behn, M., 2003. Morphology and segmentation of the western Galápagos Spreading Center, 90.5°-98° W: Plume-ridge interaction at an intermediate spreading ridge. *Geochemistry, Geophysics, Geosystems*, **4**, 8515.

Vidito, C., Herzberg, C., Gazel, E., Geist, D. & Harpp, K., 2013. Lithological structure of the Galápagos Plume. *Geochemistry, Geophysics, Geosystems*, **14**, 4214–4240.

Villagómez, D. R., Toomey, D. R., Geist, D. J., Hooft, E. E. E. & Solomon, S. C., 2014. Mantle flow and multistage melting beneath the Galápagos hotspot revealed by seismic imaging. *Nature Geoscience*, **advance online publication**.

Werner, R., Hoernle, K., Barckhausen, U. & Hauff, F., 2003. Geodynamic evolution of the Galápagos hot spot system (Central East Pacific) over the past 20 m.y.: Constraints from morphology, geochemistry, and magnetic anomalies. *Geochemistry, Geophysics, Geosystems*, **4**, 1108.

White, W., Tapia, M. M. & Schilling, J.-G., 1979. The petrology and geochemistry of the Azores Islands. *Contributions to Mineralogy and Petrology*, **69**, 201–213.

White, W. M. & Hofmann, A. W., 1978. Geochemistry of the Galápagos Islands: implications for mantle dynamics and evolution. *Year Book Carnegie Inst. Washington*, **77**, 596–606.

White, W. M., McBirney, A. R. & Duncan, R. A., 1993. Petrology and Geochemistry of the Galápagos Islands: Portrait of a Pathological Mantle Plume. *Journal of Geophysical Research*, **98**, 19533–19563.

Wilson, D. S. & Hey, R. N., 1995. History of rift propagation and magnetization intensity for the Cocos-Nazca spreading center. *Journal of Geophysical Research*, **100**, 10041–10056.

Yu, D., Fontignie, D. & Schilling, J.-G., 1997. Mantle plume-ridge interactions in the Central North Atlantic: A Nd isotope study of Mid-Atlantic Ridge basalts from 30° N to 50° N. *Earth and Planetary Science Letters*, **146**, 259–272.

Chapter 4

Plume-Ridge Interaction: Pulsing influence of Galápagos plume material along the Eastern Galápagos Spreading Center?

Antje Herbrich1[1*], Kaj Hoernle[1,2], Folkmar Hauff[1], Reinhard Werner[1], Dieter Garbe-Schönberg[2], Scott White[3]

[1] GEOMAR Helmholtz Centre for Ocean Research Kiel, Wischhofstraße 1-3, D-24148 Kiel, Germany

[2] Institute of Geosciences, University of Kiel, Ludewig-Meyn-Strasse 10, D-24118 Kiel, Germany

[3] Department of Earth and Ocean Sciences, University of South Carolina, Columbia, South Carolina, USA

Abstract

Ocean crust samples from three profiles perpendicular to the Eastern Galápagos Spreading Center (EGSC), one single on-axis seamount close to the 87°W overlapping spreading center and the area east of the 91°W Transform Fault (∼90°50'W) were sampled during the R/V Sonne 208 cruise. While the geochemistry of samples near the ridge axis around 90°50'W permit us to define the

enriched component being injected into the EGSC more closely, the samples from the profiles that extend further off-axis provide new insights into the nature of the plume-ridge interaction for the past 3.6 Ma.

Most samples have tholeiitic compositions, except those from a split formerly on-axis seamount and rare crustal samples, which have transitional compositions. Samples from individual profiles fall along the same mixing arrays on incompatible element and isotope ratio plots, indicating that the same mantle sources are involved. The well-defined trends on isotope and incompatible element ratio plots imply two component mixing between the enriched Central Galápagos component and a depleted component represented by Genovesa Island in the Eastern Galápagos Domain. Despite large variations in isotope and incompatible element ratios, no systematic temporal variations in the geochemistry are observed along individual profiles. Morphological anomalies, such as the split seamount and off-axis lava plateaus/seamounts, represent geochemical anomalies, with both more enriched and more depleted compositions than surrounding ocean crust. The fluctuations in geochemistry in off-axis samples show that Galápagos plume material doesn't simply reach the ridge axis in a single location and then flows eastward along the EGSC, but at different places along the ridge at different times, such that the fairly systematic present-day variation in geochemistry along the ridge axis can be found at single locations over time, even short time intervals.

4.1   Introduction

Mid-ocean ridges (MOR) are the longest mountain ranges on earth where the tectonic plates spread apart as new ocean crust is formed. With more than 56,000 km length, they are responsible for more than 70% of the global volcanism, building constantly new ocean crust. At least 18 of the proposed 30 to 50 mantle plumes (Ito & van Keken, 2007) interact with mid-ocean ridges (e.g., Christie *et al.*, 2005; Detrick *et al.*, 2002; Ito *et al.*, 2003; Sinton *et al.*, 2003), over distances of up to 1,000 km (Schilling *et al.*, 1976, 1982; Vogt, 1976). The Galápagos mantle plume and the adjacent Cocos-Nazca or Galápagos Spreading Center (GSC) represent a classic example of plume-ridge interaction.

The Galápagos Archipelago is thought to be the surface expression of the long-lived Galápagos mantle plume, originating from the earth's lower mantle (Duncan & Hargraves, 1984; Graham *et al.*, 1993; Montelli *et al.*, 2006; Morgan, 1971). Based on the trace element composition and isotopic geochemistry of erupted lavas from the Galápagos Archipelago, an east-facing, horseshoe-shaped geochemically enriched region encloses depleted material, interpreted to reflect entrained upper mantle (Geist *et al.*, 1988; Harpp & White, 2001; White & Hofmann, 1978; White *et al.*, 1993) or a plume component that is progressively depleted by melt extraction during flow to the spreading center (Hoernle *et al.*, 2000). The enriched "horseshoe" can be subdivided into

three different enriched sub-domains – Northern, Central and Southern Galápagos Domain (after Geldmacher *et al.*, 2003; Hoernle *et al.*, 2000; Werner *et al.*, 2003) or Floreana, Wolf-Darwin, and Plume (after Harpp & White, 2001).

The Galápagos Spreading Center separates the Nazca Plate in the south from the Cocos Plate in the north. It presumably formed when a fracture zone passed over the Galápagos hotspot resulting in the brake up of the Farallon Plate about 23 Ma ago (Lonsdale, 2005; Lonsdale & Klitgord, 1978), forming the GSC.

Morphologically, this interaction is reflected in the formation of two aseismic hotspot tracks – the Cocos Ridge with adjacent seamount province on the northeast-moving Cocos Plate and the Carnegie, Malpelo and Coiba Ridges on the eastward-moving Nazca Plate (Fig. 4.1; e.g., Canales *et al.*, 1997; Handschumacher, 1976; Hey, 1977; Holden & Dietz, 1972; Werner *et al.*, 2003; Wilson & Hey, 1995). The geochemical composition of the hotspot track lavas correlates with the geochemical domains of the Galápagos Archipelago in the same geographical pattern. The influence of the Galápagos plume on the GSC is reflected by geochemical and morphological variations along the present ridge axis. From West ($\sim$96°W) to East ($\sim$85°W) the GSC ridge morphology changes from an axial valley-and-ridge-type morphology to an axial high terrain around the 91°W Transform Fault (TF) back to valley-and-ridge-type characteristics (e.g., Christie & Sinton, 1981; Christie *et al.*, 2005; Schilling *et al.*, 1982; Sinton *et al.*, 2003). Between 92°-90°W, where the ridge axis reaches it's shallowest depth, geochemical tracers like Pb and Sr isotopic ratios, K/Ti, La/Sm, are increased, while others, e.g., ^{143}Nd/^{144}Nd and ^{176}Hf/^{177}Hf are decreased (Schilling *et al.*, 2003, 1982; Verma & Schilling, 1982; Verma *et al.*, 1983). This is interpreted as reflecting an increased thermal and material contribution from the Galápagos mantle plume (Canales *et al.*, 1997; Ito & Lin, 1995; Schilling, 1991) in this area.

The long-term geochemical zonation of the Galápagos plume serves as a good tool for investigating the plume-ridge interaction and related material transport from the plume to the ridge. This has been intensely studied in the past (e.g., Bowles *et al.*, 2014; Christie *et al.*, 2005; Detrick *et al.*, 2002; Geldmacher *et al.*, 2013; Hoernle *et al.*, 2000; Ingle *et al.*, 2010; Kokfelt *et al.*, 2005; Schilling *et al.*, 2003, 1982; Sinton *et al.*, 2003; Villagómez *et al.*, 2014, 2007, 2011), but the nature of this interaction is still under debate. The systematic decrease of the Galápagos plume signal observed in GSC ridge axis lavas with increasing distance from the plume is attributed to dilution through mixing with depleted upper mantle, but the mechanisms how the plume material reaches the GSC are a matter of ongoing debate.

Here we present major- and trace-element compositions and Sr-Nd-Pb isotopic ratios of volcanic glass and whole rock samples in order to determine how the Galápagos plume-EGSC interaction varies at specific locations along the ridge axis over time. We have sampled the ridge axis E of the 91°W TF (Study Area 2; Table 4.1), three profiles (profile 3-5; Table 4.1) perpendicular to the EGSC and one single on-axis seamount to constrain the interaction between the
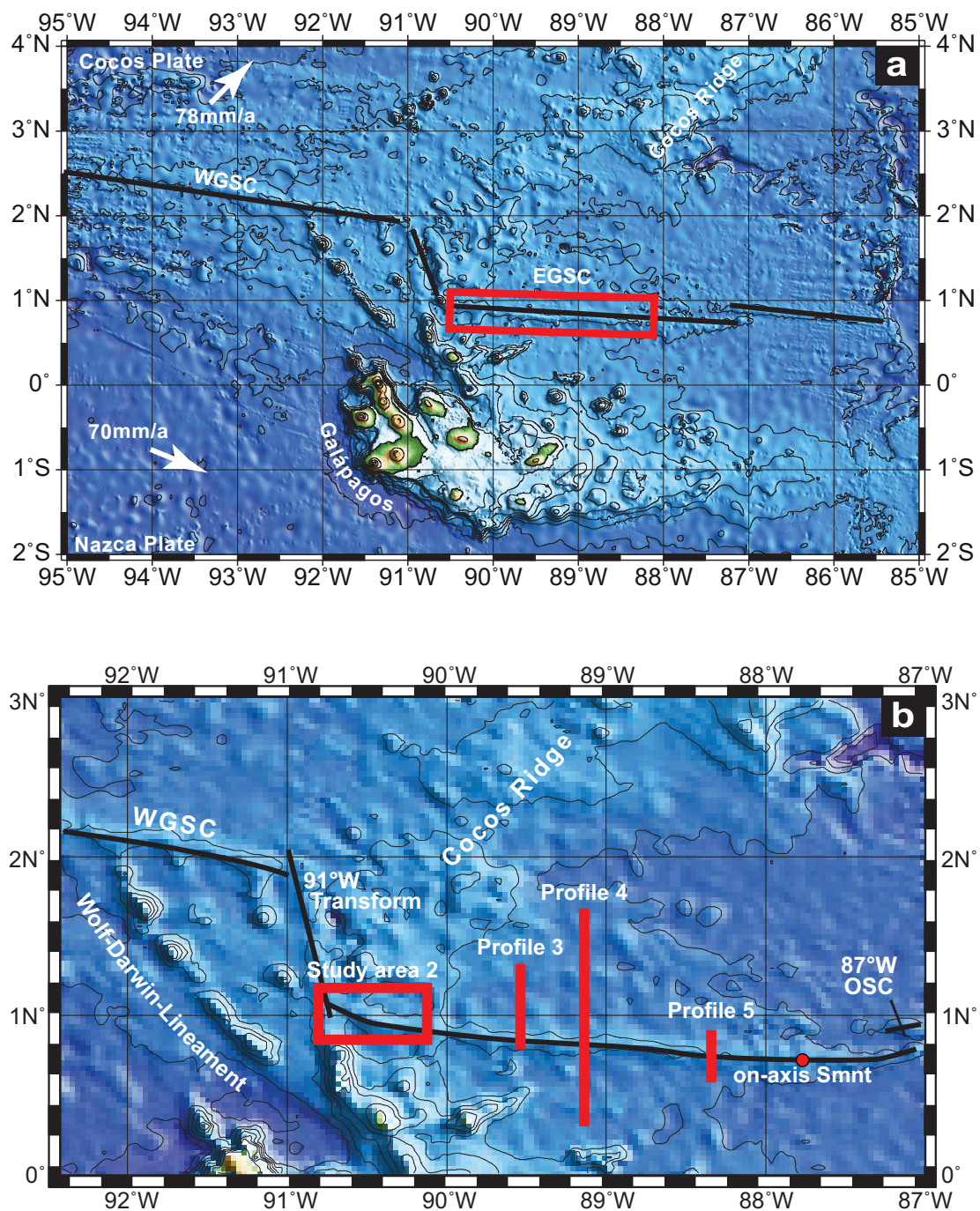
Figure 4.1: Bathymetric map of the Eastern Pacific area including all major morphological features (EPR – Eastern Pacific Rise, WGSC Western Galápagos Spreading Center, FR – Fischer Ridge, RSB – Rough-Smooth-Boundary, CR – Coiba Ridge, MR – Mapelo Ridge, Catr. Ridge – Carnegie Ridge) data are from The GEBCO_08 Grid, version 20091120, http://www.gebco.net. During cruise SO208 Leg 2 the area east of the 91°W Transform Fault, three off-axis profiles and one single on-axis seamount (red box) were sampled by dredging north of the EGSC.

Galápagos plume and the GSC. Specifically, we want to contribute to the debate whether the decreasing plume signal reflects a) radial outflow of plume material reaching the spreading center at various locations, b) injection of plume material at one location and subsequent dilution by flowing beneath the ridge axis (e.g., Ingle *et al.*, 2010; Kokfelt *et al.*, 2005; Schilling *et al.*, 2003) or c) variable input of plume material at different locations along the ridge axis, not necessarily correlated with radial distance from the plume. The increasing distance from the presumed input of Galápagos plume material at the GSC ridge axis in combination with the temporal geochemical evolution along each individual profile provides powerful constraints on the extent and nature of plume-ridge interaction over time.

4.2   Regional Setting

The position of the profiles (Table 4.1) is based on observed geochemical and/or morphological anomalies along the EGSC identified on previous cruises (SO158 MEGAPRINT) and studies (Christie *et al.*, 2005, Hoernle et al., in prep.). The profiles are related to the segmentation of the GSC ridge axis recognized by Christie *et al.* (2005), where detailed descriptions of the morphological and major and trace element geochemical variations along the ridge axis can be found.

Data from Profile 1 on the western GSC is presented in Herbrich *et al.* (2015). Study Area 2 between 90°12' and 90°43'W is located in the transition zone between the EGSC and the 91°W TF and correlates to Segment VI and VII (Christie *et al.*, 2005). Strictly speaking this is not a profile, since sampling mainly occurred along the ridge axis, and only occasionally up to ∼15 km to the N of the axis. This area forms the shallowest part of the ridge axis and is closest to the active volcanic islands of the Galápagos Archipelago. Its main features are two overlapping volcanic shields, each with a caldera-like structure (Fig. 4.2a) on top. The off-axis area is characterized by ridge-valley-like structures that become more prominent with increasing distance from the ridge axis. Worth noting is the presence of some seamounts, some of them split in half, indicating that they formed on the ridge axis and were split due to ridge spreading (e.g., seamount DR77).

Profile 3 was sampled up to 50 km to the North of the Axial Ridge Domain corresponding to Segment V of Christie *et al.* (2005) located between 89°26' and 89°36'W (Fig. 4.2b, left profile). This part of the GSC ridge axis is characterized by an axial high with a continuous narrow crest (Christie *et al.*, 2005). To both sides, in equal distance from the ridge axis, two half of a seamount (split seamount; SO158 DR28 and DR87) can be observed. The southern half was sampled during SO 158 and is described in Christie *et al.* (2005) and Hoernle et al. (in prep.). Further to the north, broader elevated ridges alternate with narrow valley-like structures with depths of up to 2,400 m below sea level (b.s.l.).

Profile 4 and 5 are two profiles where samples were taken both south and north of the ridge axis. The ridge axis of Profile 4 (Fig. 4.2b right profile; 89°-89°15'W) correlates to the transitional Segment IV after Christie *et al.* (2005). This area is characterized by an axial high morphology with a narrow axial summit trough that peters out into a narrow crest. Between 89°05' and 89°10'W the axial ridge and summit trough are offset by a left-lateral en echelon fault zone, presumably indicating the formation of an incipient overlapping spreading center. Towards the north and south the same morphological patterns exist, consisting of an alternation of valley and ridge like structures. This profile, however, shows signs of off-axis volcanism, represented by a cluster of seamounts, from which we were able to sample a large, irregular shaped volcanic plateau (DR110) to the North and a single seamount to the South (DR115).

Table 4.1: Sample locations and distance from GSC ridge axis in km. Sample locations with negative distance values are located to the south of the GSC ridge axis.

Sample location	Latitude (°N)	Longitude (°W)	distance from GSC in km
Study Area 2			
SO208 DR75	0.99	90.61	1.45
SO208 DR76	1.05	90.70	1.45
SO208 DR77	1.09	90.70	3.27
SO208 DR78	1.03	90.64	1.09
SO208 DR79	0.95	90.55	1.82
SO208 DR80	0.92	90.40	0.18
SO208 DR81	0.93	90.41	0.18
SO208 DR82	1.04	90.22	15.64
SO208 DR83	1.02	90.20	13.45
SO208 DR84	0.98	90.29	7.64
Profile 3			
SO208 DR87	0.85	89.53	4.39
SO208 DR88	0.90	89.58	9.02
SO208 DR89	0.89	89.48	8.54
SO208 DR90	0.90	89.46	9.27
SO208 DR91	0.92	89.49	12.44
SO208 DR92	0.96	89.48	17.07
SO208 DR96	1.06	89.51	27.32
SO208 DR98	1.26	89.50	49.27
Profile 4			
SO208 DR99	0.79	89.24	0.89
SO208 DR101	0.81	89.15	0.59
SO208 DR105	1.31	89.15	57.48
SO208 DR106	1.26	89.22	50.67
SO208 DR107	1.08	89.10	30.52

. . . continued

Sample location	Latitude (°N)	Longitude (°W)	distance from GSC in km
SO208 DR108	1.01	89.12	22.81
SO208 DR110	0.91	89.11	13.33
SO208 DR111	0.83	89.12	2.67
SO208 DR112	0.76	89.14	-5.04
SO208 DR114	0.37	89.13	-47.71
SO208 DR115	0.41	89.13	-43.43
SO208 DR117	0.61	89.03	-20.00
SO208 DR118	0.65	89.02	-16.00
Profile 5			
SO208 DR119	0.66	88.40	-10.00
SO208 DR120	0.84	88.36	11.56
SO208 DR121	0.73	88.23	0.00
Axial Smnt			
SO208 DR122	0.73	87.76	0.00

Profile 5 (Fig. 4.2c; 88°14'-88°24'W) comprises one site to the south, one to the north and one to the east of a lava plateau (88°20'W), filling in the valley and ridge type morphology of the Segment III region (Christie *et al.*, 2005). One single on-axis seamount located at the ridge axis at 87°45'W is the easternmost sampling location. It is an oval-shaped seamount about 200 m high in close proximity to the 87°W overlapping spreading center.

(a) Detailed bathymetric map of the EGSC off-axis study area 2. The area east of the 91° W Transform Fault is thought to be the loci of plume intput into the EGSC. Two caldera-like structures can be observed on the two volcanic shields.

(b) Detailed bathymetric map of the EGSC off-axis Profile 3 (left) and 4 (right). Profile 3 (left Profile) extends up to 50 km to the north of the ridge axis. Note the split seamount close to the ridge axis (DR87 this study, DR28 from Christie *et al.* (2005) and Hoernle et al., in prep.) Profile 4 is the longest Profile and extends up to 50 km to the south and as far as 60 km to the north of the EGSC ridge axis. Note off-axis seamount DR110 to the north and DR115 to the south. Red dashed lines mark age jumps and black solid line marks ridge axis. Arrows point towards young ages.

(c) Detailed bathymetric map of the EGSC off-axis Profile 5; Profile 5 is the shortest profile. On the ridge axis a plateau overprints the ridge-valley morphology.

Figure 4.2: Detailed bathymetric map of the EGSC off-axis profiles based on SIMRAD120 multibeam data with sample locations (white circles). Map contains data recorded on R/V SONNE cruise SO208 and on various U.S. American cruises. Larger images can be found in the appendinx Fig. C.1-Fig. C.3

4.3 Sample treatment and analytical methods

The samples from this study were obtained by dredging during the scientific cruise SO208 with the German Research vessel SONNE in July/August 2010. The majority of the sampled material comprises fresh volcanic glass, which was chipped off on board of the ship and further processed at GEOMAR (Kiel, Germany). Both, volcanic glass and whole rock samples were carefully handpicked under a binocular to avoid altered material and subsequently analyzed for their major and trace element composition and Sr-Nd-Pb isotope ratios. Details about sample treatment and analytical methods can be found in Herbrich *et al.* (2015).

Major and trace element composition of volcanic glass was determined on mounted glass chips at a JEOL JXA-8200 Electron Microprobe (EPMA) at GEOMAR and by laser ablation inductively coupled plasma mass spectrometry ((LA)-ICP-MS) at the Institute of Geoscience, University of Kiel, respectively. Five spots of each sample were measured and averaged. Multiple sample analyses of trace element concentrations were treated as individual samples and compare between different days in 5%rel (range 1-8%rel), except for Mo and Cs (12-16%rel). Major- and trace element concentrations of whole rocks were determined by X-Ray Fluorescence Analysis (XRF) at the Institute of Mineralogy and Petrography at the University of Hamburg and by solution ICP-MS at the Institute of Geoscience, University of Kiel. In order to ensure comparability between different methods and different material, two glass samples (DR99-1, DR107-1) where analysed by XRF and ICP-MS. Elements compare below 5% for SiO_2, Al_2O_3, FeO^T, CaO, TiO_2, P_2O_5, MgO and Na_2O and below 9 % for K_2O and MnO. Trace element data are provided in the appendix Table C.2.

Radiogenic isotope ratios of Sr, Nd and Pb double spike (DS) of glasses and whole rocks were analyzed by Thermal ionization mass spectrometry (TIMS) at GEOMAR. Details regarding a) sample digestion, leaching, accuracy and precision can be found in Herbrich *et al.* (2015), b) element separation is described in Hoernle *et al.* (2008) and c) information about correcting by the $^{207}Pb/^{204}Pb$ double spike technique are given in Hoernle *et al.* (2011). All replicate analyses can be reproduced within the external error of NBS987 for Sr, of La Jolla for Nd and of NBS981 for Pb. Sr, Nd Pb isotope ratios are provided in the appendix Table C.4

4.4 Results

Besides pillow basalts and pillow- and sheet lava fragments, with the majority having glass rims of up to several cm thick, also hyaloclastites with fresh pillow fragments were recovered. Sample quality ranges from fresh, for most of the samples, to moderately altered. Signs of alteration include the formation of palagonite and iron oxides, alteration halos and filling and lining of vesicles with secondary minerals. Some samples were covered with thin Mn-coatings of up 5 mm thickness.

The majority of the sampled material consists of plagioclase- and clinopyroxene-bearing lavas with olivine as a minor phase in some samples. There are, however, few samples with olivine as one of the main phases. Iron-titanium oxides (e.g., ilmenite, magnetite) are present in almost all samples.

4.4.1 Major elements

After the classification of Le Maitre *et al.* (1989, Fig. 4.3; Table C.1) all samples are of tholeiitic composition, except split seamount samples of Profile 3 and some samples of Study Area 2, which are of transitional tholeiitic composition. The MgO contents of the individual profiles range from 4.15-9.22 wt.% with Mg-numbers (Mg#=mol(Mg/(Mg+Fe^{2+}))) between 0.31 and 0.64, indicating the presence of some fairly primitive basaltic compositions. Overall, on binary diagrams with MgO on the x-axis (Fig. 4.4) the samples form reasonably well-defined trends, indicating shallow level magma differentiation for almost all EGSC samples. For all profiles, SiO_2, FeO^T, TiO_2, P_2O_5, Na_2O and K_2O increase while CaO and Al_2O_3 decrease with decreasing MgO, following the typical differentiation trend for tholeiitic melts. This observation indicates fractionation of olivine + plagioclase + clinopyroxene , which is in agreement with the observed mineral assemblage in the samples (Fig. 4.4b). Fractionation of plagioclase seems to be more prominent than clinopyroxene fractionation as indicated by the broad positive correlation of MgO with Al_2O_3. The off-axis seamounts of Study Area 2, Profile 3 and Profile 4 are shifted to higher values of Al_2O_3, TiO_2, P_2O_5 and K_2O. The variations in FeO^T (Fig. 4.4c) for whole rock samples of Profile 3 in combination with a very tight array for TiO_2 (Fig. 4.4e) indicates the fractionation of a low-titanium Fe-oxide (e.g., magnetite).
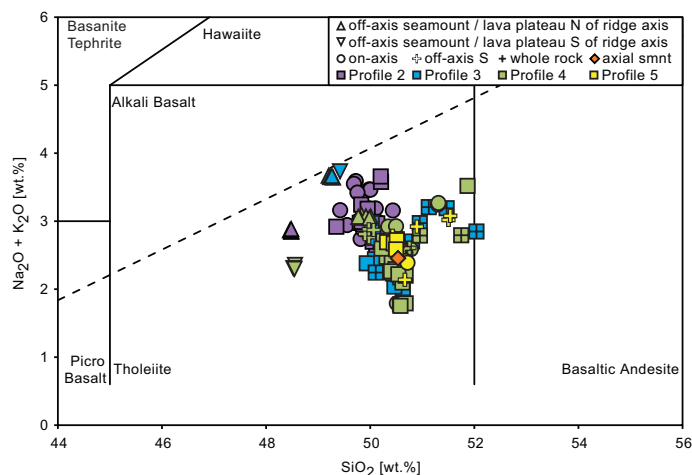
Figure 4.3: Silica versus total alkali-diagram (Le Maitre *et al.*, 1989) of the EGSC profile samples. Subdivision of volcanic rocks into alkaline and tholeiitic is after MacDonald & Katsura (1964). According to their major element composition, the profile samples are Tholeiites, except some samples of Profile 2 and the split seamount from Profile 3 with transitional composition. Symbols with a cross (+) denote that whole-rock material was analyzed all other analyses were made on fresh handpicked glass.

While the majority of the samples of Profile 3 to 5 show similar relationships in all diagrams, except the seamounts and some crustal samples, Study Area 2 samples are shifted to higher K_2O values as well as six samples of Profile 3 and two samples of Profile 5. For the whole rock samples, however, the higher K_2O might indicate seawater alteration.

All Profiles overlap the EGSC on-axis field (Christie *et al.*, 2005) except for P_2O_5 where only Study Area 2 and some samples from Profile 3 lie within the on-axis trend. In TiO_2, P_2O_5 and K_2O Profile 4 plots slightly outside the EGSC on-axis field, towards lower values.
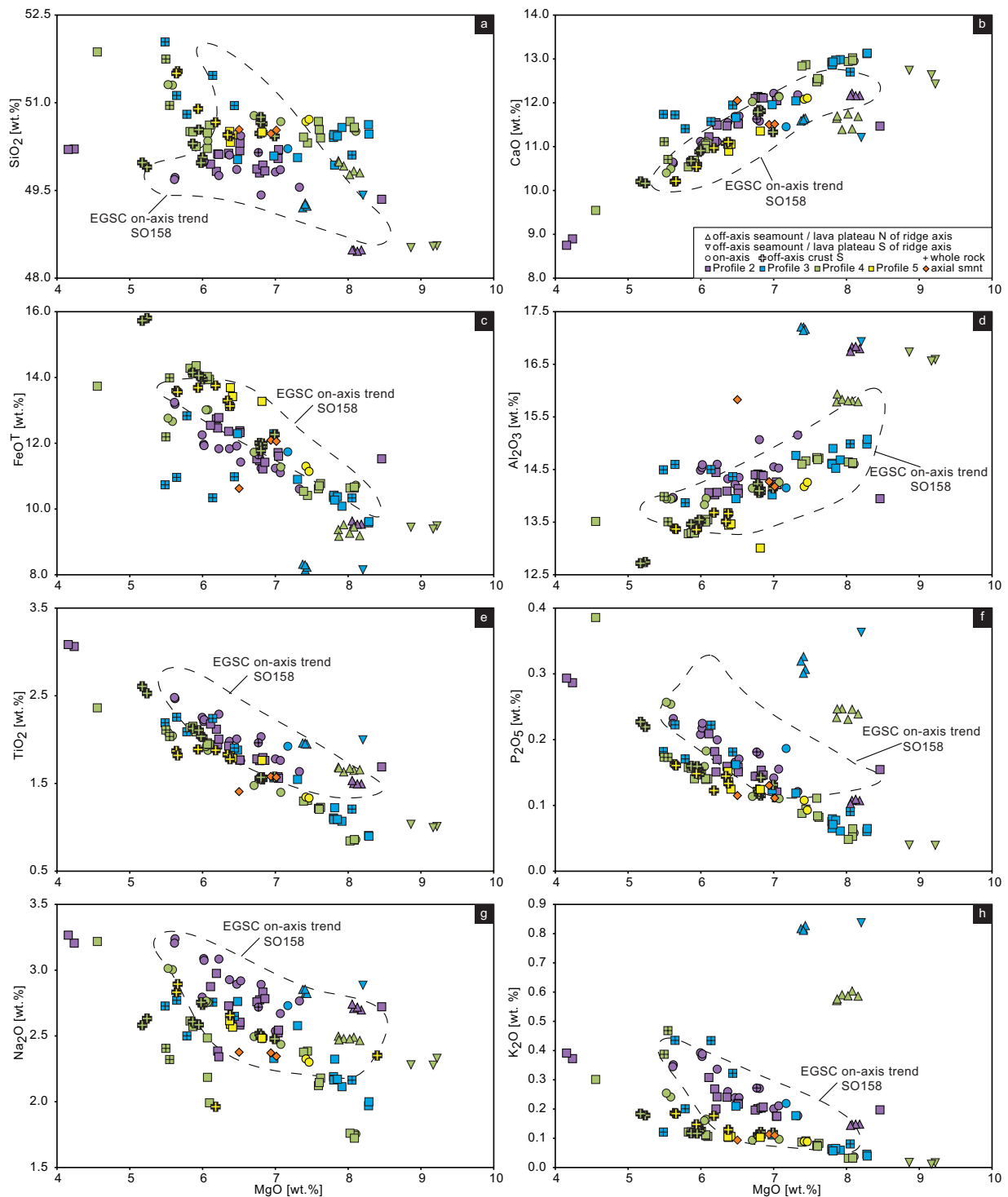
Figure 4.4: Major element concentrations versus MgO for the EGSC off-axis profiles compared to EGSC on-axis samples (Christie *et al.*, 2005) showing typical tholeiitic fractionation trends for shallow magma differentiation of olivine + plagioclase + clinopyroxene. Off-axis seamount DR115 from Profile 4 is most primitive sample (MgO=∼9 wt%). The split seamount from Profile 3 and the off-axis seamount 110 from Profile 4 tend to higher K$_2$O indicating the involvement on an enriched source component, or smaller degrees of melting.

In summary, the well-defined trends in major element composition of the individual profiles against MgO point towards a fairly constant depth of melt formation. Fractional crystallization seems to be the controlling process for the observed major element chemistry but other processes, such as mixing and assimilation, might be in operation, too.

4.4.2   Trace elements

The primitive mantle normalized trace element patterns for the individual profiles are shown in Fig. 4.5. In general, the patters are very smooth with no signs for alteration, especially in the fluid mobile elements, such as Rb, Ba or K. The patterns from the profiles range from east to west from between normal and enriched mid-ocean ridge basalt (N-, E-MORB; Fig. 4.5a) to intermediate between E-MORB and ocean island basalt (OIB; Fig. 4.5d). Exceptions are the off-axis seamounts of Profile 4 and the split seamount and some crustal samples of Profile 3 (Fig. 4.5b-c). The off-axis seamount to the North of the GSC ridge axis of Profile 4 (DR110)and the split seamount of Profile 3 (SO158 DR28 and DR87) represent the most enriched samples with the highest high to moderate incompatible trace element compositions and the characteristic depletion in the heavy rare earth elements (HREE) below N-MORB, indicating residual garnet in the source. It is worth noting, that there are crustal samples (Profile 3 – DR88, DR89, DR90; Profile 4 – DR101, DR105) and the off-axis seamount to the south of the GSC ridge axis in Profile 4 (DR115) with the lowest high to moderate incompatible element composition of all profiles, plotting well below or close to N-MORB. In addition, the off-axis seamount of Study Area 2 has the lowest high to moderate incompatible trace element abundance compared to the other samples of this profile.

On plots of distance from the ridge axis versus trace element ratios of elements with similar partition coefficients (Fig. 4.6a) Profile 4, 5 and the axial seamount clearly overlap and show only minor temporal variation over time, except the off-axis seamounts in Profile 4. Crustal samples generally fall within the range observed along the present ridge axis. Variations at single or closely located sites often show considerable variation in incompatible element ratios. The off-axis seamounts of Profile 4, DR115 to the south and DR110 to the north, have the most extreme compositions, respectively, of all samples. Study Area 2, does not overlap with Profile 4 and 5 and is characterized by overall higher more to less incompatible trace element ratios, except the off-axis seamount which tends to lower ratios. The largest range in trace element ratios can be observed in Profile 3. Apart from the elevated signature of the split seamount, five crustal samples tend to higher values, in the range of the Study Area 2 crustal samples, while the majority of the remaining samples extend to very low ratios (Fig. 4.6). Trace element ratios of HREE versus distance from the ridge axis (Fig. 4.6c) show similar relationships, with a) no temporal variation for Profile 4 and 5, b) elevated abundances for Study Area 2, c) slight overlap of five samples from Profile 3 with Study Area 2 while the others are similar to Profile 4 and 5, and d) the samples from the split seamount are the most enriched samples throughout all profiles.

4.4.3   Isotopic data

Similar to the trace elements, the samples from Profile 4 and 5 show no systematic variation in their isotopic composition with increasing distance from the ridge axis (Fig. 4.7). Study Area 2, the split seamount and five crustal samples of Profile 3, and the off-axis seamount DR110 from Profile 4 tend to
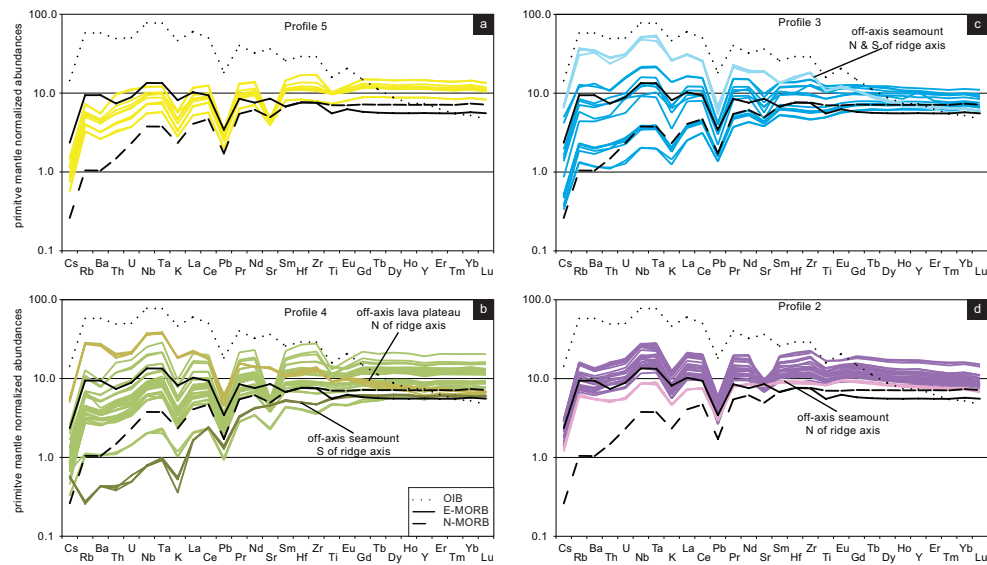
Figure 4.5: Primitive mantle normalized multi-element diagram (Hofmann, 1988) compared to N-, E-MORB and OIB (Sun & McDonough, 1989). From east towards the 91°W TF the composition from the Profiles chances from between N- and E-MORB (a) to intermediate between E-MORB and OIB. b) Exceptions are represented by the off-axis seamounts of Profile 4 with very depleted (DR115) composition. The off-axis lava plateau DR110 has the highest enrichment in incompatible trace elements but depleted HREE, similar to OIB. c) Profile 3 shows the largest variation crustal samples with patterns below N-MORB and very enriched samples. The split seamount samples follow the pattern of OIB but are not as enriched as OIB. d) Profile 2 has a clear E-MORB composition and is even slightly enriched towards OIB, except the off-axis seamount (DR77) with the lowest composition, trending towards N-MORB.
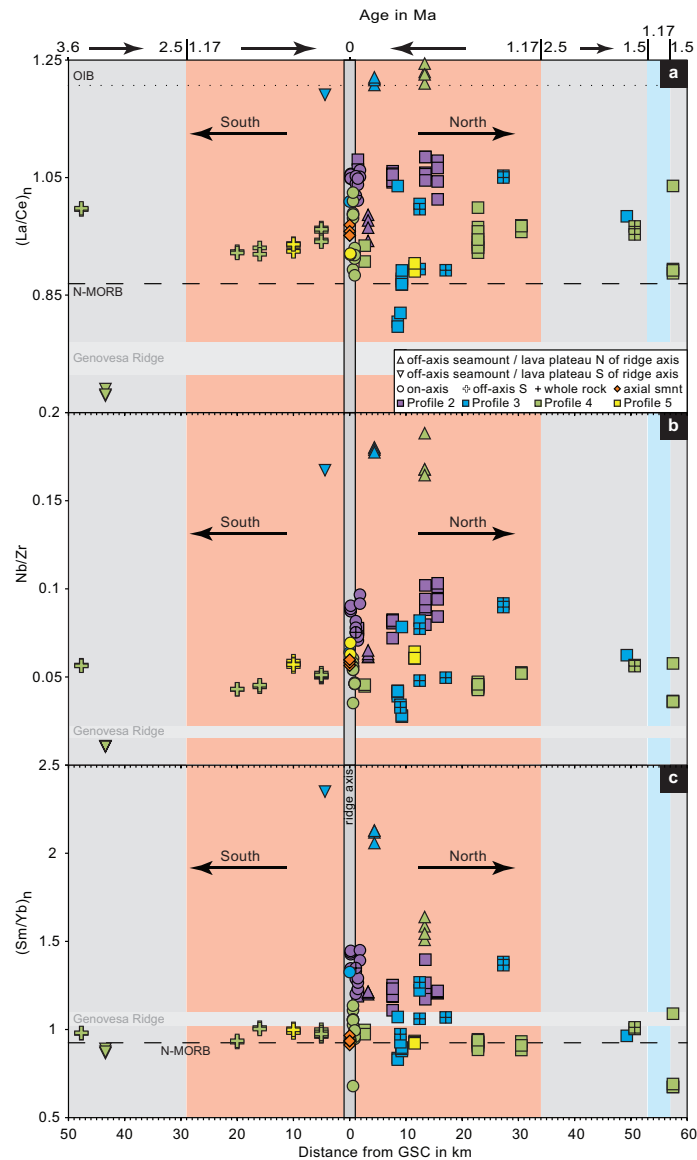
Figure 4.6: Distance from the EGSC ridge axis to the south and north versus trace element ratios permits information about changes in melt parameter over time. dark gray vertical bar symbolizes the EGSC ridge axis. horizontal bar shows the composition of the Galápagos Island Genovesa (Harpp *et al.*, 2003). N-MORB and OIB are from Sun & McDonough (1989). different coloured areas represent different age ranges of the crust - light red = 0-1.17 Ma, light blue = >1.17-1.5 Ma, gray = >1.5 Ma, Ages calculated based on spreading rate information given in Mittelstaedt *et al.* (2012, Fig. 7f). Arrows point towards younger ages. a) Ratios of highly incompatible trace element ratios indicate a clear enrichment in source composition for the off-axis lava plateau from Profile 4 and the split seamount from Profile 3. Profile 2 samples and some crustal samples of Profile 3 are also enriched, but not as much as the off-axis morphological anomalies. Profile 4 and 5 and the axial seamount are slightly more enriched than N-MORB. Note the very depleted samples of Profile 3, extending towards and overlapping Genovesa Ridge lavas. Off-axis seamount DR115 of Profile 4 is even more depleted than Genovesa samples. b) the off-axis lava plateau of Profile 4 and the split seamount lavas are the most enriched samples and clearly deviate from the rest of the samples. c) Compared to the EGSC crustal samples, the split seamounts have higher light to heavy REE ratios, indicating that melting started in >80 km depth in the presence of garnet. A gradual change from deep to shallow depth of melting can be observed from Profile 2 to the axial seamount.

more radiogenic $^{206}Pb/^{204}Pb$, $^{207}Pb/^{204}Pb$, $^{208}Pb/^{204}Pb$ (Fig. 4.7a-c), $^{87}Sr/^{86}Sr$ (Fig. 4.8a) and to less radiogenic $^{143}Nd/^{144}Nd$ (Fig. 4.8b). The off-axis seamount DR115 from Profile 4 has the lowest Pb and Sr and highest Nd ratios. The seamount samples show the most enriched and depleted isotopic compositions, as was also observed for the incompatible trace element ratios.

In contrast to the plots with distance from the ridge axis, the samples from the different profiles correlate well on isotope correlation diagrams will almost all samples falling on the same linear trends. They form a positive correlation on the uranogenic and thorogenic Pb isotope diagrams (Fig. 4.9a-b) and an inverse correlation on $^{206}Pb/^{204}Pb$ and $^{87}Sr/^{86}Sr$ versus $^{143}Nd/^{144}Nd$ (Fig. 4.9c-d). On all plots the crustal samples of Profile 4 and 5 fall within the Eastern Galápagos Domain (EGD) on mixing trajectory between the Central Galápagos Domain (CGD) and the most depleted samples from the Eastern Galápagos Domain (EGD). The off-axis seamounts of Profile 4 are the only exceptions. While DR110 plots on the radiogenic (in Pb and Sr isotope space) end of the EGD on a mixing trajectory between the Central Galápagos Domain (CGD) and the most depleted samples from the EGD represented by Genovesa Island samples. DR115 is the most depleted sample and falls near an extrapolation of the array formed by the ocean crust samples. Seamount samples from Profile 3 fall at the most radiogenic end of the Pb isotope arrays, but as is the case with the on-axis seamount from Profile 4 they fall below the array (at lower $^{208}Pb/^{204}Pb$) than the standard ocean crust samples. In Sr and Nd isotopic composition the Profile 3 seamounts do not plot at the enriched end of the array but at intermediate values and therefore cannot serve as an appropriate end member for the crustal arrays in all isotope systems. Interestingly, both, the split seamount of Profile 3 as well as the lava plateau north of the GSC in Profile 4 (DR110) deviate towards higher $(La/Ce)_n$ and La/Nd for given $^{206}Pb/^{204}Pb$ and $^{143}Nd/^{144}Nd$, respectively (Fig. 4.10).

4.5 Discussion

4.5.1 Longitudinal variations along the GSC

Due to the vicinity to the Galápagos plume the geochemical and morphological characteristics of GSC-MORB changes considerably between 101°-83°W ranging between axial high morphology combined with geochemical enrichment and ridge-valley structures with geochemical depleted composition (e.g., Christie *et al.*, 2005; Kokfelt *et al.*, 2005; Schilling *et al.*, 2003). To the east of the 91°W TF, two caldera-like centers with enriched geochemical signature were identified (Christie *et al.*, 2005; Ingle *et al.*, 2010; Schilling *et al.*, 2003, 1976, 1982; Verma & Schilling, 1982; Verma *et al.*, 1983). The ridge axis near 91°50'W and 90°30'W is characterized by axial highs, interpreted as the volcanic centers of the GSC, and peaks in geochemical composition indicating the input of Galápagos plume material into the GSC. The peaks, however, have distinct isotopic compositions, indicating the influence of two different enriched Galápagos domains (Fig. 4.9, Christie *et al.*, 2005; Kokfelt *et al.*, 2005).

Overall, along the EGSC the enriched geochemical signature decreases towards the east, with the exception of a sharp dip towards depleted compositions at the location of the incipient overlapping spreading center at 89°W (along the gray line in Fig. 4.11, Christie *et al.*, 2005; Kelley *et al.*, 2013; Schilling *et al.*, 2003, Hoernle et al., in prep.). The overall decrease in enrichment is interpreted to reflect diminishing plume influence on the geochemical composition of the on-axis lavas (Christie *et al.*, 2005; Detrick *et al.*,
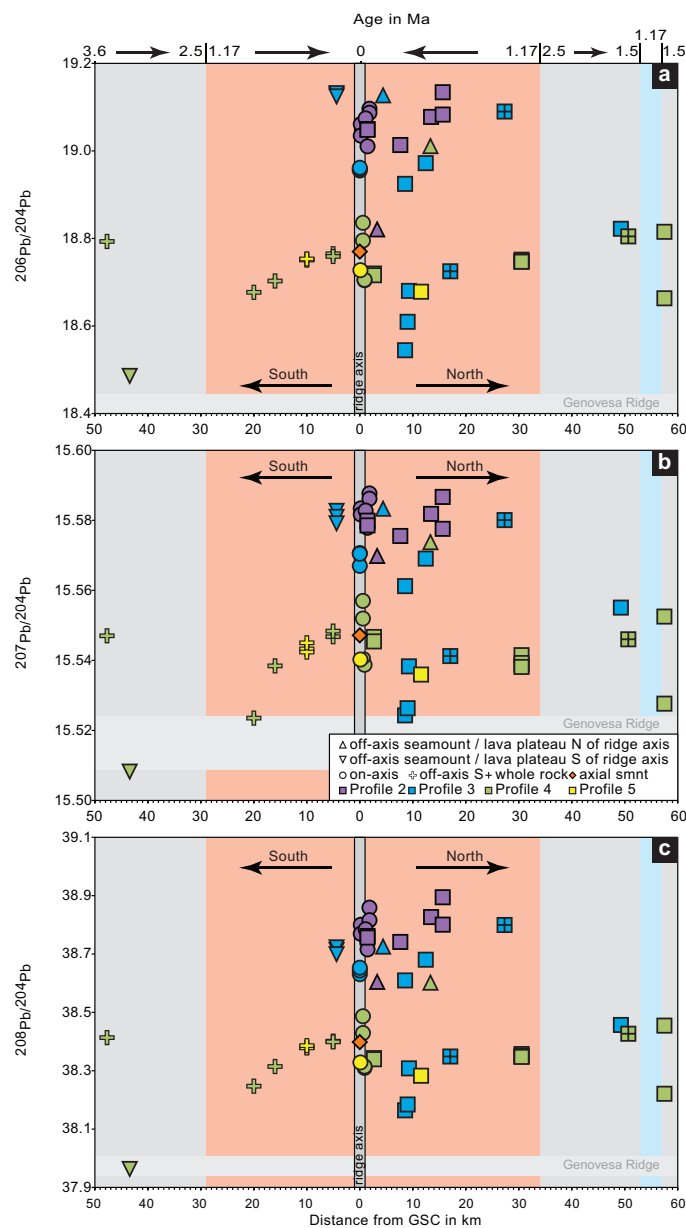
Figure 4.7: Distance from the EGSC ridge axis versus $^{206}Pb/^{204}Pb$, $^{207}Pb/^{204}Pb$, $^{208}Pb/^{204}Pb$. dark gray bar symbolizes the WGSC ridge axis, different coloured areas represent the different age ranges of the crust - light red = 0-1.17 Ma, light blue = 1.17-1.5 Ma, gray = >1.5 Ma, Ages calculated based on spreading rate information given in Mittelstaedt *et al.* (2012, Fig. 7f). Arrows point towards younger ages. The horizontal bar shows the composition of the Galápagos Island Genovesa (Harpp *et al.*, 2003). In general, the samples can be divided into two groups, one group that is more radiogenic in Pb represented by Profile 2 (purple symbols), the split seamount samples and five crustal samples of Profile 3 (blue symbols), and the off-axis lava plateau of Profile 4 (green symbol)). The second group is represented by the crustal samples of Profile 3, 4 and 5, with less isotopic enrichment. Note, that there are two crustal samples of Profile 3 and one from Profile 4 tending towards or overlapping Genovesa Ridge lavas in uranogenic and thorogenic diagrams.
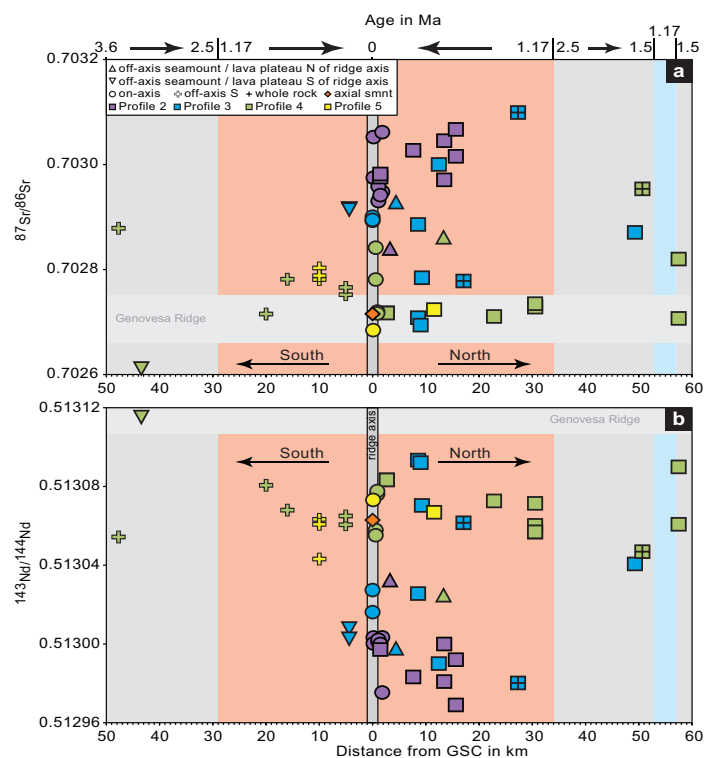
Figure 4.8: Distance from the EGSC ridge axis versus $^{87}Sr/^{86}Sr$ and $^{143}Nd/^{144}Nd$. dark gray bar symbolizes the WGSC ridge axis, different coloured areas represent the different age ranges of the crust - light red = 0-1.17 Ma, light blue = 1.17-1.5 Ma, gray = >1.5 Ma, Ages calculated based on spreading rate information given in Mittelstaedt *et al.* (2012, Fig. 7f). Arrows point towards younger ages. The horizontal bar shows the composition of the Galápagos Island Genovesa (Harpp *et al.*, 2003). Again, the samples can be divided into two groups, one group that is more radiogenic in Sr less radiogenic in Nd (Profile 2, the split seamount samples five crustal samples of Profile3, and the off-axis lava plateau of Profile 4). The crustal samples from Profile 4, Profile 5 and the on-axis seamount (orange diamond) are less radiogenic in Sr and more radiogenic in Nd. Note, while in Nd isotope space there are only two crustal samples of Profile 3 and one from Profile 4 tending towards or overlapping with Genovesa Ridge lavas in Sr isotope space the majority of Profile 4, Profile 5 and the on-axis seamount samples overlap with Genovesa ridge.
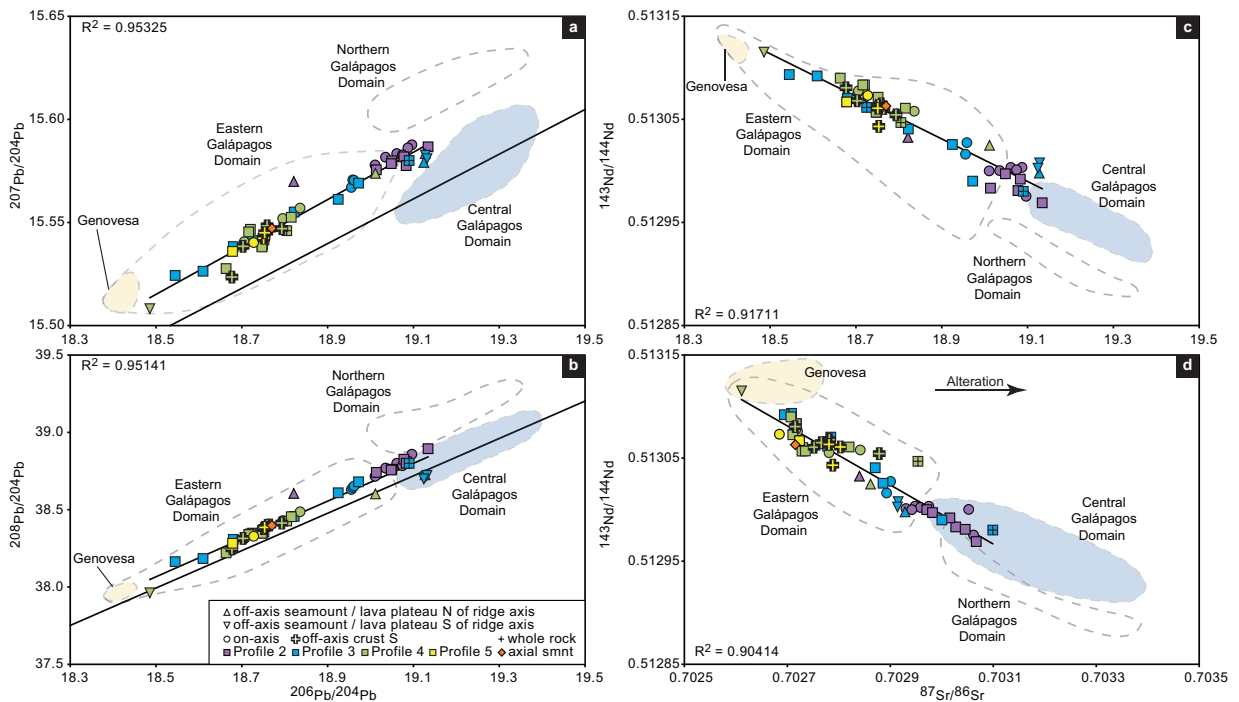
Figure 4.9: Multiple isotope correlation plots of Sr, Nd and Pb. The profile samples display a well-defined trend, indicating the involvement of the same mixing endmembers for all Profiles. Profile 2, the split seamount and some crustal samples of Profile 3 plot close to or at the lowest end of the Central Galápagos Domain (CGD) field. The rest of the crustal samples of Profile 3, the crustal samples of Profile 4 and 5 and the axial seamount sample plot within the Eastern Galápagos Domain (EGD) field trending towards Genovesa at the lowest end of the EGD. The compositions can be explained by two component mixing between an enriched source component, presumably CGD, and a depleted endmember, presumably EGD. Exceptions are the off-axis seamounts of Profile 4 and the split seamount of Profile 3. Galápagos Domains from White *et al.* (1993). Thin black line marks NHRL after Hart (1984).
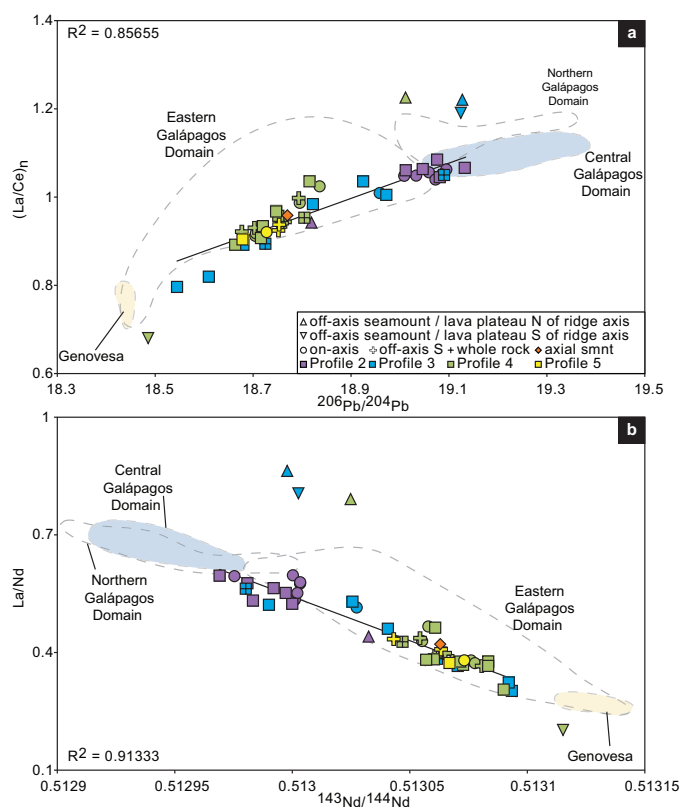
Figure 4.10: Isotope ratios versus trace element ratios. The EGSC crustal samples form a tight, well defined mixing array, supporting two component mixing between a depleted MORB-like component, possibly EGD represented by Genovesa, and the enriched Central Galápagos domain. The off-axis seamounts of Profile 4 and the split seamount sample of Profile 3 deviate from the trend. The enrichment in trace element composition for the off-axis lava Plateau and the split seamount, might be related to smaller degrees of melting.

2002; Kokfelt *et al.*, 2005; Schilling *et al.*, 2003, Hoernle et al., in prep.). The Profiles 3 and 4, where the seafloor was most extensively sampled and the furthest both to the north and south of the ridge axis, show large variations in incompatible element and isotopic composition. The most extremely enriched and depleted compositions are generally found in seamount type structures, except for the depleted end of Profile 3. Even if the seamount samples are excluded, the normal crustal samples show a greater range in composition than the entire present-day axial region of the GSC, suggesting that variable amounts of plume material reach specific locations along the ridge over time.

4.5.2 Identification of involved plume components contributing to the geochemical composition of the EGSC off-axis profile lavas

In order to determine the involved mantle endmembers in the source of the EGSC profile lavas, we compare the data from the different profiles to the distinct geochemical Galápagos domains observed at the

Galápagos Archipelago (Fig. 4.9, Geldmacher *et al.*, 2003; Hoernle *et al.*, 2000; Werner *et al.*, 2003). On all isotope correlation diagrams and also on isotope versus incompatible element ratio plots where both elements have similar partitions coefficients (Fig. 4.10), the well-defined linear arrays (generally with $R^2 > 0.9$) extend from the enriched Central Galápagos Domain to the depleted Genovesa Island field (Harpp *et al.*, 2003; Harpp & White, 2001; White *et al.*, 1993), consistent with mixing of these two components explaining the range of geochemical composition found in the >3.6 Ma ocean crust. After Christie *et al.* (2005), the Central Galápagos Domain enters the GSC at about 90°70'W and becomes progressively diluted by either mixing with local depleted MORB-like mantle (DMM), or Eastern Galápagos Domain. The latter is thought to represent entrained upper mantle, or recycled oceanic crust or lithospheric mantle that formed by gradually extracting melt from the fertile plume material as it flowed to the GSC (Hoernle *et al.*, 2000; Phipps Morgan & Morgan, 1999; Phipps Morgan *et al.*, 1995; Villagómez *et al.*, 2014, 2007, 2011; White *et al.*, 1993).

As is observed on the Pb isotope correlation diagrams and on the Pb and Nd isotope versus highly incompatible element diagrams (Fig. 4.10), the seamounts from Study Area 2 and Profiles 3 and 4 in most cases have anomalous compositions, i.e., lie well off the trends formed by the other samples. The extreme compositions observed in the seamounts and their deviation from the array formed by the standard ocean floor samples (crust) indicate that they represent local heterogeneities. In contrast to the seamount samples on the western portion of the GSC, most of those that formed on- or off-axis near the EGSC do not represent the composition of the bulk of the plume material entering the ridge system.

Ratios of highly incompatible to compatible trace elements (e.g., Nb/Y or Nb/Zr; Fig. 4.6) are very sensitive to changes in degree of melting with higher ratios indicating smaller degrees of melting. The split seamount samples of Profile 3 and the off-axis plateau of Profile 4 tend to significantly higher Nb/Zr (0.17-0.18) and Nb/Y (0.74-1.43) ratios compared to the crustal samples (Nb/Zr=0.03, Nb/Y=0.05) and thus indicate smaller degrees of melting. This is supported by the major element composition, as the split seamount samples are of transitional tholeiitic composition. These samples also show fractionated HREE ratios, indicating the presence of residual garnet in their sources. Residual garnet reflects deeper melting (in the garnet stability field) and lower degrees of melting such that garnet is not exhausted during melting.

The off-axis seamount DR115 to the south of the ridge axis in Profile 4 deviates from the major trend as well but tends towards more depleted compositions. These samples are the most mafic samples (MgO=8.86-9.22; Mg#=0.63; Fig. 4.4) with highly depleted incompatible trace element patterns, even more depleted than N-MORB (Fig. 4.5b) and represent the most unradiogenic samples of all profiles (Fig. 4.7), plotting close to Genovesa samples (Fig. 4.7-4.9 Harpp *et al.*, 2003, 2002). Seamount DR115 is similar depleted ($(La/Sm)_n = <0.32$; $K_2O/TiO_2 = <0.02$) as a single seamount (SO158 DR30) to the south of the ridge axis at 89°39.7'W (Christie *et al.*, 2005) and numerous other seamounts between the Galápagos Platform and the GSC ridge axis (Harpp & Geist, 2002; Harpp *et al.*, 2002, 2003; Harpp & White, 2001, Hoernle et al., in prep.). The depleted signature is referred to an unusually depleted mantle component, that is normally not observed at the ridge axis (Christie *et al.*, 2005) but as observed in Profile 3 seems to be sometimes influencing the GSC geochemistry, as currently observed on the ridge axis of Profile 4 (Hoernle et al., in prep.). It is surprising that seamounts (positive bathymetric anomalies) are even formed from highly depleted sources as is the case with the depleted off-axis seamount south of the EGSC from Profile 4.
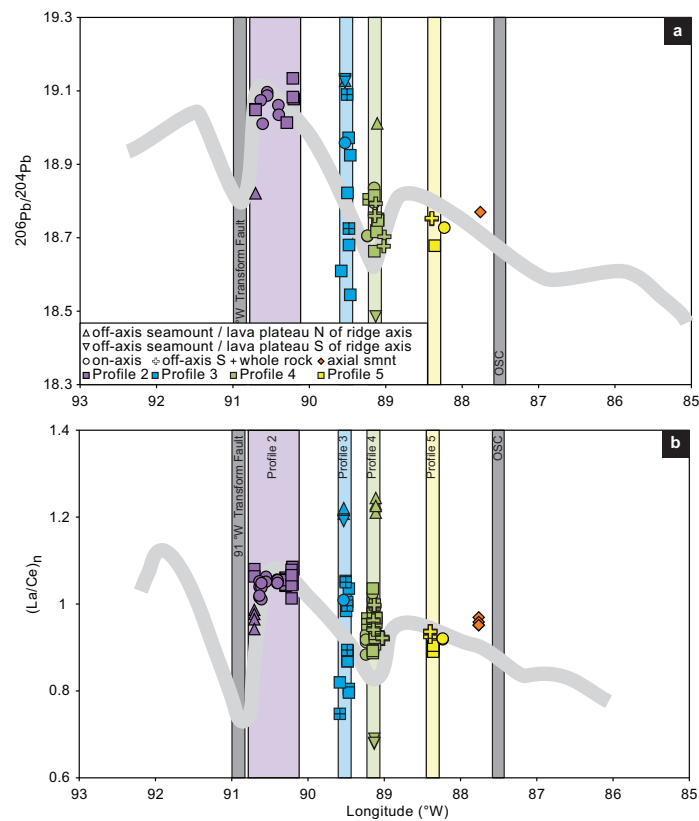
Figure 4.11: Trace element and isotopic longitudinal variations along the EGSC. OSC indicates 87°W overplapping spreading center. The gray line shows the EGSC on-axis trend based on data from Hoernle et al., (unpub.data) for a) and Christie *et al.* (2005) for b). The profiles follow the observed decreasing input of plume material from west to east. Profile 2 with the highest enrichment represents a clear plume signal and correlates with the on-axis trend. Profile 3 shows the largest variations. The on-axis trend shows a kink for Profile 4, but the profile samples do not show this depleted composition. Exceptions are the off-axis seamounts to the north and south of the ridge axis and on-axis morphological anomalies.

4.5.3 Variations through time – implications for pulsing plume input?

4.5.3.1 Crustal evolution at the EGSC

Based on magnetic, multibeam and sidescan sonar data Mittelstaedt *et al.* (2012) reconstructed the evolution of the GSC over the past ∼5 Ma. At least four southward ridge jumps towards the plume occurred during this time from which 3 appear to have established new ridge axes. The youngest ridge jump occurred 1.17 Ma ago and caused a jump of the EGSC ridge axis of approximately 35 km to the south associated with a westward propagation of the ridge axis (Mittelstaedt *et al.*, 2012). The authors also provided three magnetic anomaly profiles from 90.5°W, 90.37°W and 90.0°W describing the changes in spreading rate and spreading symmetry on varying locations along the EGSC. The information of the magnetic anomaly profile at 90.0°W, which is located between study area 2 and Profile 3, were used to allocate the geochemical evolution of Profile 3 and Profile 4 into a chronological frame (Fig. 4.12). Before 1.5 Ma asymmetric spreading (41% to the south and 59% to the north) with a full-spreading rate of 46 km/Ma was assumed (Fig. 4.12a). It was followed by a period of very slow spreading (1.5-1.17 Ma) with a full-spreading rate of 12 km/Ma (Fig. 4.12b). Since there is no indication about the nature of spreading, symmetric spreading was assumed. During this time about 2 km of ocean crust formed (blue stripes in Fig. 4.12). At around ∼1.17 Ma, the spreading ridge jumped 21 km to the south (Fig. 4.12c) and therefore closer to the Galápagos hotspot. The new ridge axis formed in crust that was 2.5 Ma old (gray stripes in Fig. 4.12). Since 1.17 Ma, spreading at the EGSC has remained nearly symmetrical (46% to the south and 54% to the north) with a full-spreading rate of 54 km/Ma (red stripes in Fig. 4.12). The youngest ridge jump resulted in non-linear age progressions both to the north and south of the ridge axis. The reconstructed crustal evolution at the EGSC between 89.40'W and 89°00'W yields a very unsteady crustal age pattern including age jumps of about 1.3 Ma between crust that formed 1.17 Ma and 2.5 Ma ago (Fig. 4.2b; Fig 4.12d). To the north of the ridge axis ages the EGSC crust changes from crust that formed >1.17 Ma (red area in Fig. 4.12d) to crust that is between 1.5 Ma and 2.5 Ma old (gray area in Fig. 4.12d) to crust that formed between 1.17 Ma and 1.5 Ma (blue area in Fig. 4.12d). To the south there is a much larger age range with only one age jump between 1.17 Ma old crust and 2.5 Ma old crust but covers crust of an age of up to 3.6 Ma. The majority of the sampled locations in this study is located in crust that is not older than 1.17 Ma old (Fig. 4.6-4.8) and therefore uninfluenced by a proposed ridge jump. At Profile 3 and 4, however, there are a few samples (1 from Profile 3 and 3 from Profile 4) that represent much older crust.

4.5.3.2 Geochemical variations through time

Geochemical parameters plotted against the distance from the GSC ridge axis reflect a first approximation of crustal age, permitting interpretations related to temporal changes in melt conditions, e.g., depth or degree of melting, and/or source composition (Fig. 4.6-4.8). Fig. 4.6-4.8 show various trace element and isotope ratios plotted against distance from the GSC ridge axis. There are only minor variations within the crustal samples of Profile 4 and 5 with increasing distance from the ridge axis. The observed variations show a similar range as those observed on the ridge axis, indicating that changes in melt conditions (source composition (Fig. 4.6a), degrees of melting (Fig. 4.6b) and depth of melting (Fig. 4.6c)) did not change

systematically over the last 3.6 Ma.

Profile 3 samples show the biggest variations in geochemical composition, ranging from very depleted to the most enriched samples (e.g., $^{206}Pb/^{204}Pb$=18.545-19.127, $^{143}Nd/^{144}Nd$=0.51298-0.51309). Besides the split seamount samples with the most enriched compositions, four locations (DR87, DR90, DR91, DR96) also have elevated trace element and isotope ratios. Even though these samples are not as enriched as the split seamount samples, they clearly overlap with the enriched signatures of Study Area 2 (Fig. 4.6-4.8), indicating the influence of the enriched Central Galápagos plume component. On the other hand, there are two crustal samples in Profile 3 with very depleted compositions. These samples overlap with or tend towards samples from the Genovesa Ridge (Harpp *et al.*, 2003, Fig. 4.6-4.9). The extremely large range in composition at one location at the ridge axis and that this variation can happen over a very short time period points towards significant changes in the amount of plume material reaching the ridge. The changes in composition seem to represent short-term events (blobs?), indicating, that Galápagos plume material (enriched and depleted) reaches the ridge axis in a highly irregular manner causing a temporal increase or decrease in the geochemical signature of the erupted material. We propose that this heterogeneous material is not entering the ridge at a specific location and then flows down the ridge (e.g., Christie *et al.*, 2005; Ingle *et al.*, 2010; Kokfelt *et al.*, 2005; Schilling *et al.*, 2003) but that it is able to enter the ridge at variable locations completely unrelated to radial distance from the plume. These variations seem only to be present at Profile 3, even though there are implications at Profile 4 who support a local short term input of enriched or depleted material (off-axis seamount to the south and lava plateau to the north). These short-term events indicate, that even Study Area 2 is the main area where Galápagos plume material is injected into the ridge there are additional local spots where plume material in introduced into the GSC.

Finally the question needs to be addressed why Profile 3 shows a much greater compositional variation than Profile 4, although the latter represents a more extensive sampling to the north and south of the ridge. In this context is interesting to note, that there is essentially no compositional difference between the samples from the south and north of the EGSC at Profile 4 (Fig. 4.6-4.8). Profile 3 with the large of geochemical composition seems to represent the transition from Study Area 2 with almost exclusively enriched character to Profile 4 with almost only depleted compositions (with one exception), to Profile 5 and on-axis seamount DR122 that are of exclusively depleted character (Fig. 4.9). While at Study Area 2 the EGSC experiences a constant input of enriched CGD material, at Profile 3 not only enriched plume material reaches the ridge but also depleted material in a highly irregular and heterogeneous fashion. At Profile 4 the majority of the erupted material is of depleted composition with an occasional lump of enriched or very depleted material causing single short-term events of enriched character.

4.6   Conclusions

The aim of this study was to investigate the nature of plume input at the EGSC. All samples can be explained by two component mixing between a depleted N-MORB-like component, e.g., Eastern Galápagos Domain and one enriched plume component. The Central Galápagos Domain was indentified as the enriched plume component contributing to the geochemistry of the ridge axis lavas, up to 3.6 Ma, which mostly reaches the ridge axis at Study Area 2 just east of the 91°W TF. We were able to show that neither a simple radial outflow model nor an injection of plume material at one location at the EGSC and
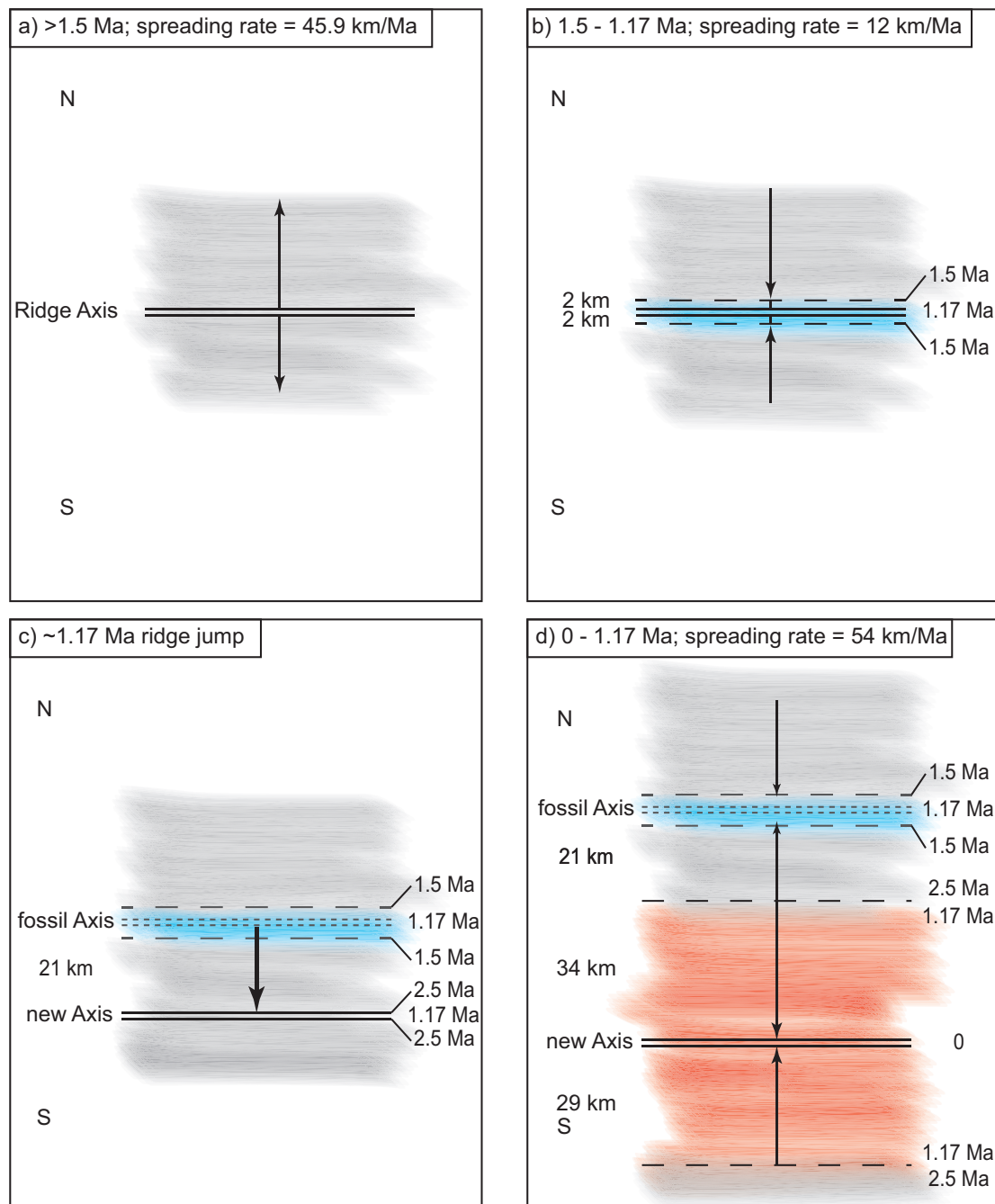
Figure 4.12: Schematic reconstruction of the crustal age development of the EGSC at 90°W based on Mittelstaedt *et al.* (Fig. 7f from, 2012). a) Situation >1.5 Ma. with asymmetric spreading (41% to the south and 59% to the north) and a full-spreading rate of 45.9 km/Ma, b) 1.5-1.17 Ma assumed symmetric spreading with full-spreading rate of 12 km/Ma, c) ∼1.17 Ma time of proposed ridge jump where the old ridge was abandoned and the new one was established about 21 km further to the south, d) 0-1.17 Ma nearly symmetric spreading (46% to the south and 54% to the north) with a full-spreading rate of 54 km/Ma. Thin arrows in a, b and d point towards younger ages, thick arrow in c symbolizes the ridge jump.

subsequent dilution by flowing beneath the ridge axis can explain the extremely large range in geochemical composition observed at Profile 3 and at on- and off-axis morphological anomalies further along the ridge towards the east. Instead we propose a variable input of heterogeneous material in a highly irregular manner, unrelated to the radial distance from the plume. These chances in variation (enriched plume signature and very depleted composition) can happen over very short time intervals, suggesting that there are large variations in the amount of plume material reaching the GSC at any given spot, even over short time periods.

Acknowledgements

References

Bowles, J. A., Colman, A., McClinton, J. T., Sinton, J. M., White, S. M. & Rubin, K. H., 2014. Eruptive timing and 200 year episodicity at 92 °W on the hot spot-influenced Galápagos Spreading Center derived from geomagnetic paleointensity. *Geochemistry, Geophysics, Geosystems*, **15**, 2211–2224.

Canales, J. P., Dañobeitia, J. J., Detrick, R. S., Hooft, E. E. E., Bartolomé, R. & Naar, D. F., 1997. Variations in axial morphology along the Galápagos spreading center and the influence of the Galápagos hotspot. *Journal of Geophysical Research: Solid Earth*, **102**, 27341–27354.

Christie, D. M. & Sinton, J. M., 1981. Evolution of abyssal lavas along propagating segments of the Galápagos spreading center. *Earth and Planetary Science Letters*, **56**, 321–335.

Christie, D. M., Werner, R., Hauff, F., Hoernle, K. & Hanan, B. B., 2005. Morphological and geochemical variations along the eastern Galápagos Spreading Center. *Geochemistry, Geophysics, Geosystems*, **6**, Q01006.

Detrick, R. S., Sinton, J. M., Ito, G., Canales, J. P., Behn, M., Blacic, T., Cushman, B., Dixon, J. E., Graham, D. W. & Mahoney, J. J., 2002. Correlated geophysical, geochemical, and volcanological manifestations of plume-ridge interaction along the Galápagos Spreading Center. *Geochemistry, Geophysics, Geosystems*, **3**, 8501.

Duncan, R. A. & Hargraves, R. B., 1984. Plate tectonic evolution of the Caribbean region in the mantle reference frame. *Geological Society of America Memoirs*, **162**, 81–94.

Geist, D. J., White, W. M. & McBirney, A. R., 1988. Plume-asthenosphere mixing beneath the Galápagos archipelago. *Nature*, **333**, 657–660.

Geldmacher, J., Hanan, B. B., Blichert-Toft, J., Harpp, K., Hoernle, K., Hauff, F., Werner, R. & Kerr, A. C., 2003. Hafnium isotopic variations in volcanic rocks from the Caribbean Large Igneous Province and Galápagos hot spot tracks. *Geochemistry, Geophysics, Geosystems*, **4**, 1062.

Geldmacher, J., Höfig, T., Hauff, F., Hoernle, K., Garbe-Schönberg, D. & Wilson, D., 2013. Influence of the Galápagos hotspot on the East Pacific Rise during Miocene superfast spreading. *Geology*, **41**, 183–186.

Graham, D. W., Christie, D. M., Harpp, K. S. & Lupton, J. E., 1993. Mantle Plume Helium in Submarine Basalts from the Galápagos Platform. *Science*, **262**, 2023–2026.

Handschumacher, D. W., 1976. Post-Eocene Plate Tectonics of the Eastern Pacific. In: *The Geophysics of the Pacific Ocean Basin and Its Margin*, American Geophysical Union. 177–202.

Harpp, K. & Geist, D., 2002. Wolf-Darwin lineament and plume-ridge interaction in northern Galápagos. *Geochemistry, Geophysics, Geosystems*, **3**, 8504.

Harpp, K. S., Fornari, D. J., Geist, D. J. & Kurz, M. D., 2003. Genovesa Submarine Ridge: A manifestation of plume-ridge interaction in the northern Galápagos Islands. *Geochemistry, Geophysics, Geosystems*, **4**, 8511.

Harpp, K. S. & White, W. M., 2001. Tracing a mantle plume: Isotopic and trace element variations of Galápagos seamounts. *Geochemistry, Geophysics, Geosystems*, **2**, 1042.

Harpp, K. S., Wirth, K. R. & Korich, D. J., 2002. Northern Galápagos Province: Hotspot-induced, near-ridge volcanism at Genovesa Island. *Geology*, **30**, 399–402.

Hart, S. R., 1984. A large-scale isotope anomaly in the Southern Hemisphere mantle. *Nature*, **309**, 753–757.

Herbrich, A., Hoernle, K., Werner, R., Hauff, F., Bogaard, P. v. d. & Garbe-Schönberg, D., 2015. Cocos Plate Seamounts offshore NW Costa Rica and SW Nicaragua: Implications for large-scale distribution of Galápagos plume material in the upper mantle. *Lithos*, **212–215**, 214–230.

Hey, R., 1977. Tectonic evolution of the Cocos-Nazca spreading center. *Geological Society of America Bulletin*, **88**, 1404–1420.

Hoernle, K., Abt, D. L., Fischer, K. M., Nichols, H., Hauff, F., Abers, G. A., van den Bogaard, P., Heydolph, K., Alvarado, G., Protti, M. & Strauch, W., 2008. Arc-parallel flow in the mantle wedge beneath Costa Rica and Nicaragua. *Nature*, **451**, 1094–1097.

Hoernle, K., Hauff, F., Kokfelt, T. F., Haase, K., Garbe-Schönberg, D. & Werner, R., 2011. On- and off-axis chemical heterogeneities along the South Atlantic Mid-Ocean-Ridge (5-11 °S): Shallow or deep recycling of ocean crust and/or intraplate volcanism? *Earth and Planetary Science Letters*, **306**, 86–97.

Hoernle, K., Werner, R., Morgan, J. P., Garbe-Schönberg, D., Bryce, J. & Mrazek, J., 2000. Existence of complex spatial zonation in the Galápagos plume. *Geology*, **28**, 435–438.

Hofmann, A. W., 1988. Chemical differentiation of the Earth: the relationship between mantle, continental crust, and oceanic crust. *Earth and Planetary Science Letters*, **90**, 297–314.

Holden, J. C. & Dietz, R. S., 1972. Galápagos Gore, NazCoPac Triple Junction and Carnegie/Cocos Ridges. *Nature*, **235**, 266–269.

Ingle, S., Ito, G., Mahoney, J. J., Chazey, I., William, Sinton, J., Rotella, M. & Christie, D. M., 2010. Mechanisms of geochemical and geophysical variations along the western Galápagos Spreading Center. *Geochemistry, Geophysics, Geosystems*, **11**, Q04003.

Ito, G. & Lin, J., 1995. Oceanic spreading center-hotspot interactions: Constraints from along-isochron bathymetric and gravity anomalies. *Geology*, **23**, 657–660.

Ito, G., Lin, J. & Graham, D., 2003. Observational and theoretical studies of the dynamics of mantle plume & mid-ocean ridge interaction. *Reviews of Geophysics*, **41**, 1017.

Ito, G. & van Keken, P. E., 2007. Hot Spots and Melting Anomalies. In: *Treatise on Geophysics* (ed. Editor-in Chief: Gerald, S.), Elsevier, Amsterdam. 371–435.

Kelley, K. A., Kingsley, R. & Schilling, J.-G., 2013. Composition of plume-influenced mid-ocean ridge lavas and glasses from the Mid-Atlantic Ridge, East Pacific Rise, Galápagos Spreading Center, and Gulf of Aden. *Geochemistry, Geophysics, Geosystems*, **14**, 223–242.

Kokfelt, T. F., Lundstrom, C., Hoernle, K., Hauff, F. & Werner, R., 2005. Plume-ridge interaction studied at the Galápagos spreading center: Evidence from ^{226}Ra-^{230}Th-^{238}U and ^{231}Pa-^{235}U isotopic disequilibria. *Earth and Planetary Science Letters*, **234**, 165–187.

Le Maitre, R. W., Bateman, P., Dudek, A., Keller, J., Lameyre, J., Le Bas, M. J., Sabine, P. A., Schmid, R., Sorensen, H., Streckeisen, A., Woolley, A. R. & Zanettin, B., 1989. *A classification of igneous rocks and glossary of terms, recommendations of the International Union of Geological Sciences, Subcommission on the Systematics of Igneous Rocks*. Blackwell Scientific. Oxford. GB.

Lonsdale, P., 2005. Creation of the Cocos and Nazca plates by fission of the Farallon plate. *Tectonophysics*, **404**, 237–264.

Lonsdale, P. & Klitgord, K. D., 1978. Structure and tectonic history of the eastern Panama Basin. *Geological Society of America Bulletin*, **89**, 981–999.

MacDonald, G. A. & Katsura, T., 1964. Chemical Composition of Hawaiian Lavas1. *Journal of Petrology*, **5**, 82–133.

Mittelstaedt, E., Soule, S., Harpp, K., Fornari, D., McKee, C., Tivey, M., Geist, D., Kurz, M. D., Sinton, C. & Mello, C., 2012. Multiple expressions of plume-ridge interaction in the Galápagos: Volcanic lineaments and ridge jumps. *Geochemistry, Geophysics, Geosystems*, **13**, Q05018.

Montelli, R., Nolet, G., Dahlen, F. A. & Masters, G., 2006. A catalogue of deep mantle plumes: New results from finite-frequency tomography. *Geochemistry, Geophysics, Geosystems*, **7**, Q11007.

Morgan, W. J., 1971. Convection Plumes in the Lower Mantle. *Nature*, **230**, 42–43.

Phipps Morgan, J. & Morgan, W. J., 1999. Two-stage melting and the geochemical evolution of the mantle: a recipe for mantle plum-pudding. *Earth and Planetary Science Letters*, **170**, 215–239.

Phipps Morgan, J., Morgan, W. J. & Price, E., 1995. Hotspot melting generates both hotspot volcanism and a hotspot swell? *Journal of Geophysical Research: Solid Earth*, **100**, 8045–8062.

Schilling, J., Kingsley, R. & Devine, J., 1982. Galápagos Hot Spot-Spreading Center System 1. Spatial Petrological and Geochemical Variations (83 °W–111 °W). *Journal of Geophysical Research*, **87**, 18.

Schilling, J.-G., 1991. Fluxes and excess temperatures of mantle plumes inferred from their interaction with migrating mid-ocean ridges. *Nature*, **352**, 397–403.

Schilling, J. G., Anderson, R. N. & Vogt, P., 1976. Rare earth, Fe and Ti variations along the Galápagos spreading centre, and their relationship to the Galápagos mantle plume. *Nature*, **261**, 108–113.

Schilling, J.-G., Fontignie, D., Blichert-Toft, J., Kingsley, R. & Tomza, U., 2003. Pb-Hf-Nd-Sr isotope variations along the Galápagos Spreading Center (101 °-83 °W): Constraints on the dispersal of the Galápagos mantle plume. *Geochemistry, Geophysics, Geosystems*, **4**, 8512.

Sinton, J., Detrick, R., Canales, J. P., Ito, G. & Behn, M., 2003. Morphology and segmentation of the western Galápagos Spreading Center, 90.5 °-98 °W: Plume-ridge interaction at an intermediate spreading ridge. *Geochemistry, Geophysics, Geosystems*, **4**, 8515.

Sun, S.-s. & McDonough, W. F., 1989. Chemical and isotopic systematics of oceanic basalts: implications for mantle composition and processes. *Geological Society, London, Special Publications*, **42**, 313–345.

Verma, S. P. & Schilling, J. G., 1982. Galápagos hot spot-spreading center system 2. 87Sr/86 Sr and large ion lithophile element vaiations (85°W-101°W). *Journal of Geophysical Research*, **87**, 19.

Verma, S. P., Schilling, J. G. & Waggoner, D. G., 1983. Neodymium isotopic evidence for Galápagos hotspot-spreading centre system evolution. *Nature*, **306**, 654–657.

Villagómez, D. R., Toomey, D. R., Geist, D. J., Hooft, E. E. E. & Solomon, S. C., 2014. Mantle flow and multistage melting beneath the Galápagos hotspot revealed by seismic imaging. *Nature Geoscience*, **advance online publication**.

Villagómez, D. R., Toomey, D. R., Hooft, E. E. E. & Solomon, S. C., 2007. Upper mantle structure beneath the Galápagos Archipelago from surface wave tomography. *Journal of Geophysical Research*, **112**, B07303.

Villagómez, D. R., Toomey, D. R., Hooft, E. E. E. & Solomon, S. C., 2011. Crustal structure beneath the Galápagos Archipelago from ambient noise tomography and its implications for plume-lithosphere interactions. *Journal of Geophysical Research*, **116**, B04310.

Vogt, P. R., 1976. Plumes, subaxial pipe flow, and topography along the Mid-Oceanic Ridge. *Earth and Planetary Science Letters*, **29**, 309–325.

Werner, R., Hoernle, K., Barckhausen, U. & Hauff, F., 2003. Geodynamic evolution of the Galápagos hot spot system (Central East Pacific) over the past 20 m.y.: Constraints from morphology, geochemistry, and magnetic anomalies. *Geochemistry, Geophysics, Geosystems*, **4**, 1108.

White, W. M. & Hofmann, A. W., 1978. Geochemistry of the Galápagos Islands: implications for mantle dynamics and evolution. *Year Book Carnegie Inst. Washington*, **77**, 596–606.

White, W. M., McBirney, A. R. & Duncan, R. A., 1993. Petrology and Geochemistry of the Galápagos Islands: Portrait of a Pathological Mantle Plume. *Journal of Geophysical Research*, **98**, 19533–19563.

Wilson, D. S. & Hey, R. N., 1995. History of rift propagation and magnetization intensity for the Cocos-Nazca spreading center. *Journal of Geophysical Research*, **100**, 10041–10056.

List of Figures

List of Tables

Appendix A

Cocos Plate Seamounts
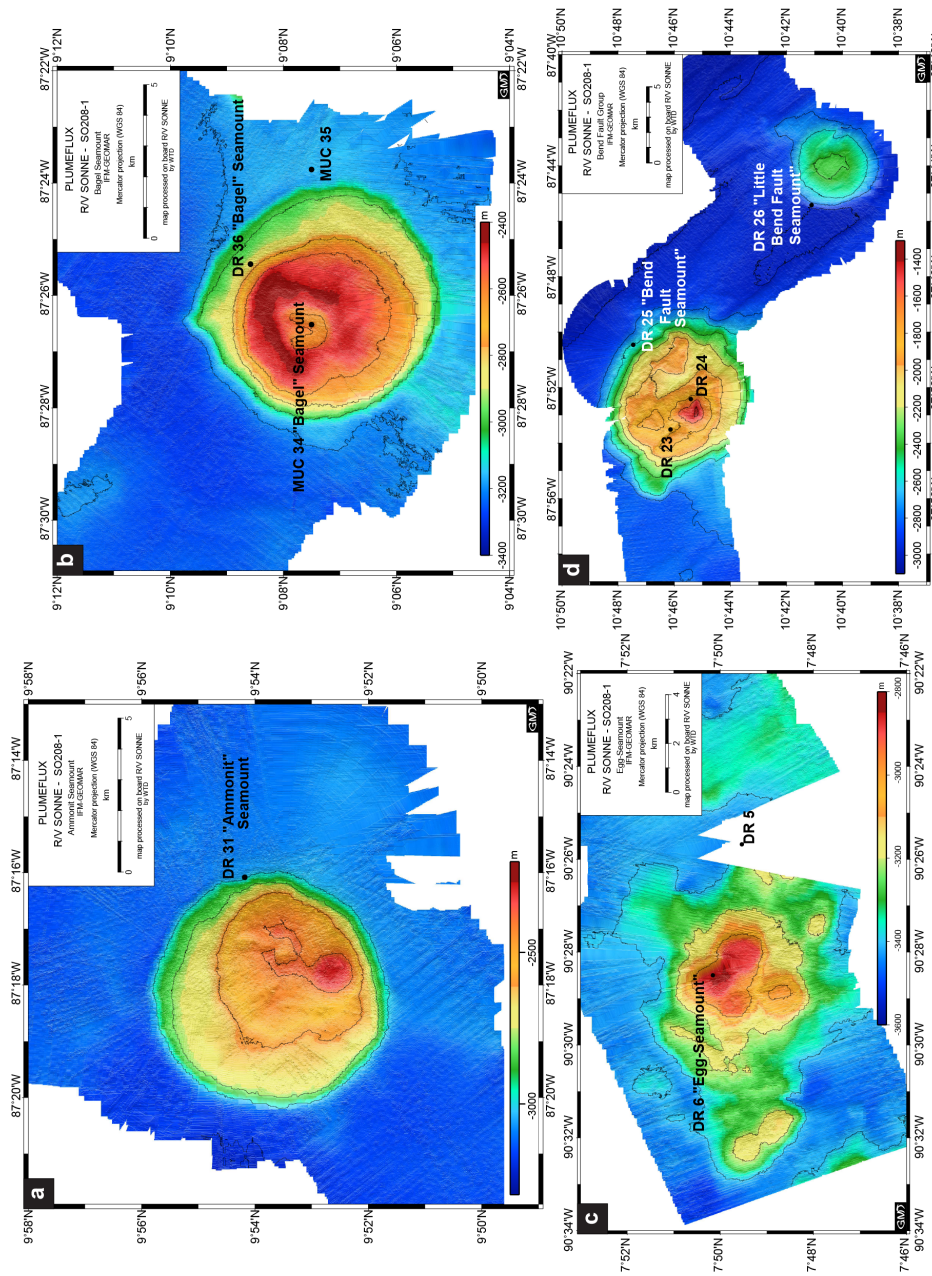
Figure A.1: Bathymetric map of some representative seamount structures

Table A.1: Major element composition (in wt.%) of all samples of the CPS.

Element/ Sample (SO208)	SiO_2	Al_2O_3	MgO	FeO^T	Fe_2O_3	CaO	Na_2O	K_2O	TiO_2	P_2O_5	MnO	Cr_2O_3	SO_3	LOI%	Total
Near-Ridge Cocos Plate Seamount Samples															
Egg															
DR6-2	48.36	17.38	7.16	9.11		10.34	3.25	0.77	1.99	0.30	0.15		0.24		99.09
Bend Fault															
DR23-5	49.93	14.51	7.05	10.53		11.72	2.78	0.11	1.68	0.12	0.19		0.30		98.99
DR23-5_wr	49.79	16.57	6.45	8.24		12.44	2.58	0.15	1.40	0.11	0.15		0.00	1.5	100.29
DR24-6	48.38	16.70	7.35	10.02		11.17	3.12	0.23	1.86	0.15	0.12		0.29		99.42
Kringel															
DR33-1	49.94	15.82	7.70	9.44		12.15	2.54	0.12	1.31	0.10	0.19		0.19		99.54
DR33-1_wr	48.38	16.20	6.44		10.20	12.61	2.43	0.18	1.27	0.25	0.23		0.15	1.3	99.66
Intraplate Seamount Samples															
Pan-Cake															
DR1-1_wr	50.22	14.94	7.47		9.82	13.22	2.17	0.14	1.10	0.09	0.17		0.01	0.5	99.87
Spiegelei															
DR15-4	48.21	17.43	5.67	9.29		8.84	4.02	1.00	2.66	0.43	0.15		0.17		97.93
DR15-4	47.67	17.31	5.93	9.27		9.04	4.00	0.98	2.58	0.41	0.14		0.26		97.64
DR15-4_wr	48.54	17.12	3.55		9.36	9.13	3.64	1.11	2.56	0.64	0.19		0.05	3.6	99.48
Pickel															
DR21-3	48.08	16.95	6.81	9.60		10.33	3.46	0.42	2.15	0.33	0.17		0.24		98.56
DR21-3_wr	48.55	17.80	3.85		10.10	10.61	3.52	0.58	2.05	0.37	0.13		0.00	2.4	99.94
Unnamed															
TVG22-3	48.38	17.43	7.56	9.54		10.95	3.09	0.18	1.73	0.18	0.17		0.20		99.43
Bend Fault															
DR25-2	50.93	14.76	7.18	9.89		12.23	2.64	0.08	1.43	0.11	0.18		0.20		99.67
DR25-2_wr	49.84	16.28	6.54		8.66	13.26	2.46	0.17	1.31	0.12	0.15		0.00	1.0	99.77
Little Bend															
DR26-2_wr	51.05	14.85	7.82		9.72	12.94	2.24	0.12	1.14	0.09	0.17		0.00	0.2	100.32
Schrippe															
DR30-4_wr	49.32	15.25	7.58		10.16	13.13	1.93	0.17	0.96	0.07	0.16		0.01	1.4	100.10
Ammonit															
DR31-3_wr	50.38	15.33	7.26		10.12	13.48	1.90	0.12	0.94	0.06	0.17		0.00	0.7	100.42
Undated Seamounts Samples															
Pan-Cake															
DR1-5	49.65	15.92	8.74	9.28		12.98	2.03	0.04	0.88	0.05	0.17		0.27		100.01
Half-Moon															
DR2-1_wr	49.20	16.14	6.23		9.34	10.95	2.91	0.48	1.49	0.15	0.12		0.01	3.1	100.12
Boxer															
DR7-2_wr[a]	48.63	17.01	6.86		7.64	11.99	2.80	0.32	1.20	0.15	0.08	0.049		3.0	99.82
Horseshoe															
DR9-5_wr[a]	48.55	16.11	8.78		9.65	13.12	1.77	0.15	0.70	0.05	0.15	0.064		0.7	99.79
Spiegelei															
DR15-5	48.18	17.40	6.01	9.50		8.80	3.97	0.98	2.62	0.42	0.15		0.18		98.26
DR15-6_wr	49.14	17.13	3.50		9.26	9.29	3.69	1.18	2.56	0.73	0.35		0.03	3.1	99.92
Eye															
DR17-1	49.04	14.96	6.88	11.11		11.79	3.02	0.13	1.83	0.15	0.20		0.32		99.47
DR17-1_wr	48.98	15.30	5.93		10.43	11.92	2.90	0.28	1.70	0.16	0.16		0.00	2.2	99.96
DR17-7	48.12	16.62	8.25	9.98		11.93	2.62	0.07	1.28	0.09	0.16		0.26		99.40
DR17-7_wr	48.48	19.24	4.07		10.05	12.63	2.68	0.22	1.17	0.10	0.18		0.02	1.7	100.55
DR17-19	50.38	15.16	6.98	9.92		11.53	2.97	0.19	1.71	0.17	0.15		0.21		99.39
DR17-20	50.24	15.26	6.91	10.01		11.60	3.02	0.18	1.70	0.14	0.17		0.21		99.44
Pickel															
DR21-1	48.59	17.15	6.69	9.34		10.39	3.51	0.42	2.08	0.33	0.17		0.17		98.84
DR21-2	48.86	17.00	6.76	9.24		10.42	3.36	0.41	2.03	0.29	0.20		0.17		98.75
Unnamed															
TVG22-1	48.45	17.37	7.56	9.51		10.89	3.10	0.18	1.71	0.17	0.17		0.19		99.33
TVG22-4_wr	47.94	17.24	4.85		10.35	10.82	3.22	0.38	1.73	0.19	0.14		0.00	3.1	100.00
Bend Fault															
DR23-1_wr	48.00	17.49	8.12		8.74	12.02	2.32	0.05	1.05	0.06	0.13		0.07	1.8	99.89
DR23-6	49.69	15.84	8.10	9.33		12.37	2.62	0.05	1.28	0.08	0.17		0.30		99.87
DR24-2_wr	45.38	15.63	9.01		10.11	9.42	2.78	0.24	1.64	0.17	0.13		0.14	5.4	100.06
DR24-20_wr[a]	45.67	15.32	9.43		9.42	9.47	3.02	0.19	1.54	0.16	0.15	0.048		5.3	99.72
DR25-4	50.75	14.89	7.38	9.86		12.25	2.67	0.07	1.39	0.09	0.17		0.20		99.75
Little Bend															
DR26-3	50.71	14.77	7.57	9.94		12.48	2.32	0.07	1.13	0.08	0.18		0.21		99.47

. . . continued

Element/Sample (SO208)	SiO$_2$	Al$_2$O$_3$	MgO	FeO^T	Fe$_2$O$_3$	CaO	Na$_2$O	K$_2$O	TiO$_2$	P$_2$O$_5$	MnO	Cr$_2$O$_3$	SO$_3$	LOI %	Total
Schrippe															
DR30-1	47.76	16.76	6.45	10.67		10.09	3.40	0.39	2.31	0.28	0.19		0.20		98.50
DR30-1_wr	48.59	17.12	3.18		10.83	10.54	3.02	0.60	2.17	0.44	0.11		0.01	3.6	100.24
DR30-2	48.38	17.86	5.34	9.45		8.27	4.27	1.48	2.85	0.50	0.15		0.13		98.75
Ammonit															
DR31-1	50.54	14.35	6.98	10.77		11.91	2.66	0.06	1.46	0.10	0.21		0.22		99.27
DR31-2	50.35	15.29	8.05	9.45		13.02	1.97	0.02	0.94	0.06	0.16		0.19		99.50
DR31-2_wr	49.00	15.01	7.67		10.12	13.17	1.87	0.16	0.93	0.05	0.16		0.03	1.0	99.21
Guardian															
DR32-1	50.17	14.93	7.08	10.71		12.02	2.79	0.08	1.39	0.08	0.20		0.23		99.76
DR32-2_wr	44.35	16.68	3.32		9.97	12.05	3.07	0.83	2.39	0.67	0.13		0.04	6.5	100.03
DR32-6_wr	48.32	18.58	4.37		9.82	12.95	2.56	0.23	1.31	0.14	0.14		0.00	2.3	100.68
Bagel															
DR36-1_wr	49.38	16.93	5.44		9.60	12.95	2.23	0.28	1.09	0.09	0.13		0.02	2.4	100.50
Ojo															
DR37-1_wr	51.31	14.38	7.33		10.27	12.25	2.50	0.22	1.41	0.11	0.20		0.01	0.8	100.75
DR37-3_wr	50.79	14.22	7.31		10.75	12.18	2.48	0.19	1.40	0.13	0.20		0.03	0.0	99.68
Zecke															
DR38-1	49.58	16.22	8.85	8.86		12.79	1.96	0.02	0.87	0.06	0.14		0.18		99.53
DR38-2	50.15	15.66	8.40	9.07		12.82	2.04	0.03	0.91	0.05	0.17		0.18		99.51
DR38-4_wr	48.43	16.31	8.00		10.30	13.32	1.96	0.12	1.02	0.08	0.16		0.00	0.9	100.64
Hook															
DR39-1_wr	49.39	15.04	6.98		10.61	12.98	2.15	0.19	1.10	0.09	0.17		0.00	1.8	100.48
DR39-2_wr	49.58	15.71	6.95		9.01	13.22	2.21	0.13	1.09	0.12	0.20		0.00	1.6	99.78
DR39-8-VC	50.11	15.38	8.17	9.27		12.72	2.26	0.03	1.02	0.06	0.20		0.19		99.42
DR39-9-VC	49.95	15.39	8.20	9.53		12.60	2.21	0.03	1.06	0.06	0.20		0.19		99.42
DR40-1_wr	50.13	15.31	7.22		10.19	13.10	2.19	0.24	1.07	0.12	0.16		0.01	0.4	100.16

^{a} = major element concentrations determined by ICP-OES

wr = denotes powders of whole rock samples analysed by XRF

all glass samples (including samples marked with VC) analysed by EPMA
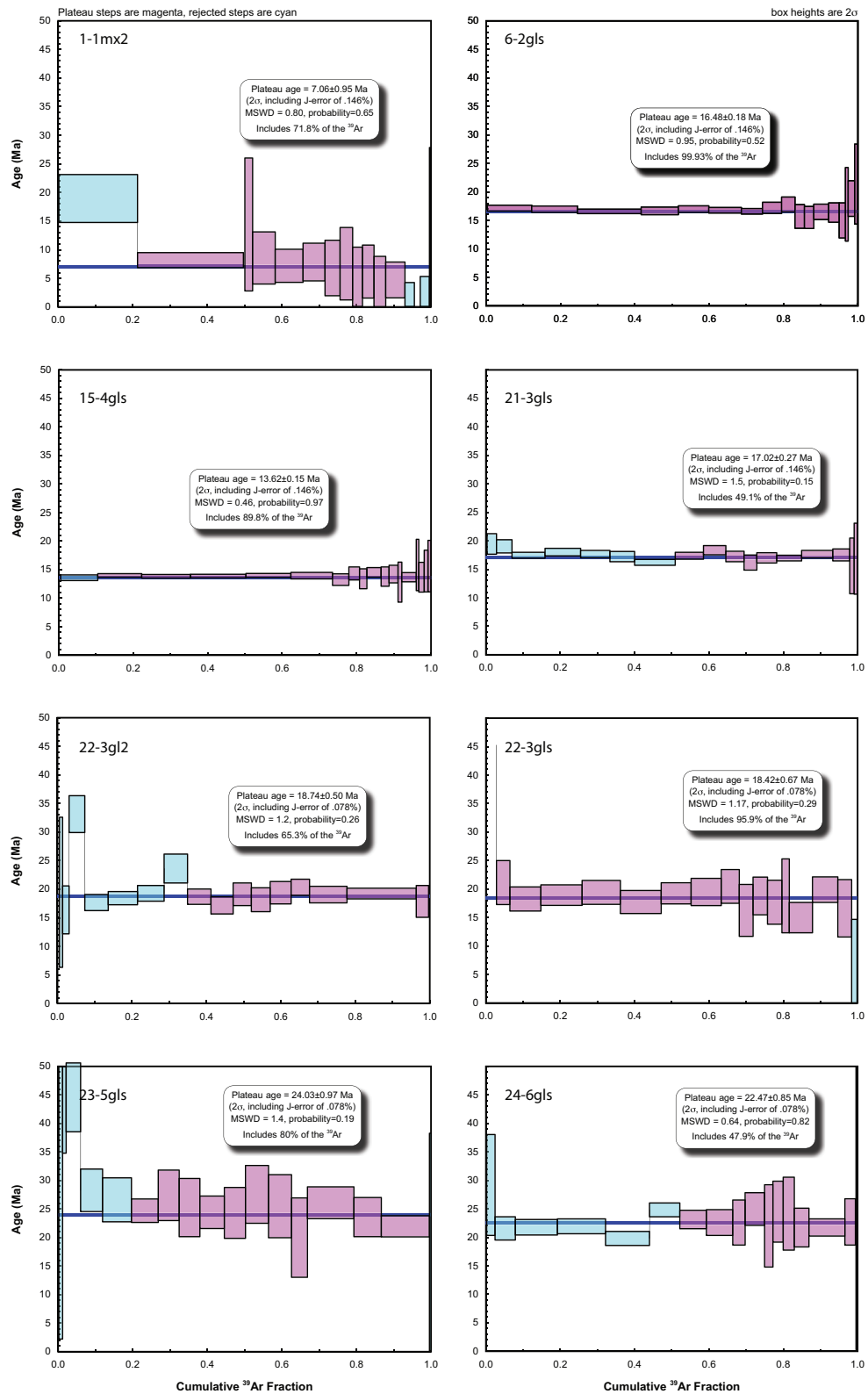
Figure A.2: ^{40}Ar/^{39}Ar plateau diagrams of all age dated seamounts - Part1
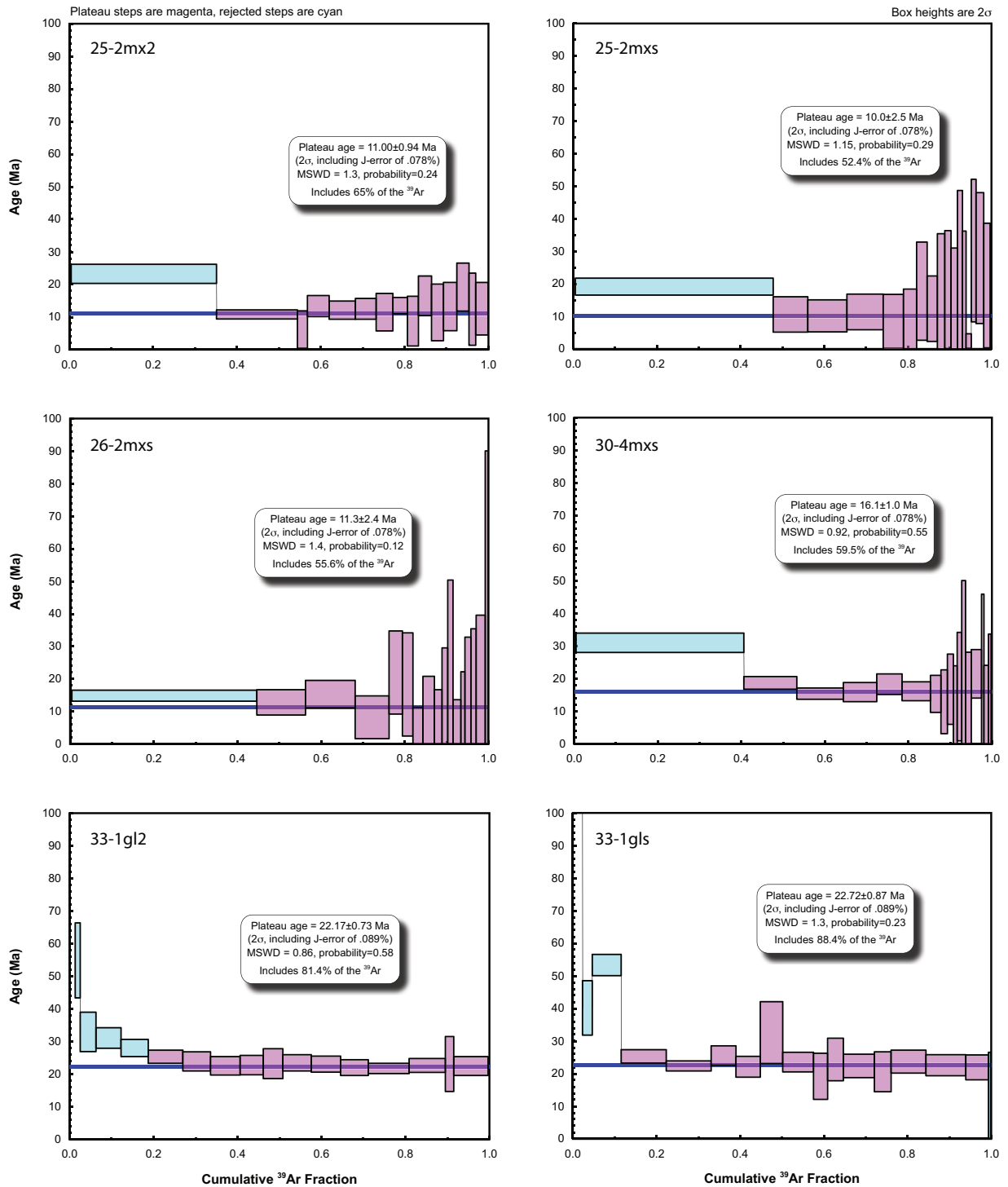
Figure A.3: ^{40}Ar/^{39}Ar plateau diagrams of all age dated seamounts - Part2

Table A.2: Major element composition (in wt.%) of all samples of the CPS.

Element/Sample (SO208)	Rb	Sr	Y	Zr	Nb	Ba	La	Ce	Pr	Nd	Sm	Eu	Gd	Tb	Dy	Ho	Er	Tm	Yb	Lu	Hf	Ta	Pb	Th	U
Near-Ridge Cocos Plate Seamount Samples																									
Egg																									
DR6-2	21.4	357	26.5	159	29.3	217	18.0	36.9	4.54	20.2	4.95	1.67	5.23	0.816	5.16	1.01	2.87	0.401	2.65	0.381	3.70	1.73	1.23	2.65	0.636
Bend Fault																									
DR23-5	1.37	125	33.2	97.6	2.95	15.5	3.79	11.1	1.87	10.6	3.78	1.36	5.11	0.896	6.14	1.29	3.82	0.545	3.72	0.531	2.65	0.186	0.496	0.254	0.082
DR23-5_wr	2.59	144	30.7	89.0	2.53	11.9	3.07	9.91	1.72	9.31	3.28	1.24	4.42	0.802	5.37	1.13	3.15	0.468	3.10	0.451	2.34	0.169	0.499	0.210	0.090
DR24-6	3.52	216	37.6	147	6.57	35.1	6.70	18.4	2.90	14.9	4.69	1.74	5.98	1.03	6.56	1.41	3.91	0.576	3.76	0.542	3.60	0.395	1.19	0.477	0.138
Kringel																									
DR33-1	2.06	134	26.1	76.2	2.76	16.0	3.27	9.41	1.59	8.57	2.96	1.15	3.97	0.686	4.79	1.04	2.99	0.441	2.85	0.443	2.11	0.180	0.472	0.202	0.064
DR33-1_wr	2.47	155	29.7	78.9	2.54	31.8	4.39	9.48	1.66	9.01	3.02	1.16	4.03	0.719	4.84	1.03	2.88	0.426	2.81	0.428	2.07	0.155	0.652	0.217	0.146
Intraplate Seamount Samples																									
Pan-Cake																									
DR1-1_wr	2.59	86.4	28.0	53.3	0.822	2.41	1.64	5.47	1.08	6.27	2.45	0.957	3.57	0.668	4.62	1.00	2.82	0.428	2.86	0.429	1.60	0.076	0.320	0.066	0.211
DR1-1_wr	2.57	86.6	27.8	53.2	0.797	2.26	1.64	5.47	1.08	6.29	2.46	0.965	3.56	0.665	4.61	1.00	2.83	0.429	2.83	0.428	1.60	0.071	0.316	0.062	0.210
Spiegelei																									
DR15-4	23.6	386	41.4	241	34.3	223	21.6	47.0	6.01	25.8	6.50	2.23	7.24	1.18	6.99	1.46	3.92	0.572	3.70	0.525	5.09	1.79	1.67	2.54	0.683
DR15-4	23.0	384	37.8	242	35.7	238	22.2	47.6	6.17	27.2	6.71	2.28	7.22	1.13	7.27	1.49	4.16	0.599	3.88	0.584	5.58	2.18	1.75	2.64	0.709
DR15-4_wr	16.2	422	43.8	247	31.8	245	24.2	47.3	6.29	27.4	6.70	2.23	7.40	1.20	7.34	1.48	4.07	0.591	3.87	0.578	5.21	1.74	1.50	2.37	0.660
Pickel																									
DR21-3	4.76	232	35.5	210	11.5	38.4	11.0	28.1	4.01	19.6	5.45	1.82	6.19	1.03	6.73	1.37	4.04	0.575	3.92	0.553	4.56	0.725	1.12	0.927	0.293
DR21-3_wr	8.44	249	39.1	228	10.9	42.7	11.7	28.3	4.20	20.1	5.44	1.89	6.35	1.05	6.75	1.39	3.87	0.570	3.76	0.571	4.59	0.639	1.19	0.750	0.377
Unnamed																									
TVG22-3	3.07	237	31.3	137	5.41	29.7	5.98	16.7	2.65	13.6	4.20	1.53	5.22	0.869	5.89	1.25	3.62	0.523	3.38	0.518	3.44	0.368	0.836	0.426	0.127
Bend Fault																									
DR25-2	0.920	110	30.5	83.2	1.91	9.73	2.85	8.91	1.57	8.87	3.21	1.23	4.49	0.791	5.65	1.22	3.58	0.526	3.42	0.530	2.42	0.131	0.488	0.147	0.049
DR25-2_wr	3.12	134	29.8	78.4	1.76	6.70	2.48	8.45	1.50	8.34	3.03	1.16	4.18	0.762	5.16	1.09	3.04	0.455	2.98	0.444	2.09	0.121	0.406	0.128	0.458
Little Bend																									
DR26-2_wr	2.06	105	27.6	63.2	2.02	22.4	2.69	7.64	1.30	7.27	2.64	1.02	3.69	0.681	4.71	1.02	2.90	0.433	2.91	0.442	1.77	0.135	0.461	0.172	0.105
DR26-2_wr	2.04	105	27.6	63.1	1.94	22.0	2.66	7.59	1.29	7.22	2.63	1.02	3.68	0.685	4.74	1.02	2.89	0.433	2.89	0.440	1.76	0.125	0.458	0.167	0.104
Schrippe																									
DR30-4_wr	11.7	272	40.9	188	10.2	45.1	10.5	25.3	3.86	19.0	5.62	1.94	6.69	1.12	7.08	1.44	3.94	0.571	3.74	0.552	4.17	0.614	1.15	0.781	0.255
Ammonit																									
DR31-3_wr	2.16	59.9	24.5	36.5	0.403	0.800	0.630	3.47	0.731	4.55	1.96	0.793	3.02	0.581	4.11	0.899	2.58	0.395	2.62	0.392	1.24	0.049	0.243	0.043	0.029
Undated Seamounts Samples																									
Pan-Cake																									
DR1-5	0.227	81.6	20.5	42.1	0.645	2.23	1.31	4.53	0.816	4.92	1.92	0.775	2.80	0.515	3.67	0.781	2.36	0.341	2.37	0.341	1.24	0.045	0.195	0.049	0.015
Half-Moon																									
DR2-1_wr	24.3	174	30.4	101	3.05	93.0	3.77	11.5	1.96	10.4	3.48	1.31	4.56	0.806	5.33	1.11	3.07	0.453	2.98	0.440	2.49	0.197	0.548	0.214	0.195
Boxer																									
DR7-2_wr	9.50	147	26.1	85.1	4.50	33.0	4.66	10.9	1.79	9.42	2.96	1.12	3.82	0.663	4.40	0.924	2.57	0.375	2.48	0.378	2.14	0.263	0.549	0.310	0.184
Horseshoe																									
DR9-5_wr	2.96	68.2	18.0	29.9	0.639	8.18	1.18	3.43	0.628	3.76	1.51	0.618	2.27	0.427	3.02	0.664	1.91	0.290	1.96	0.300	0.973	0.045	0.321	0.064	0.038
Spiegelei																									
DR15-5	22.7	381	37.1	238	34.9	232	21.7	46.3	6.05	26.6	6.58	2.23	7.09	1.10	7.14	1.46	4.00	0.593	3.79	0.580	5.40	2.14	1.74	2.63	0.685
DR15-6_wr	19.2	423	40.8	243	31.7	289	22.9	47.1	6.18	26.7	6.60	2.21	7.23	1.17	7.19	1.45	3.90	0.569	3.72	0.551	5.22	1.73	1.44	2.36	0.712
Eye																									
DR17-1_wr	6.41	169	34.7	115	3.03	13.1	3.91	12.7	2.20	11.9	4.00	1.49	5.19	0.915	6.05	1.26	3.49	0.519	3.41	0.507	2.83	0.194	0.532	0.194	0.125

. . . continued

Element/Sample (SO208)	Rb	Sr	Y	Zr	Nb	Ba	La	Ce	Pr	Nd	Sm	Eu	Gd	Tb	Dy	Ho	Er	Tm	Yb	Lu	Hf	Ta	Pb	Th	U
DR17-7	0.552	142	25.5	76.0	1.63	6.09	2.71	8.60	1.44	8.17	2.86	1.10	3.82	0.676	4.70	0.986	2.96	0.435	2.99	0.428	2.01	0.109	0.361	0.130	0.041
DR17-7_wr	5.45	166	24.3	75.0	1.47	31.5	2.58	7.91	1.36	7.57	2.62	1.05	3.52	0.631	4.27	0.901	2.55	0.380	2.53	0.384	1.91	0.098	0.479	0.110	0.400
DR17-7_wr	5.44	168	24.6	75.2	1.47	31.0	2.58	7.97	1.37	7.62	2.63	1.06	3.52	0.635	4.31	0.911	2.57	0.383	2.53	0.387	1.90	0.098	0.571	0.112	0.406
DR17-19	2.52	165	32.7	120	5.13	25.8	5.42	15.0	2.41	12.7	4.12	1.49	5.32	0.895	6.13	1.32	3.76	0.557	3.53	0.538	3.27	0.354	0.747	0.381	0.118
DR17-20	2.56	170	32.7	120	5.20	27.0	5.49	15.3	2.46	13.0	4.15	1.53	5.36	0.913	6.19	1.32	3.77	0.551	3.51	0.545	3.23	0.348	1.16	0.382	0.118
Pickel																									
DR21-1	4.88	232	36.3	219	11.8	38.4	11.1	28.3	4.15	19.8	5.40	1.82	6.31	1.02	6.86	1.46	4.16	0.609	3.91	0.608	4.95	0.785	1.33	0.858	0.286
DR21-2	4.62	219	36.3	209	11.2	36.8	10.7	27.1	3.98	19.2	5.33	1.80	6.25	1.01	6.79	1.45	4.12	0.605	3.90	0.608	4.78	0.763	1.22	0.826	0.272
Unnamed																									
TVG22-1	3.06	237	30.7	135	5.40	29.9	5.97	16.9	2.66	13.7	4.18	1.54	5.19	0.866	5.82	1.24	3.56	0.522	3.36	0.526	3.40	0.364	0.843	0.427	0.129
TVG22-4_wr	6.77	253	33.5	142	5.23	32.3	6.30	17.4	2.80	14.2	4.33	1.57	5.31	0.908	5.89	1.21	3.35	0.494	3.24	0.477	3.23	0.321	0.727	0.381	0.208
Bend Fault																									
DR23-1_wr	0.658	118	24.0	58.9	1.11	3.76	1.55	6.04	1.13	6.45	2.42	0.973	3.38	0.620	4.18	0.891	2.48	0.370	2.42	0.360	1.64	0.084	0.243	0.089	0.035
DR23-6	0.813	111	34.2	82.0	1.77	9.52	2.63	8.12	1.46	8.46	3.28	1.24	4.73	0.857	5.73	1.28	3.58	0.536	3.50	0.510	2.36	0.111	0.509	0.151	0.040
DR24-2_wr	2.39	257	29.4	125	5.86	32.1	5.67	15.8	2.51	12.7	3.91	1.43	4.81	0.825	5.30	1.09	2.96	0.436	2.85	0.424	2.94	0.348	0.612	0.403	0.133
DR24-20_wr	1.46	183	29.2	118	5.36	28.0	5.32	15.0	2.41	12.3	3.79	1.40	4.70	0.802	5.22	1.07	2.95	0.434	2.85	0.422	2.83	0.329	0.320	0.376	0.125
DR25-4	0.874	109	29.2	79.3	1.85	9.41	2.74	8.71	1.54	8.59	3.13	1.20	4.33	0.762	5.35	1.15	3.38	0.497	3.24	0.499	2.26	0.128	1.91	0.141	0.046
Little Bend																									
DR26-3	1.07	90.6	24.7	60.0	2.05	11.0	2.37	6.85	1.20	6.59	2.41	0.950	3.50	0.611	4.44	0.975	2.84	0.426	2.79	0.429	1.74	0.133	0.346	0.156	0.049
Schrippe																									
DR30-1	7.29	231	39.9	195	11.8	63.7	10.2	26.1	3.96	19.7	5.89	2.02	7.09	1.13	7.64	1.60	4.46	0.654	4.13	0.632	4.75	0.784	1.13	0.919	0.265
DR30-1_wr	12.6	267	40.2	192	10.6	48.4	10.1	25.6	3.89	19.1	5.62	1.96	6.72	1.13	7.15	1.45	3.92	0.574	3.72	0.552	4.24	0.621	0.980	0.784	0.236
DR30-2	40.8	595	31.3	267	57.1	421	34.4	68.5	8.34	34.6	7.49	2.47	7.21	1.05	6.36	1.24	3.33	0.463	2.89	0.435	6.19	3.62	2.65	4.71	1.14
Ammonit																									
DR31-1	0.684	86.7	32.5	80.5	1.57	6.90	2.39	7.89	1.49	8.73	3.32	1.27	4.69	0.823	5.87	1.30	3.79	0.560	3.67	0.565	2.41	0.110	0.377	0.109	0.035
DR31-2	0.095	56.3	21.5	36.5	0.329	1.18	0.90	3.40	0.699	4.39	1.87	0.767	2.85	0.527	3.86	0.860	2.54	0.382	2.50	0.391	1.23	0.026	0.194	0.021	0.008
DR31-2_wr	3.15	65.3	23.4	37.2	0.366	2.90	0.64	3.47	0.731	4.55	1.95	0.784	2.95	0.559	3.96	0.863	2.46	0.373	2.48	0.372	1.25	0.041	0.192	0.027	0.066
DR31-3_wr	2.16	59.9	24.5	36.5	0.403	0.800	0.630	3.47	0.731	4.55	1.96	0.793	3.02	0.581	4.11	0.899	2.58	0.395	2.62	0.392	1.24	0.049	0.243	0.043	0.029
Guardian																									
DR32-1	1.02	109	30.6	76.9	2.14	11.7	2.77	8.20	1.44	8.08	3.03	1.17	4.38	0.776	5.54	1.22	3.55	0.529	3.41	0.537	2.21	0.144	0.445	0.167	0.050
DR32-2_wr	16.5	481	34.2	277	41.0	218	29.5	60.1	7.75	32.4	7.27	2.36	7.29	1.11	6.53	1.26	3.31	0.469	3.02	0.439	5.79	2.26	1.81	3.16	0.767
DR32-6_wr	5.02	172	28.1	84.5	2.02	10.8	3.13	9.24	1.56	8.56	2.94	1.15	3.97	0.716	4.85	1.03	2.91	0.432	2.89	0.440	2.08	0.127	0.477	0.148	0.132
Bagel																									
DR36-1_wr	6.43	107	24.7	56.1	1.27	14.0	1.68	5.88	1.09	6.26	2.38	0.934	3.35	0.621	4.25	0.904	2.52	0.381	2.50	0.374	1.61	0.093	0.304	0.092	0.111
DR36-1_wr	6.45	107	24.7	56.1	1.26	14.2	1.68	5.86	1.09	6.25	2.36	0.938	3.38	0.620	4.21	0.898	2.51	0.376	2.49	0.371	1.58	0.089	0.291	0.090	0.111
Ojo																									
DR37-1_wr	5.88	121	33.6	71.6	1.06	26.2	1.71	6.70	1.30	7.69	3.05	1.19	4.47	0.830	5.65	1.21	3.40	0.511	3.37	0.501	2.07	0.080	0.394	0.074	0.104
DR37-3_wr	3.60	115	32.6	67.8	0.996	26.8	2.07	6.84	1.29	7.79	3.06	1.19	4.42	0.816	5.59	1.19	3.36	0.500	3.29	0.505	2.02	0.070	0.440	0.081	0.217
Zecke																									
DR38-1	0.150	58.9	19.5	34.4	0.427	1.66	0.906	3.39	0.664	4.07	1.74	0.724	2.62	0.480	3.51	0.768	2.26	0.342	2.223	0.351	1.12	0.028	0.180	0.027	0.011
DR38-2	0.177	62.6	20.9	39.4	0.495	1.88	1.06	3.94	0.757	4.61	1.91	0.779	2.85	0.518	3.71	0.821	2.45	0.364	2.370	0.369	1.26	0.034	0.213	0.035	0.013
DR38-4_wr	1.65	78.4	24.5	45.6	0.620	3.17	0.916	4.31	0.871	5.20	2.16	0.865	3.21	0.606	4.19	0.900	2.54	0.385	2.548	0.382	1.41	0.059	0.251	0.047	0.055
Hook																									
DR39-1_wr	4.27	88.5	26.7	51.0	0.811	8.90	1.19	5.03	0.990	5.94	2.41	0.953	3.50	0.653	4.55	0.979	2.77	0.416	2.756	0.413	1.56	0.067	0.230	0.059	0.105
DR39-2_wr	2.19	85.9	27.3	49.8	0.750	28.3	1.70	5.02	0.978	5.95	2.40	0.954	3.51	0.649	4.51	0.978	2.80	0.420	2.790	0.428	1.56	0.053	0.343	0.074	0.159
DR39-8-VC	0.176	74.4	23.2	46.6	0.543	2.10	1.24	4.37	0.855	5.21	2.13	0.863	3.16	0.569	4.17	0.903	2.67	0.402	2.642	0.400	1.44	0.038	0.221	0.041	0.014

. . . continued

Element/Sample (SO208)	Rb	Sr	Y	Zr	Nb	Ba	La	Ce	Pr	Nd	Sm	Eu	Gd	Tb	Dy	Ho	Er	Tm	Yb	Lu	Hf	Ta	Pb	Th	U
DR39-9-VC	0.294	73.6	23.9	48.7	0.751	3.18	1.35	4.63	0.908	5.53	2.22	0.901	3.29	0.599	4.33	0.960	2.83	0.414	2.741	0.425	1.54	0.052	0.237	0.051	0.017
DR40-1_wr	5.36	85.6	25.2	49.5	0.598	6.60	1.16	4.72	0.955	5.72	2.33	0.921	3.39	0.635	4.41	0.949	2.66	0.402	2.661	0.400	1.52	0.052	0.264	0.037	0.165

wr = denotes powders of whole rock samples analysed by solution ICP-MS

all glass samples (including samples marked with VC) analysed by LA-ICP-MS

RM/ Elements	BCR-2G N=407 Average (ppm)	±	SD ppm	RSD %	BIR-1G N=64 Average (ppm)	±	SD ppm	RSD %	BHVO-2G N=59 Average (ppm)	±	SD ppm	RSD %
Rb	49.2	±	1.5	3.1	0.209	±	0.02	8.1	9.48	±	0.21	2.2
Sr	327	±	9.6	2.9	111	±	2.62	2.4	402	±	9.27	2.3
Y	31.0	±	1.9	6.0	13.9	±	0.68	4.9	24.3	±	0.85	3.5
Zr	164	±	10.9	6.7	13.2	±	0.54	4.1	164	±	6.30	3.8
Nb	12.2	±	0.3	2.5	0.532	±	0.02	4.0	18.3	±	0.47	2.5
Ba	671	±	22.0	3.3	6.43	±	0.23	3.6	130	±	6.08	4.7
La	24.0	±	0.8	3.3	0.585	±	0.02	3.5	15.0	±	0.60	4.0
Ce	52.5	±	1.5	2.8	1.90	±	0.07	3.6	37.6	±	1.47	3.9
Pr	6.39	±	0.2	3.2	0.363	±	0.01	2.8	5.20	±	0.18	3.4
Nd	27.4	±	0.9	3.4	2.32	±	0.10	4.3	24.1	±	1.19	4.9
Sm	6.18	±	0.3	4.1	1.06	±	0.05	4.7	5.99	±	0.32	5.3
Eu	1.845	±	0.1	3.6	0.511	±	0.02	4.7	2.03	±	0.10	5.0
Gd	6.08	±	0.4	6.2	1.73	±	0.09	5.3	6.04	±	0.31	5.2
Tb	0.912	±	0.1	6.9	0.329	±	0.02	5.7	0.885	±	0.05	5.8
Dy	5.93	±	0.4	6.0	2.42	±	0.13	5.2	5.23	±	0.29	5.5
Ho	1.17	±	0.1	6.2	0.526	±	0.03	5.6	0.949	±	0.05	5.6
Er	3.30	±	0.2	7.2	1.59	±	0.09	5.5	2.49	±	0.15	5.9
Tm	0.472	±	0.0	6.8	0.234	±	0.01	5.8	0.324	±	0.02	6.2
Yb	3.24	±	0.2	5.6	1.61	±	0.09	5.5	2.02	±	0.13	6.2
Lu	0.466	±	0.0	6.7	0.234	±	0.01	6.2	0.274	±	0.02	6.4
Hf	4.29	±	0.4	8.7	0.534	±	0.03	5.5	4.34	±	0.23	5.2
Ta	0.760	±	0.0	5.6	0.036	±	0.00	9.8	1.19	±	0.07	5.7
Pb	10.9	±	0.5	4.9	3.55	±	0.17	4.8	1.73	±	0.14	8.0
Th	5.63	±	0.5	9.1	0.031	±	0.01	16.4	1.31	±	0.12	9.3
U	1.72	±	0.1	5.1	0.049	±	0.02	46.0	0.443	±	0.03	7.8

Figure A.4: Standard values for LA-ICP-MS measurements.

RM/ Elements	GOR128-G N=43 Average (ppm)	±	SD ppm	RSD %	GOR132-G N=39 Average (ppm)	±	SD ppm	RSD %	St.HS. 6|80-G N=43 Average (ppm)	±	SD ppm	RSD %	KL-2G N=37 Average (ppm)	±	SD ppm	RSD %
Rb	0.423	±	0.02	4.2	2.242	±	0.08	3.8	31.3	±	1.15	3.7	9.16	±	0.34	3.7
Sr	28.5	±	1.02	3.6	14.3	±	0.68	4.7	480	±	16.55	3.4	345	±	7.21	2.1
Y	10.8	±	0.58	5.4	11.6	±	0.90	7.7	10.6	±	0.71	6.7	21.4	±	1.59	7.4
Zr	8.80	±	0.57	6.5	8.76	±	0.79	9.0	108	±	8.22	7.6	127	±	9.58	7.6
Nb	0.094	±	0.00	4.8	0.063	±	0.01	15.7	6.86	±	0.18	2.6	14.5	±	0.27	1.8
Ba	1.04	±	0.06	6.0	0.776	±	0.06	7.8	308	±	11.93	3.9	122	±	4.27	3.5
La	0.111	±	0.01	10.0	0.080	±	0.00	4.5	11.7	±	0.41	3.5	12.5	±	0.38	3.0
Ce	0.455	±	0.02	5.1	0.371	±	0.02	6.4	26.5	±	0.70	2.6	32.8	±	0.88	2.7
Pr	0.096	±	0.00	5.1	0.082	±	0.00	4.4	3.07	±	0.11	3.5	4.37	±	0.13	3.1
Nd	0.730	±	0.03	3.8	0.670	±	0.06	9.2	12.6	±	0.44	3.5	20.5	±	0.68	3.3
Sm	0.495	±	0.02	4.4	0.482	±	0.03	6.7	2.65	±	0.12	4.5	5.17	±	0.21	4.0
Eu	0.255	±	0.01	3.3	0.243	±	0.01	5.1	0.902	±	0.04	4.2	1.82	±	0.06	3.1
Gd	1.06	±	0.06	6.1	1.07	±	0.09	8.2	2.38	±	0.17	7.3	5.11	±	0.32	6.3
Tb	0.224	±	0.01	6.1	0.238	±	0.02	8.6	0.337	±	0.03	7.9	0.751	±	0.06	7.6
Dy	1.80	±	0.10	5.5	1.95	±	0.14	7.4	2.06	±	0.13	6.3	4.61	±	0.27	5.8
Ho	0.409	±	0.02	5.5	0.450	±	0.04	8.3	0.389	±	0.03	7.0	0.840	±	0.05	6.2
Er	1.24	±	0.08	6.7	1.39	±	0.12	8.8	1.08	±	0.09	8.5	2.17	±	0.16	7.3
Tm	0.187	±	0.01	6.0	0.210	±	0.02	8.7	0.154	±	0.01	8.6	0.286	±	0.02	7.1
Yb	1.30	±	0.06	4.9	1.47	±	0.10	6.4	1.08	±	0.07	6.5	1.88	±	0.10	5.4
Lu	0.186	±	0.01	6.8	0.213	±	0.02	8.4	0.154	±	0.01	8.0	0.248	±	0.02	6.8
Hf	0.300	±	0.03	9.9	0.309	±	0.03	10.8	2.73	±	0.26	9.6	3.27	±	0.26	8.1
Ta	0.018	±	0.00	13.8	0.026	±	0.00	15.0	0.413	±	0.03	6.2	0.883	±	0.04	4.0
Pb	0.321	±	0.03	8.7	20.7	±	1.01	4.9	11.6	±	0.71	6.1	1.97	±	0.07	3.8
Th	0.008	±	0.00	26.3	0.006	±	0.00	39.4	2.20	±	0.22	10.1	0.907	±	0.05	5.9
U	0.012	±	0.00	18.0	0.045	±	0.00	9.5	1.06	±	0.05	4.7	0.589	±	0.04	7.2

RM/Elements	BCR-2 N=3 Average (ppm)	SD ppm	RSD %	BIR-1 N=6 Average (ppm)	SD ppm	RSD %	BHVO-2 N=6 Average (ppm)	SD ppm	RSD %
Rb	49.0 ±	0.1	0.2	0.214 ±	0.0	3.2	9.53 ±	0.0	0.5
Sr	350 ±	0.8	0.2	107 ±	3.2	3.0	387 ±	12.3	3.2
Y	35.7 ±	0.2	0.5	15.4 ±	0.2	1.1	25.5 ±	0.2	1.0
Zr	190 ±	0.3	0.1	14.1 ±	0.2	1.6	175 ±	4.5	2.6
Nb	12.1 ±	0.0	0.4	0.536 ±	0.0	3.9	17.7 ±	0.1	0.5
Ba	684 ±	2.5	0.4	6.18 ±	0.1	1.3	132 ±	0.9	0.7
La	26.0 ±	0.0	0.2	0.571 ±	0.1	11.4	15.3 ±	0.2	1.3
Ce	53.4 ±	0.1	0.2	1.88 ±	0.0	0.8	37.5 ±	0.5	1.2
Pr	6.96 ±	0.0	0.1	0.373 ±	0.0	0.8	5.31 ±	0.1	1.3
Nd	29.3 ±	0.1	0.4	2.42 ±	0.0	0.5	24.8 ±	0.1	0.4
Sm	6.71 ±	0.0	0.3	1.11 ±	0.0	0.5	6.13 ±	0.0	0.7
Eu	1.98 ±	0.0	0.6	0.526 ±	0.0	0.8	2.08 ±	0.0	0.4
Gd	6.83 ±	0.0	0.3	1.82 ±	0.0	0.6	6.22 ±	0.0	0.6
Tb	1.07 ±	0.0	0.2	0.358 ±	0.0	0.8	0.930 ±	0.0	1.4
Dy	6.55 ±	0.0	0.4	2.57 ±	0.0	0.8	5.32 ±	0.1	1.2
Ho	1.30 ±	0.0	0.1	0.570 ±	0.0	0.5	0.977 ±	0.0	1.2
Er	3.55 ±	0.0	0.5	1.63 ±	0.0	0.6	2.43 ±	0.0	0.8
Tm	0.521 ±	0.0	0.2	0.246 ±	0.0	0.6	0.326 ±	0.0	1.2
Yb	3.42 ±	0.0	0.1	1.64 ±	0.0	0.7	1.98 ±	0.0	1.4
Lu	0.508 ±	0.0	0.5	0.252 ±	0.0	1.2	0.281 ±	0.0	0.5
Hf	4.84 ±	0.0	0.3	0.579 ±	0.0	0.6	4.36 ±	0.0	0.6
Ta	0.710 ±	0.0	0.1	0.039 ±	0.0	11.5	1.03 ±	0.0	1.6
Pb	10.1 ±	0.1	1.0	3.03 ±	0.1	4.9	1.76 ±	0.1	8.4
Th	5.79 ±	0.0	0.1	0.031 ±	0.0	5.0	1.17 ±	0.0	1.7
U	1.65 ±	0.0	0.5	0.012 ±	0.0	5.5	0.415 ±	0.0	0.6

Figure A.5: Standard values for solution ICP-MS measurements.

Table A.3: Sr and Nd radiogenic isotope ratios of all samples of the CPS, including initial values.

Element/Sample (SO208)	age used for isotope initials	2SE (M)	$^{87}Sr/^{86}Sr\_L$	2SE (M)	$^{87}Rb/^{86}Sr$	$^{87}Sr/^{86}Sr\_i$	$^{143}Nd/^{144}Nd$	2SE (M)	εNd	$^{147}Sm/^{144}Nd$	$^{143}Nd/^{144}Nd\_i$	εNd_i
Near-Ridge Cocos Plate Seamount Samples												
Egg												
DR6-2	16.5	0.000003			0.173	0.704014	0.512948	0.000002	6.04	0.147	0.512932	5.73
Bend Fault												
DR23-5	24.0	0.000002			0.032	0.702745	0.513119	0.000003	9.38	0.215	0.513085	8.72
DR23-5_wr	24.0	0.000003	0.702753	0.000002	0.052	0.702834	0.513112	0.000003	9.24	0.212	0.513078	8.59
DR24-6	22.5	0.000003			0.047	0.702762	0.513082	0.000003	8.67	0.190	0.513054	8.12
Kringel												
DR33-1	22.4	0.000003			0.044	0.702804	0.513103	0.000003	9.06	0.208	0.513072	8.47
DR33-1_wr	22.4	0.000003			0.046	0.702844	0.513105	0.000002	9.10	0.202	0.513075	8.53
Intraplate Cocos Plate Seamount Samples												
Pan-Cake												
DR1-1_wr	7.1	0.000003			0.086	0.702537	0.513163	0.000003	10.25	0.235	0.513152	10.03
DR1-1_wr	7.1	0.000003			0.086	0.702592	0.513164	0.000003	10.26	0.235	0.513153	10.04
DR1-1_wr_average		0.000003			0.086	0.702564	0.513164	0.000003	10.25	0.235	0.513153	10.04
DR1-1_wr	7.1	0.000003			0.086	0.702562	0.513162	0.000003	10.22	0.235	0.513151	10.00
DR1-1_wr	7.1	0.000003			0.086	0.702562	0.513166	0.000003	10.30	0.235	0.513155	10.09
DR1-1_wr_average		0.000003			0.086	0.702562	0.513164	0.000003	10.26	0.235	0.513153	10.05
Spiegelei												
DR15-4	13.6	0.000003			0.175	0.702977	0.512992	0.000003	6.91	0.150	0.512979	6.65
DR15-4	13.6	0.000003			0.175	0.702985	0.513000	0.000003	7.06	0.150	0.512987	6.80
DR15-4_wr	13.6	0.000003			0.111	0.703055	0.512994	0.000003	6.93	0.147	0.512980	6.68
Pickel												
DR21-3	17.0	0.000003			0.059	0.702668	0.513072	0.000003	8.46	0.167	0.513053	8.09
DR21-3_wr	17.0	0.000003			0.098	0.702709	0.513069	0.000003	8.40	0.163	0.513051	8.05
Unnamed												
TVG22-3	18.6	0.000003			0.037	0.702739	0.513072	0.000003	8.46	0.186	0.513049	8.02
Bend Fault												
DR25-2_wr	10.9	0.000003			0.067	0.702686	0.513130	0.000002	9.59	0.219	0.513114	9.28
Little Bend												
DR26-2_wr	11.3	0.000004	0.702743	0.000003	0.056	0.702971	0.513116	0.000002	9.33	0.219	0.513100	9.02
Schrippe												
DR30-4_wr	16.1	0.000003			0.124	0.702948	0.513033	0.000002	7.71	0.178	0.513015	7.35
Ammonit												
DR31-3_wr	11.9	0.000003			0.104	0.702764	0.513123	0.000002	9.46	0.260	0.513103	9.06
Undated Cocos Plate Seamounts Samples												
Pan-Cake												
DR1-5	7.10	0.000002			0.008	0.702576	0.513168	0.000002	10.33	0.235	0.513157	10.12
DR1-5	7.10	0.000003			0.008	0.702526	0.513154	0.000003	10.06	0.235	0.513143	9.85
Half-Moon												
DR2-1_wr	18.55	0.000002			0.405	0.702700	0.513106	0.000002	9.14	0.201	0.513082	8.66
Boxer												
DR7-2_wr	16.35	0.000002			0.187	0.702884	0.513064	0.000003	8.31	0.189	0.513044	7.92
Horseshoe												

. . . continued

Element/Sample (SO208)	age used for isotope initials	2SE (M)	87Sr/86Sr _L	2SE (M)	87Rb/86Sr	87Sr/86Sr _i	143Nd/144Nd	2SE (M)	eNd	147Sm/144Nd	143Nd/144Nd _i	eNd _i
DR9-5_wr	15.75	0.000005			0.125	0.702773	0.513119	0.000002	9.38	0.242	0.513094	8.89
DR9-5_wr*	15.75	0.000003			0.125	0.702708	0.513117	0.000004	9.35	0.242	0.513092	8.86
Eye												
DR17-1_wr	18.05	0.000003			0.110	0.702735	0.513118	0.000002	9.36	0.202	0.513094	8.90
DR17-7	18.05	0.000003			0.011	0.702564	0.513099	0.000003	8.99	0.211	0.513074	8.51
DR17-7_wr	18.05	0.000004			0.094	0.702588	0.513105	0.000003	9.10	0.208	0.513080	8.62
DR17-20	18.05	0.000003			0.044	0.702749	0.513107	0.000002	9.14	0.192	0.513084	8.70
Unnamed												
TVG22-4_wr	18.6	0.000003			0.077	0.702778	0.513076	0.000003	8.55	0.184	0.513054	8.11
Bend Fault												
DR23-1_wr	24.0	0.000003			0.098	0.702788	0.513116	0.000002	9.32	0.225	0.513080	8.63
DR23-6	24.0	0.000003			0.021	0.702773	0.513107	0.000003	9.15	0.233	0.513071	8.44
DR24-20_wr	22.5	0.000003			0.023	0.702833	0.513080	0.000003	8.62	0.186	0.513052	8.09
Little Bend												
DR26-3	11.30	0.000003			0.034	0.702703	0.513114	0.000002	9.28	0.220	0.513097	8.96
Schrippe												
DR30-1	16.10	0.000003			0.091	0.702962	0.513026	0.000003	7.56	0.180	0.513007	7.19
DR30-2	16.10	0.000003			0.198	0.703338	0.512884	0.000003	4.79	0.130	0.512870	4.53
Guardian												
DR32-1	22.25	0.000003			0.027	0.702766	0.513087	0.000003	8.76	0.225	0.513054	8.12
DR32-2_wr	22.25	0.000003			0.099	0.703046	0.512953	0.000003	6.15	0.135	0.512934	5.77
DR32-2_wr	22.25	0.000003			0.099	0.703055	0.512952	0.000002	6.13	0.135	0.512933	5.75
DR32-6_wr	22.25	0.000003			0.084	0.702747	0.513118	0.000003	9.37	0.207	0.513088	8.78
Bagel												
DR36-1_wr	22.05	0.000003			0.116	0.702902	0.513099	0.000003	9.00	0.228	0.513067	8.36
Ojo												
DR37-1_wr	22.85	0.000003	0.702893	0.000003	0.140	0.703597	0.513107	0.000002	9.15	0.238	0.513071	8.45
DR37-3_wr	22.85	0.000003	0.702897	0.000003	0.091	0.703676	0.513101	0.000002	9.04	0.236	0.513066	8.35
DR37-3_wr	22.85	0.000003			0.091	0.703534	0.513108	0.000003	9.18	0.236	0.513073	8.49
Zecke												
DR38-1	22.85	0.000003			0.007	0.702684	0.513100	0.000002	9.02	0.257	0.513062	8.27
DR38-4_wr	22.85	0.000003	0.702694	0.000003	0.061	0.702965	0.513112	0.000002	9.25	0.250	0.513075	8.52
Hook												
DR39-2_wr	22.85	0.000005	0.702692	0.000003	0.074	0.702942	0.513116	0.000003	9.32	0.243	0.513079	8.61
DR39-2_wr	22.85	0.000003			0.074	0.702959	0.513117	0.000003	9.34	0.243	0.513081	8.64
DR39-9-VC	22.85	0.000003			0.012	0.702755	0.513112	0.000001	9.24	0.242	0.513076	8.54
DR40-1_wr	22.85	0.000002			0.181	0.702692	0.513124	0.000002	9.47	0.245	0.513087	8.76

* = isotope replicate analyses conducted on whole rock powder

_i = initial isotope ratio

_L = analysis using leached powder

wr = denotes powders of whole rock samples analysed by solution ICP-MS

all glass samples (including samples marked with VC) analysed by LA-ICP-MS

Sample / Seamount	age used for isotope initials (Ma)	206Pb/204Pb	2 SE(M)	207Pb/204Pb	2 SE(M)	208Pb/204Pb	2 SE(M)	207Pb/206Pb	2 SE(M)	208Pb/206Pb	2 SE(M)	238U/204Pb	232Th/204Pb	206Pb/204Pb_i	207Pb/204Pb_i	208Pb/204Pb_i	207Pb/206Pb_i	208Pb/206Pb_i
Near-Ridge Cocos Plate Seamount Samples																		
EGG																		
SO208 DR6-2	16.5	19.1039	0.0007	15.5985	0.0007	39.0140	0.0021	0.81651	0.00001	2.04220	0.00005	33.51	144.41	19.018	15.594	38.896	0.8200	2.0452
BEND FAULT																		
SO208 DR23-5	24.0	18.5517	0.0011	15.5135	0.0014	38.2039	0.0046	0.83623	0.00003	2.05932	0.00013	10.42	33.57	18.513	15.512	38.164	0.8379	2.0615
SO208 DR23-5_wr	24.0	18.5746	0.0023	15.5185	0.0019	38.2175	0.0046	0.83547	0.00002	2.05752	0.00004	11.45	27.57	18.532	15.517	38.185	0.8373	2.0605
SO208 DR24-6	22.5	18.6492	0.0008	15.5238	0.0008	38.2612	0.0022	0.83241	0.00001	2.05163	0.00004	7.32	26.18	18.624	15.523	38.232	0.8335	2.0529
KRINGEL																		
SO208 DR33-1	22.4	18.5404	0.0006	15.5193	0.0006	38.1697	0.0016	0.83706	0.00001	2.05874	0.00002	8.57	27.98	18.511	15.518	38.139	0.8383	2.0604
SO208 DR33-1_wr	22.4	18.5396	0.0014	15.5171	0.0012	38.1636	0.0032	0.83697	0.00002	2.05849	0.00006	14.20	21.75	18.490	15.515	38.139	0.8391	2.0627
Intraplate Cocos Plate Seamount Samples																		
PAN-CAKE																		
SO208 DR1-1_wr	7.1	18.8240	0.0038	15.5094	0.0033	38.0442	0.0092	0.82392	0.00004	2.02104	0.00017	41.96	13.23	18.778	15.507	38.040	0.8258	2.0258
SO208 DR1-1_wr	7.1	18.8002	0.0061	15.5046	0.0052	38.0284	0.0129	0.82471	0.00005	2.02277	0.00016	41.93	13.22	18.754	15.503	38.024	0.8266	2.0275
SO208 DR1-1_wr_average	7.1	18.8121	0.0050	15.5070	0.0043	38.0363	0.0111	0.82431	0.00004	2.02191	0.00016	41.94	13.22	18.766	15.505	38.032	0.8262	2.0266
SO208 DR1-1_wr	7.1	18.7266	0.0036	15.5001	0.0031	38.0218	0.0070	0.82771	0.00002	2.03036	0.00007	41.88	13.21	18.680	15.498	38.017	0.8296	2.0351
SO208 DR1-1_wr	7.1	18.6937	0.0068	15.4930	0.0055	38.0092	0.0145	0.82878	0.00009	2.03326	0.00040	41.85	13.20	18.648	15.491	38.005	0.8307	2.0380
SO208 DR1-1_wr_average	7.1	18.7101	0.0052	15.4966	0.0043	38.0155	0.0107	0.82825	0.00006	2.03181	0.00023	41.87	13.20	18.664	15.494	38.011	0.8302	2.0366
SPIEGELEI																		
SO208 DR15-4	13.6	18.9614	0.0010	15.5692	0.0009	38.7551	0.0023	0.82110	0.00001	2.04390	0.00005	26.15	100.52	18.906	15.567	38.687	0.8234	2.0463
SO208 DR15-4	13.6	18.9603	0.0016	15.5672	0.0014	38.7536	0.0037	0.82104	0.00002	2.04394	0.00007	26.15	100.52	18.905	15.565	38.686	0.8233	2.0463
SO208 DR15-4_wr	13.6	18.9383	0.0016	15.5717	0.0014	38.7494	0.0036	0.82223	0.00002	2.04609	0.00006	28.24	104.58	18.879	15.569	38.679	0.8247	2.0488
PICKEL																		
SO208 DR21-3	17.0	18.7395	0.0008	15.5357	0.0006	38.3547	0.0016	0.82903	0.00001	2.04673	0.00002	16.65	54.54	18.696	15.534	38.309	0.8309	2.0491
SO208 DR21-3_wr	17.0	18.7399	0.0019	15.5328	0.0017	38.3462	0.0047	0.82886	0.00002	2.04623	0.00009	20.16	41.49	18.687	15.530	38.311	0.8311	2.0502
UNNAMED																		
SO208 TVG22-3	18.6	18.5755	0.0005	15.5240	0.0004	38.2188	0.0010	0.83572	0.00001	2.05748	0.00002	9.64	33.39	18.548	15.523	38.188	0.8369	2.0589
BEND FAULT																		
SO208 DR25-2_wr	10.9	18.6933	0.0012	15.5206	0.0012	38.1694	0.0037	0.83028	0.00002	2.04188	0.00009	71.45	20.67	18.572	15.515	38.158	0.8354	2.0546
LITTLE BEND																		
SO208 DR26-2_wr	11.3	18.5697	0.0017	15.5145	0.0015	38.1690	0.0038	0.83547	0.00002	2.05545	0.00006	14.39	24.16	18.544	15.513	38.156	0.8365	2.0575
SCHRIPPE																		
SO208 DR30-4_wr	16.1	18.8618	0.0007	15.5832	0.0007	38.6718	0.0019	0.82617	0.00001	2.05027	0.00005	14.13	44.78	18.827	15.582	38.636	0.8276	2.0522
AMMONIT																		
SO208 DR31-3_wr	11.9	18.5410	0.0015	15.5172	0.0016	38.1442	0.0052	0.83691	0.00003	2.05729	0.00013	7.60	11.55	18.527	15.517	38.137	0.8375	2.0585
Undated Cocos Plate Seamount Samples																		
PAN-CAKE																		
SO208 DR1-5	7.10	18.4644	0.0015	15.4919	0.0013	38.0240	0.0034	0.83901	0.00002	2.05932	0.00007	4.82	16.20	18.459	15.492	38.018	0.8392	2.0596
SO208 DR1-5	7.10	18.4586	0.0027	15.4871	0.0023	38.0137	0.0057	0.83902	0.00002	2.05940	0.00008	4.82	16.20	18.453	15.487	38.008	0.8392	2.0597
HALF-MOON																		
SO208 DR2-1_wr	18.55	18.5817	0.0018	15.5125	0.0016	38.1380	0.0044	0.83482	0.00002	2.05245	0.00007	22.52	25.49	18.517	15.509	38.115	0.8376	2.0584
BOXER																		
SO208 DR7-2_wr	16.35	18.6840	0.0015	15.5319	0.0013	38.3582	0.0038	0.83129	0.00002	2.05300	0.00006	21.27	37.05	18.630	15.529	38.328	0.8336	2.0573

Figure A.6: Pb radiogenic isotope ratios of all samples of the CPS, including initial values.

Sample / Seamount	age used for isotope initials (Ma)	$^{206}Pb/^{204}Pb$	2 SE(M)	$^{207}Pb/^{204}Pb$	2 SE(M)	$^{208}Pb/^{204}Pb$	2 SE(M)	$^{207}Pb/^{206}Pb$	2 SE(M)	$^{208}Pb/^{206}Pb$	2 SE(M)	$^{238}U/^{204}Pb$	$^{232}Th/^{204}Pb$	$^{206}Pb/^{204}Pb\_i$	$^{207}Pb/^{204}Pb\_i$	$^{208}Pb/^{204}Pb\_i$	$^{207}Pb/^{206}Pb\_i$	$^{208}Pb/^{206}Pb\_i$
HORSESHOE																		
SO208 DR9-5_wr	15.75	18.5640	0.0017	15.5384	0.0014	38.2660	0.0036	0.83702	0.00002	2.06131	0.00006	7.49	12.98	18.546	15.538	38.256	0.8378	2.0628
SO208 DR9-5_wr*	15.75	18.5665	0.0029	15.5394	0.0025	38.2642	0.0062	0.83996	0.00002	2.06093	0.00005	7.49	12.98	18.548	15.539	38.254	0.8377	2.0624
EYE																		
SO208 DR17-1	18.05																	
SO208 DR17-1_wr	18.05	18.5324	0.0014	15.5090	0.0012	38.0995	0.0031	0.83686	0.00002	2.05583	0.00007	14.79	23.78	18.491	15.507	38.078	0.8386	2.0593
SO208 DR17-7	18.05	18.6719	0.0008	15.5236	0.0006	38.2351	0.0016	0.83138	0.00001	2.04773	0.00002	7.20	23.62	18.652	15.523	38.214	0.8322	2.0488
SO208 DR17-7_wr	18.05	18.6723	0.0015	15.5221	0.0013	38.2312	0.0035	0.83129	0.00002	2.04749	0.00006	48.69	13.86	18.536	15.516	38.219	0.8371	2.0619
SO208 DR17-7_wr	18.05																	
SO208 DR17-19	18.05																	
SO208 DR17-20	18.05	18.5408	0.0007	15.5151	0.0007	38.1656	0.0021	0.83681	0.00001	2.05846	0.00005	6.45	21.48	18.523	15.514	38.146	0.8376	2.0594
UNNAMED																		
SO208 TVG22-4_wr	18.6	18.5907	0.0018	15.5226	0.0016	38.2154	0.0043	0.83497	0.00002	2.05562	0.00009	18.16	34.35	18.538	15.520	38.184	0.8372	2.0597
BEND FAULT																		
SO208 DR23-1_wr	24.0	18.4649	0.0044	15.5005	0.0037	38.0528	0.0090	0.83946	0.00003	2.06081	0.00007	9.21	23.79	18.431	15.499	38.025	0.8409	2.0631
SO208 DR23-6	24.0	18.5005	0.0010	15.5136	0.0012	38.1168	0.0035	0.83855	0.00002	2.06031	0.00008	4.97	19.37	18.482	15.513	38.094	0.8393	2.0611
SO208 DR24-20_wr	22.5	18.6762	0.0016	15.5230	0.0013	38.2936	0.0034	0.83116	0.00002	2.05039	0.00006	24.80	77.23	18.589	15.519	38.208	0.8348	2.0553
LITTLE BEND																		
SO208 DR26-3	11.30	18.5343	0.0013	15.5084	0.0011	38.1534	0.0028	0.83674	0.00001	2.05853	0.00002	8.99	29.52	18.519	15.508	38.137	0.8374	2.0594
SCHRIPPE																		
SO208 DR30-1	16.10	18.8728	0.0012	15.5602	0.0010	38.5833	0.0028	0.82447	0.00001	2.04438	0.00005	14.99	53.73	18.835	15.558	38.541	0.8260	2.0462
SO208 DR30-1_wr	16.10																	
SO208 DR30-2	16.10	19.2816	0.0010	15.6243	0.0008	39.3096	0.0020	0.81032	0.00001	2.03872	0.00002	27.84	119.09	19.212	15.621	39.215	0.8131	2.0412
GUARDIAN																		
SO208 DR32-1	22.25	18.6035	0.0013	15.5204	0.0011	38.2100	0.0027	0.83428	0.00002	2.05392	0.00003	7.06	24.60	18.579	15.519	38.183	0.8353	2.0552
SO208 DR32-2_wr	22.25	19.3216	0.0009	15.6037	0.0008	39.1663	0.0024	0.80758	0.00001	2.02708	0.00005	27.58	117.35	19.226	15.599	39.037	0.8114	2.0304
SO208 DR32-2_wr	22.25	19.3308	0.0015	15.6058	0.0017	39.1835	0.0054	0.80731	0.00003	2.02700	0.00013	27.59	117.40	19.235	15.601	39.054	0.8111	2.0303
SO208 DR32-6_wr	22.25	18.4915	0.0014	15.5039	0.0013	38.0423	0.0035	0.83843	0.00002	2.05728	0.00007	17.46	20.28	18.431	15.501	38.020	0.8410	2.0628
BAGEL																		
SO208 DR36-1_wr	22.05	18.7659	0.0012	15.5367	0.0014	38.3073	0.0047	0.82792	0.00003	2.04133	0.00013	23.71	20.22	18.685	15.533	38.285	0.8313	2.0490
SO208 DR36-1_wr	22.05																	
OJO																		
SO208 DR37-1_wr	22.85	18.7181	0.0007	15.5326	0.0006	38.2493	0.0015	0.82982	0.00001	2.04344	0.00003	16.75	12.35	18.659	15.530	38.235	0.8323	2.0492
SO208 DR37-3_wr	22.85	18.8232	0.0023	15.5353	0.0020	38.2462	0.0051	0.82533	0.00002	2.03187	0.00008	31.39	12.07	18.712	15.530	38.233	0.8300	2.0432
SO208 DR37-3_wr	22.85	18.8264	0.0009	15.5348	0.0008	38.2438	0.0022	0.82516	0.00001	2.03140	0.00005	31.39	12.07	18.715	15.530	38.230	0.8298	2.0428
ZECKE																		
SO208 DR38-1	22.85	18.5571	0.0016	15.5144	0.0016	38.1485	0.0051	0.83604	0.00002	2.05574	0.00012	3.96	9.97	18.543	15.514	38.137	0.8366	2.0567
SO208 DR38-4_wr	22.85	18.6000	0.0011	15.5188	0.0012	38.1590	0.0038	0.83434	0.00002	2.05156	0.00010	13.95	12.15	18.551	15.517	38.145	0.8364	2.0563
HOOK																		
SO208 DR39-1_wr	22.85																	
SO208 DR39-2_wr	22.85	18.6885	0.0017	15.5256	0.0015	38.1692	0.0040	0.83076	0.00002	2.04239	0.00008	29.47	14.09	18.584	15.521	38.153	0.8352	2.0530
SO208 DR39-2_wr	22.85	18.6533	0.0020	15.5295	0.0018	38.1362	0.0053	0.83253	0.00002	2.04447	0.00011	29.44	14.07	18.549	15.525	38.120	0.8370	2.0551
SO208 DR39-9-VC	22.85	18.5940	0.0013	15.5243	0.0014	38.1719	0.0043	0.83491	0.00002	2.05291	0.00010	4.47	14.04	18.578	15.524	38.156	0.8356	2.0538
SO208 DR40-1_wr	22.85	18.7221	0.0010	15.5266	0.0010	38.1236	0.0027	0.82932	0.00001	2.03629	0.00006	39.66	9.12	18.581	15.520	38.113	0.8353	2.0512

_wr denotes powders of whole rock samples
* isotope replicate analyses conducted on whole rock powder
_i initial isotope ratio

Appendix B

Western Galápagos Spreading Center

Table B.1: Major element composition of all samples of the WGSC Profile 1.

Element/ Sample (SO208)	SiO$_2$	Al$_2$O$_3$	MgO	FeO^T	CaO	Na$_2$O	K$_2$O	TiO$_2$	P$_2$O$_5$	MnO	SO$_3$	Cl	LOI%	Total
on-axis Seamount														
DR45-1	50.6	13.7	4.56	14.3	8.90	3.29	0.556	2.75	0.341	0.268	0.294	0.086		99.6
DR45-1$^\$$	50.1	13.4	4.63	13.9	9.13	3.24	0.559	2.70	0.319	0.172	0.435	0.088		98.7
DR45-2	50.6	13.5	4.55	14.1	8.92	3.25	0.558	2.74	0.304	0.243	0.283	0.085		99.1
DR45-3	50.6	13.5	4.55	14.1	8.87	3.27	0.553	2.72	0.307	0.241	0.299	0.084		99.1
DR45-3$^\$$	50.2	13.3	4.62	14.1	9.15	3.20	0.540	2.72	0.309	0.208	0.451	0.087		99.0
DR45-4	50.6	13.6	4.54	14.1	8.90	3.24	0.556	2.70	0.329	0.219	0.296	0.086		99.2
DR45-5	50.8	13.6	4.54	14.3	8.91	3.28	0.551	2.76	0.336	0.260	0.287	0.089		99.7
off-axis Seamount														
DR63-1_wr	49.5	14.5	8.63	9.10	12.2	1.86	0.590	1.59	0.240	0.170	0.060		0.040	98.5
young seafloor basalts <30 km from ridge axis														
DR46-1	49.8	14.3	6.56	10.9	11.8	2.59	0.387	1.82	0.181	0.163	0.330	0.049		98.9
DR48-1	50.4	13.7	5.19	13.3	9.58	3.09	0.444	2.51	0.314	0.250	0.269	0.168		99.2
DR48-1$^\$$	49.6	13.5	5.33	13.0	9.93	3.09	0.447	2.46	0.295	0.175	0.390	0.173		98.3
DR48-2	50.1	13.7	5.20	13.0	9.57	3.08	0.447	2.47	0.300	0.196	0.256	0.168		98.6
DR48-3	50.2	13.7	5.22	13.0	9.65	3.11	0.452	2.49	0.298	0.233	0.268	0.168		98.8
DR48-4	50.2	13.7	5.19	13.0	9.62	3.12	0.448	2.49	0.295	0.216	0.263	0.167		98.7
DR48-6	50.2	13.6	5.08	13.2	9.54	3.10	0.453	2.54	0.297	0.256	0.268	0.165		98.6
DR48-7	49.9	13.6	5.04	13.3	9.55	3.16	0.458	2.53	0.289	0.217	0.270	0.176		98.5
DR49-1	50.5	14.4	6.31	11.0	11.1	2.69	0.427	1.69	0.177	0.142	0.331	0.046		98.7
DR49-2	50.6	14.3	6.27	11.2	11.1	2.68	0.435	1.67	0.192	0.167	0.335	0.050		98.9
DR49-3	50.6	14.3	6.27	11.1	11.1	2.64	0.431	1.70	0.173	0.157	0.359	0.049		99.0
DR49-4	50.9	15.3	5.99	10.5	11.4	2.68	0.410	1.62	0.190	0.135	0.327	0.045		99.4
DR50-1	48.7	15.8	8.12	9.61	12.8	2.35	0.120	1.19	0.096	0.132	0.293	0.009		99.1
DR50-2	48.6	15.5	8.07	9.56	12.8	2.36	0.126	1.21	0.093	0.150	0.297	0.009		98.8
DR50-3	48.8	15.7	8.11	9.60	12.8	2.33	0.126	1.20	0.092	0.134	0.274	0.013		99.1
DR51-4	49.9	13.0	5.23	14.2	9.89	2.78	0.314	2.37	0.202	0.176	0.465	0.079		98.7
DR51-5	49.9	13.1	5.33	14.2	9.83	2.84	0.311	2.35	0.227	0.178	0.451	0.077		98.8
DR51-6_wr	50.6	13.2	5.35	14.0	9.93	2.65	0.460	2.43	0.260	0.240	0.030		n.a.	99.2
DR53-1_wr	49.6	15.5	7.73	8.96	12.5	2.25	0.470	1.37	0.170	0.160	0.080		0.040	98.8
DR53-2_wr	49.4	15.5	7.83	8.75	12.5	2.21	0.440	1.36	0.160	0.160	0.090		n.a.	98.4
DR55-1	49.8	14.0	5.69	12.3	10.5	3.03	0.496	2.17	0.227	0.179	0.392	0.046		98.9
DR55-2_wr	50.2	14.5	6.36	10.5	12.0	2.64	0.300	1.70	0.170	0.190	0.090		n.a.	98.6
DR56-1	49.2	15.3	7.71	10.1	12.8	2.29	0.154	1.26	0.083	0.153	0.308	0.011		99.4
DR56-2_wr	48.9	16.5	8.23	9.21	12.7	2.07	0.150	1.11	0.100	0.170	0.090		n.a.	99.2
DR57-1	49.3	14.0	6.28	11.8	11.4	2.88	0.227	1.85	0.147	0.157	0.384	0.033		98.6
DR57-2	49.2	14.1	6.44	11.6	11.6	2.84	0.224	1.78	0.145	0.151	0.370	0.038		98.4
DR57-3	49.4	13.7	5.89	12.3	11.0	2.74	0.370	2.08	0.219	0.180	0.401	0.040		98.3
DR57-4	49.3	14.1	6.41	11.5	11.6	2.85	0.228	1.79	0.155	0.167	0.362	0.029		98.4
DR57-5	48.6	15.2	7.02	10.5	12.0	2.86	0.245	1.77	0.168	0.153	0.349	0.035		98.8
DR58-1	50.1	14.4	6.67	11.4	11.6	2.74	0.182	1.69	0.157	0.214	0.229	0.048		99.4

. . . continued

Element/Sample	SiO$_2$	Al$_2$O$_3$	MgO	FeO^T	CaO	Na$_2$O	K$_2$O	TiO$_2$	P$_2$O$_5$	MnO	SO$_3$	Cl	LOI%	Total
DR58-2	50.1	14.3	6.71	11.5	11.5	2.72	0.186	1.68	0.150	0.206	0.226	0.047		99.3
DR58-4	49.9	14.3	6.37	11.9	11.2	2.79	0.210	1.73	0.147	0.195	0.232	0.067		99.0
DR58-5	49.9	14.3	6.29	11.7	11.2	2.80	0.209	1.74	0.162	0.201	0.240	0.064		98.7
DR60-1	49.7	14.8	6.95	10.6	12.2	2.65	0.256	1.60	0.149	0.158	0.198	0.050		99.2
DR60-2	49.7	14.8	6.91	10.5	12.1	2.62	0.255	1.62	0.177	0.188	0.195	0.052		99.1
DR60-3	49.8	15.0	7.04	10.6	12.3	2.66	0.257	1.62	0.142	0.177	0.197	0.050		99.7
DR60-3$^\$$	49.5	14.7	7.10	11.0	12.0	2.62	0.265	1.59	0.159	0.176	0.279	0.059		99.5
DR60-4	49.9	14.9	7.00	10.3	12.2	2.66	0.251	1.63	0.176	0.153	0.201	0.049		99.5
DR61-1	50.5	14.5	6.74	11.4	12.0	2.48	0.177	1.53	0.116	0.223	0.226	0.015		99.9
DR61-1$^\$$	50.1	14.2	6.86	11.2	12.0	2.43	0.171	1.51	0.121	0.191	0.340	0.012		99.1
DR61-2	50.4	14.3	6.71	11.3	12.0	2.42	0.176	1.54	0.116	0.217	0.232	0.014		99.5
DR61-3	50.4	14.3	6.71	11.2	12.0	2.46	0.170	1.54	0.129	0.204	0.216	0.015		99.4
DR61-4	50.3	14.4	6.73	11.4	12.0	2.43	0.176	1.53	0.124	0.198	0.222	0.014		99.5
DR61-5	50.2	14.4	6.69	11.2	12.0	2.46	0.176	1.53	0.128	0.193	0.228	0.017		99.3
DR61-6	50.2	14.4	6.78	11.4	12.0	2.48	0.176	1.51	0.125	0.216	0.229	0.013		99.6
DR61-7	50.2	14.4	6.79	11.2	12.0	2.47	0.168	1.52	0.118	0.215	0.228	0.012		99.4
DR61-8	50.3	14.4	6.78	11.2	12.0	2.49	0.178	1.53	0.128	0.215	0.226	0.019		99.5
DR62-1	50.1	13.8	6.23	12.4	11.3	2.64	0.200	1.75	0.148	0.167	0.382	0.036		99.2
DR62-2	50.1	13.7	6.26	12.2	11.2	2.66	0.210	1.73	0.160	0.213	0.375	0.035		98.8
DR66-1	50.5	14.7	7.60	10.3	12.7	2.16	0.121	1.17	0.086	0.183	0.190	0.021		99.7
DR66-2	50.5	14.6	7.57	10.4	12.7	2.17	0.120	1.14	0.092	0.178	0.187	0.024		99.8
DR66-3_wr	51.0	14.7	7.88	9.17	12.8	2.10	0.150	1.18	0.100	0.190	0.040		n.a.	99.4
DR69-1	50.0	13.8	6.33	12.1	11.2	2.45	0.265	1.80	0.169	0.196	0.382	0.049		98.8
DR69-2	50.1	13.9	6.28	12.2	11.3	2.47	0.262	1.80	0.167	0.175	0.374	0.045		99.0
DR69-5	50.0	13.8	6.24	12.3	11.3	2.44	0.263	1.80	0.157	0.163	0.385	0.044		98.7
DR72-1	52.8	12.6	2.90	15.8	7.62	3.08	0.666	2.64	0.571	0.221	0.475	0.209		99.6
DR72-2	52.5	12.5	2.88	15.9	7.66	3.11	0.671	2.64	0.559	0.224	0.456	0.205		99.3
DR72-4	52.4	12.4	2.98	15.8	7.80	3.07	0.647	2.66	0.553	0.226	0.448	0.199		99.1
old seafloor basalts >30 km from ridge axis														
DR67-1	50.1	13.1	5.64	14.1	10.2	2.50	0.260	1.91	0.181	0.209	0.440	0.054		98.7
DR67-2	49.9	13.3	5.95	13.6	10.5	2.53	0.249	1.79	0.161	0.186	0.412	0.048		98.7
DR67-3	50.2	13.4	6.04	13.5	10.6	2.49	0.247	1.80	0.168	0.178	0.405	0.048		99.1
DR67-4	50.2	13.4	6.06	13.4	10.6	2.51	0.246	1.77	0.153	0.188	0.401	0.051		99.0
DR67-5	50.5	13.2	5.67	14.1	10.2	2.49	0.259	1.93	0.159	0.232	0.426	0.054		99.2
DR68-1_wr	49.8	14.2	4.89	12.8	10.9	2.58	0.530	1.85	0.180	0.210	0.020		0.680	98.0
DR73-1	50.1	14.1	6.75	11.7	11.6	2.42	0.205	1.45	0.128	0.170	0.341	0.030		99.1
DR73-2_wr	51.7	14.2	6.60	10.3	11.4	2.47	0.360	1.69	0.160	0.220	0.080		0.160	99.2
DR74-1	52.3	13.1	4.43	13.8	8.92	2.88	0.467	1.94	0.232	0.252	0.257	0.109		98.8
DR74-1$^\$$	51.9	13.0	4.64	14.5	8.85	2.82	0.471	2.03	0.231	0.252	0.402	0.110		99.1

$\$$ = XRF/EPMA Replicates

wr = whole rock samples

all others are volcanic glass samples

n.a. = not analyzed

Table B.2: Trace element data (in ppm) of all samples of the WGSC Profile 1.

Element/ Sample (SO208)	Sc	V	Cr	Co	Ni	Cu	Zn	Ga	Rb	Sr	Y	Zr	Nb	Cs	Ba	La	Ce
on-axis Seamount																	
DR45-1	38.2	428	46.9	40.7	29.4	62.5	148	21.1	13.7	146	48.9	194	22.4	0.147	132	14.8	36.0
DR45-1[#]	38.6	424	44.8	42.6	30.5	70.4	131	24.5	14.7	151	60.8	213	21.6	0.148	130	15.2	35.9
DR45-1[#]	40.8	416	43.0	38.8	28.0	59.3	146	21.1	13.7	151	55.4	215	22.5	0.145	131	15.4	34.7
DR45-2	39.0	425	46.5	40.3	29.0	62.6	148	21.3	13.8	149	51.0	201	22.5	0.145	132	15.2	36.4
DR45-2[#]	41.5	417	43.1	38.9	28.0	60.4	151	21.2	13.6	150	55.9	217	22.4	0.147	131	15.6	34.9
DR45-3	38.9	428	47.6	40.5	29.4	63.0	146	21.3	13.8	148	50.8	199	22.2	0.145	134	15.2	36.6
DR45-3[#]	39.0	417	44.9	41.9	30.1	69.6	126	23.8	14.5	150	61.0	215	21.6	0.143	130	15.1	35.4
DR45-3[#]	41.2	406	42.1	37.6	27.1	57.8	143	20.4	13.2	148	55.6	216	22.0	0.141	130	15.4	34.1
DR45-4	39.5	427	47.1	40.8	29.3	63.0	150	21.5	13.9	151	52.1	205	22.6	0.147	133	15.3	36.4
DR45-4[#]	41.7	403	41.6	37.5	27.1	58.2	143	20.7	13.5	149	56.6	219	22.1	0.141	130	15.6	34.4
DR45-5	40.8	403	41.8	37.6	26.7	58.6	144	20.8	13.4	148	55.0	214	22.1	0.142	129	15.3	34.3
off-axis Seamount																	
DR63-1_wr	37.73	276	377	43.6	137	138	76.8	15.7	12.4	269	20.0	126	21.6	0.138	154	16.0	34.9
DR63-1_wr[#]	37.21	271	389	43.4	136	137	76.1	15.7	12.1	268	19.8	126	21.5	0.129	155	15.9	34.5
DR63-1_wr[#]	37.26	278	383	43.8	137	138	75.5	15.8	12.3	270	20.0	127	21.6	0.134	155	16.0	34.9
young seafloor basalts <30 km from ridge axis																	

. . . continued

Element/Sample	Sc	V	Cr	Co	Ni	Cu	Zn	Ga	Rb	Sr	Y	Zr	Nb	Cs	Ba	La	Ce
DR46-1	41.9	335	156	43.8	63.7	119	87.6	20.2	9.10	177	34.3	126	14.0	0.095	96.3	9.83	23.1
DR48-1	39.4	373	92.5	41.4	44.7	99.4	108	22.2	10.7	143	57.2	204	18.3	0.105	95.7	13.4	31.7
DR48-1[#]	40.8	373	86.5	38.1	42.3	87.4	128	19.7	10.2	143	50.5	197	18.6	0.108	97.9	13.5	31.2
DR48-2	40.9	365	85.1	37.4	41.6	85.1	126	19.4	10.0	142	50.1	197	18.6	0.102	96.9	13.4	30.7
DR48-3	40.4	375	94.5	39.2	44.2	90.4	126	19.8	10.1	141	47.8	189	18.6	0.101	98.0	13.5	31.5
DR48-4	40.6	380	92.0	39.8	43.9	91.9	130	20.2	10.4	144	49.0	194	19.0	0.107	99.7	13.8	32.0
DR48-6	40.5	381	94.2	39.6	44.4	90.3	129	19.8	10.2	141	48.0	191	18.8	0.107	98.8	13.6	31.8
DR48-7	40.0	369	87.9	37.6	38.6	88.2	126	19.7	10.1	143	48.5	193	18.7	0.104	98.8	13.7	31.5
DR49-1	41.4	332	79.1	44.5	50.9	98.3	88.8	19.7	9.93	173	35.6	123	14.2	0.098	111	9.29	21.6
DR49-2	41.3	329	74.2	47.8	67.0	96.2	90.4	20.0	10.0	175	35.6	123	14.1	0.099	111	9.39	21.7
DR49-3	40.7	337	75.2	45.0	50.7	100	92.0	20.0	10.2	172	34.9	121	14.2	0.102	115	9.53	22.4
DR49-4	42.4	344	75.6	46.1	51.7	102	95.1	20.5	10.5	177	36.8	127	14.7	0.104	118	9.81	22.9
DR50-1	42.5	281	356	49.4	130	144	75.7	18.6	2.98	119	27.3	68.2	4.61	0.032	30.6	3.92	10.5
DR50-2	42.7	284	360	49.8	130	143	76.7	18.7	2.97	119	27.4	68.4	4.63	0.033	30.9	3.96	10.6
DR50-3	44.4	281	353	49.4	131	137	72.5	18.4	2.99	120	28.8	72.5	4.56	0.029	30.6	3.98	10.1
DR51-4	45.2	459	41.9	48.5	35.4	96.6	120	22.6	7.70	113	56.8	169	13.1	0.079	73.5	10.1	24.1
DR51-5	44.9	448	41.3	47.7	36.9	94.2	117	22.1	7.40	113	56.0	166	12.9	0.077	72.1	9.94	23.6
DR51-6_wr	43.9	455	45.1	45.6	34.4	85.0	126	20.8	8.71	121	49.7	157	12.4	0.205	77.5	9.69	24.1
DR53-1_wr	41.5	279	324	41.2	106	110	71.6	16.6	9.15	178	24.7	90.6	11.6	0.195	98.0	8.02	18.1
DR53-2_wr	40.1	279	325	41.0	108	102	71.0	16.7	8.37	179	24.7	90.7	11.7	0.127	98.9	8.04	18.2
DR53-2_wr[#]	40.6	281	327	41.3	109	102	72.2	16.7	8.37	181	24.9	91.1	11.7	0.129	101	8.05	18.3
DR53-2_wr[#]	40.1	282	324	40.6	108	102	71.0	16.6	8.43	183	24.8	91.3	11.7	0.129	101	8.13	18.3
DR53-2_wr[#]	40.4	282	324	40.9	108	102	71.4	16.6	8.45	184	25.0	91.6	11.8	0.129	102	8.13	18.4
DR53-2_wr[#]	39.6	282	320	40.1	107	100	70.2	16.6	8.53	190	25.0	92.2	11.9	0.130	105	8.21	18.5
DR55-1	42.7	372	19.0	44.3	35.8	87.9	99.0	20.9	12.7	185	45.2	164	18.8	0.132	140	13.4	29.1
DR55-2_wr	47.2	350	132	41.1	55.9	122	88.9	18.6	5.46	143	34.4	106	8.27	0.140	57.8	6.62	16.7
DR56-1	45.3	298	351	47.5	99.8	132	76.0	18.2	3.38	118	28.7	73.4	5.56	0.037	37.3	4.60	11.3
DR56-2_wr	37.5	263	333	44.5	131	96.0	75.4	16.6	2.80	126	22.7	61.3	4.65	0.036	33.3	3.66	9.61
DR57-1	44.7	371	71.2	47.6	47.5	122	97.8	21.2	5.53	140	39.8	117	9.14	0.055	54.8	7.31	18.5
DR57-2	45.1	360	89.9	47.6	52.6	124	95.2	21.1	5.36	142	38.8	113	8.81	0.052	53.4	7.08	17.9
DR57-3	43.5	390	98.6	45.7	49.4	103	106	21.9	9.47	163	43.2	145	15.0	0.093	91.2	11.1	26.0
DR57-4	45.7	352	85.0	46.2	51.7	120	91.2	20.6	5.16	140	39.1	114	8.66	0.050	52.4	7.10	17.5
DR57-5	43.9	314	283	45.7	85.1	136	84.4	20.7	6.10	166	37.1	122	10.1	0.061	63.8	8.36	20.5
DR58-1	46.3	336	120	42.3	59.7	119	104	17.3	3.81	121	31.3	93.0	6.80	0.040	40.9	5.56	14.0
DR58-2	44.9	337	121	43.0	60.9	120	100	17.4	3.83	117	29.5	87.5	6.73	0.040	40.2	5.36	13.7
DR58-4	45.7	345	79.3	42.4	51.9	117	104	17.3	4.62	120	31.8	95.1	8.30	0.049	48.5	6.31	15.4
DR58-5	45.6	345	79.3	42.7	53.1	116	102	17.4	4.62	120	31.6	95.0	8.29	0.045	48.7	6.36	15.5
DR60-1	48.4	308	272	42.2	77.8	115	88.0	16.8	6.19	142	32.9	106	9.81	0.064	66.0	7.63	16.9
DR60-2	47.4	319	278	44.0	79.5	120	90.3	17.0	6.26	144	31.7	104	10.1	0.066	67.1	7.63	17.4
DR60-3	48.5	322	272	43.1	79.0	115	87.7	16.5	6.15	139	31.9	104	9.91	0.064	65.8	7.57	17.0
DR60-4	48.0	315	270	42.1	77.0	114	85.1	16.1	5.95	139	31.2	102	9.77	0.058	64.0	7.40	16.6
DR61-1	48.9	352	211	43.4	64.1	101	97.1	16.2	3.92	102	31.7	84.4	6.78	0.044	40.7	5.36	12.8
DR61-1[#]	47.1	364	208	47.3	68.6	116	91.0	19.4	4.29	104	35.5	87.0	6.95	0.043	42.4	5.53	13.8
DR61-2	50.1	352	201	44.2	64.7	103	102	17.0	4.16	105	34.0	89.4	6.93	0.042	41.6	5.47	13.0
DR61-3	48.5	351	205	44.0	63.9	96.4	101	16.7	4.12	103	31.8	84.6	6.77	0.048	41.2	5.33	12.9
DR61-4	50.9	357	202	45.4	67.2	105	102	17.5	4.22	106	34.6	92.0	7.01	0.048	42.2	5.70	13.3
DR61-5	50.0	372	210	47.2	69.0	108	105	17.9	4.34	108	34.3	91.0	7.24	0.046	44.0	5.78	13.9
DR61-6	48.0	366	206	44.8	66.2	103	97.4	16.5	3.95	98.5	30.5	81.3	6.61	0.040	38.6	5.00	12.3
DR61-7	49.4	362	205	44.7	66.3	105	98.7	16.6	3.98	99.8	32.1	84.6	6.77	0.044	40.1	5.27	12.6
DR61-8	49.9	355	201	44.1	64.4	102	97.2	16.4	3.91	99.7	31.9	84.7	6.76	0.044	40.0	5.27	12.5
DR62-1	45.6	379	55.4	48.8	47.4	114	102	21.0	5.13	117	41.4	111	8.84	0.050	50.5	6.94	17.2
DR62-2	45.2	384	53.3	48.4	46.7	112	102	21.1	5.27	113	40.7	108	8.56	0.051	49.4	6.72	16.7
DR66-1	48.0	314	276	45.2	92.9	126	85.8	15.2	2.62	91.0	24.3	58.7	4.60	0.028	28.6	3.68	8.93
DR66-2	45.5	302	264	42.8	87.7	119	80.4	14.1	2.47	86.9	22.5	54.7	4.41	0.022	27.0	3.44	8.38
DR69-1	46.0	385	118	46.7	62.1	107	103	20.7	6.72	119	42.4	120	11.0	0.066	63.0	8.17	19.2
DR69-2	45.9	384	116	46.0	60.6	105	101	20.5	6.63	121	42.3	121	11.0	0.068	63.2	8.18	19.2
DR69-5	45.9	382	114	45.7	60.2	104	101	20.3	6.61	121	42.9	122	11.0	0.066	63.5	8.24	19.3
DR72-1	37.1	149	7.24	32.7	5.54	39.4	180	26.5	18.6	126	114	373	31.9	0.191	160	24.1	55.3
DR72-2	37.6	147	5.85	32.5	4.54	35.5	181	26.4	18.5	126	117	378	32.2	0.188	163	24.6	56.2
DR72-4	38.0	153	8.38	33.1	6.08	180	26.8	18.7	128	116	379	32.0	0.185	159	24.1	54.9
old seafloor basalts >30 km from ridge axis																	
DR67-1	46.6	431	52.7	49.4	41.5	96.3	115	21.3	6.81	98.3	47.6	122	11.3	0.069	62.3	8.43	19.8
DR67-2	45.4	415	42.7	51.1	46.7	110	112	21.4	6.71	105	44.0	114	10.7	0.070	60.8	7.99	18.7
DR67-3	45.6	404	49.7	49.6	46.9	110	109	20.8	6.44	108	43.5	112	10.5	0.063	58.9	7.73	18.1
DR67-4	46.0	409	48.9	49.8	47.3	106	109	20.8	6.39	101	43.5	113	10.4	0.064	59.2	7.82	18.2
DR67-5	47.3	440	53.5	50.5	42.4	98.4	118	21.7	6.95	97.7	48.4	124	11.3	0.070	61.8	8.43	19.6
DR68-1_wr	43.5	394	118	41.2	37.1	78.8	107	18.6	15.2	111	37.8	114	9.29	0.828	62.9	7.39	17.7
DR73-1	47.5	355	108	47.8	63.0	119	89.0	18.9	5.10	110	36.1	89.0	8.06	0.052	50.4	6.26	14.4

. . . continued

Element/Sample	Sc	V	Cr	Co	Ni	Cu	Zn	Ga	Rb	Sr	Y	Zr	Nb	Cs	Ba	La	Ce
DR73-2_wr	48.9	400	81.1	50.4	58.2	115	114	19.3	5.93	140	41.0	99.1	8.83	0.086	77.2	7.38	17.5
DR74-1	40.4	343	16.0	39.8	27.3	68.4	146	20.0	11.7	108	54.5	185	18.0	0.111	108	14.1	30.0

= ICPMS Replicates

wr = whole rock samples

all others are volcanic glass samples

Element/Sample (SO208)	Pr	Nd	Sm	Eu	Gd	Tb	Dy	Ho	Er	Tm	Yb	Lu	Hf	Ta	W	Pb	Th	U
on-axis Seamount																		
DR45-1	4.95	23.4	6.61	2.21	7.83	1.31	8.90	1.92	5.50	0.843	5.58	0.824	4.89	1.36	0.247	1.30	1.61	0.451
DR45-1#	5.02	23.6	6.98	2.25	8.85	1.54	9.80	2.13	6.02	0.895	5.94	0.849	5.19	1.17	0.269	1.21	1.67	0.429
DR45-1#	5.08	24.5	7.11	2.27	8.81	1.46	10.0	2.16	6.33	0.944	6.13	0.950	5.64	1.45	0.238	1.28	1.76	0.430
DR45-2	5.05	24.0	6.80	2.25	8.17	1.37	9.19	1.99	5.73	0.869	5.74	0.864	5.10	1.38	0.248	1.28	1.67	0.454
DR45-2#	5.10	24.7	7.17	2.31	8.94	1.49	10.32	2.22	6.45	0.958	6.26	0.992	5.74	1.44	0.239	1.26	1.78	0.433
DR45-3	5.06	23.9	6.83	2.25	8.16	1.36	9.21	1.98	5.73	0.881	5.70	0.849	5.08	1.35	0.244	1.26	1.66	0.459
DR45-3#	4.99	23.8	7.05	2.29	8.89	1.54	9.83	2.15	5.97	0.898	5.95	0.865	5.20	1.19	0.253	1.20	1.64	0.418
DR45-3#	5.01	24.3	7.07	2.25	8.76	1.46	10.20	2.18	6.41	0.947	6.19	0.967	5.67	1.44	0.237	1.21	1.77	0.423
DR45-4	5.09	24.1	6.84	2.27	8.27	1.38	9.39	2.03	5.83	0.892	5.79	0.874	5.17	1.38	0.246	1.28	1.69	0.460
DR45-4#	5.03	24.5	7.20	2.26	8.95	1.51	10.32	2.22	6.51	0.966	6.29	0.985	5.80	1.45	0.239	1.24	1.80	0.425
DR45-5	5.01	24.3	7.00	2.26	8.63	1.45	10.03	2.15	6.25	0.936	6.08	0.945	5.57	1.40	0.232	1.22	1.72	0.421
off-axis Seamount																		
DR63-1_wr	4.56	19.3	4.23	1.37	4.18	0.640	3.83	0.748	2.01	0.290	1.90	0.279	3.00	1.24	0.309	1.28	1.65	0.448
DR63-1_wr#	4.51	19.2	4.19	1.35	4.14	0.634	3.77	0.745	1.98	0.286	1.85	0.275	2.94	1.22	0.374	1.25	1.55	0.438
DR63-1_wr#	4.56	19.4	4.23	1.38	4.19	0.638	3.81	0.753	2.00	0.290	1.88	0.278	2.98	1.24	0.350	1.25	1.59	0.444
young seafloor basalts <30 km from ridge axis																		
DR46-1	3.21	15.3	4.42	1.58	5.47	0.937	5.85	1.27	3.56	0.531	3.43	0.493	3.19	0.800	0.164	0.814	1.02	0.273
DR48-1	4.59	21.9	6.57	2.13	8.39	1.45	9.16	2.00	5.61	0.831	5.50	0.785	4.96	1.02	0.203	0.945	1.43	0.367
DR48-1#	4.62	22.4	6.61	2.10	8.01	1.35	9.24	1.99	5.73	0.850	5.52	0.853	5.14	1.19	0.190	0.987	1.46	0.383
DR48-2	4.56	22.2	6.50	2.10	8.02	1.32	9.14	1.94	5.68	0.843	5.50	0.841	5.13	1.19	0.179	0.967	1.45	0.367
DR48-3	4.59	22.1	6.40	2.10	7.82	1.29	8.74	1.89	5.41	0.832	5.36	0.805	4.87	1.17	0.186	0.986	1.43	0.375
DR48-4	4.66	22.5	6.50	2.12	7.84	1.30	8.88	1.90	5.46	0.839	5.45	0.806	4.94	1.20	0.186	1.00	1.46	0.382
DR48-6	4.60	22.3	6.45	2.11	7.76	1.29	8.74	1.89	5.41	0.827	5.37	0.809	4.96	1.17	0.190	0.994	1.43	0.386
DR48-7	4.60	22.2	6.48	2.10	7.80	1.30	8.79	1.90	5.42	0.831	5.39	0.806	4.90	1.20	0.183	0.974	1.45	0.374
DR49-1	3.04	14.4	4.26	1.50	5.43	0.94	6.03	1.32	3.69	0.555	3.66	0.528	3.13	0.833	0.149	0.747	0.975	0.254
DR49-2	3.05	14.5	4.29	1.51	5.38	0.947	6.12	1.32	3.70	0.559	3.67	0.533	3.14	0.846	0.157	0.755	0.990	0.249
DR49-3	3.12	14.5	4.34	1.54	5.39	0.938	6.00	1.32	3.66	0.550	3.64	0.518	3.10	0.843	0.164	0.796	1.00	0.269
DR49-4	3.22	15.1	4.38	1.58	5.59	0.987	6.27	1.37	3.79	0.568	3.80	0.553	3.26	0.870	0.174	0.809	1.04	0.272
DR50-1	1.62	8.26	2.80	1.12	3.87	0.705	4.58	1.03	2.96	0.439	2.91	0.423	1.93	0.263	0.066	0.450	0.374	0.100
DR50-2	1.63	8.33	2.80	1.12	4.00	0.705	4.69	1.05	2.98	0.446	2.99	0.429	1.95	0.269	0.075	0.451	0.371	0.100
DR50-3	1.58	8.19	2.80	1.09	3.97	0.722	4.75	1.05	2.98	0.437	2.94	0.426	1.92	0.258	0.058	0.412	0.380	0.093
DR51-4	3.64	18.2	5.85	1.99	8.02	1.43	9.28	2.08	5.88	0.887	5.82	0.844	4.48	0.765	0.151	0.792	1.08	0.275
DR51-5	3.57	17.9	5.76	1.94	7.78	1.39	9.12	2.03	5.74	0.864	5.70	0.831	4.39	0.751	0.141	0.783	1.07	0.265
DR51-6_wr	3.61	18.1	5.61	1.89	7.24	1.30	8.68	1.84	5.18	0.779	5.21	0.779	4.09	0.713	0.204	0.751	0.938	0.330
DR53-1_wr	2.50	11.6	3.26	1.17	3.95	0.680	4.43	0.921	2.54	0.377	2.49	0.371	2.26	0.648	0.213	0.620	0.804	0.255
DR53-2_wr	2.51	11.7	3.28	1.18	3.98	0.686	4.44	0.924	2.56	0.378	2.50	0.372	2.27	0.657	0.179	0.608	0.778	0.259
DR53-2_wr#	2.53	11.6	3.27	1.18	3.95	0.678	4.43	0.922	2.56	0.379	2.49	0.371	2.25	0.650	0.175	0.602	0.770	0.258
DR53-2_wr#	2.53	11.7	3.28	1.18	3.96	0.682	4.44	0.923	2.56	0.382	2.51	0.371	2.26	0.656	0.178	0.604	0.773	0.260
DR53-2_wr#	2.53	11.8	3.26	1.17	3.99	0.683	4.43	0.922	2.56	0.378	2.50	0.370	2.25	0.643	0.181	0.596	0.771	0.254
DR53-2_wr#	2.56	11.8	3.29	1.18	3.99	0.683	4.45	0.924	2.54	0.377	2.50	0.371	2.26	0.680	0.186	0.611	0.773	0.260
DR55-1	4.09	19.1	5.61	1.89	6.91	1.19	7.62	1.66	4.63	0.691	4.52	0.654	4.18	1.11	0.237	1.00	1.56	0.372
DR55-2_wr	2.50	12.5	3.97	1.43	5.13	0.912	6.06	1.27	3.54	0.529	3.49	0.515	2.76	0.477	0.156	0.623	0.648	0.225
DR56-1	1.72	8.65	2.91	1.12	4.11	0.738	4.83	1.08	3.03	0.457	3.04	0.436	1.98	0.326	0.065	0.441	0.450	0.113
DR56-2_wr	1.47	7.43	2.44	0.944	3.24	0.589	3.98	0.845	2.37	0.356	2.36	0.353	1.65	0.283	0.121	0.459	0.361	0.108
DR57-1	2.76	13.7	4.33	1.61	5.69	1.01	6.41	1.41	3.96	0.585	3.84	0.550	2.94	0.499	0.098	0.632	0.680	0.187
DR57-2	2.67	13.2	4.26	1.56	5.54	0.985	6.27	1.38	3.86	0.575	3.79	0.542	2.90	0.473	0.105	0.614	0.656	0.177
DR57-3	3.68	17.3	5.07	1.79	6.47	1.12	7.02	1.53	4.31	0.638	4.23	0.613	3.61	0.815	0.193	0.910	1.14	0.307
DR57-4	2.65	13.3	4.25	1.56	5.66	1.00	6.39	1.41	3.93	0.584	3.87	0.549	2.97	0.488	0.109	0.612	0.673	0.180
DR57-5	2.98	14.4	4.41	1.65	5.71	1.00	6.27	1.36	3.74	0.551	3.63	0.520	3.17	0.571	0.131	0.714	0.870	0.231
DR58-1	2.21	11.4	3.74	1.41	4.82	0.832	5.72	1.24	3.53	0.538	3.55	0.530	2.55	0.423	0.068	0.516	0.512	0.138
DR58-2	2.15	11.0	3.57	1.35	4.58	0.776	5.36	1.14	3.30	0.507	3.32	0.482	2.36	0.400	0.067	0.512	0.482	0.131
DR58-4	2.38	12.0	3.78	1.42	4.85	0.833	5.72	1.25	3.59	0.551	3.60	0.541	2.60	0.513	0.082	0.547	0.619	0.164
DR58-5	2.38	12.1	3.83	1.44	4.89	0.829	5.72	1.23	3.59	0.546	3.60	0.530	2.56	0.509	0.085	0.542	0.622	0.163
DR60-1	2.51	12.7	3.85	1.35	5.15	0.862	5.84	1.27	3.59	0.541	3.44	0.536	2.87	0.608	0.120	0.774	0.824	0.201
DR60-2	2.54	12.7	3.90	1.36	5.00	0.846	5.72	1.25	3.48	0.524	3.34	0.528	2.74	0.619	0.125	0.974	0.815	0.203
DR60-3	2.50	12.6	3.81	1.33	4.99	0.846	5.71	1.24	3.45	0.512	3.29	0.519	2.87	0.608	0.125	0.647	0.817	0.205

. . . continued

Element/Sample	Pr	Nd	Sm	Eu	Gd	Tb	Dy	Ho	Er	Tm	Yb	Lu	Hf	Ta	W	Pb	Th	U
DR60-4	2.45	12.3	3.74	1.31	4.90	0.824	5.59	1.20	3.39	0.517	3.25	0.506	2.67	0.597	0.122	0.649	0.786	0.195
DR61-1	1.99	10.3	3.34	1.23	4.59	0.805	5.56	1.23	3.51	0.524	3.40	0.533	2.30	0.403	0.075	0.530	0.536	0.136
DR61-1$^{\#}$	2.08	10.5	3.58	1.32	4.94	0.902	5.81	1.31	3.72	0.560	3.72	0.540	2.43	0.392	0.093	0.524	0.580	0.145
DR61-2	2.01	10.7	3.50	1.25	4.77	0.841	5.76	1.28	3.63	0.556	3.58	0.563	2.43	0.416	0.079	0.558	0.550	0.142
DR61-3	2.01	10.3	3.41	1.25	4.66	0.817	5.59	1.24	3.51	0.539	3.45	0.541	2.29	0.414	0.080	0.544	0.532	0.136
DR61-4	2.09	11.0	3.62	1.30	5.02	0.891	6.11	1.36	3.87	0.588	3.72	0.597	2.52	0.444	0.080	0.546	0.579	0.142
DR61-5	2.15	11.3	3.72	1.32	5.05	0.879	6.06	1.33	3.83	0.575	3.71	0.585	2.50	0.440	0.094	0.574	0.563	0.154
DR61-6	1.88	9.75	3.27	1.16	4.39	0.781	5.36	1.18	3.37	0.507	3.27	0.519	2.22	0.401	0.077	0.526	0.523	0.138
DR61-7	1.94	10.3	3.37	1.21	4.64	0.817	5.64	1.24	3.52	0.543	3.43	0.543	2.33	0.416	0.082	0.504	0.532	0.138
DR61-8	1.94	10.2	3.39	1.21	4.65	0.807	5.59	1.22	3.55	0.529	3.50	0.536	2.31	0.416	0.080	0.510	0.541	0.136
DR62-1	2.62	13.2	4.35	1.57	5.92	1.07	6.91	1.55	4.34	0.652	4.39	0.636	3.09	0.509	0.100	0.619	0.727	0.178
DR62-2	2.50	12.6	4.17	1.51	5.59	1.01	6.49	1.44	4.10	0.615	4.04	0.579	2.80	0.463	0.104	0.588	0.676	0.167
DR66-1	1.41	7.48	2.54	0.948	3.50	0.628	4.29	0.948	2.73	0.411	2.68	0.408	1.62	0.280	0.045	0.336	0.347	0.091
DR66-2	1.31	6.91	2.35	0.886	3.17	0.573	3.89	0.869	2.49	0.370	2.48	0.388	1.49	0.265	0.051	0.344	0.325	0.087
DR69-1	2.84	13.9	4.44	1.54	5.90	1.05	6.77	1.50	4.24	0.637	4.20	0.614	3.12	0.613	0.121	0.640	0.858	0.210
DR69-2	2.83	13.9	4.43	1.54	5.89	1.04	6.73	1.49	4.22	0.644	4.23	0.611	3.10	0.604	0.133	0.635	0.844	0.209
DR69-5	2.84	14.0	4.48	1.55	5.94	1.06	6.76	1.51	4.26	0.645	4.27	0.618	3.13	0.610	0.130	0.656	0.872	0.212
DR72-1	8.10	39.6	12.1	3.55	15.8	2.78	17.8	3.97	11.2	1.70	11.2	1.62	9.23	1.81	0.380	1.70	2.75	0.644
DR72-2	8.25	40.4	12.4	3.63	16.2	2.84	18.3	4.08	11.6	1.75	11.5	1.67	9.50	1.86	0.397	1.72	2.82	0.642
DR72-4	8.10	39.9	12.2	3.59	16.1	2.81	18.0	4.01	11.4	1.71	11.3	1.65	9.36	1.82	0.362	1.73	2.75	0.633
old seafloor basalts >30 km from ridge axis																		
DR67-1	2.89	14.2	4.53	1.57	6.22	1.13	7.42	1.67	4.80	0.737	4.87	0.712	3.21	0.615	0.133	0.666	0.895	0.213
DR67-2	2.73	13.5	4.30	1.52	5.89	1.06	6.91	1.56	4.42	0.675	4.46	0.649	2.99	0.579	0.137	0.642	0.860	0.204
DR67-3	2.65	12.9	4.17	1.46	5.72	1.03	6.79	1.52	4.33	0.667	4.43	0.639	2.93	0.563	0.123	0.637	0.850	0.203
DR67-4	2.66	13.0	4.24	1.47	5.83	1.05	6.88	1.55	4.44	0.678	4.53	0.649	3.02	0.573	0.130	0.622	0.863	0.203
DR67-5	2.88	14.1	4.55	1.56	6.29	1.14	7.51	1.68	4.85	0.742	4.94	0.723	3.26	0.626	0.134	0.674	0.913	0.213
DR68-1_wr	2.60	13.1	3.99	1.41	5.31	0.944	6.47	1.39	3.97	0.602	4.06	0.624	2.92	0.526	9.216	0.830	0.728	0.445
DR73-1	2.12	10.4	3.47	1.26	4.89	0.880	5.83	1.31	3.74	0.564	3.75	0.548	2.46	0.463	0.106	0.640	0.713	0.160
DR73-2_wr	2.56	12.7	4.07	1.43	5.51	1.00	6.81	1.46	4.14	0.626	4.15	0.636	2.62	0.509	0.166	0.588	0.708	0.212
DR74-1	4.36	21.3	6.30	1.90	8.10	1.39	9.84	2.15	6.29	0.973	6.28	0.964	5.06	1.17	0.230	1.11	1.88	0.421

$^{\#}$ = ICPMS Replicates

wr = whole rock samples

all others are volcanic glass samples

Table B.4: Radiogenic isotope ratios of Sr, Nd and Pb of all samples of the WGSC Profile 1. Pb determined based on double spike technique.

Ratio / Sample (SO208)	$^{87}Sr/^{86}Sr$	±2SE	$^{143}Nd/^{144}Nd$	±2SE	εNd	$^{206}Pb/^{204}Pb$	±2SE	$^{207}Pb/^{204}Pb$	±2SE	$^{208}Pb/^{204}Pb$	±2SE	$^{207}Pb/^{206}Pb$	±2SE	$^{208}Pb/^{206}Pb$	±2SE
on-axis Smnt															
DR45-1	0.703007	0.000002	0.512995	0.000003	6.97	18.9751	0.0010	15.5908	0.0009	38.8272	0.0025	0.82164	0.00001	2.04621	0.00004
DR45-1*	0.703002	0.000003				18.9770	0.0008	15.5932	0.0006	38.8343	0.0017	0.82169	0.00001	2.04638	0.00002
off-axis Smnt															
DR63-1_wr	0.703338	0.000003	0.512880	0.000003	4.72	19.5526	0.0017	15.6648	0.0016	39.6227	0.0044	0.80116	0.00002	2.02647	0.00007
DR63-1_wr*	0.703428	0.000002	0.512880	0.000002	4.73	19.5466	0.0011	15.6586	0.0011	39.6005	0.0032	0.80109	0.00002	2.02596	0.00006
DR63-1_wr*	0.703364	0.000004	0.512872	0.000003	4.56	19.5420	0.0015	15.6564	0.0013	39.5911	0.0036	0.80117	0.00002	2.02595	0.00007
young seafloor basalts <30 km from ridge axis															
DR46-1	0.703028	0.000002	0.512975	0.000002	6.58	19.0513	0.0009	15.5907	0.0008	38.8555	0.0021	0.81835	0.00001	2.03952	0.00005
DR48-1	0.703026	0.000003	0.512996	0.000003	6.98	19.0282	0.0010	15.5907	0.0012	38.8345	0.0037	0.81935	0.00002	2.04089	0.00009
DR48-2	0.703007	0.000003	0.512998	0.000003	7.02	19.0268	0.0013	15.5899	0.0011	38.8319	0.0029	0.81936	0.00001	2.04090	0.00004
DR49-1	0.702975	0.000003	0.513011	0.000002	7.28	18.8165	0.0019	15.5644	0.0022	38.5803	0.0071	0.82717	0.00003	2.05035	0.00018
DR49-1*	0.702998	0.000003	0.513008	0.000003	7.22										
DR49-1*			0.513004	0.000003	7.15										
DR50-2	0.702958	0.000003	0.513005	0.000003	7.17	18.8844	0.0008	15.5767	0.0007	38.7149	0.0018	0.82484	0.00001	2.05010	0.00004
DR51-4	0.702979	0.000003	0.513007	0.000003	7.19	18.8970	0.0010	15.5893	0.0010	38.7930	0.0032	0.82062	0.00002	2.04206	0.00008
DR51-6_wr	0.703000	0.000003	0.512999	0.000003	7.04	19.0622	0.0013	15.5966	0.0010	38.8936	0.0028	0.81820	0.00001	2.04036	0.00003
DR53-1_wr	0.702970	0.000003	0.513015	0.000003	7.36										
DR55-1	0.703037	0.000003	0.512981	0.000003	6.70	19.0357	0.0011	15.5934	0.0011	38.8574	0.0031	0.81916	0.00001	2.04129	0.00006
DR56-1	0.702971	0.000003	0.513018	0.000003	7.41	18.9643	0.0024	15.5823	0.0021	38.8044	0.0054	0.82167	0.00002	2.04619	0.00005
DR57-3	0.703050	0.000002	0.512986	0.000003	6.79	19.0857	0.0017	15.6034	0.0014	38.9372	0.0038	0.81754	0.00001	2.04012	0.00006
DR57-5	0.702961	0.000003	0.513005	0.000002	7.16	19.0259	0.0009	15.5888	0.0009	38.7787	0.0025	0.81935	0.00001	2.03821	0.00005
DR58-1	0.702915	0.000002	0.513019	0.000003	7.44	18.9267	0.0013	15.5766	0.0011	38.6585	0.0029	0.82300	0.00001	2.04254	0.00004
DR58-1*	0.702912	0.000003	0.513018	0.000003	7.41	18.9264	0.0014	15.5745	0.0011	38.6557	0.0030	0.82290	0.00002	2.04242	0.00004
DR58-2	0.702910	0.000003	0.513011	0.000003	7.28	18.9282	0.0019	15.5767	0.0015	38.6585	0.0038	0.82294	0.00001	2.04237	0.00004
DR58-5	0.702959	0.000003	0.513014	0.000003	7.33	18.8904	0.0011	15.5860	0.0010	38.7858	0.0023	0.82073	0.00001	2.04239	0.00002
DR60-1	0.703000	0.000004	0.512987	0.000002	6.81	19.0351	0.0012	15.5977	0.0011	38.8870	0.0033	0.81942	0.00001	2.04291	0.00006
DR60-2	0.702994	0.000003	0.512987	0.000003	6.81	19.0331	0.0011	15.5958	0.0011	38.8790	0.0025	0.81940	0.00002	2.04270	0.00004
DR60-3	0.702983	0.000003	0.512998	0.000003	7.02	19.0341	0.0014	15.5944	0.0013	38.8814	0.0037	0.81929	0.00002	2.04273	0.00008
DR61-1	0.703000	0.000003	0.512992	0.000003	6.90	19.0051	0.0007	15.5928	0.0006	38.8743	0.0017	0.82046	0.00001	2.04547	0.00003
DR61-1*	0.703000	0.000003	0.513004	0.000002	7.14	19.0012	0.0010	15.5890	0.0010	38.8663	0.0029	0.82042	0.00001	2.04546	0.00006
DR61-6	0.703003	0.000002	0.513008	0.000003	7.22	19.0085	0.0011	15.5935	0.0009	38.8802	0.0024	0.82034	0.00001	2.04541	0.00003
DR62-1	0.702951	0.000003	0.513022	0.000003	7.49	18.9975	0.0007	15.5891	0.0008	38.8359	0.0029	0.82059	0.00002	2.04426	0.00008
DR66-1	0.702964	0.000003	0.513020	0.000003	7.45	18.9740	0.0010	15.5798	0.0010	38.7407	0.0027	0.82111	0.00002	2.04178	0.00006
DR66-2	0.702960	0.000003	0.513017	0.000003	7.39	18.9721	0.0014	15.5774	0.0014	38.7339	0.0038	0.82107	0.00002	2.04163	0.00007
DR69-1	0.703019	0.000002	0.512995	0.000003	6.96	19.0292	0.0018	15.5949	0.0019	38.8670	0.0063	0.81952	0.00003	2.04249	0.00015
DR72-4	0.703069	0.000004	0.512991	0.000002	6.89	18.9942	0.0011	15.5957	0.0011	38.8810	0.0031	0.82108	0.00002	2.04700	0.00006
old seafloor basalts >30 km from ridge axis															
DR67-1	0.703092	0.000003	0.512989	0.000003	6.86	18.9945	0.0011	15.6014	0.0012	38.9137	0.0036	0.82137	0.00002	2.04868	0.00008
DR68-1_wr	0.703117	0.000003	0.512985	0.000003	6.77	19.0175	0.0018	15.5897	0.0015	38.8437	0.0044	0.81975	0.00002	2.04252	0.00007
DR73-1	0.703142	0.000003	0.512976	0.000003	6.60	18.9583	0.0016	15.6065	0.0016	38.9363	0.0044	0.82320	0.00002	2.05379	0.00009
DR73-1*	0.703134	0.000004	0.512978	0.000004	6.64	18.9462	0.0011	15.6044	0.0011	38.9135	0.0033	0.82362	0.00002	2.05390	0.00008
DR73-2_wr*	0.703284	0.000004	0.512981	0.000004	6.70	18.9844	0.0014	15.6054	0.0011	38.9345	0.0030	0.82201	0.00001	2.05086	0.00003
DR74-1	0.703242	0.000003	0.512964	0.000003	6.36	19.0032	0.0012	15.6186	0.0012	39.0053	0.0035	0.82189	0.00002	2.05257	0.00008
DR74-1*	0.703235	0.000004	0.512979	0.000010	6.66	19.0037	0.0012	15.6183	0.0010	39.0048	0.0027	0.82186	0.00001	2.05186	0.00003

* = TIMS Replicates

. . . continued

| Ratio | | | | | | | | | | | | | | | | |
| Sample (SO208) | ^{87}Sr/^{86}Sr | ±2SE | ^{143}Nd/^{144}Nd | ±2SE | ϵNd | ^{206}Pb/^{204}Pb | ±2SE | ^{207}Pb/^{204}Pb | ±2SE | ^{208}Pb/^{204}Pb | ±2SE | ^{207}Pb/^{206}Pb | ±2SE | ^{208}Pb/^{206}Pb | ±2SE |

wr = whole rock samples
all others are volcanic glass samples

Appendix C

Eastern Galápagos Spreading Center

Figure C.1
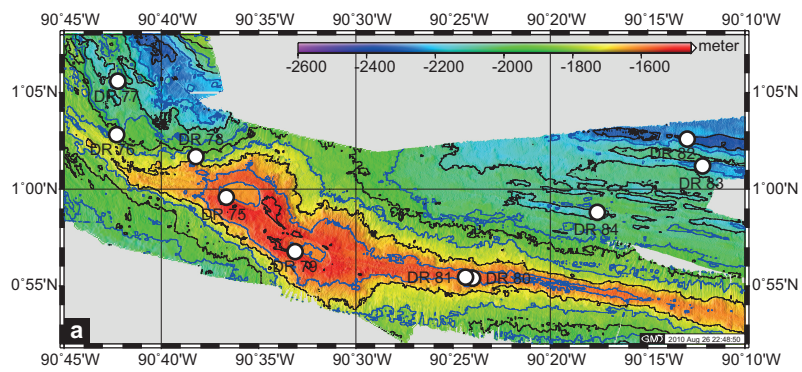
Figure C.2
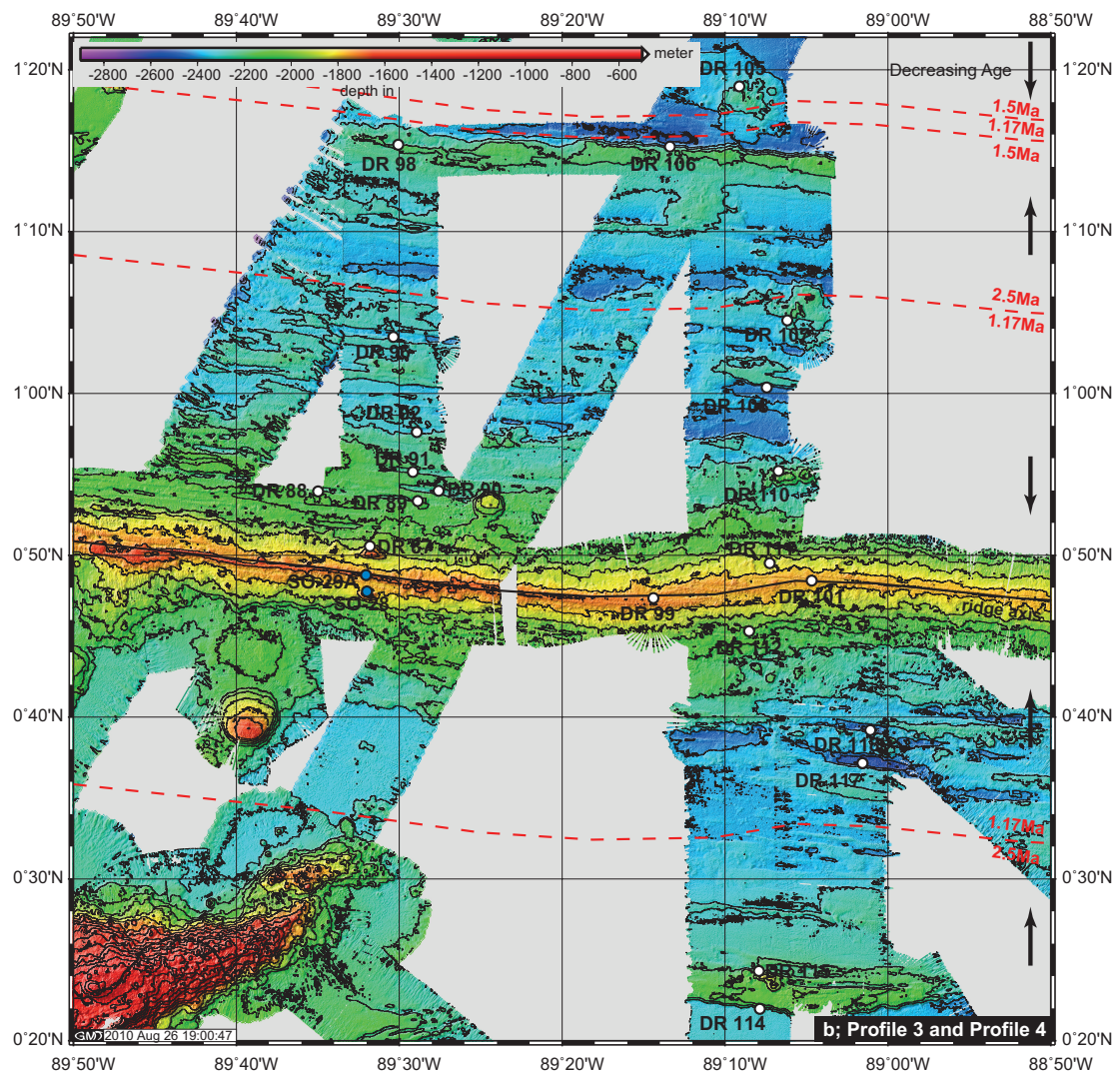
Figure C.3
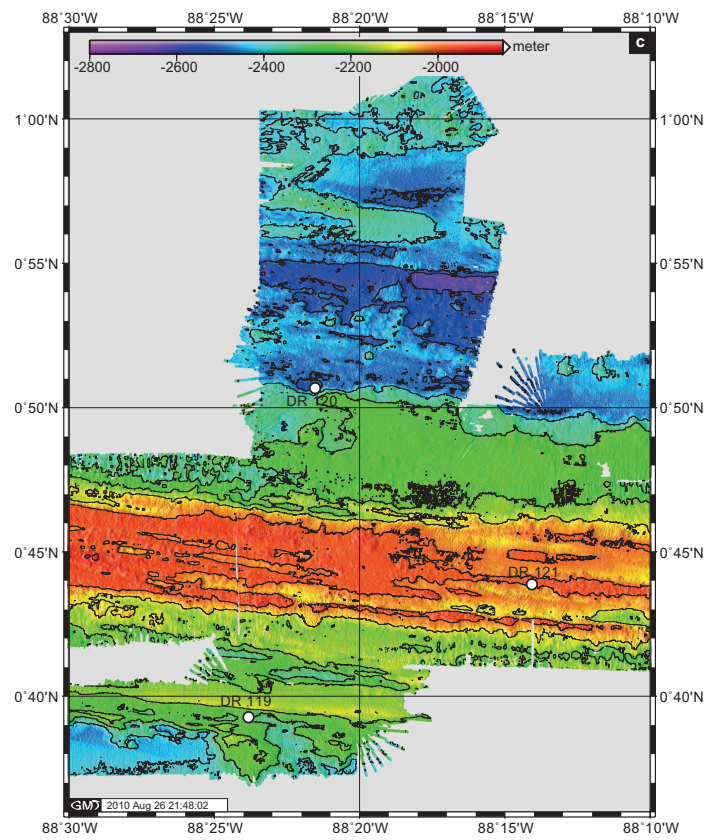
Table C.1: Major element composition (in wt.% and % for LOI) of all samples of the EGSC profiles.

Element/ Sample (SO208)	SiO$_2$	Al$_2$O$_3$	FeO^T	Fe$_2$O$_3$	MgO	CaO	Na$_2$O	K$_2$O	TiO$_2$	P$_2$O$_5$	MnO	SO$_3$	Cl	LOI%	Total
						Study Area 2									
Profile 2 on-axis															
DR75-1	49.33	14.37	10.99		6.99	12.02	2.64	0.21	1.74	0.15	0.14	0.35	0.05		98.99
DR75-2	49.82	14.55	11.24		7.00	12.22	2.54	0.20	1.78	0.14	0.16	0.36	0.05		100.07
DR75-19	49.09	15.01	10.51		7.26	12.07	2.74	0.18	1.62	0.12	0.16	0.31	0.04		99.10
DR78-1	49.87	14.19	11.30		6.45	11.57	2.89	0.24	1.74	0.17	0.15	0.33	0.12		99.00
DR78-2	49.18	14.03	11.75		6.38	11.53	2.85	0.24	1.98	0.16	0.16	0.37	0.07		98.72
DR78-3	49.53	14.16	11.70		6.30	11.42	2.89	0.26	1.96	0.15	0.14	0.35	0.09		98.94
DR79-1	48.92	14.91	11.13		6.73	11.46	2.86	0.27	2.01	0.18	0.13	0.37	0.07		99.05
DR79-4	49.10	14.41	11.68		6.14	10.97	3.04	0.33	2.26	0.20	0.15	0.40	0.12		98.80
DR80-1	49.12	14.33	11.72		5.91	10.78	3.02	0.38	2.19	0.22	0.17	0.38	0.15		98.39
DR80-3	49.07	14.27	11.75		5.91	10.83	3.03	0.37	2.17	0.21	0.17	0.39	0.15		98.33
DR80-5	49.86	14.45	12.22		5.98	11.09	2.79	0.39	2.25	0.21	0.14	0.37	0.16		99.91
DR81-1	49.10	13.81	13.09		5.55	10.52	3.17	0.34	2.45	0.22	0.16	0.42	0.12		98.94
DR81-2	49.13	13.79	13.03		5.55	10.49	3.20	0.35	2.44	0.23	0.16	0.43	0.12		98.92
Profile 2 Smnt/Plateau N off-axis															
DR77-1	47.96	16.56	9.53		7.97	12.03	2.71	0.14	1.52	0.10	0.13	0.26	0.02		98.94
DR77-6-X	47.98	16.67	9.44		8.05	12.04	2.69	0.15	1.48	0.11	0.15	0.26	0.02		99.03
DR77-7-X	47.97	16.65	9.44		7.99	12.09	2.68	0.15	1.48	0.11	0.13	0.26	0.02		98.96
DR77-8-X	47.92	16.60	9.43		8.09	12.02	2.67	0.15	1.48	0.11	0.12	0.27	0.02		98.85
Profile 2 N off-axis															
DR76-1	49.61	12.27	16.48		4.11	8.65	3.23	0.39	3.05	0.29	0.20	0.56	0.10		98.93
DR76-2	49.59	12.18	16.41		4.18	8.79	3.17	0.37	3.02	0.28	0.20	0.58	0.09		98.86
DR76-3	49.59	12.33	16.31		4.24	8.95	3.13	0.37	2.98	0.28	0.23	0.58	0.09		99.08
DR82-1	50.00	13.96	12.25		6.47	11.45	2.59	0.22	1.76	0.15	0.19	0.35	0.07		99.46
DR82-1	49.77	14.02	12.28		6.46	11.44	2.56	0.22	1.75	0.16	0.17	0.36	0.07		99.25
DR82-2	49.60	14.04	11.47		6.96	11.91	2.51	0.17	1.54	0.12	0.17	0.31	0.05		98.85
DR82-3	49.67	14.16	11.63		6.98	11.96	2.50	0.17	1.56	0.11	0.17	0.33	0.05		99.29
DR83-1	49.17	13.84	12.35		6.01	11.05	2.83	0.30	2.14	0.21	0.16	0.37	0.06		98.50
DR83-8	49.20	13.84	12.58		6.11	10.98	2.94	0.27	2.09	0.18	0.17	0.38	0.06		98.80
DR83-9	49.47	13.90	12.20		6.27	11.32	2.69	0.24	1.90	0.16	0.16	0.36	0.06		98.73
DR83-10	50.17	14.08	12.79		6.23	11.50	2.34	0.24	2.01	0.17	0.18	0.38	0.06		100.17
DR83-13	50.10	14.44	12.46		6.20	11.54	2.38	0.20	1.94	0.15	0.17	0.37	0.05		99.99
DR84-1	49.06	14.16	11.24		6.75	11.92	2.74	0.20	1.74	0.14	0.16	0.33	0.06		98.51
DR84-2	49.07	14.15	11.02		6.71	11.91	2.78	0.20	1.76	0.15	0.16	0.35	0.06		98.32
DR84-3	48.81	13.79	11.40		8.37	11.34	2.69	0.20	1.67	0.15	0.16	0.33	0.06		98.97
DR84-4	49.31	14.24	11.40		6.67	11.96	2.73	0.19	1.76	0.14	0.15	0.32	0.05		98.93
DR84-5	49.15	14.23	11.32		6.69	11.98	2.74	0.20	1.74	0.14	0.15	0.35	0.06		98.75
Profile 2 on-axis wr															
DR78-2_wr	49.80	14.28		12.85	6.72	11.55	2.70	0.27	1.95	0.18	0.20	0.09		0.00	100.59
						Profile 3									
Profile 3 Smnt/Plateau N off-axis															
DR87-1	48.49	16.87	8.17		7.29	11.43	2.81	0.80	1.92	0.30	0.10	0.24	0.06		98.49
DR87-2	48.18	16.80	8.05		7.28	11.40	2.76	0.81	1.91	0.30	0.14	0.24	0.05		97.91
DR87-3	48.43	16.94	8.19		7.26	11.41	2.81	0.80	1.93	0.31	0.11	0.24	0.06		98.50
DR87-4	48.42	16.90	8.00		7.28	11.44	2.78	0.80	1.93	0.32	0.13	0.24	0.06		98.30
Profile 3 N off-axis															
DR88-2	49.25	14.70	10.13		7.71	12.76	2.29	0.06	1.21	0.07	0.15	0.31	0.03		98.67
DR89-1	49.76	14.33	10.24		7.75	12.80	2.14	0.06	1.08	0.08	0.12	0.31	0.02		98.69
DR89-2	50.14	14.51	10.35		7.75	12.79	2.15	0.06	1.08	0.06	0.17	0.31	0.02		99.41
DR89-3	50.10	14.50	10.35		7.75	12.77	2.16	0.06	1.08	0.08	0.14	0.30	0.02		99.32
DR89-5	50.14	14.56	10.00		7.85	12.87	2.10	0.06	1.06	0.06	0.15	0.30	0.02		99.15
DR89-8	49.97	14.49	10.26		7.73	12.81	2.17	0.06	1.10	0.08	0.16	0.30	0.02		99.16
DR90-1	49.48	14.60	10.77		7.22	11.90	2.55	0.18	1.53	0.12	0.17	0.33	0.03		98.87
DR90-3	50.02	14.94	9.53		8.21	13.02	1.98	0.04	0.89	0.06	0.15	0.27	0.01		99.12
DR90-5	50.12	14.84	9.48		8.20	12.99	1.95	0.04	0.90	0.06	0.15	0.27	0.01		99.02
DR91-1	49.37	13.76	12.13		6.40	11.51	2.73	0.21	1.86	0.16	0.18	0.39	0.06		98.75
DR98-1	49.51	13.86	12.15		6.90	11.82	2.30	0.11	1.55	0.12	0.18	0.36	0.04		98.88
Profile 3 N off-axis wr															
DR88-1_wr	49.78	14.89		11.41	8.00	12.62	2.15	0.08	1.20	0.09	0.19	0.08		0.00	100.49
DR91-3_wr	50.58	14.26		12.11	6.39	11.86	2.63	0.32	1.89	0.18	0.21	0.05		0.06	100.54
DR92-1_wr	50.59	13.81		14.20	5.76	11.36	2.49	0.20	2.08	0.17	0.23	0.11		0.00	101.00
DR92-3_wr	51.52	14.35		11.81	5.43	11.62	2.70	0.12	2.17	0.18	0.21	0.07		0.00	100.18
DR96-1_wr	50.97	14.36		11.38	6.08	11.46	2.73	0.43	2.22	0.22	0.22	0.10		0.44	100.61
DR96-2_wr	50.54	14.43		12.04	5.58	11.59	2.74	0.43	2.23	0.22	0.20	0.06		0.18	100.24

continued on next page ...

. . . continued

Element/Sample	SiO$_2$	Al$_2$O$_3$	FeO^T	Fe$_2$O$_3$	MgO	CaO	Na$_2$O	K$_2$O	TiO$_2$	P$_2$O$_5$	MnO	SO$_3$	Cl	LOI%	Total
Profile 4															
Profile 4 on-axis															
DR99-1	50.26	14.14	11.18		7.02	12.04	2.42	0.10	1.39	0.11	0.18	0.35	0.04		99.22
DR99-2	50.51	14.07	11.66		6.67	11.96	2.48	0.09	1.47	0.11	0.19	0.24	0.04		99.51
DR101-1	50.17	13.74	12.93		6.01	11.02	2.75	0.16	1.91	0.16	0.24	0.26	0.08		99.45
DR101-2	49.98	13.85	12.92		6.03	11.04	2.74	0.16	1.86	0.18	0.24	0.27	0.09		99.36
DR101-4	50.48	14.60	10.72		8.10	12.95	1.75	0.04	0.86	0.06	0.19	0.19	0.03		99.96
DR101-6	50.81	13.81	12.64		5.47	10.30	2.98	0.25	2.06	0.25	0.21	0.24	0.18		99.20
DR101-14	50.62	13.75	12.50		5.51	10.36	2.96	0.24	2.02	0.25	0.23	0.24	0.17		98.85
Profile 4 Smnt/Plateau N off-axis															
DR110-1	49.13	15.66	9.01		7.74	11.50	2.43	0.57	1.65	0.24	0.18	0.18	0.05		98.34
DR110-1	49.01	15.56	9.12		7.90	11.56	2.44	0.58	1.65	0.23	0.15	0.28	0.05		98.52
DR110-1	49.40	15.67	9.42		7.86	11.27	2.45	0.58	1.62	0.24	0.18	0.26	0.05		99.01
DR110-2	49.45	15.61	9.27		7.78	11.52	2.47	0.56	1.67	0.23	0.14	0.19	0.05		98.94
DR110-2	49.01	15.54	9.04		8.03	11.50	2.43	0.58	1.63	0.24	0.14	0.29	0.05		98.46
DR110-2	48.96	15.53	9.29		7.94	11.20	2.45	0.59	1.62	0.24	0.16	0.27	0.05		98.30
Profile 4 N off-axis															
DR105-1	50.38	14.57	10.63		8.05	12.92	1.72	0.03	0.86	0.06	0.19	0.19	0.03		99.63
DR105-2	50.43	14.57	10.59		7.99	12.88	1.75	0.03	0.84	0.05	0.18	0.20	0.03		99.53
DR105-3	50.39	14.56	10.60		8.05	12.98	1.74	0.03	0.85	0.05	0.20	0.18	0.03		99.66
DR105-4	51.64	13.45	13.67		4.53	9.50	3.20	0.30	2.35	0.38	0.26	0.25	0.23		99.79
DR107-2	50.40	14.65	10.67		7.58	12.52	2.14	0.07	1.20	0.08	0.18	0.22	0.02		99.75
DR107-2	50.38	14.64	10.55		7.55	12.40	2.11	0.08	1.21	0.11	0.18	0.20	0.02		99.42
DR107-3	50.03	14.61	10.70		7.57	12.43	2.16	0.08	1.22	0.08	0.19	0.21	0.02		99.29
DR108-1	50.15	13.49	14.01		6.06	10.94	2.48	0.11	1.95	0.14	0.27	0.28	0.04		99.91
DR108-4	49.90	13.20	14.26		5.87	10.62	2.57	0.12	2.07	0.14	0.25	0.30	0.07		99.37
DR108-5	50.64	13.59	13.98		6.09	11.07	2.19	0.11	1.97	0.14	0.25	0.29	0.03		100.34
DR108-6	50.78	13.59	13.99		6.11	11.11	2.00	0.11	1.95	0.14	0.26	0.28	0.03		100.34
DR108-7	49.89	13.14	13.96		5.80	10.53	2.54	0.12	2.13	0.15	0.25	0.29	0.08		98.87
DR108-8	49.89	13.12	14.10		5.76	10.41	2.58	0.12	2.11	0.16	0.23	0.30	0.08		98.86
DR111-1	50.23	14.55	10.50		7.36	12.79	2.37	0.09	1.29	0.09	0.17	0.20	0.02		99.65
DR111-2	50.13	14.61	10.37		7.41	12.82	2.38	0.09	1.30	0.09	0.21	0.21	0.03		99.66
Profile 4 N off-axis wr															
DR106-1_wr	50.06	13.27		15.27	5.45	10.52	2.28	0.46	2.00	0.17	0.22	0.07		0.98	100.75
DR106-2_wr	50.76	13.72		13.29	5.39	10.90	2.36	0.38	2.07	0.17	0.22	0.16		0.82	100.24
Profile 4 Smnt/Plateau S off-axis															
DR115-1	48.20	16.44	9.32		9.10	12.55	2.26	0.01	0.99	0.06	0.17	0.18	0.00		99.29
DR115-2	48.33	16.67	9.41		8.83	12.69	2.27	0.02	1.03	0.04	0.14	0.18	0.01		99.62
DR115-3	48.43	16.55	9.46		9.20	12.40	2.32	0.02	1.01	0.04	0.14	0.18	0.00		99.74
Profile 4 S off-axis															
DR112-1	50.26	13.96	11.66		6.74	11.70	2.48	0.11	1.55	0.12	0.23	0.23	0.03		99.07
DR112-1	49.83	13.95	12.12		6.91	11.20	2.45	0.12	1.56	0.13	0.22	0.34	0.03		98.85
DR112-2	50.38	13.98	11.83		6.76	11.77	2.48	0.11	1.55	0.12	0.24	0.24	0.03		99.48
DR112-3	50.66	14.17	12.03		6.84	11.84	2.49	0.12	1.58	0.12	0.23	0.24	0.03		100.35
DR112-4	50.33	13.98	11.82		6.78	11.75	2.48	0.11	1.54	0.14	0.23	0.24	0.03		99.42
DR112-5	50.20	14.13	11.94		6.75	11.72	2.50	0.11	1.55	0.12	0.18	0.24	0.04		99.49
DR114-1	49.56	12.61	15.59		5.13	10.12	2.56	0.18	2.59	0.23	0.26	0.34	0.08		99.24
DR114-2	49.67	12.68	15.73		5.21	10.12	2.62	0.18	2.52	0.22	0.25	0.35	0.08		99.61
DR117-4	50.18	13.28	13.96		5.91	10.52	2.57	0.12	2.09	0.16	0.24	0.28	0.08		99.37
DR117-5	49.79	13.32	14.00		5.81	10.57	2.58	0.12	2.10	0.16	0.24	0.29	0.09		99.07
DR118-1	49.73	13.48	13.96		5.95	10.83	2.74	0.12	2.03	0.15	0.24	0.28	0.04		99.56
DR118-4	49.68	13.42	13.84		5.95	10.83	2.72	0.13	2.01	0.15	0.23	0.28	0.04		99.28
Profile 5															
Profile 5 on-axis															
DR121-1	49.99	14.05	10.98		7.36	11.93	2.27	0.09	1.31	0.09	0.16	0.34	0.04		98.61
DR121-2	50.08	14.01	11.17		7.33	11.94	2.30	0.09	1.33	0.11	0.13	0.34	0.04		98.86
Profile 5 S off-axis															
DR119-1	50.69	13.15	13.33		5.56	10.04	2.85	0.18	1.79	0.16	0.19	0.41	0.20		98.54
DR119-2	50.99	13.25	13.46		5.58	10.10	2.80	0.18	1.85	0.16	0.20	0.41	0.19		99.18
DR119-3	50.41	13.23	13.56		5.88	10.44	2.75	0.15	1.87	0.15	0.20	0.42	0.11		99.16
DR119-4	49.93	13.53	13.00		6.31	11.00	2.63	0.13	1.76	0.13	0.20	0.39	0.06		99.07
DR119-13	49.93	13.37	13.16		6.28	10.96	2.58	0.14	1.81	0.14	0.18	0.41	0.07		99.04
DR119-16	50.62	13.67	13.74		6.17	10.96	1.96	0.18	1.88	0.12	0.18	0.43	0.04		99.96
Profile 5 N off-axis															
DR120-1	49.88	12.85	13.11		6.73	11.21	2.45	0.10	1.74	0.12	0.17	0.40	0.05		98.82
DR120-2	50.13	13.57	13.02		6.32	10.97	2.60	0.10	1.78	0.15	0.17	0.42	0.05		99.30
DR120-3	49.93	13.33	13.28		6.35	10.94	2.54	0.11	1.77	0.12	0.18	0.42	0.05		99.01

. . . continued

Element/Sample	SiO$_2$	Al$_2$O$_3$	FeO^T	Fe$_2$O$_3$	MgO	CaO	Na$_2$O	K$_2$O	TiO$_2$	P$_2$O$_5$	MnO	SO$_3$	Cl	LOI%	Total
DR120-4	49.85	13.32	13.56		6.32	10.79	2.56	0.10	1.80	0.13	0.19	0.43	0.05		99.10
Axial Seamount															
Axial Smnt															
DR122-1	49.99	14.02	11.93		6.94	11.39	2.32	0.11	1.55	0.11	0.18	0.38	0.06		98.98
DR122-2	50.28	15.75	10.57		6.47	11.99	2.36	0.09	1.40	0.11	0.15	0.31	0.05		99.53
DR122-14	49.89	14.11	11.95		6.86	11.37	2.34	0.11	1.56	0.13	0.15	0.37	0.06		98.91

Table C.2: Trace element composition (in ppm) of all samples of the EGSC profiles.

Element Sample (SO208)	Li	Sc	V	Cr	Co	Ni	Cu	Zn	Ga	Rb	Sr	Y	Zr	Nb	Mo	Sn	Cs	Ba	La
Study Area 2																			
Study Area 2 on-axis																			
DR75-1	6.06	45.9	330	200	45.8	78.3	135	86.0	19.7	4.22	148	37.0	116	8.47	0.469	1.20	0.038	43.1	6.92
DR75-2	6.20	46.6	345	208	47.6	81.5	141	91.6	20.6	4.39	151	37.4	117	8.71	0.493	1.26	0.040	44.2	7.04
DR75-19	5.78	43.7	322	293	48.7	104	140	84.8	20.1	3.61	142	34.5	102	7.21	0.425	1.13	0.034	37.1	5.90
DR78-1	6.74	44.7	343	118	46.6	61.3	152	90.2	20.6	5.11	139	41.2	136	10.3	0.552	1.45	0.047	48.6	8.24
DR78-2	6.50	46.0	369	168	45.7	66.2	160	94.1	21.2	5.08	155	40.5	128	9.98	0.536	1.40	0.047	52.2	7.89
DR78-3	7.20	43.8	363	170	47.2	69.0	161	100	22.5	5.97	154	40.7	133	10.8	0.599	1.50	0.057	55.6	8.42
DR79-1	6.43	40.5	336	210	45.7	84.2	132	96.5	22.0	6.21	177	39.6	134	12.3	0.659	1.47	0.056	61.7	9.27
DR79-4	7.22	40.5	376	165	46.0	74.7	119	105	23.3	7.93	180	45.5	160	15.5	0.788	1.71	0.067	75.2	11.4
DR80-1	8.38	38.5	351	195	44.7	72.3	120	106	23.1	8.61	171	47.6	182	16.4	0.860	1.87	0.077	80.3	12.3
DR80-3	8.49	38.9	349	192	44.2	71.4	119	107	22.9	8.52	171	48.2	183	16.2	0.836	1.85	0.079	79.5	12.2
DR80-5	8.62	39.8	352	193	44.7	71.7	121	115	23.3	8.58	174	48.5	186	16.6	0.840	1.91	0.077	82.4	12.6
DR81-1	8.85	41.4	401	100	46.9	48.1	123	118	23.9	8.21	157	52.1	178	15.6	0.846	1.90	0.076	74.5	11.8
DR81-2	8.88	41.2	402	98.2	46.4	47.0	123	118	24.0	8.40	157	51.9	178	15.6	0.832	1.93	0.076	75.2	11.9
Study Area 2 Smnt/Plateau N off-axis																			
DR77-1	5.67	37.3	280	273	48.5	149	127	81.8	20.7	3.38	146	30.2	82.5	5.36	0.342	1.09	0.036	33.5	4.42
DR77-6-X	5.30	38.2	286	272	48.2	158	119	75.0	20.1	3.18	147	30.7	84.7	5.34	0.347	1.04	0.034	33.2	4.45
DR77-7-X	5.36	38.7	285	268	48.1	156	119	75.4	20.1	3.26	149	31.4	86.6	5.34	0.344	1.06	0.035	33.3	4.52
DR77-8-X	5.40	39.1	284	264	47.6	154	119	74.5	19.9	3.17	147	31.8	87.3	5.35	0.321	1.04	0.032	32.8	4.50
Study Area 2 N off-axis																			
DR76-1	10.35	39.7	506	7.6	47.8	17.1	100	148	24.7	8.04	126	65.5	213	16.5	0.884	2.20	0.078	76.5	12.9
DR76-2	10.60	40.4	505	7.5	48.0	17.1	101	146	24.9	8.12	130	67.8	219	16.9	0.891	2.19	0.078	76.9	13.2
DR76-3	11.08	38.7	510	11.6	50.1	19.5	109	158	26.0	8.60	132	62.7	204	17.2	0.933	2.26	0.082	79.3	12.8
DR82-1	6.90	43.8	384	92.4	51.3	71.9	171	103	21.7	5.19	130	37.1	107	11.1	0.544	1.22	0.048	51.5	8.09
DR82-1#	7.02	44.2	380	92.2	51.2	71.5	170	104	21.5	5.08	125	37.4	108	10.9	0.517	1.17	0.047	50.9	8.14
DR82-2	6.35	44.3	350	118	50.9	82.5	168	93.6	20.3	3.82	122	33.7	91.5	8.61	0.406	1.02	0.035	39.4	6.38
DR82-3	6.50	44.2	349	121	51.0	82.2	167	94.7	20.4	3.90	124	33.0	89.8	8.46	0.418	1.03	0.037	39.6	6.35
DR83-1	6.81	41.7	368	68.2	47.2	59.0	174	109	22.2	6.50	176	40.1	140	14.2	0.707	1.51	0.058	65.3	10.3
DR83-8	7.26	44.9	383	55.4	48.6	58.6	154	103	21.7	5.59	167	45.4	150	11.9	0.590	1.49	0.050	56.1	9.41
DR83-9	6.97	46.0	371	87.4	47.8	61.4	156	102	21.0	5.07	140	41.4	126	11.3	0.558	1.29	0.048	52.5	8.74
DR83-10	6.98	47.2	389	88.5	49.9	63.6	155	110	21.7	5.17	141	43.3	132	11.6	0.556	1.33	0.048	52.3	8.99
DR83-13	5.45	48.6	393	59.4	49.8	57.5	154	106	21.5	4.47	145	45.9	136	9.77	0.503	1.37	0.043	46.6	8.07
DR84-1	6.27	45.4	338	156	47.4	72.4	152	94.0	20.6	4.18	151	37.3	110	9.05	0.460	1.20	0.038	44.0	7.17
DR84-2	6.24	45.8	335	165	46.3	69.0	147	89.6	19.9	4.09	150	37.4	111	9.10	0.469	1.17	0.038	43.3	7.09
DR84-3	5.83	44.0	318	168	44.3	66.1	138	85.8	19.2	3.87	144	35.6	106	8.57	0.433	1.09	0.038	41.3	6.78
DR84-4	6.11	46.2	335	167	46.3	69.2	148	91.1	20.0	4.09	151	37.5	113	9.12	0.470	1.16	0.038	43.7	7.17
DR84-5	6.15	45.7	346	171	47.7	71.0	152	92.3	20.0	4.11	151	37.4	111	9.20	0.464	1.20	0.039	44.8	7.24
Study Area 2 on-axis wr																			
DR78-2_wr	5.88	44.4	352	185	42.8	70.0	133	94.7	19.0	4.60	158	36.0	121	9.10	0.718	1.18	0.061	52.3	7.31
Profile 3																			
Profile 3 Smnt/Plateau N off-axis																			
DR87-1	4.86	33.9	244	228	39.5	108	78.5	68.4	19.7	19.09	344	28.1	177	31.5	1.40	1.50	0.176	207	19.1
DR87-2	4.83	33.4	244	229	39.5	107	78.3	68.0	20.1	19.16	339	27.3	174	31.1	1.39	1.49	0.179	207	18.8
DR87-3	5.01	33.5	248	234	40.9	111	81.1	71.3	20.9	19.91	349	27.9	177	31.9	1.42	1.52	0.185	212	19.1
DR87-4	4.96	33.8	245	231	39.8	106	79.4	69.1	20.3	19.23	343	28.0	178	31.9	1.42	1.53	0.184	213	19.3
Profile 3 N off-axis																			
DR88-2	5.46	46.7	334	369	51.1	108	145	81.7	18.8	0.995	79.8	30.9	64.4	2.20	0.174	0.770	0.010	10.2	2.32
DR89-1	5.55	46.4	325	319	51.1	94.2	140	82.0	18.4	1.20	75.8	27.7	55.8	2.34	0.168	0.685	0.012	12.0	2.31
DR89-2	5.47	47.3	325	307	51.5	94.4	143	83.2	18.6	1.24	76.7	28.2	56.9	2.40	0.169	0.697	0.013	12.2	2.40
DR89-3	5.52	47.0	325	305	51.9	95.0	143	82.7	18.6	1.24	76.6	28.4	57.1	2.38	0.161	0.712	0.014	12.4	2.40
DR89-5	5.31	47.1	323	346	51.2	98.0	140	81.4	18.6	1.12	74.0	27.4	54.4	2.12	0.155	0.672	0.013	11.2	2.22
DR89-8	5.35	47.4	324	320	50.7	92.9	141	82.0	18.7	1.21	76.1	28.3	56.8	2.31	0.163	0.700	0.013	12.0	2.36
DR90-1	5.90	44.5	332	232	47.4	88.6	130	88.8	19.5	3.80	124	34.8	95.4	7.48	0.401	1.06	0.039	40.0	5.84
DR90-3	4.97	45.3	306	449	49.3	117	129	75.4	17.4	0.719	69.4	24.2	44.7	1.26	0.123	0.568	0.009	7.14	1.54
DR90-5	4.85	46.2	302	440	48.5	114	130	73.4	17.1	0.700	69.3	24.8	45.4	1.25	0.110	0.516	0.010	7.05	1.55
DR91-1	6.93	44.7	382	87.9	50.5	61.0	154	101	21.6	4.52	139	40.1	120	9.85	0.520	1.31	0.043	44.9	7.47
DR98-1	7.12	45.4	390	251	51.5	91.5	140	102	20.6	2.36	85.8	38.8	90.9	5.67	0.326	1.04	0.023	26.5	4.83
Profile 3 N off-axis wr																			
DR88-1_wr	5.35	45.0	309	313	45.5	105	116	78.1	16.3	1.37	88.9	28.2	63.7	2.09	0.261	0.709	0.035	10.4	2.01
DR91-3_wr	5.47	46.5	375	102	48.2	64.5	131	102	19.3	5.28	162	36.7	115	8.92	0.952	1.16	0.149	53.9	7.06
DR92-1_wr	6.46	48.4	441	101	46.9	54.8	101	118	19.9	3.12	104	45.5	120	5.76	0.537	1.24	0.037	28.6	5.20
DR92-3_wr	7.05	50.7	461	104	68.5	102	100	134	20.9	1.25	124	47.9	123	6.11	0.480	1.14	0.036	59.4	5.49
DR96-1_wr	5.22	45.6	400	105	50.2	63.5	122	115	20.4	6.38	178	42.2	144	12.9	1.03	1.38	0.133	80.3	10.0
DR96-2_wr	4.55	45.6	395	115	48.4	61.2	125	115	20.6	6.86	162	41.4	145	13.3	1.18	1.39	0.111	73.5	10.1

. . . continued

Element Sample (SO208)	Li	Sc	V	Cr	Co	Ni	Cu	Zn	Ga	Rb	Sr	Y	Zr	Nb	Mo	Sn	Cs	Ba	La
Profile 4																			
Profile 4 on-axis																			
DR99-1	6.18	48.2	372	131	50.3	72.4	116	108	18.3	1.88	88.7	32.4	80.7	3.73	0.245	0.979	0.022	18.2	3.49
DR99-1[#]	5.36	47.4	332	117	45.3	62.6	105	103	16.6	1.68	85.0	31.3	79.7	3.69	0.217	0.936	0.018	17.8	3.42
DR99-1[#]	6.71	46.0	355	128	51.0	69.7	124	94.3	20.2	1.94	87.1	35.0	80.2	3.70	0.241	0.912	0.017	17.7	3.38
DR99-2	6.41	48.2	376	107	50.2	63.1	115	110	18.4	1.97	89.9	33.7	84.6	3.90	0.269	1.01	0.022	19.0	3.64
DR99-2[#]	5.47	46.6	339	92.8	44.5	54.3	103	105	16.6	1.73	85.2	31.8	81.9	3.83	0.225	0.954	0.018	18.6	3.57
DR101-1	7.74	47.3	399	98.3	48.3	59.1	144	130	19.7	3.43	95.4	45.4	129	6.99	0.451	1.49	0.034	31.6	6.19
DR101-1[#]	6.69	45.7	369	90.3	44.6	50.7	97.3	122	18.0	3.19	92.7	42.8	127	7.06	0.391	1.37	0.031	30.9	6.01
DR101-2	7.49	47.3	394	96.5	47.4	56.4	104	127	19.5	3.42	95.2	44.9	128	6.89	0.427	1.43	0.036	31.2	6.11
DR101-2[#]	6.74	45.7	358	89.6	43.7	50.3	97.3	124	18.2	3.15	92.7	42.2	124	6.94	0.372	1.36	0.023	30.6	5.91
DR101-4	4.86	46.9	309	170	50.5	108	127	93.6	17.4	0.601	42.9	22.8	35.8	1.26	0.121	0.529	0.018	6.53	1.29
DR101-6	8.67	43.5	322	143	42.0	55.1	89.2	132	20.1	5.83	103	62.2	214	12.4	0.713	1.99	0.058	48.6	10.3
DR101-14	7.73	42.3	317	141	40.1	52.5	87.9	133	19.8	5.48	98.5	56.4	197	11.9	0.629	1.95	0.053	46.9	9.67
Profile 4 Smnt/Plateau N off-axis																			
DR110-1	4.54	36.9	273	301	41.5	124	78.4	89.0	17.1	14.7	253	24.2	123	23.1	0.954	1.30	0.136	167	13.3
DR110-1[#]	5.12	38.7	270	304	43.4	124	86.3	74.6	18.4	14.9	251	30.1	135	22.3	0.983	1.21	0.144	162	13.7
DR110-2	4.86	39.1	275	300	43.0	126	80.5	87.7	17.3	14.6	243	27.3	132	22.1	1.07	1.31	0.150	157	13.2
DR110-2[#]	5.26	38.3	275	310	45.3	134	88.6	77.2	18.9	15.2	252	30.0	134	22.5	0.971	1.24	0.148	166	13.8
Profile 4 N off-axis																			
DR105-1	4.41	45.4	299	164	48.6	102	126	95.9	14.9	0.572	41.4	21.5	34.6	1.25	0.105	0.505	0.009	6.39	1.25
DR105-2	4.35	45.5	293	159	47.5	100	125	95.8	14.8	0.557	41.0	21.3	34.4	1.23	0.098	0.522	0.009	6.35	1.26
DR105-3	4.41	45.3	293	159	47.7	100	125	95.4	14.7	0.564	41.3	21.2	34.4	1.25	0.104	0.516	0.009	6.38	1.25
DR105-4	9.02	40.9	281	85.8	36.0	33.7	67.0	147	20.7	6.84	96.7	75.3	270	15.6	0.773	2.47	0.069	56.6	12.7
DR107-1	4.70	45.7	306	305	43.5	91.1	107	96.0	15.5	1.46	69.3	27.0	62.8	3.26	0.202	0.794	0.014	15.4	2.84
DR107-2	4.75	45.6	302	303	43.2	90.8	107	96.9	15.6	1.46	69.0	26.8	62.5	3.24	0.200	0.814	0.014	15.4	2.85
DR107-3	4.79	45.8	321	324	44.5	93.2	110	98.7	16.0	1.50	68.1	26.8	62.4	3.28	0.204	0.829	0.014	15.4	2.84
DR108-1	6.94	47.9	430	78.7	45.6	50.8	85.8	137	18.6	2.19	75.1	42.0	107	4.89	0.278	1.29	0.021	21.4	4.42
DR108-1[#]	8.22	49.0	446	80.1	48.8	54.0	95.7	114	20.7	2.29	73.9	50.0	113	4.83	0.299	1.21	0.022	21.1	4.51
DR108-4	7.00	48.1	449	72.1	45.8	49.8	92.4	137	18.6	2.31	77.7	44.9	117	5.52	0.316	1.41	0.019	23.4	4.93
DR108-4[#]	8.25	48.4	469	73.4	48.7	52.0	101	114	20.8	2.44	75.9	52.1	121	5.37	0.324	1.31	0.026	23.0	5.01
DR108-5	5.54	48.3	433	79.1	46.4	51.6	86.4	139	18.7	2.23	76.4	42.8	109	4.93	0.276	1.33	0.021	21.6	4.48
DR108-6	6.59	49.0	426	78.7	46.1	53.7	84.5	139	18.5	2.18	75.6	43.1	109	4.91	0.269	1.29	0.018	21.3	4.44
DR108-6[#]	8.04	49.2	457	82.4	50.5	55.4	98.6	121	21.4	2.37	75.1	50.3	114	4.90	0.313	1.22	0.024	21.8	4.60
DR108-7	7.25	47.9	474	102	46.7	56.0	89.0	137	19.5	2.39	77.2	45.8	119	5.60	0.321	1.48	0.023	23.6	4.97
DR108-7[#]	8.33	48.7	480	86.5	48.7	56.1	101	110	20.7	2.42	74.8	54.0	126	5.51	0.319	1.33	0.025	22.8	5.03
DR108-8	7.24	49.1	458	105	44.3	53.5	95.6	128	18.3	3.70	92.6	47.5	128	5.68	0.441	1.41	0.035	25.4	5.17
DR111-1	5.03	49.5	313	331	45.8	84.8	126	91.5	16.9	1.61	89.0	29.2	71.9	3.28	0.234	0.877	0.012	16.3	3.04
DR111-2	5.07	50.5	311	327	44.7	82.2	125	91.3	16.5	1.62	86.7	29.9	72.8	3.25	0.228	0.843	0.020	15.9	3.03
Profile 4 N off-axis wr																			
DR106-1_wr	6.06	46.1	446	123	44.3	59.8	105	116	19.3	9.48	107	44.5	113	6.36	0.566	1.12	0.407	33.4	5.47
DR106-2_wr	5.86	48.1	470	127	50.9	72.4	110	133	20.1	6.56	113	48.4	116	6.61	0.821	1.17	0.264	40.9	6.02
Profile 4 Smnt/Plateau S off-axis																			
DR115-1	3.82	43.5	264	385	50.9	205	118	78.1	15.8	0.14	83.1	23.2	45.6	0.478	0.106	0.620	0.016	2.60	1.00
DR115-2	3.90	44.1	268	388	50.0	187	118	78.9	16.0	0.144	83.3	23.2	45.8	0.490	0.087	0.618	0.015	2.61	1.01
DR115-3	3.77	43.0	261	379	49.2	193	116	78.2	15.8	0.148	82.9	23.0	45.6	0.478	0.083	0.639	0.015	2.61	1.02
Profile 4 S off-axis																			
DR112-1	6.06	48.2	368	114	47.4	65.9	113	110	18.3	2.27	86.3	34.9	87.7	4.49	0.289	1.05	0.024	21.2	3.97
DR112-2	6.03	49.3	362	111	46.6	64.6	109	108	17.7	2.15	84.1	34.9	87.9	4.46	0.287	1.02	0.022	21.0	3.97
DR112-3	5.93	49.7	360	110	46.4	64.4	107	106	17.5	2.14	84.2	35.2	88.6	4.45	0.289	1.02	0.024	20.6	3.94
DR112-4	5.92	49.1	360	111	45.8	63.9	107	107	17.5	2.13	84.9	35.5	89.2	4.45	0.282	1.02	0.022	20.9	4.00
DR112-5	5.86	48.5	352	107	45.8	63.5	107	105	17.2	2.12	84.5	34.3	87.8	4.58	0.275	0.995	0.026	20.8	3.97
DR114-1	8.79	48.6	511	46.0	45.5	40.4	100	152	20.6	3.69	88.6	58.7	160	8.99	0.520	1.75	0.044	37.8	7.51
DR114-2	8.81	49.0	512	45.8	46.9	45.5	103	158	20.8	3.72	89.5	58.6	158	8.96	0.528	1.76	0.036	37.2	7.42
DR117-4	7.34	49.2	454	90.6	46.0	58.1	91.2	130	18.9	2.25	74.0	47.7	119	5.14	0.337	1.36	0.022	21.1	4.65
DR117-5	7.52	50.4	465	92.0	47.2	58.3	93.4	134	19.5	2.32	75.8	49.1	124	5.33	0.350	1.37	0.028	21.9	4.82
DR118-1	7.47	48.6	428	52.1	48.0	46.1	104	132	19.3	2.38	94.6	44.1	119	5.38	0.350	1.33	0.024	23.6	4.98
DR118-4	7.63	49.2	424	52.1	47.3	45.4	104	129	19.2	2.35	94.6	44.5	120	5.34	0.345	1.27	0.019	23.0	4.88
Profile 5																			
Profile 5 on-axis																			
DR121-1	6.26	46.0	350	128	49.2	75.2	112	89.8	18.9	1.74	71.8	34.6	77.1	3.39	0.235	0.853	0.015	15.8	3.20
DR121-2	6.39	46.2	354	128	49.6	75.3	112	90.8	18.9	1.76	71.2	34.5	76.9	3.42	0.215	0.846	0.015	15.8	3.20
Profile 5 N off-axis																			
DR120-1	8.27	48.5	444	91.8	53.2	59.7	109	114	21.5	2.14	79.4	47.2	107	4.52	0.274	1.16	0.021	19.4	4.21
DR120-2	8.23	47.2	442	90.8	53.2	60.4	110	114	21.5	2.16	78.4	46.0	103	4.49	0.289	1.20	0.023	19.4	4.15
DR120-3	8.16	47.4	442	91.7	52.6	60.1	109	112	21.4	2.13	78.8	46.4	105	4.47	0.270	1.20	0.020	19.3	4.16

. . . continued

Element Sample (SO208)	Li	Sc	V	Cr	Co	Ni	Cu	Zn	Ga	Rb	Sr	Y	Zr	Nb	Mo	Sn	Cs	Ba	La
DR120-4	7.98	46.8	430	86.9	51.3	58.1	107	111	20.9	2.07	76.7	45.6	103	4.40	0.267	1.17	0.020	19.0	4.09
Profile 5 S off-axis																			
DR119-1	11.1	43.5	410	47.0	49.3	47.1	101	118	22.4	3.91	81.9	57.1	164	7.35	0.419	1.75	0.040	33.3	7.13
DR119-2	10.6	44.0	409	47.0	49.2	47.5	100	117	22.4	3.82	83.1	58.0	166	7.47	0.429	1.76	0.039	33.7	7.21
DR119-3	9.31	45.8	422	47.7	50.4	49.5	105	115	21.9	3.08	83.3	50.9	131	6.27	0.350	1.42	0.031	28.3	5.75
DR119-4	8.01	46.2	415	68.9	51.0	57.4	116	107	21.0	2.67	86.7	44.3	109	5.38	0.318	1.21	0.025	25.0	4.81
DR119-13	8.31	46.2	428	67.1	52.3	57.9	114	111	21.6	2.94	88.6	46.2	116	5.91	0.341	1.29	0.033	27.0	5.23
DR119-16	9.08	46.8	443	50.7	53.5	53.5	111	117	21.9	2.84	88.6	45.9	111	5.82	0.336	1.27	0.030	26.8	5.06
Axial Seamount																			
Axial Smnt																			
DR122-1	7.09	44.8	384	194	52.8	112	104	103	19.9	2.35	70.1	40.0	95.3	4.89	0.292	1.03	0.026	20.9	4.21
DR122-2	7.50	47.2	405	200	51.1	86.8	106	104	20.6	2.50	73.5	42.3	100	5.15	0.299	1.09	0.025	22.3	4.55
DR122-14	7.03	44.7	386	193	49.4	84.8	102	99.4	19.9	2.40	69.8	39.9	94.5	4.92	0.294	1.06	0.023	21.1	4.30
DR122-15	7.08	46.1	377	186	47.2	81.3	99.0	98.1	19.0	2.33	70.8	42.4	100	4.92	0.278	1.03	0.021	21.1	4.41

= ICPMS Replicates

wr = whole rock samples

all others are volcanic glass samples

Element Sample (SO208)	Ce	Pr	Nd	Sm	Eu	Gd	Tb	Dy	Ho	Er	Tm	Yb	Lu	Hf	Ta	W	Pb	Th	U
Study Area 2																			
Study Area 2 on-axis																			
DR75-1	17.2	2.61	13.1	4.28	1.55	5.62	0.980	6.19	1.35	3.73	0.558	3.55	0.515	3.07	0.501	0.088	0.652	0.679	0.179
DR75-2	17.7	2.67	13.5	4.39	1.59	5.74	0.993	6.37	1.38	3.81	0.572	3.72	0.530	3.17	0.519	0.113	0.597	0.693	0.190
DR75-19	15.2	2.33	11.8	3.89	1.47	5.30	0.910	5.92	1.27	3.53	0.518	3.39	0.494	2.81	0.419	0.081	0.508	0.558	0.153
DR78-1	20.4	3.02	14.9	4.68	1.64	6.17	1.09	6.96	1.51	4.24	0.642	4.17	0.596	3.70	0.607	0.117	0.617	0.968	0.256
DR78-2	19.8	2.96	14.8	4.80	1.73	6.16	1.08	6.92	1.50	4.14	0.618	4.00	0.571	3.37	0.595	0.123	0.655	0.768	0.211
DR78-3	21.6	3.15	15.2	4.80	1.72	6.11	1.06	6.64	1.41	3.97	0.585	3.87	0.539	3.37	0.584	0.119	0.664	0.862	0.245
DR79-1	23.0	3.31	16.0	4.86	1.79	6.22	1.06	6.62	1.42	3.92	0.565	3.74	0.527	3.42	0.665	0.130	0.714	0.895	0.256
DR79-4	28.0	4.00	19.2	5.63	1.98	7.09	1.21	7.45	1.60	4.37	0.644	4.17	0.584	3.88	0.807	0.163	0.789	1.11	0.313
DR80-1	30.6	4.35	20.6	6.03	2.06	7.39	1.25	7.83	1.68	4.59	0.679	4.47	0.627	4.37	0.863	0.172	0.888	1.20	0.335
DR80-3	30.2	4.34	20.6	6.06	2.05	7.44	1.27	7.97	1.69	4.67	0.688	4.52	0.641	4.46	0.868	0.184	0.897	1.22	0.343
DR80-5	31.3	4.44	21.1	6.20	2.11	7.72	1.29	8.12	1.73	4.82	0.704	4.65	0.652	4.58	0.907	0.173	0.972	1.28	0.363
DR81-1	29.2	4.22	20.5	6.23	2.18	7.96	1.37	8.64	1.87	5.16	0.752	4.96	0.707	4.46	0.852	0.172	0.886	1.20	0.331
DR81-2	29.6	4.24	20.5	6.21	2.16	8.00	1.36	8.57	1.84	5.11	0.748	4.96	0.702	4.45	0.852	0.183	0.888	1.19	0.337
Study Area 2 Smnt/Plateau N off-axis																			
DR77-1	12.2	1.93	10.0	3.42	1.36	4.58	0.804	5.15	1.12	3.09	0.456	3.02	0.426	2.31	0.294	0.075	0.545	0.407	0.117
DR77-6-X	12.0	1.91	10.1	3.47	1.37	4.66	0.833	5.25	1.16	3.18	0.471	3.07	0.435	2.42	0.313	0.074	0.516	0.415	0.115
DR77-7-X	12.1	1.94	10.3	3.55	1.37	4.76	0.833	5.40	1.17	3.26	0.488	3.17	0.455	2.45	0.315	0.082	0.516	0.431	0.111
DR77-8-X	11.9	1.92	10.1	3.55	1.37	4.77	0.855	5.41	1.19	3.25	0.473	3.14	0.448	2.49	0.313	0.076	0.504	0.422	0.112
Study Area 2 N off-axis																			
DR76-1	31.7	4.72	23.4	7.34	2.47	9.63	1.70	10.8	2.39	6.71	1.00	6.62	0.946	5.54	0.974	0.191	0.974	1.29	0.353
DR76-2	31.8	4.76	23.7	7.49	2.49	9.89	1.73	11.1	2.45	6.84	1.03	6.68	0.969	5.71	1.00	0.180	1.03	1.32	0.355
DR76-3	32.9	4.76	23.0	7.18	2.47	9.30	1.63	10.4	2.26	6.38	0.944	6.32	0.901	5.26	0.960	0.180	1.03	1.25	0.364
DR82-1	19.8	2.83	13.6	4.16	1.50	5.48	0.945	6.03	1.31	3.73	0.551	3.67	0.530	2.78	0.594	0.111	0.549	0.776	0.210
DR82-1#	19.7	2.83	13.6	4.20	1.50	5.42	0.954	6.11	1.35	3.81	0.556	3.72	0.538	2.81	0.607	0.126	0.541	0.794	0.209
DR82-2	16.0	2.33	11.4	3.61	1.34	4.76	0.837	5.41	1.18	3.34	0.492	3.21	0.463	2.35	0.459	0.078	0.468	0.576	0.155
DR82-3	15.8	2.29	11.3	3.53	1.32	4.69	0.831	5.37	1.17	3.26	0.488	3.23	0.463	2.32	0.451	0.082	0.461	0.569	0.160
DR83-1	25.5	3.61	17.0	4.94	1.73	6.11	1.03	6.52	1.40	3.89	0.565	3.79	0.522	3.41	0.784	0.141	0.751	0.974	0.278
DR83-8	23.2	3.49	17.3	5.35	1.87	6.90	1.20	7.73	1.68	4.65	0.698	4.53	0.646	3.99	0.712	0.135	0.738	0.924	0.248
DR83-9	21.0	3.11	15.2	4.70	1.65	6.17	1.08	6.85	1.50	4.26	0.634	4.16	0.583	3.36	0.670	0.121	0.626	0.858	0.236
DR83-10	21.6	3.19	15.8	4.89	1.74	6.43	1.13	7.24	1.60	4.44	0.666	4.36	0.622	3.57	0.698	0.110	0.659	0.881	0.242
DR83-13	20.0	3.04	15.4	4.97	1.78	6.84	1.19	7.83	1.73	4.86	0.727	4.81	0.702	3.80	0.620	0.104	0.835	0.805	0.212
DR84-1	17.9	2.70	13.3	4.21	1.53	5.43	0.968	6.18	1.34	3.76	0.553	3.66	0.519	2.96	0.534	0.105	0.573	0.691	0.197
DR84-2	17.5	2.65	13.1	4.17	1.51	5.47	0.955	6.12	1.32	3.70	0.535	3.57	0.517	2.96	0.535	0.093	0.565	0.700	0.191
DR84-3	16.7	2.53	12.7	4.02	1.46	5.32	0.938	6.00	1.31	3.66	0.542	3.62	0.512	2.94	0.528	0.091	0.542	0.689	0.189
DR84-4	17.7	2.68	13.4	4.29	1.56	5.67	1.00	6.42	1.39	3.87	0.566	3.73	0.541	3.07	0.560	0.094	0.572	0.707	0.197
DR84-5	18.1	2.72	13.5	4.35	1.59	5.86	1.03	6.68	1.45	4.04	0.603	3.93	0.564	3.25	0.582	0.090	0.672	0.760	0.213
Study Area 2 on-axis wr																			
DR78-2_wr	18.7	2.84	14.2	4.42	1.60	5.61	0.981	6.41	1.32	3.65	0.541	3.51	0.524	3.12	0.522	0.149	0.584	0.670	0.256
Profile 3																			
Profile 3 Smnt/Plateau N off-axis																			
DR87-1	40.9	5.23	22.2	5.16	1.78	5.49	0.873	5.19	1.09	2.90	0.420	2.69	0.381	4.33	1.90	0.409	1.10	2.32	0.636

. . . continued

Element Sample (SO208)	Ce	Pr	Nd	Sm	Eu	Gd	Tb	Dy	Ho	Er	Tm	Yb	Lu	Hf	Ta	W	Pb	Th	U
DR87-2	40.4	5.14	21.8	5.18	1.75	5.45	0.860	5.10	1.05	2.79	0.410	2.61	0.379	4.34	1.85	0.409	1.15	2.27	0.630
DR87-3	41.3	5.23	22.3	5.26	1.80	5.52	0.860	5.10	1.05	2.81	0.402	2.65	0.382	4.30	1.87	0.403	1.15	2.26	0.630
DR87-4	41.4	5.22	22.2	5.20	1.76	5.47	0.858	5.15	1.06	2.85	0.408	2.63	0.369	4.27	1.83	0.387	1.20	2.27	0.630
Profile 3 N off-axis																			
DR88-2	7.40	1.28	7.18	2.76	1.09	4.05	0.743	4.92	1.11	3.19	0.473	3.19	0.452	1.84	0.122	0.038	0.304	0.162	0.055
DR89-1	6.94	1.17	6.42	2.42	0.959	3.61	0.667	4.50	1.01	2.90	0.438	2.89	0.420	1.64	0.132	0.038	0.286	0.182	0.051
DR89-2	7.03	1.19	6.57	2.44	0.972	3.61	0.678	4.50	1.02	2.91	0.440	2.94	0.428	1.63	0.134	0.047	0.293	0.181	0.049
DR89-3	7.14	1.20	6.56	2.48	0.987	3.69	0.683	4.58	1.03	2.97	0.443	3.03	0.429	1.67	0.127	0.046	0.276	0.184	0.055
DR89-5	6.67	1.14	6.24	2.39	0.947	3.60	0.664	4.45	1.00	2.90	0.437	2.89	0.418	1.59	0.123	0.039	0.277	0.162	0.046
DR89-8	7.04	1.20	6.52	2.49	0.984	3.67	0.692	4.62	1.04	2.94	0.448	3.00	0.426	1.66	0.139	0.034	0.290	0.182	0.049
DR90-1	14.7	2.22	11.0	3.67	1.36	5.03	0.903	5.95	1.31	3.71	0.554	3.67	0.537	2.74	0.459	0.099	0.526	0.614	0.170
DR90-3	5.04	0.896	5.09	2.02	0.818	3.08	0.576	3.87	0.880	2.55	0.386	2.62	0.375	1.33	0.070	0.038	0.242	0.090	0.028
DR90-5	5.03	0.906	5.16	2.05	0.844	3.10	0.593	3.93	0.903	2.60	0.394	2.62	0.382	1.37	0.070	0.045	0.237	0.092	0.026
DR91-1	19.4	2.91	14.3	4.55	1.67	6.01	1.05	6.74	1.48	4.09	0.604	3.99	0.573	3.22	0.552	0.109	0.586	0.716	0.202
DR98-1	12.8	2.00	10.5	3.65	1.35	5.23	0.954	6.33	1.41	3.98	0.605	4.06	0.569	2.58	0.312	0.066	0.386	0.404	0.114
Profile 3 N off-axis wr																			
DR88-1_wr	7.01	1.27	7.22	2.68	1.03	3.81	0.707	4.87	1.05	2.92	0.445	2.95	0.440	1.83	0.144	0.072	0.349	0.159	0.081
DR91-3_wr	18.5	2.82	14.2	4.38	1.57	5.58	0.982	6.51	1.36	3.77	0.564	3.71	0.551	3.04	0.534	0.136	0.535	0.611	0.290
DR92-1_wr	15.2	2.51	13.5	4.65	1.65	6.29	1.15	7.83	1.68	4.71	0.707	4.70	0.702	3.29	0.360	0.105	0.545	0.423	0.176
DR92-3_wr	16.1	2.67	14.3	4.94	1.77	6.67	1.23	8.30	1.77	4.94	0.744	4.95	0.728	3.41	0.368	0.108	0.335	0.443	0.286
DR96-1_wr	24.9	3.65	17.8	5.28	1.82	6.53	1.14	7.46	1.54	4.28	0.630	4.15	0.613	3.66	0.746	0.133	0.739	0.865	0.312
DR96-2_wr	25.1	3.70	17.9	5.29	1.83	6.51	1.12	7.34	1.53	4.20	0.623	4.11	0.607	3.72	0.767	0.155	0.699	0.892	0.324
Profile 4																			
Profile 4 on-axis																			
DR99-1	9.92	1.67	9.36	3.30	1.20	4.66	0.817	5.70	1.27	3.60	0.553	3.56	0.551	2.20	0.226	0.039	0.401	0.256	0.079
DR99-1[#]	9.59	1.65	9.18	3.22	1.20	4.46	0.796	5.67	1.25	3.63	0.555	3.60	0.548	2.27	0.241	0.029	0.377	0.272	0.078
DR99-1[#]	9.98	1.65	8.85	3.19	1.21	4.56	0.827	5.42	1.21	3.46	0.518	3.47	0.488	2.10	0.198	0.035	0.340	0.241	0.073
DR99-2	10.4	1.74	9.58	3.42	1.25	4.72	0.843	5.83	1.31	3.73	0.565	3.70	0.573	2.30	0.235	0.039	0.405	0.267	0.087
DR99-2[#]	10.1	1.72	9.49	3.26	1.22	4.50	0.808	5.70	1.26	3.65	0.559	3.69	0.557	2.29	0.241	0.035	0.380	0.276	0.081
DR101-1	16.3	2.69	14.4	4.84	1.66	6.63	1.16	8.01	1.76	5.01	0.766	4.93	0.774	3.50	0.442	0.075	0.583	0.519	0.160
DR101-1[#]	16.0	2.63	14.2	4.79	1.65	6.21	1.09	7.69	1.66	4.84	0.742	4.86	0.746	3.43	0.451	0.066	0.536	0.531	0.155
DR101-2	16.2	2.65	14.4	4.85	1.68	6.56	1.16	7.97	1.75	5.03	0.766	4.92	0.762	3.48	0.444	0.069	0.574	0.514	0.156
DR101-2[#]	15.6	2.59	13.8	4.50	1.60	6.05	1.06	7.49	1.63	4.69	0.727	4.70	0.722	3.36	0.434	0.064	0.532	0.520	0.149
DR101-4	3.76	0.692	4.11	1.70	0.673	2.78	0.515	3.80	0.878	2.57	0.399	2.68	0.420	1.10	0.071	0.015	0.172	0.089	0.030
DR101-6	26.1	4.17	22.0	6.99	2.09	9.28	1.59	10.8	2.39	6.78	1.04	6.60	1.03	5.53	0.761	0.116	0.783	0.973	0.284
DR101-14	25.0	3.98	20.8	6.62	2.01	8.41	1.47	10.2	2.22	6.42	0.978	6.40	0.969	5.23	0.748	0.113	0.784	0.968	0.270
Profile 4 Smnt/Plateau N off-axis																			
DR110-1	28.2	3.77	16.8	4.09	1.42	4.36	0.695	4.65	0.979	2.71	0.408	2.67	0.385	2.93	1.35	0.253	0.808	1.49	0.421
DR110-1[#]	28.8	3.77	16.7	4.29	1.49	4.99	0.820	5.22	1.11	3.08	0.453	2.98	0.434	3.32	1.30	0.293	0.809	1.62	0.417
DR110-2	28.4	3.75	16.9	4.10	1.41	4.70	0.760	4.96	1.05	2.96	0.445	2.77	0.425	3.22	1.33	0.257	1.10	1.49	0.424
DR110-2[#]	29.3	3.81	16.6	4.25	1.47	4.96	0.837	5.28	1.13	3.16	0.457	3.02	0.437	3.43	1.30	0.280	0.993	1.67	0.443
Profile 4 N off-axis																			
DR105-1	3.65	0.678	4.08	1.69	0.661	2.60	0.492	3.68	0.847	2.53	0.390	2.62	0.408	1.08	0.078	0.014	0.171	0.092	0.029
DR105-2	3.66	0.684	4.07	1.67	0.663	2.61	0.497	3.73	0.847	2.51	0.390	2.65	0.410	1.09	0.078	0.014	0.169	0.094	0.029
DR105-3	3.69	0.690	4.08	1.67	0.665	2.60	0.497	3.70	0.842	2.49	0.400	2.66	0.403	1.08	0.082	0.014	0.161	0.092	0.029
DR105-4	31.9	5.20	27.4	8.63	2.50	11.2	1.93	13.6	2.96	8.56	1.31	8.49	1.30	7.19	1.01	0.146	0.930	1.29	0.349
DR107-1	7.66	1.33	7.44	2.70	1.00	3.69	0.680	4.89	1.09	3.15	0.480	3.18	0.492	1.81	0.209	0.028	0.305	0.246	0.074
DR107-2	7.67	1.33	7.45	2.66	1.00	3.69	0.673	4.89	1.07	3.14	0.477	3.23	0.482	1.84	0.216	0.030	0.317	0.253	0.076
DR107-3	7.75	1.35	7.55	2.70	1.01	3.73	0.678	4.81	1.06	3.09	0.480	3.11	0.474	1.80	0.212	0.030	0.317	0.239	0.074
DR108-1	12.2	2.15	12.0	4.30	1.52	5.93	1.06	7.51	1.67	4.88	0.756	4.90	0.744	3.03	0.310	0.046	0.466	0.359	0.103
DR108-1[#]	12.6	2.15	11.7	4.37	1.56	6.50	1.21	8.05	1.82	5.23	0.793	5.29	0.766	3.29	0.294	0.056	0.484	0.361	0.099
DR108-4	13.4	2.34	13.1	4.60	1.61	6.31	1.12	8.02	1.78	5.21	0.798	5.22	0.793	3.34	0.352	0.051	0.474	0.406	0.116
DR108-4[#]	13.9	2.37	12.8	4.79	1.69	6.92	1.27	8.49	1.89	5.46	0.826	5.56	0.806	3.55	0.335	0.062	0.506	0.422	0.114
DR108-5	12.4	2.17	12.1	4.30	1.54	5.93	1.07	7.60	1.69	4.90	0.751	4.96	0.749	3.08	0.307	0.044	0.466	0.357	0.101
DR108-6	12.0	2.13	12.0	4.32	1.52	5.91	1.07	7.54	1.70	4.94	0.756	4.98	0.754	3.08	0.314	0.044	0.496	0.361	0.097
DR108-6[#]	13.0	2.21	12.1	4.53	1.62	6.57	1.22	8.18	1.85	5.23	0.794	5.34	0.776	3.36	0.294	0.050	0.500	0.385	0.102
DR108-7	13.9	2.41	13.4	4.66	1.68	6.39	1.16	8.23	1.82	5.33	0.818	5.38	0.808	3.40	0.352	0.049	0.486	0.404	0.118
DR108-7[#]	14.0	2.39	13.0	4.84	1.72	7.12	1.31	8.78	1.97	5.65	0.867	5.77	0.834	3.65	0.337	0.057	0.782	0.422	0.119
DR108-8	13.5	2.40	13.7	4.86	1.68	6.61	1.19	8.57	1.91	5.52	0.868	5.72	0.848	3.68	0.373	0.064	0.491	0.431	0.126
DR111-1	8.74	1.49	8.31	2.90	1.12	4.22	0.744	5.17	1.15	3.28	0.504	3.19	0.485	2.06	0.206	0.029	0.628	0.226	0.070
DR111-2	8.45	1.45	8.02	2.91	1.09	4.16	0.729	5.12	1.13	3.24	0.496	3.12	0.485	2.05	0.206	0.033	0.408	0.237	0.068
Profile 4 N off-axis wr																			
DR106-1_wr	15.0	2.42	12.8	4.39	1.54	6.06	1.11	7.56	1.63	4.59	0.696	4.65	0.698	3.06	0.384	0.103	0.523	0.449	0.156
DR106-2_wr	16.2	2.60	13.8	4.72	1.66	6.50	1.20	8.18	1.76	4.98	0.760	5.05	0.759	3.20	0.401	0.110	0.454	0.470	0.213
Profile 4 Smnt/Plateau S off-axis																			
DR115-1	3.84	0.778	4.94	2.00	0.843	3.06	0.562	3.90	0.868	2.50	0.376	2.46	0.375	1.32	0.033	0.010	0.231	0.033	0.012

. . . continued

Element Sample (SO208)	Ce	Pr	Nd	Sm	Eu	Gd	Tb	Dy	Ho	Er	Tm	Yb	Lu	Hf	Ta	W	Pb	Th	U
DR115-2	3.87	0.806	5.07	2.07	0.882	3.19	0.576	4.00	0.889	2.56	0.396	2.50	0.385	1.34	0.035	0.010	0.245	0.035	0.010
DR115-3	3.85	0.793	5.02	2.00	0.878	3.14	0.567	3.96	0.873	2.53	0.383	2.48	0.382	1.34	0.033	0.012	0.224	0.031	0.010
Profile 4 S off-axis																			
DR112-1	11.0	1.81	9.97	3.41	1.26	4.86	0.862	6.04	1.34	3.84	0.600	3.75	0.577	2.46	0.286	0.053	0.429	0.328	0.092
DR112-2	11.0	1.83	10.2	3.44	1.28	5.00	0.888	6.14	1.37	3.91	0.602	3.82	0.594	2.52	0.288	0.048	0.546	0.326	0.096
DR112-3	10.7	1.78	9.87	3.36	1.25	4.90	0.873	6.01	1.35	3.85	0.592	3.75	0.589	2.48	0.275	0.040	0.443	0.321	0.092
DR112-4	10.9	1.80	10.0	3.46	1.26	4.92	0.876	6.11	1.35	3.91	0.597	3.77	0.586	2.49	0.282	0.048	0.429	0.328	0.090
DR112-5	10.7	1.80	9.98	3.39	1.25	4.82	0.845	5.91	1.30	3.72	0.575	3.64	0.560	2.38	0.280	0.044	0.437	0.319	0.092
DR114-1	19.6	3.20	17.2	5.79	1.95	8.13	1.43	10.0	2.23	6.39	0.990	6.33	0.971	4.34	0.544	0.077	0.646	0.656	0.193
DR114-2	19.4	3.14	17.0	5.69	1.93	8.13	1.42	9.87	2.20	6.33	0.985	6.24	0.971	4.31	0.542	0.086	0.622	0.652	0.187
DR117-4	13.1	2.25	12.7	4.48	1.58	6.56	1.15	8.08	1.79	5.16	0.799	5.14	0.791	3.33	0.319	0.044	0.480	0.375	0.112
DR117-5	13.6	2.33	13.2	4.64	1.64	6.75	1.21	8.36	1.88	5.35	0.833	5.36	0.822	3.44	0.340	0.050	0.502	0.392	0.110
DR118-1	14.1	2.38	13.1	4.44	1.62	6.26	1.10	7.60	1.69	4.80	0.737	4.74	0.721	3.23	0.338	0.046	0.531	0.377	0.117
DR118-4	13.7	2.34	12.9	4.38	1.59	6.17	1.08	7.57	1.67	4.77	0.727	4.65	0.711	3.18	0.338	0.042	0.578	0.370	0.113
Profile 5																			
Profile 5 on-axis																			
DR121-1	9.08	1.52	8.43	3.13	1.18	4.57	0.840	5.62	1.25	3.59	0.535	3.60	0.528	2.22	0.201	0.045	0.340	0.270	0.076
DR121-2	9.09	1.54	8.43	3.13	1.16	4.54	0.842	5.58	1.24	3.58	0.537	3.56	0.525	2.23	0.203	0.047	0.352	0.259	0.076
Profile 5 N off-axis																			
DR120-1	12.2	2.08	11.3	4.29	1.55	6.15	1.14	7.61	1.72	4.87	0.754	4.99	0.726	3.11	0.270	0.057	0.454	0.343	0.102
DR120-2	12.2	2.06	11.2	4.17	1.52	6.05	1.10	7.37	1.66	4.72	0.715	4.82	0.689	2.95	0.258	0.054	0.445	0.331	0.097
DR120-3	12.1	2.05	11.4	4.16	1.52	6.04	1.12	7.36	1.66	4.73	0.717	4.77	0.696	2.94	0.256	0.048	0.429	0.337	0.098
DR120-4	11.9	2.01	11.1	4.16	1.52	6.07	1.11	7.40	1.67	4.75	0.723	4.81	0.698	2.95	0.258	0.043	0.440	0.324	0.098
Profile 5 S off-axis																			
DR119-1	19.9	3.14	16.2	5.57	1.76	7.62	1.40	9.22	2.08	5.90	0.896	5.99	0.861	4.54	0.426	0.069	0.596	0.794	0.227
DR119-2	20.1	3.19	16.6	5.57	1.81	7.67	1.39	9.23	2.08	5.88	0.900	5.95	0.851	4.53	0.425	0.076	0.590	0.779	0.222
DR119-3	16.0	2.59	13.6	4.84	1.66	6.75	1.22	8.11	1.82	5.21	0.789	5.28	0.755	3.65	0.358	0.053	0.536	0.558	0.165
DR119-4	13.6	2.22	11.8	4.22	1.50	5.94	1.08	7.13	1.61	4.55	0.689	4.58	0.664	3.05	0.308	0.058	0.468	0.448	0.134
DR119-13	14.6	2.37	12.7	4.41	1.57	6.33	1.14	7.47	1.67	4.75	0.719	4.76	0.690	3.26	0.346	0.053	0.490	0.492	0.145
DR119-16	14.3	2.32	12.4	4.37	1.59	6.21	1.13	7.43	1.67	4.77	0.716	4.76	0.691	3.10	0.342	0.068	0.481	0.440	0.130
Axial Seamount																			
Axial Smnt																			
DR122-1	11.5	1.88	10.1	3.68	1.31	5.23	0.962	6.44	1.46	4.15	0.634	4.19	0.621	2.69	0.292	0.060	0.415	0.381	0.106
DR122-2	12.4	2.03	10.8	3.92	1.40	5.52	1.03	6.81	1.53	4.41	0.666	4.47	0.646	2.86	0.308	0.068	0.443	0.398	0.111
DR122-14	11.8	1.93	10.3	3.76	1.33	5.27	0.978	6.41	1.44	4.09	0.622	4.15	0.598	2.65	0.289	0.047	0.409	0.374	0.106
DR122-15	11.9	1.98	10.8	3.84	1.36	5.56	1.03	6.84	1.57	4.43	0.664	4.49	0.655	2.90	0.305	0.054	0.418	0.381	0.106

= ICPMS Replicates

wr = whole rock samples

all others are volcanic glass samples

Table C.4: Radiogenic isotope ratios of Sr, Nd and Pb of all samples of the EGSC Profile 1. Pb determined based on double spike technique.

Ratio/ Sample (SO208)	^{87}Sr/^{86}Sr	±2SE	^{143}Nd/^{144}Nd	±2SE	εNd	^{206}Pb/^{204}Pb	±2SE	^{207}Pb/^{204}Pb	±2SE	^{208}Pb/^{204}Pb	±2SE	^{207}Pb/^{206}Pb	±2SE	^{208}Pb/^{206}Pb	±2SE
Study Area 2 on-axis															
DR75-1	0.702942	0.000002	0.513000	0.000003	7.06	19.0105	0.0008	15.5779	0.0007	38.7158	0.0019	0.81944	0.00001	2.03655	0.00004
DR78-1	0.702958	0.000003	0.513002	0.000003	7.10										
DR78-2	0.702930	0.000002	0.513001	0.000003	7.08	19.0743	0.0013	15.5828	0.0014	38.7848	0.0043	0.81695	0.00002	2.03335	0.00011
DR79-1	0.702948	0.000003	0.513003	0.000002	7.13	19.0871	0.0007	15.5862	0.0008	38.8160	0.0027	0.81658	0.00002	2.03362	0.00007
DR79-4	0.703062	0.000002	0.512975	0.000003	6.58	19.0964	0.0010	15.5877	0.0008	38.8589	0.0021	0.81626	0.00001	2.03488	0.00003
DR80-1	0.703052	0.000003	0.513000	0.000003	7.07	19.0349	0.0010	15.5817	0.0011	38.7693	0.0036	0.81858	0.00002	2.03675	0.00010
DR81-1	0.702975	0.000003	0.513003	0.000003	7.13	19.0610	0.0014	15.5834	0.0017	38.8003	0.0054	0.81755	0.00003	2.03558	0.00014
Study Area 2 Smnt./Plateau N off-axis															
DR77-1	0.702840	0.000003	0.513032	0.000003	7.70	18.8211	0.0009	15.5699	0.0008	38.6052	0.0021	0.82726	0.00001	2.05117	0.00004
Study Area 2 N off-axis															
DR76-1	0.702982	0.000003	0.512997	0.000002	7.01	19.0482	0.0009	15.5786	0.0008	38.7566	0.0024	0.81785	0.00001	2.03466	0.00005
DR76-1*	0.702976	0.000002				19.0499	0.0013	15.5799	0.0012	38.7618	0.0034	0.81785	0.00002	2.03475	0.00006
DR82-1	0.703067	0.000003	0.512969	0.000003	6.46	19.1341	0.0015	15.5867	0.0016	38.8946	0.0050	0.81460	0.00002	2.03274	0.00011
DR82-3	0.703016	0.000003	0.512992	0.000003	6.91	19.0831	0.0011	15.5776	0.0010	38.8007	0.0028	0.81630	0.00001	2.03325	0.00005
DR83-9	0.703045	0.000003	0.512981	0.000003	6.69	19.0777	0.0012	15.5819	0.0010	38.8267	0.0027	0.81676	0.00001	2.03519	0.00004
DR83-13	0.702971	0.000003	0.513000	0.000003	7.06										
DR84-3	0.703027	0.000003	0.512983	0.000003	6.73	19.0135	0.0010	15.5755	0.0009	38.7414	0.0024	0.81918	0.00001	2.03757	0.00003
Profile 3															
Profile 3 Smnt./Plateau N off-axis															
SO208	0.702929	0.000002	0.512998	0.000003	7.02	19.1273	0.0009	15.5834	0.0007	38.7259	0.0007	0.81472	0.00001	2.02464	0.00003
DR87-1															
Profile 3 N off-axis															
DR88-2	0.702694	0.000003	0.513092	0.000003	8.86	18.6095	0.0017	15.5264	0.0019	38.1843	0.0063	0.83432	0.00003	2.05187	0.00017
DR89-2	0.702784	0.000003	0.513070	0.000003	8.43	18.6802	0.0010	15.5383	0.0010	38.3082	0.0030	0.83181	0.00002	2.05074	0.00007
DR90-1	0.702886	0.000006	0.513026	0.000006	7.56	18.9247	0.0010	15.5612	0.0011	38.6095	0.0032	0.82227	0.00002	2.04017	0.00009
DR90-3	0.702708	0.000003	0.513093	0.000001	8.88	18.5446	0.0013	15.5243	0.0015	38.1644	0.0050	0.83713	0.00002	2.05798	0.00012
DR91-1	0.703000	0.000003	0.512990	0.000003	6.87	18.9721	0.0009	15.5691	0.0007	38.6805	0.0020	0.82063	0.00001	2.03881	0.00002
DR98-1	0.702871	0.000002	0.513041	0.000002	7.85	18.8221	0.0010	15.5551	0.0009	38.4568	0.0022	0.82643	0.00001	2.04317	0.00003
Profile 3 N off-axis wr															
DR92-1_wr	0.702778	0.000003	0.513062	0.000003	8.26	18.7250	0.0007	15.5412	0.0007	38.3488	0.0023	0.82997	0.00001	2.04800	0.00006
DR96-1_wr	0.703099	0.000003	0.512980	0.000003	6.68	19.0900	0.0011	15.5801	0.0012	38.7995	0.0034	0.81614	0.00002	2.03245	0.00007
Profile 4															
Profile 4 Smnt./Plateau N off-axis															
DR110-1	0.702862	0.000003	0.513025	0.000003	7.55	19.0113	0.0007	15.5738	0.0006	38.6023	0.0017	0.81919	0.00001	2.03049	0.00004
Profile 4 N off-axis															
DR105-1	0.702707	0.000003	0.513090	0.000002	8.82	18.6633	0.0016	15.5276	0.0014	38.2211	0.0033	0.83199	0.00001	2.04793	0.00004
DR105-4	0.702820	0.000002	0.513061	0.000002	8.25	18.8152	0.0007	15.5525	0.0007	38.4547	0.0022	0.82660	0.00001	2.04381	0.00006
DR107-1	0.702735	0.000003	0.513057	0.000003	8.17	18.7469	0.0010	15.5381	0.0008	38.3475	0.0023	0.82884	0.00001	2.04554	0.00004
DR107-1*	0.702728	0.000002	0.513057	0.000003	8.17	18.7483	0.0008	15.5393	0.0007	38.3518	0.0018	0.82884	0.00001	2.04562	0.00004
DR107-2	0.702730	0.000002	0.513060	0.000002	8.24	18.7471	0.0010	15.5386	0.0010	38.3491	0.0029	0.82885	0.00001	2.04561	0.00006
DR107-3			0.513071	0.000002	8.45	18.7515	0.0017	15.5415	0.0015	38.3572	0.0038	0.82881	0.00002	2.04556	0.00005
DR108-1	0.702711	0.000002	0.513073	0.000003	8.48										
DR111-1	0.702717	0.000003	0.513083	0.000003	8.69	18.7160	0.0007	15.5454	0.0007	38.3394	0.0021	0.83060	0.00001	2.04848	0.00005
DR111-2	0.702718	0.000002	0.513083	0.000003	8.69	18.7199	0.0022	15.5467	0.0019	38.3434	0.0048	0.83049	0.00003	2.04827	0.00008

. . . continued

Ratio Sample (SO208)	$^{87}Sr/^{86}Sr$	±2SE	$^{143}Nd/^{144}Nd$	±2SE	εNd	$^{206}Pb/^{204}Pb$	±2SE	$^{207}Pb/^{204}Pb$	±2SE	$^{208}Pb/^{204}Pb$	±2SE	$^{207}Pb/^{206}Pb$	±2SE	$^{208}Pb/^{206}Pb$	±2SE
Profile 4 N off-axis wr															
DR106-1_wr	0.702954	0.000003	0.513047	0.000003	7.98	18.8047	0.0022	15.5460	0.0018	38.4269	0.0044	0.82671	0.00002	2.04347	0.00004
Profile 4 Smnt/Plateau S off-axis															
DR115-1	0.702611	0.000003	0.513115	0.000003	9.31	18.4856	0.0015	15.5082	0.0012	37.9628	0.0030	0.83893	0.00001	2.05364	0.00005
Profile 4 S off-axis															
DR112-1	0.702766	0.000002	0.513065	0.000002	8.33	18.7589	0.0007	15.5484	0.0007	38.3990	0.0019	0.82885	0.00001	2.04697	0.00003
DR112-2	0.702752	0.000002	0.513061	0.000002	8.24	18.7650	0.0007	15.5468	0.0006	38.4012	0.0018	0.82850	0.00001	2.04643	0.00003
DR114-1	0.702879	0.000002	0.513054	0.000002	8.12	18.7931	0.0011	15.5470	0.0012	38.4135	0.0039	0.82727	0.00002	2.04402	0.00010
DR117-4†	0.702715	0.000003	0.513081	0.000003	8.63	18.6769		15.5235		38.2471		0.83117		2.04771	
DR118-4	0.702781	0.000002	0.513068	0.000002	8.39	18.7028	0.0009	15.5384	0.0010	38.3145	0.0007	0.83081	0.00002	2.04860	0.00007
Profile 5															
Profile 5 on-axis															
DR121-1	0.702685	0.000002	0.513073	0.000002	8.49	18.7275	0.0008	15.5403	0.0007	38.3285	0.0007	0.82981	0.00001	2.04664	0.00003
Profile 5 N off-axis															
DR120-1	0.702724	0.000002	0.513067	0.000002	8.37	18.6783	0.0008	15.5360	0.0007	38.2830	0.0007	0.83176	0.00001	2.04959	0.00002
Profile 5 S off-axis															
DR119-2	0.702788	0.000002	0.513043	0.000002	7.90	18.7532	0.0015	15.5450	0.0015	38.3859	0.0045	0.82893	0.00002	2.04690	0.00010
DR119-2*	0.702803	0.000004	0.513061	0.000004	8.25	18.7508	0.0009	15.5424	0.0008	38.3784	0.0020	0.82889	0.00001	2.04676	0.00004
DR119-4	0.702781	0.000003	0.513063	0.000003	8.30	18.7517	0.0008	15.5433	0.0007	38.3794	0.0019	0.82890	0.00001	2.04672	0.00004
Axial Seamount															
Axial Smnt															
DR122-2	0.702715	0.000002	0.513063	0.000002	8.29	18.7700	0.0008	15.5472	0.0008	38.3982	0.0022	0.82830	0.00001	2.04572	0.00005

† = only conventional Pb
* = TIMS Replicates
wr = whole rock samples
all others are volcanic glass samples

Danksagung

Mein größter Dank geht jedoch an die beiden Menschen, die leider an diesem Ereignis nicht mehr teilhaben können. Ohne ihren Glauben an und ihr Vertrauen in mich wäre ich nie so weit gekommen und dafür werde ich ihnen immer dankbar sein.

Lebenslauf

Persönliche Daten

Name	Herbrich
Vorname	Antje
Geburtsdatum	27.02.1980
Geburtsort	Bautzen, Sachsen

Persönliche Daten

1996-1999	Schiller-Gymnasiums Bautzen (Abitur)
1999-2002	Universität Leipzig, Studium der Chemie
2002-2004	Universität Leipzig, Studium der Geologie
2004-2006	Universität Bremen, Studium der Geowissenschaften (B.Sc.)
2006-2009	Universität Bremen, Studium der Geowissenschaften (M.Sc.)
Seit 2010	Universität Kiel, Promotionsstudium (Geochemie)

Erklärung

Hier mit erkläre ich, Antje Herbrich, dass ich die hier vorgelegte Abhandlung, selbstständig und ohne Zuhilfenahme unerlaubter Hilfsmittel erstellt habe. Sie ist, abgesehen von der Beratung durch meinen Betreuer, in Form und Inhalt meine eigene Arbeit, die unter Einhaltung der Regeln guter wissenschaftlicher Praxis der Deutschen Forschungsgemeinschaft entstanden ist. Ferner erkläre ich, dass ich weder diese noch eine ähnliche oder Teile dieser Arbeit an anderer Stelle im Rahmen eines Prüfungsverfahren vorgelegt habe.

Kiel, 30.10.2014 ....

Antje Herbrich